Photonic Devices for Sensing and Security Applications

Adrian Dzipalski

A thesis submitted for the degree of

Doctor of Philosophy

Heriot-Watt University

School of Engineering and Physical Sciences

August 2017

Abstract

The main aim of this thesis is the numerical and experimental verification of structured micro- and nano-scaled optical devices fabricated with e-beam, photolithography, reactive ion etching and embossing. Two separate themes were addressed; sensing of electromagnetic pulses by electro-optic non-linear guided wave photonic devices and free space photonic devices for security and anti-counterfeiting in polymer banknotes.

The first theme was led by a comparison between two photonic devices used as extrinsic fibre optic sensors for the detection of short duration electromagnetic pulses (EMPs). A suitable electro-optic substrate was used for the fabrication of both micron sized waveguide-based evanescent coupling photonic devices, modelled using beam envelope methods, and its nano-structured surface Plasmon enhanced counterpart, modelled using FDTD. Both devices are capable of detecting EMPs with field strengths ranging from 50 – 500kV/m with pulse durations from 200ns – 2000ns. The surface enhanced plasmonic device showed improved device sensitivity and tunability, with a more linearized response along with greater ease of integration with optical fibres.

In the second theme the photonic devices were used for image formation through diffractive optical methods with a view to polymeric mass replication. Multilevel 2μm - 8μm feature size diffractive optical elements, designed for dual colour operation in the scalar domain, were compared to 250nm feature size binary phase modulated Bragg gratings for single colour operation in the resonance domain. Both devices are capable of generating high fidelity images under appropriate illumination. The scalar domain elements, designed for 450nm and 650nm illumination, showed measured diffraction efficiencies of 37% and 55% in the 0th order for each of the respective illumination wavelengths. Operating at 532nm, the diffraction efficiency of the resonance domain element was measured to be 70%. The resonance domain element is significantly shallower than the scalar domain device with a reduced number of phase levels (2 compared to 16). With the final aim of this application area being replication on a flexible base substrate, the elements with larger feature sizes would represent challenging replication process (in terms of linearization of depth profile) whereas the smaller feature sizes would be more challenging in lateral dimensions. In both cases the potential for counterfeiting would be reduced and the addition of a second image at a different illumination wavelength for the scalar domain element would lead to a further enhanced degree of security.

Acknowledgements

First of all, I would like to thank Prof. Mohammad R. Taghizadeh who was my mentor during my undergraduate degree, and my supervisor during this PhD. His supervision, patience and advice through the years has been invaluable and has always guided me in the right direction.

I would also like to thank Dr. Andrew Waddie for his supervision and assistance during the PhD. For the numerical and modelling assistance as well as reading through all the drafts of papers and taking the time to proof read this thesis.

I would also like to thank Neil Ross for the endless help in micro fabrication, tutorage and for all the long hours spent in the clean room.

I would like to thank the collaborators from AWE, Ian Thurston and Mike Moutrie for funding and believing in the project.

I was also helped by so many people during my PhD and it is hard to mention them all by name here. Dr William MacPherson for sparking my interest in research. I would like to thank Ioannis Bitharas for those Thursdays spent going through COMSOL models. Dr.Jonathon Morton for his help during the PhD. Dr. Wojiciech Gora for the motivational and up lifting speeches.

I would also like to thank the guys with whom I shared an office with, Dr.Ross Donaldson and Dr.Aurora Maccarone for putting up with me from the start of the PhD and all those cakes.

I would like to thank Jennifer Welz for the support, understanding and help relighting a passion which was nearly lost.

Finally, I would like to thank my parents, for without their endless support and encouragement it would have been really hard. You would be happy to know that the end is near.

Research Thesis Submission

Name*:*	Adrian Dzipalski		
School:	School of Engineering and Physical Sciences		
Version: *(i.e. First, Resubmission, Final)*	First	Degree Sought:	Doctor Of Philosophy

Declaration

In accordance with the appropriate regulations I hereby submit my thesis and I declare that:

1) the thesis embodies the results of my own work and has been composed by myself

2) where appropriate, I have made acknowledgement of the work of others and have made reference to work carried out in collaboration with other persons

3) the thesis is the correct version of the thesis for submission and is the same version as any electronic versions submitted*.

4) my thesis for the award referred to, deposited in the Heriot-Watt University Library, should be made available for loan or photocopying and be available via the Institutional Repository, subject to such conditions as the Librarian may require

5) I understand that as a student of the University I am required to abide by the Regulations of the University and to conform to its discipline.

6) I confirm that the thesis has been verified against plagiarism via an approved plagiarism detection application e.g. Turnitin.

*   *Please note that it is the responsibility of the candidate to ensure that the correct version of the thesis is submitted.*

Signature of Candidate*:*		Date:	

Submission

Submitted By *(name in capitals):*	
Signature of Individual Submitting:	
Date Submitted:	

For Completion in the Student Service Centre (SSC)

Received in the SSC by *(name in capitals):*			
Method of Submission *(Handed in to SSC; posted through internal/external mail):*			
E-thesis Submitted (**mandatory for final theses)**			
Signature:		Date:	

Contents

List of Figures

List of Tables

Authors Journal Contributions

Publications

A.J. Waddie, **A. Dzipalski**, M. Taghizadeh et al, Lithium Niobate Waveguides for electromagnetic pulse sensing (EMP), IEEE sensors, Volume 16, Issue 14, Pg5603-5609, July 2016.

A.J Waddie, **A. Dzipalski**, M. Taghizadeh et al, A coupled waveguide based optical sensor for EMP Detection, AWE Journal of Plasma Physics, Volume 2, Pg179-182, 2016.

Conferences

Gold on Lithium Niobate Nanostructured Plasmonic surfaces for sensing applications, **A. Dzipalski**, Photon 16, Leeds, Oral Presentation.

Lithium Niobate Waveguides For Sensing High Powered and Short Duration Electromagnetic Pulses (EMP) , **A. Dzipalski** A.J. Waddie, M. Taghizadeh, EUROEM 2016, London, Oral Presentation.

Effects of RF Electromagnetic Fields on optically Non-Linear Nanostructured Plasmonic Surfaces, A.J. Waddie, **A. Dzipalski**, M. Taghizadeh, EUROEM 2016, London.

Lithium Niobate Optical Waveguide Sensing of RF Electromagnetic Pulses, **A.Dzipalski,** A.J. Waddie, M. Taghizadeh, CLEO 2015, Munich, Oral Presentation.

Chapter 1. Introduction

The main theme of this thesis is the numerical and experimental verification of structured micro and nano scaled optical devices fabricated with e-beam lithography and embossing. The focus of the thesis is split up into two parts, the first of which deals with the application of photonic devices for sensing applications and the second with the applications of these devices in the field of security printing. The question posed in this thesis is whether or not the improvement trend in device performance observed in integrated circuits obtained through the reduction of transistor sizes and increased packing densities can be applied to micro optic devices used for sensing and security applications through the reduction of feature sizes in their design. Both the benefits and drawbacks that this feature size reduction has on the device performance are considered using components which have sub- wavelength structures with feature sizes ranging from 200nm to 1μm. As well as diffractive phase elements with features sizes much larger than the illumination wavelength are produced.

Optical lithography and electron beam lithography are mature technologies which have been widely used for the production of micro structured devices.

The miniaturisation of photonic devices has gone a long way with the development of fabrication technologies that progressively reduce the dimensions of components. Optical devices have advantages in the form of immunity to electromagnetic interference and compact device sizes. The novelty of the optical sensors described in this thesis comes in the form of capabilities of measuring intense short duration electro-magnetic pulses with minimal perturbations of the measured fields, allowing measurements in enclosed spaces as well as being shielded through encapsulation from potentially hazardous environments, offers a smart , reliable and real time sensing capacities of EMPs.

The applications of optical devices ranging from sensing to security, diffractive optical elements which are capable of adding an extra layer of protection against counterfeiting are developed. The novelty of the diffractive phase elements in this thesis comes from that fact that the fabricated fused silica elements are designed to be used as hard masters for the replication onto flexible substrates. To our knowledge this is the first demonstration of pseudo dual colour operation from a DPE embossed on a flexible polymer substrates. The operation is achieved through the illumination with a white light source, commonly available in most smart phones today, producing an easily

distinguishable and visually appealing image to the eye. The complete linearization of the surface relief profile adds an extra layer of protection against forgery and counterfeiting.

In chapter 2 of the thesis the theoretical background behind the fundamental theory of optical waveguides and plasmonics is provided. The various techniques that have been used by other research groups previously for the fabrication of both waveguides and nanostructures are reviewed. The advantages and limitations of each of those in terms of feature sizes, process time and economic viability are considered. Further on, the design and modelling algorithms used in further chapters of the thesis are described with distinctions between the domains used in terms of feature size provided.

Chapter 3 of the thesis deals with e-beam lithography and reactive ion etching parameters and problems commonly encountered during the fabrication of the photonic devices interrogated in the thesis. The focus is on electron beam lithography and the effects the various patterning parameters have on the final structures. These parameters include Write fields, Aperture Size, Stitch Fields, and Acceleration Voltages. An investigation into the properties and tuning of negative tone resists for electron beam lithography is carried out to match the desired properties. An outline of reactive ion etching is presented as well as the effects that various etching parameters have on the selectivity, etch rate, side wall verticality and etched trench quality is investigated. Finally a structured check list of the exact procedure to fabricate the devices is given.

Chapter 4 of the thesis presents the design and experimental results from the electro-optic waveguide based photonic sensor for the detection of intense and short duration electromagnetic pulses (EMP). The modelling of the electric field and the evanescent coupling between waveguides is carried out using the Beam Envelope Method with COMSOL. The optical measurement of different electric field strengths by the sensor as well as the noise removal algorithm based on the Short time Fourier transform are presented. Measurements of the temporal pulse shapes by the optical sensor are carried out and compared to the commercially available d-dot sensors. Potential means for further improvements of the sensing system are discussed.

In Chapter 5 of the thesis an alternative and inherently simpler optical sensor is presented and experimentally tested. The problems identified and associated with the first sensor are addressed and the sensor is designed to alleviate those. It works based on the principle of transmission changes in Surface Plasmon Resonance peaks associated with the reception of an incident Electromagnetic Pulse. The modelling of the device using FDTD

is carried out and an investigation is performed on the effects that various geometric attributes have on the positions of the resonance peaks. As a proof of concept a free space system is designed and experimentally tested and finally an integrated and encapsulated device is fabricated. The optical measurements of different electric field strengths and temporal pulse shapes measured by the sensor are shown and compared the waveguide sensors.

Chapter 6 of the thesis presents a pulse modulated Bragg grating optical device designed in the resonance domain. The design and testing of this device are presented as well as the advantages of using devices with features comparable to the wavelength of illumination. Transmission devices are fabricated to verify the optical performance. Effects that various grating geometries in the forms of under-cut and slanted side walls have on the diffraction efficiency as well as the diffraction angles of the device are investigated. Finally a reflection based device is presented which was designed and optimised to be used as a hard master for replication on flexible substrates.

In Chapter 7 diffractive phase elements which have a two colour pseudo operation characteristics are designed and fabricated for replication and mass production on flexible substrates. An outline of conventionally used mass replication techniques is given and compared to the replication process used and the major sources of material shrinkage occurring are identified. A number of compensation techniques are developed in order to overcome the material shrinkage and produce the desired phase profiles in the replicated copies. The optical outputs of these devices are measured and the effects that different refractive index differences between the substrate and the overcoat have on the optical output are investigated. The effects that surface roughness have on the optical scattering are investigated and an estimation on a level which produces minimal scattering is presented. A novel technique for the application of over coats is developed which achieves a complete planarization of the device.

Chapter 8 of the thesis provides a summary of the work conducted during the PhD and a discussion of the key findings as well as presenting an outlook for future work.

Chapter 2. Guided Wave Optics and Diffractive Optical Elements: Theory, Modelling and Applications

2.1. Waveguides and Plasmonic Devices

Micro fabrication lies at the heart of fabricating miniature structures of micrometre or nanometre sizes for photonic applications. The earliest examples of micro fabrication processes have been in the integrated circuits especially in the semiconductor industry in the fabrication of CMOS devices. The techniques have since gone through a lot of development and applications have found their ways in Micro Electro Mechanical Devices (MEMS), micro machines, micro fluidics and optical devices in particular which is where the focus of this thesis lies.

2.1.1. Waveguide Theory

The first proposed structure for guiding of waves was proposed in the 1890's by Jean Daniel Colladon[1]. In this experiment light was guided by the flow of water discharging from a cylinder filled with water through a hole cut out in it with the guided light being produced by a white light source and can be seen in *Figure 2.1*.
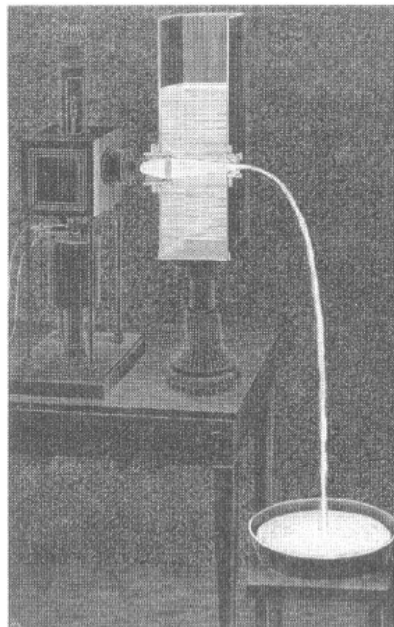
Figure 2.1. Showing the first demonstration of optical wave guiding from 1890 in which light was guided through a discharging water cylinder [1].

A waveguide is a structure that guides waves, either electromagnetic or acoustic, with a minimal loss of energy by restricting the expansion directions to one or two dimensions.

Without applying these physical constraints, waves decrease according to an inverse square law as they expand in three dimensions. Considering a coherent light beam propagating through an optical waveguide via a series of total internal reflections from the interfaces between the core and the cladding of the waveguide. In order for total internal reflection to occur the refractive index of the core must be larger than the refractive index of the surrounding cladding. This can be seen from the *Figure 2.2* below, where θ corresponds to the angle between the wave front and the normal to the interface. Another condition for guidance is that this angle must be larger than the critical angle in order for propagation to occur. In this case, the light confined in the waveguide is a guided mode.
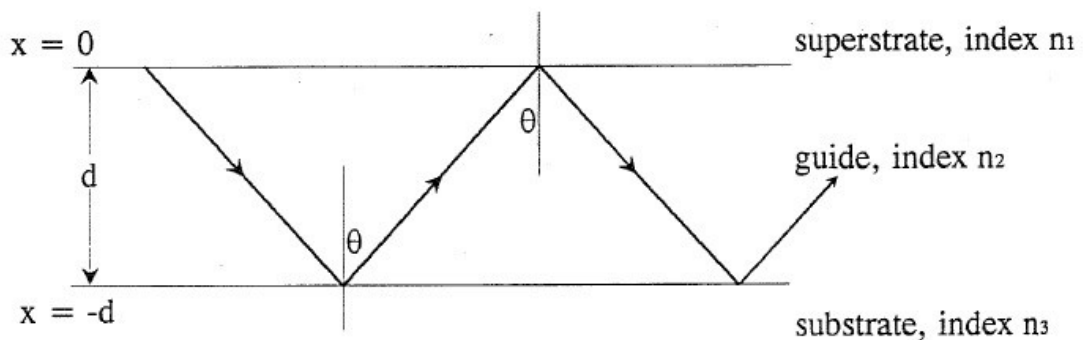
Figure 2.2. Propagation of light through a planar optical waveguide through total internal reflection [2].

Another important parameter to be considered when dealing with waveguides comes in the form of the propagation constant. This is shown from Equation 1 below.

$$\beta = \frac{2\pi}{\lambda} \qquad (2.1)$$

Where β is the propagation constant and λ is the wavelength in free space. In regards to coupling light into the waveguide there exist a number of different approaches that can be used. Approaches worth considering in this section are edge coupling and prism coupling. Edge coupling is the easiest way of launching light into a waveguide in which the light is focused through an objective lens or an optical fibre, propagates through the length of the waveguide and emerges as a divergent beam at the other end. The light can then be gathered by another objective lens or an optical fibre. In planar waveguides a bright horizontal line (dependent on the wavelength of the light source) is observed when guidance is achieved. On comparing edge coupling with prism coupling which will be discussed next, a major advantage becomes apparent in the form of excitation of all the

guided modes at the same time at the expense of coupling efficiency. Single mode operation can be achieved by matching the waist of the input beam to the spot size of the waveguide mode. Fresnel reflections occurring at both facets of the waveguide can be reduced through polishing to achieve an optically smooth surface. A schematic of the technique described can be seen from the *Figure 2.3* below.
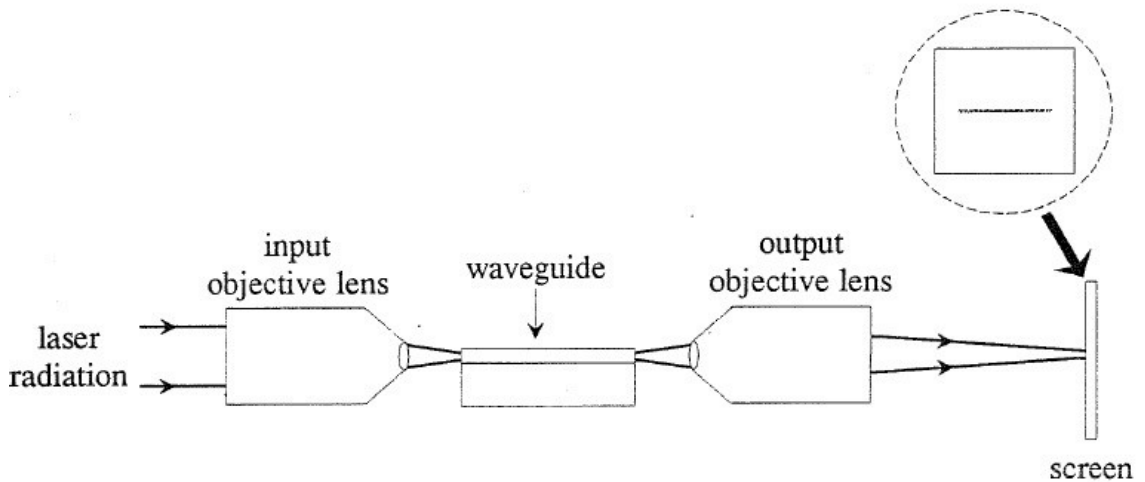
Figure 2.3. Schematic of launching light into a waveguide achieved through edge coupling [2].

The second method of launching light into a waveguide can be accomplished by using a high refractive index prism. The prism in question is pressed down on the surface of the waveguide in order to minimise the air gap between the two surfaces[2]. Typically the air gap should be no larger than half of the operational wavelength. On considering θ (the angle formed between the incident light and the normal to the base of the prism), exceeding the critical angle. The light is totally internally reflected at the base of the prism and a stationary wave is formed. An evanescent field is created in the air gap and the interaction of this evanescent field with the evanescent field of the guided mode results in the coupling of the input light into the waveguide mode. This can only occur when the propagation constant of the light in the prism matches the propagation constant of the light in the guided mode.

$$sin\theta n_p = \sin \Phi n_2 \qquad\qquad (2.2)$$

As a rule of thumb, n_p > n_2 necessitating the use of high refractive index and expensive prisms. The positive attribute of this approach lies in the fact that the guided modes in the

waveguide can be individually excited by altering the angle of incidence. In order to couple light back out from the waveguide, another prism can be used on the output end. The use of two prisms is referred to as the light mode and the use of just one prism is called the dark mode (mainly used in the estimation of propagation constants, refractive index and thickness). The coupling losses using this approach are of the order of ~50 %. A schematic of the approach using 2 prisms can be seen from *Figure 2.4* below. In the figure only the input end of the waveguide is shown, the output coupling end looks the same and another prism is used to gather the output light.
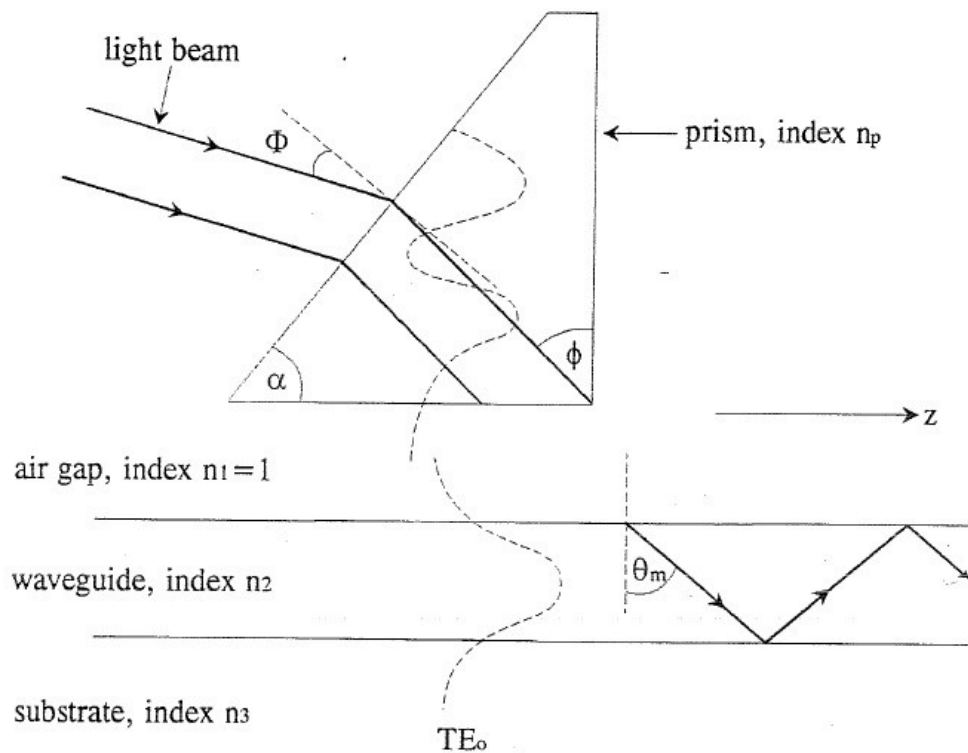
Figure 2.4. Schematic of launching light into a waveguide achieved through prism coupling [2].

Having described the theory behind waveguides and a few of the methods that can be used to couple light into them, the concept of optical switching is introduced next. The idea of optical switching enables signals carried in waveguides or integrated optical circuits to be selectively switched from one circuit to another. The switching mechanism might be triggered through mechanical means such as the physical shifts in the waveguide or through electro optic or magneto optic means. The first are slow switches which are mainly used for changes in the path and the second are fast switches which can be used to perform logic operations or sensing of measurands. The effects mentioned above are both prime examples of non-linear optical properties, in which the behaviour of the propagated light and dielectric polarisation respond non-linearly to the electric field of

the light. The Pockels and Kerr effects, in which the material produces a birefringence proportional to the electric field applied, have been at the heart of research and development with application such as Pockels cells, optical switches and optical sensors. The concept behind the optical switching will be further described in later chapters of this thesis as it forms the basis of the sensing mechanism of one of the devices investigated.

Fibre optic sensors can generally be divided into two categories: intrinsic and extrinsic[3]. In an extrinsic fibre optic sensor, the optical sensors are positioned close to the fibre end which quantify the measurand and couple the corresponding light back into another fibre. A diagrammatic representation is seen in *Figure 2.5*. The fibres only act as a transmission medium. In intrinsic fibre optic sensors on the other hand, the fibre itself is used to quantify the measurand. In this case the fibre is used both as a transmission medium and as a sensor, hence minimising the overall size of the device. Another discrimination that can be made comes in the form of device size. If the quantity is only measured at one point this arrangement can be referred to as point sensing, which is where the operational basis behind electrical sensors lies, providing no further information about the spatial resolution of the quantity. Almost all extrinsic fibre optic sensors work on this basis.
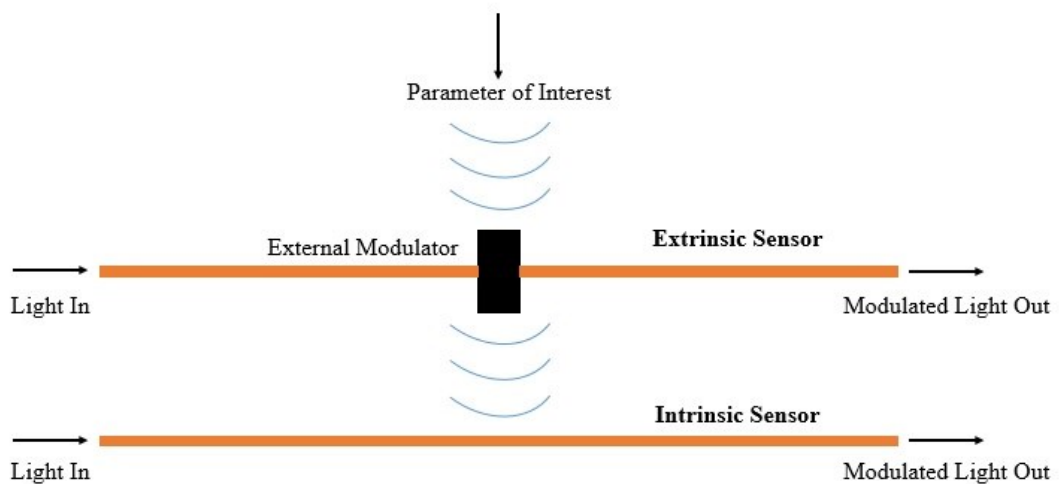
Figure 2.5. Comparison between an intrinsic and extrinsic fibre optic sensors [3].

In order to obtain the full potential, a distributed sensing arrangement must be introduced which is only available when using intrinsic fibre optic sensors. For example by writing multiple Bragg gratings creating a multiplexer in which information about the measurand can be obtained from different points which are all on the same channel. In this arrangement spatial information about the quantity can be obtained.

2.1.2. Surface Plasmon Theory

The field of plasmonics has received a large amount of interest in the last few decades. But the concept behind plasmonics originated with the 4th century Lycurgus cup[4] made out of dichroic glass, or even gothic stained glass in churches which show a different colour depending on the direction of illumination. The glass appears red when back lit and green when illuminated from the front (seen in *Figure 2.6* below). This effect can be attributed to the presence of tiny proportions of gold and silver nanoparticles dispersed in colloidal form throughout the glass. It wasn't until the early 1990's that the glass was carefully inspected under a microscope and the presence of gold and silver nanoparticles with dimensions down to 50 nm in diameter was discovered. The images below show the cup under both illuminations and the associated observable colour changes.

Figure 2.6. Pictures of the 4th Century Lycurgus Cup upon illumination from the front appearing green (LEFT) and appearing red upon back illumination (RIGHT)[4].

Plasmonics have had numerous applications but the most prominent of these comes in the form of Surface Enhanced Raman Scattering (SERS)[5], which is a surface sensitive technique through which the Raman scattering is enhanced by the adsorption of molecules on either a roughened metallic surface or a surface patterned with a nanostructure. The

exact mechanism of the enhancement effect exhibited by SERS can be explained by two theories (both of which are debatable from the literature). The two existing theories are the electromagnetic therory[6] and the chemical theory[7]. In this thesis focus will be paid to the electromagnetic theory which proposes that the enhancement effect can be attributed to the excitation of localised surface plasmons[8].

The increase in Raman signal for adsorbates is due to the enhancement in the electric field provided by the surface. Upon illumination of the metallic surface with incident light, localised surface plasmons are excited. The greatest enhancement is observed when the plasmon frequency is resonant with the illumination source. In order for scattering to occur, the plasmonic oscillations must be perpendicular to the surface, as no scattering would occur if they are in the same plane. This is the reason why a roughened surface or a surface coated with nanoparticles is employed in SERS, as they provide an area for localised surface oscillations to take place. The effect is pronounced because the enhancement occurs twice. The first field enhancement magnifies the intensity of the incident light, exciting the Raman modes of the molecule studies and increasing the Raman scattering. The Raman signal is then excited again by the same mechanism exciting the incident light but this time the total output is even larger. At each increment the enhancement is E^2 equalling E^4 as the total enhancement.

The aforementioned enhancement is frequency dependent and not equal for all frequencies, the frequency is dictated by the metallic surface or the size and arrangement of nanoparticles. It wasn't until 1998 that Ebbesen[9] theory came into light, stating that the intensity of transmitted light through a nanohole surpasses the intensity as suggested by the classical diffraction theory[10] by a few orders of magnitude. Hence the combination of an array of nanoholes in a thin noble metal on a non-linear base substrate brings about another interesting area of research where the induced refractive index changes can be explored by changes in the transmission of the plasmonic resonances, offering a potential for sensing by observing changes in the transmission spectra of the incident light.

2.2. Methods of fabricating optical waveguides in Lithium Niobate

Lithium Niobate is a key material in the photonics industry because of its combination of functional properties as well as commercial availability. It is these characteristics that have placed it at the fabrication fore front of integrated optical devices since the late 60's when its capabilities were understood. In this section of the chapter a review of the

existing technologies used for the fabrication of waveguides in lithium niobate will be carried out.

2.2.1. Titanium In diffusion

This technique was discovered in the early 1970's. It is the most wide spread waveguide fabrication technique for Lithium Niobate and has been extensively studied since its introduction[11]. Although other waveguide fabrication techniques have been found to allow for a much higher optical confinement, it is particularly advantageous because it maintains the electro optic properties of the base substrate and ensures good confinement in both the ordinary and extra ordinary propagation orientations, allowing the propagation of both Transverse Electric and Transverse Magnetic modes. This makes it insensitive to light polarisation[12]. Typically achievable waveguide widths range from 5-10μm and depths from 30-100nm.

The process is started with the deposition of titanium through evaporation or sputtering over the entire substrate. This layer measures 30-100nm based on the guidance wavelength and the degree of confinement required. Through photolithography and lift off the titanium is selectively removed leaving behind the desired pattern. The metal is then diffused into the substrate by heating at temperatures between 900°C and 1050°C for durations ranging from 4-12 hours. (The heating is carried out at temperatures below the Curie temperature of lithium niobate which is 1210°C). A lot of research has been carried out in the diffusion parameters to ensure minimal surface roughness as well as optimisation of the optical properties[13]. To prevent lithium out diffusion, the titanium in diffusion is recommend to be carried out in a wet oxygen atmosphere[14]. This causes the prevention of the out-diffusion of LiO_2 through the neutralisation of Li ions[15] forming a stable LiOH[16] on the surface.

Titanium in-diffused waveguides have been demonstrated to have problems supporting high power densities in single mode operation due to the optical damage occurring during the fabrication.

2.2.2. Annealed Proton Exchange

Annealed proton exchange is another classic technique for the fabrication of waveguides in Lithium Niobate[17]. This technique produces a much larger refractive index

difference between the core and the cladding when compared to the previous process. The achievable refractive index difference is 0.1 but the waveguides fabricated are unsuitable for ordinary light confinement[18]. Proton exchange is often accompanied by subsequent annealing. It permits for a high level of polarisation rejection and resistance to optical damage, in applications requiring shorter operational wavelengths. Annealing was found to be helpful in the recovery of the non-linear coefficients which were compromised during the proton exchange process.

The process is commenced through the immersion of the lithium niobate wafer in a liquid source of hydrogen at a high temperature. These conditions prompt the replacement of Li ions with H ions, causing the change in the extra ordinary refractive index. This leads to the formation of waveguides that only support propagation of light in the extraordinary polarisation or transverse magnetic modes.

Commonly either Benzoic or Toluic acid[19] sources of hydrogen ions are heated to 150 – 400°C and the substrates are left in the bath for several hours, in which the Li ions out diffuse making the mass transfer occur between the substrate and the melt. Waveguides with widths of 1μm and depths of 500nm have been demonstrated using this approach.

2.2.3. Femtosecond Laser Writing

It has been recently demonstrated that waveguides can be fabricated by translating a transparent Lithium Niobate substrate through the focus of a femtosecond laser pulse train[20]. This induces a change in the refractive index of the material through laser induced strain in the crystal matrix of the substrate[21]. The dimensions of the fabricated waveguides are 8μm in width and depth with a waveguide separation of 2μm. The fabricated waveguides can only guide light in the transverse magnetic polarisation and offer a low refractive index change in the waveguides. In this technique the waveguides are fabricated in a 500μm thick z-cut Lithium Niobate substrate, using a Yb (Ytterbium) glass mode locked cavity dumping femtosecond laser emitting at 1040nm. 370nJ pulses are focused at 150μm below the surface of the wafer using a x60 0.5NA objective lens. The beam diameter of the fabrication laser in the medium was estimated to be ~2.5μm. The substrate was translated along the x-axis while the writing laser was polarised along the y-axis. The propagation of light along the fabricated waveguide was found to be highly polarisation sensitive only allowing for Transverse Magnetic propagation. The

fabricated waveguides are designed for single mode operation at an operational wavelength of 1550nm with an estimated loss of 0.3dB.

2.2.4. Smart Cut or Crystal Ion Slicing

The waveguides fabricated using this technique are formed from a thin (>1μm) Lithium Niobate film bonded to a silicon dioxide layer of 50-100nm thickness which can then be attached to the carrier wafer to facilitate the mechanical handling and processing[22]. Waveguides with widths of up to 800nm have been demonstrated to offer a high degree of optical confinement and insensitivity to propagation polarisation.

The process is started by obtaining a thin film of Lithium Niobate bonded to a lithium niobate carrier wafer. The advantages brought by this process come in the form of uniform film thickness quality of the bulk crystal as well as highly tuneable film thicknesses. A chromium metallic mask is first laid to protect the waveguides followed by the spin coating of a resist. The resist is patterned through e-beam lithography and the pattern transferred to the substrate through reactive ion etching (RIE), with the waveguides left behind after the etching. The fabricated waveguides support both polarisations and have a high refractive index contrast due to their ridge nature.

2.2.5. Optical Grade Dicing

This is yet another fabrication technique which has come into the spot light in the last few years due to the significant improvements made in wafer dicing technology[23]. In optical grade dicing the formation of ridge waveguides of width 6μm and depth of 10μm has been demonstrated in Lithium Niobate substrates. One of the major limitations associated with this technique is that the spacing between adjacent waveguides is limited by the width of the dicing saw blade used (~100μm). In the first step both 6μm wide channels are milled on a x-cut Lithium Niobate wafer. 90nm of titanium is then deposited over the substrate and diffused at 1000°C for 10hrs. The taper ridge waveguides are produced by the dicing of the in diffused wafer with a precision saw. The waveguides support a high refractive index contrast and can be used in the propagation of both Transverse Electric and Transverse Magnetic polarisations.

2.3.   Methods of Fabricating Nanostructures Supporting Surface Plasmons.

2.3.1.   Nanosphere Lithography

Nanosphere lithography is an inexpensive promising fabrication tool for the production of regular and homogeneous arrays of nanoparticles with different sizes [24]. This method combines both the advantages of the top down and bottom up approaches. The top down approach involves selectively removing material from the top of the surface until the desired depth and the bottom up involves the building up of material from the base of the substrate until the desired height is reached.

The process is commenced through the coating of the substrate with a suspension containing a monodisperse spherical colloid composed of polystyrene nanospheres, only after a chemical treatment enhancing their hydrophilic characteristics. The surface is then dried and a hexagonally close packed (HCP) monolayer is left behind. This mask is then used to selectively pattern the substrate through the deposition of a metal or material of interest through the interstices of the ordered polystyrene spheres. The mask lift off, which subsequently occurs through sonification or submersion in a stripper, leaves behind an array of nanoholes on the surface of the substrate. This techniques was first reported in 1981[25].

The advantages held by this technique are that large substrate areas can be patterned quickly, it is a relatively inexpensive, the final feature sizes can be controlled by adjusting the sizes of the polystyrene balls ranging from a few microns to a few nanometres, or etching of the suspension to get to the desired size and packing factor of the array can be changed by the alteration of the colloidal suspension or deposition technique used.

2.3.2.   Focused Ion Beam Milling

Focused ion beam milling was first used to fabricate nanohole arrays in metallic films[26]. The focused ion beam makes use of a beam of low energy ions to selectively remove material from the sample through collisions and is capable of achieving resolutions down to 10nm[27]. The most commonly used source material is gallium. It is a mask less, direct writing technique in which the incursion depth of the ions can be tuned by adjusting the ion energy hence facilitating the fabrication of nanoholes[28]. There exist

two mechanisms in FIB, namely sputtering and redeposition. During sputtering the high energy ions remove material from the substrate through collisions, reducing their momentum in doing so. The milled depth and volume can be controlled by the ion beam current and is governed by the material properties. On the other hand, during redeposition material removed from the substrate and is either relocated on the surface or sputtered away. The redeposited volume can be estimated from both the material properties as well as the ion beam current. The parameters have been extensively researched in the past in order to achieve nanohole arrays with excellent mechanical and optical properties. The disadvantages of this technique lies in the fact that it is expensive, time consuming , not suited for mass fabrication and requires a conducting surface.

2.3.3. Thermal Scanning Probe Lithography

This is a new and emerging technology that can be used for patterning of nanostructures with <20nm lateral and <2nm vertical resolution[29]. It is a proximity effect free technique, which has a low cost and can be carried out in an inert atmosphere for the creation of dense guiding patterns. The operational principles in this techniques rely on the resistive heating of the cantilever of an Atomic Force Microscope (AFM) to temperatures of up to 1000°C. The bringing of this tip in contact with the heat sensitive resist (PPA[30]) results in the evaporation of the polymer in nano meter sized areas. The resist used is a self-amplified depolymerizing material with a decomposition temperature of 150°C[31]. Through heating the tip above the aforementioned temperature, the polymer evaporation is enhanced by the short-tip resist time interactions. The patterning parameters of highest significance are the tip temperature, the contact duration and the force applied. Due to the quick evaporation time, a high throughput is achievable of sizes up to $10^4 - 10^5 \, \mu m^2/h$, where the tip contact pressure is used to modulate the writing depth. The resist is applied through spin coating and a high resolution is achieved through the use of super sharp silicon tips with a nominal apex radius of 3nm. The temperature is set to 700°C and 10-40nN of force is applied at 5ms durations. Another inherent advantage is the combination of writing and imaging at the same time which is a closed loop lithography, allowing for the correction of lithographic conditions directly during the writing process. After writing, an oxygen plasma is used to ash the resist, removing the remainder of the resist from the trenches. The minimum achievable features are dependent on the shape and geometry of the tip. Due to the fact that it is conical, recommendation follows the use of really thin resist layers to push the resolution. Writing of deep patterns

in thick resists has a limiting effect because the material will also be removed by the upper conical part of the cantilever tip, if the writing depth is larger than the radius of the tip. Thusly the resolution at small writing depths is determined by the radius of the tip.

2.3.4. X-ray Lithography

X-rays generated through a synchrotron are most suited for the fabrication of sub-micron structures with high aspect ratios[32]. The resist layer thicknesses are of the order of 50-100μm. In this technique the resolution is set by the tow phenomena (Fresnel diffraction and the paths of photoelectrons from an irradiated area to the area of geometric shadows). These tend to have opposing tendencies in their influence on resolution. The diffraction effect on the lateral dimensions increases whereas the photo electron range decreases with an increase in wavelength. Therefore the total deviation has a minimum at a certain spectral range close to the cross over point of the two functions. Thus structures with dimensions of around 1μm and height of 50μm are achievable. This technique is however very expensive, has a low throughput, requires a mask and suffers from proximity effects.

2.4.   Modelling Methods Used For Photonic Devices

In this section a review of the modelling techniques used in the design of photonic devices will be carried out showing the inherent advantages and disadvantages of each. The background principles behind the beam envelope method (BEM) are first described and it application to electromagnetic wave propagation in waveguides is shown in Chapter 4. The scalar domain for DOE design is then looked at as well as the associated limitations arising from feature size (larger than wavelength) with an application shown in Chapter 6. The resonance domain is then compared, which considers much smaller feature sizes (comparable to wavelength) as well as accounting for polarisation scattering effects, this method is used in Chapter 7. Finally FDTD which is a fully vectorial method producing both time and frequency domain information about photonic devices, is described and can be used for the modelling of the sub-wavelength features used in Chapter 5.

But first, we will state the basic electromagnetic equations and show a derivation of the wave equation. Assuming that the electric and magnetic fields are constrained to the y and z-directions and are functions of x and t, this gives rise to a linearly polarised plane wave traveling in the x direction. Maxwell's equations[33] are as follows;

$$\nabla . E = 0 \tag{2.3}$$

$$\nabla \times E = -\frac{\partial B}{\partial t} \tag{2.4}$$

$$\nabla . B = 0 \tag{2.5}$$

$$\nabla \times B = \mu_0 \varepsilon_0 \frac{\partial E}{\partial t} \tag{2.6}$$

Now taking the curl of E and B,

$$\nabla \times E(x,t)\boldsymbol{j} = \frac{\partial E}{\partial x}\boldsymbol{k} \tag{2.7}$$

$$\nabla \times B(x,t)\boldsymbol{k} = -\frac{\partial B}{\partial x}\boldsymbol{j} \tag{2.8}$$

And equating the magnitudes,

$$\frac{\partial E}{\partial x} = -\frac{\partial B}{\partial t} \tag{2.9}$$

Implying that the spatial variation of the magnetic field gives rise to a time varying electric field and vice versa. On taking a partial derivative,

$$\frac{\partial^2 E}{\partial x^2} = \mu_0 \varepsilon_0 \frac{\partial^2 E}{\partial t^2} \tag{2.10}$$

$$\frac{\partial^2 B}{\partial x^2} = \mu_0 \varepsilon_0 \frac{\partial^2 B}{\partial t^2} \qquad (2.11)$$

Both the electric field and magnetic field equations have the form of the wave equation shown below

$$\frac{\partial^2 \psi}{\partial x^2} = \frac{1}{v^2} \frac{\partial^2 \psi}{\partial t^2} \qquad (2.12)$$

2.4.1. Beam Envelope Method

The beam envelope method is used for the modelling of the electromagnetic full wave propagation[34]. In an attempt to simulate the transmission of an electromagnetic wave, which propagates in an optical waveguide, a problem arises, which comes in the form of the rapid oscillation of the propagating electromagnetic wave in the direction of propagation. In order for the above mentioned scenario to be computed using standard methods such as Finite Element Method (FEM), a really fine mesh is required which must be much smaller than the propagation wavelength, hence making the processing quite intensive in terms of computer resources. The beam envelope method , provides a way of solving for a slowly varying electric field envelope rather than the computationally intensive rapid electric field. This occurs on the assumption that the direction of propagation is well defined in the optical components.
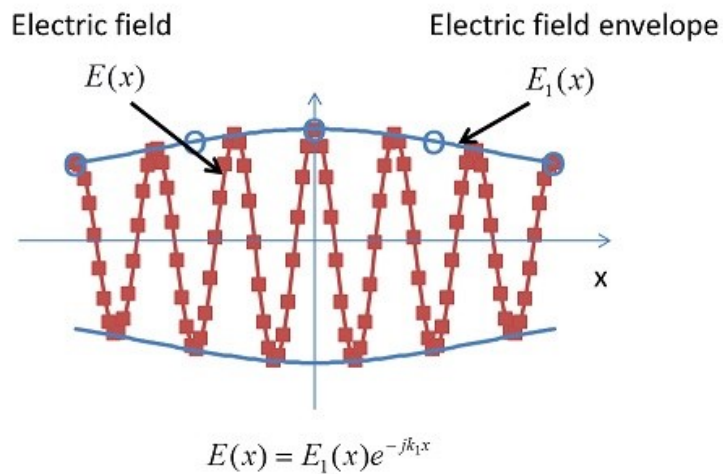
Figure 2.7. The high frequency electric field wave and the sampling points required to resolve it in comparison to the electric field envelope and the sampling position required to resolve it [34].

18

The direct solution of the electric field requires for the oscillation to be resolved with sample points that are dense enough to avoid aliasing. This can be seen from the *Figure 2.7* , which provides a graphic comparison of the number of data points required for the computation of the electric field and the electric field envelope. The Nyquist theorem suggests at least 3 sample points per wavelength to resolve the wave. Numerical modelling suggest more than 3 points, in discretization of the problem. The finite elements method can be used to solve the electromagnetic field propagation. In this method it is recommended having at least 5 quadratic elements per wavelength. However, solving the slowly varying field envelope, requires a lot less sample points as well as a much coarser mesh size. The beam envelope gets factorised hence eliminating the rapidly oscillating component. The wave vector is provided as an input to this method. To recover the real field, the solution E1(x) can be multiplied with the fast varying field vector. There are no particular approximations applied in this method.

2.4.2. Scalar Domain

The scalar diffraction theory is often used in the design and characterisation of diffractive optical elements[35]. It is a straightforward approach with minimal computational burden. However in practise, this theory is only valid if the feature sizes are much greater than the wavelength of the incident illumination. There exist two fundamental assumptions associated with the use of the scalar diffraction theory when relating to DOE design. The first is that the optical field past the DOE can be related to the incident field by a transmission function[36] and the second involves the method used to propagate the field to the plane of interest. For most applications, this can be considered to be in the far field. In the near field the Fraunhoffer diffraction method is inadequate. Fresnel propagation is used for near field which is still just an approximation. In general it is found that, if the feature sizes are a few wavelengths, the error associated with the scalar diffraction theory is ±5% and it does not account for polarisation. It is applicable to infinitely thin substrates and works best at shallow diffraction angles. A reduction in feature size makes the elements polarisation sensitive. The angular spectrum approach hence becomes handy, which is rigorous within the scalar domain and equivalent to TE and TM field propagations[37]. Alternatively the rigorous coupled wave approach, which is computationally more demanding and insensitive to feature sizes can be used.

2.4.3. Resonance Domain

In a situation in which the feature sizes drop down to sizes comparable to the wavelength of the incident light the resonance domain has to be used. In this circumstance, the effects that scattering and polarisation can no longer be ignored as in the scalar theory. Both the electric and magnetic field are calculated here, as opposed to only one with the scalar theory. In the scalar domain the output is restricted to low spatial frequencies and small diffraction angles. Usually higher diffraction orders accompany the first diffraction order. In the resonance domain the contributions from the higher diffraction orders are avoided because they are all evanescent apart from the -1st and the 0th. The two orders are well separated by a large diffraction angle and the diffraction efficiencies attainable are of the order of ~99% without the need for anti-reflection coatings in comparison to ~93% for the scalar diffraction theory. In the resonance domain surface relief gratings can be modelled with the effective grating model[38] which includes both the 0th and -1st diffraction orders. The high diffraction efficiency of the gratings can be explained by the two wave Bragg diffraction phenomena[39]. In the model the profile of the grating groove is decomposed into sub layers. Light diffracted from the sub layers constructively interferes and results in the previously mentioned high diffraction efficiencies.

2.4.4. FDTD

In this computational method, Maxwell's time dependent curl equations are solved through their conversion to finite difference equations. The equations then get solved in a time marching sequence by alternating the computation of the electric and magnetic fields in an interlaced spatial grid. This method was first proposed by Yee[40] for the analysis of the scattering of an electromagnetic pulse by a perfectly conducting cylinder. Since the initial demonstration of its potential, the FDTD method has become a useful tool in modelling a variety of applications including electromagnetic waves, interference effects and surface plasmons. This computational technique has a number of inherent advantages and has grown into wider use because of them. These advantages include;

- It is robust and accurate, sources of errors are well understood and documented.
- Treats non-linear behaviour naturally being time domain, FDTD can directly calculate the non-linear response.

- Treats impulsive behaviour naturally, can provide ultra wide band waveforms or steady state responses at any frequency.
- It provides a systematic approach to solving problems.

With the increase in computing resources available, a positive trend can be observed in terms of numerical simulations, and becomes increasingly important when discretizing a spatial units over a volume, inherently requiring large amounts of random access memory (RAM). The FDTD method that was used in the solution of various problems and multiple publications are based on this method[41].

In order to solve an electromagnetic problem, we need to discretise Maxwell's equations in both time and space using a central difference approximation. The electric and magnetic field components are allocated space and marched in time. For a one dimensional representation, assuming a free space propagation medium Ex and Hy are shifted in space by half a cell and in time by half a time step. This can be seen from the figure below showing a 1 dimensional sketch of the Yee Cell[42] used in the solution of the problem.
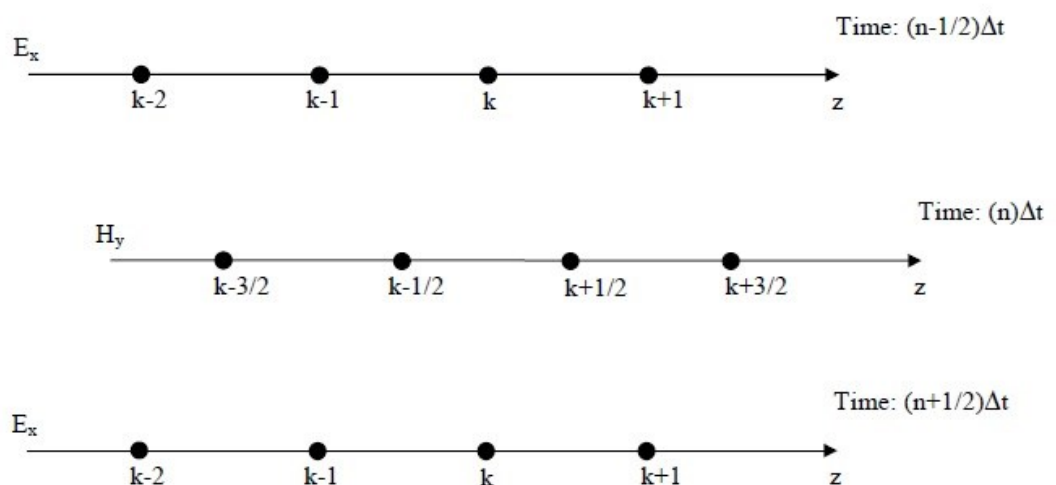
Figure 2.8. Positions and shifts of the electric and magnetic field vectors on a 1D of the Yee space lattice [42].

The Yee Cell

The first step in running the FDTD algorithm is the discretization of the computational space into cells and the definition of the location in which the electric and magnetic field vectors are located in a staggered fashion. A graphic representation of the cell can be seen from *Figure 2.11*.
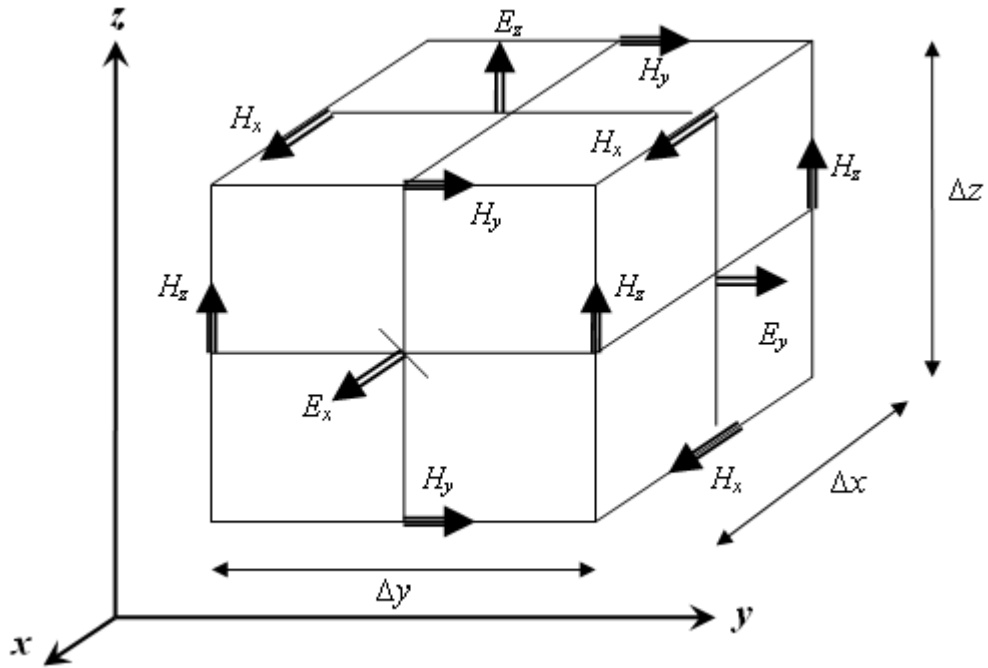
Figure 2.10. Positions of the electric and magnetic field vectors on a cubic cell of the Yee space lattice [41].

In each cell there are 3 electric field vectors and 3 magnetic field vectors which are defined. They are not located at the same positions. The magnetic field component is located at the centre of the face of the cell and points normal to the face. The electric field component is located at the centre of the edge of the cell and is parallel to the edge of the face. The two configurations depicted above demonstrate Faraday's and Ampere's Laws. The electric field vector forms loops around the magnetic field (Faraday's Law) and the magnetic field vector forms loops around the electric field (Ampere's Law).

The computation of both the electric field values and the magnetic field values in every cell is carried out iteratively in time. Hence at each time step there are 6 individual values of field vectors computed. The electric and magnetic fields are not only offset in space but also in time, as they are not calculated at the same time. This is the reason why this algorithm is called the leap frog[43]method.

The FDTD computations in this thesis were carried out using a commercially available software package from Lumerical[44]. It provides a state of the art method of solving Maxwell's curl equations in complex geometries. It is a fully vectorial method capable of producing both frequency and time domain information, offering a substantial amount of insight into problems and applications in electro magnetics and photonics. It is discrete in both time and space. Fields and materials are described on a discrete mesh made up of

Yee cells. The Maxwell equations are solved discretely in time, where the time step is related to the mesh size through the speed of light.

2.5. References

[1] J. Hecht, "Daniel Colladon and the origin of light guiding Daniel Colladon," *Ecoc*, pp. 1–34, 2011.

[2] P. K. Tien and R. Ulrich, "Theory of Prism-Film Coupler and Thin-Film Light Guides," *J. Opt. Soc. Am.*, vol. 60, no. 10, p. 1325, 1970.

[3] P. M. Tracey, "Intrinsic Fiber-Optic Sensors," *IEEE Trans. Ind. Appl.*, vol. 27, no. 1, pp. 96–98, 1991.

[4] I. Freestone, N. Meeks, M. Sax, and C. Higgitt, "The Lycurgus Cup - A Roman nanotechnology," *Gold Bull.*, vol. 40, no. 4, pp. 270–277, 2007.

[5] T. Vo-Dinh, "Surface-enhanced Raman spectroscopy using metallic nanostructures," *TrAC - Trends Anal. Chem.*, vol. 17, no. 8–9, pp. 557–582, 1998.

[6] G. C. Schatz, M. A. Young, and R. P. Van Duyne, "Electromagnetic mechanism of SERS," *Top. Appl. Phys.*, vol. 103, pp. 19–46, 2006.

[7] H. Daniell, "NIH Public Access," vol. 76, no. October 2009, pp. 211–220, 2012.

[8] K. A. Willets and R. P. Van Duyne, "Localized Surface Plasmon Resonance Spectroscopy and Sensing," *Annu. Rev. Phys. Chem.*, vol. 58, no. 1, pp. 267–297, 2007.

[9] T. W. Ebbesen *et al.*, "Extraordinary optical transmission through sub-wavelength hole arrays," *Nature*, vol. 86, no. 6, pp. 1114–7, 1998.

[10] J. Weiner, "The physics of light transmission through subwavelength apertures and aperture arrays," *2009 Opt. Data Storage Top. Meet. ODS 2009*, pp. 13–15, 2009.

[11] G. J. Griffiths and R. J. Esdaile, "Analysis of Titanium Diffused Planar Optical Waveguides in Lithium Niobate," *IEEE J. Quantum Electron.*, vol. 20, no. 2, pp. 149–159, 1984.

[12] R. V. Schmidt and I. P. Kaminow, "Metal-diffused optical waveguides in LiNbO3," *Appl. Phys. Lett.*, vol. 25, no. 8, pp. 458–460, 1974.

[13] S. Fouchet, A. Carenco, C. Daguet, R. Guglielmi, and L. Riviere, "Wavelength

Dispersion of Ti Induced Refractive Index Change in LiNbO3 as a Function of Diffusion Parameters," *J. Light. Technol.*, vol. 5, no. 5, pp. 700–708, 1987.

[14]   T.Crasto,V.Sivan and T.Nguyen, "Titanium Free Optical Waveguides In Lithium Niobate Produced by Etching During Indiffusion of Titanium", 2011 Conference on Lasers and Electro-Optics Europe and 12th European Quantum Electronics Conference, Munich, 2011.

[15]   J. L. Jackel, C. E. Rice, and J. J. Veselka, "Proton exchange for high-index waveguides in LiNbO3," *Appl. Phys. Lett.*, vol. 41, no. 7, pp. 607–608, 1982.

[16]   R. J. Holmes and D. M. Smyth, "Titanium diffusion into LiNbO3 as a function of stoichiometry," *J. Appl. Phys.*, vol. 55, no. 10, pp. 3531–3535, 1984.

[17]   P. Nekvindová *et al.*, "Annealed proton exchanged optical waveguides in lithium niobate: Differences between the X- and Z-cuts," *Opt. Mater. (Amst).*, vol. 19, no. 2, pp. 245–253, 2002.

[18]   W. Liao, X. Chen, Y. Chen, and Y. Xia, "Waveguides From Effective Indices," *America (NY).*, vol. 22, no. 7, pp. 1334–1340, 2005.

[19]   K. K. Wong, I. of Electrical Engineers, and I. (Information service), *Properties of Lithium Niobate*. INSPEC/Institution of Electrical Engineers, 2002.

[20]   R. R. Thomson, S. Campbell, I. J. Blewett, A. K. Kar, and D. T. Reid, "Optical waveguide fabrication in z-cut lithium niobate (LiNbO3) using femtosecond pulses in the low repetition rate regime," *Appl. Phys. Lett.*, vol. 88, no. 11, pp. 1–4, 2006.

[21]   D. J. Little, M. Ams, P. Dekker, G. D. Marshall, and M. J. Withford, "Mechanism of femtosecond-laser induced refractive index change in phosphate glass under a low repetition-rate regime," *J. Appl. Phys.*, vol. 108, no. 3, 2010.

[22]   H. Lu *et al.*, "Enhanced electro-optical lithium niobate photonic crystal wire waveguide on a smart-cut thin film," *Opt. Express*, vol. 20, no. 3, p. 2974, 2012.

[23]   N. Courjal *et al.*, "Low-loss LiNbO3 tapered-ridge waveguides made by optical-grade dicing," *Opt. Express*, vol. 23, no. 11, p. 13983, 2015.

[24]   S. M. Gruner, "Feature article," *Biochemistry*, pp. 7562–7570, 1989.

[25]   Fischer, U.C. and Zingsheim, H.P., Submicroscopic pattern replication with visible light. Journal of Vacuum Science and Technology, 19(4), pp.881-885,1981 .

[26] L. A. Giannuzzi and F. A. Stevie, "A review of focused ion beam milling techniques for TEM specimen preparation," *Micron*, vol. 30, no. 3, pp. 197–204, 1999.

[27] H.-W. Li, D.-J. Kang, M. G. Blamire, and W. T. S. Huck, "Focused ion beam fabrication of silicon print masters," *Nanotechnology*, vol. 14, no. 2, pp. 220–223, 2003.

[28] C. Escobedo, "On-chip nanohole array based sensing: a review.," *Lab Chip*, vol. 13, no. 13, pp. 2445–63, 2013.

[29] R. Garcia, A. W. Knoll, and E. Riedo, "Advanced Scanning Probe Lithography.," *Nat. Nanotechnol.*, vol. 9, no. 8, p. 577., 2014.

[30] A. W. Knoll *et al.*, "Probe-based 3-D nanolithography using self-amplified depolymerization polymers," *Adv. Mater.*, vol. 22, no. 31, pp. 3361–3365, 2010.

[31] S. Gottlieb *et al.*, "Thermal scanning probe lithography for the directed self-assembly of block copolymers," *Nanotechnology*, vol. 28, no. 17, p. 175301, 2017.

[32] E. Di Fabrizio *et al.*, "X-ray lithography for micro- and nano-fabrication at ELETTRA for interdisciplinary applications," *J. Phys. Condens. Matter*, vol. 16, no. 33, pp. S3517–S3535, 2004.

[33] B. Lynda Williams, "Simple Derivation of Electromagnetic Waves from Maxwell's Equations," vol. 2, no. 4, pp. 2–3.

[34] S. Friedel and C. M. Gmbh, "Novelties in COMSOL for Modeling Optical Nanostructures COMSOL – an integrated simulation environment Multiphysics Optical Nanostructures - Multiphysics Systems ? COMSOL Applications of Nano - Optical Systems," 2013.

[35] S. Mellin and G. Nordin, "Limits of scalar diffraction theory and an iterative angular spectrum algorithm for finite aperture diffractive optical element design," *Opt. Express*, vol. 8, no. 13, p. 705, 2001.

[36] J. W. Goodman, *Introduction to Fourier Optics*. W. H. Freeman, 2005.

[37] Smith, G.S., An introduction to classical electromagnetic radiation. Cambridge University Press. 1997 .

[38] M. Golub and A. Friesem, "Effective grating theory for resonance domain

surface-relief diffraction gratings.," *J. Opt. Soc. Am. A. Opt. Image Sci. Vis.*, vol. 22, no. 6, pp. 1115–26, 2005.

[39]   J. Turunent, P. Blair, J. M. Miller, M. R. Taghizadeh, and E. Noponen, "Bragg Holograms With Binary Synthetic Surface-Relief Profile," *Opt. Lett.*, vol. 18, no. 12, pp. 1022–1024, 1993.

[40]   K. Yee, "Numerical solution of initial boundary value problems involving Maxwell's equations in isotropic media," *Antennas and Propagation, IEEE Transactions on*, vol. 14, no. 3. pp. 302–307, 1966.

[41]   J. B. Schneider, "Understanding the Finite-Difference Time-Domain Method," 2017.

[42]   H. Loui, "1D-FDTD using MATLAB," *Ecee.Colorado.Edu*, no. September, pp. 1–13, 2004.

[43]   P. Young, "The leapfrog method and other 'symplectic' algorithms for integrating Newtons's laws of motion," *Lect. notes Univ. california, St. cruz*, no. 1, pp. 1–15, 2009.

[44]   http//:www.lumerical.com .

Chapter 3. Fabrication of Photonic Devices

3.1. Introduction

Lithography has been at the heart of photonic device design and fabrication for micro and nano scaled components. It is a process through which a pattern can be transferred (be it regularly geometric or random) onto a surface covered with a thin layer of photo sensitive polymer (photoresist) through the irradiation with light of appropriate wavelength, thereby possessing the ability to selectively either remove the exposed area (positive tone) or alternatively the unexposed area (negative tone) of the photoresist. The majority of the challenges, which have been experienced in lithography, have been driven by the semi-conductor industry and reductions in exposure wavelengths.

In the most basic form of lithography[1] visible light is used to pattern features with sizes of the order of a few microns. In the mid-1970 and early 1980 mercury lamps became the irradiation source choice for optical lithography with UV emission wavelengths of G-line (λ=436nm)[2] and I-line (λ=365nm)[3] capable of producing devices with feature sizes of the order of 2 and 1 microns, respectively. The next trend in lithography was the use of excimer lasers with wavelengths deeper in the UV range (λ= 248nm and 193nm) [4] which lead to the further reduction of the feature sizes to sub-micron features. Currently the trend sits at the deep UV level with an irradiation wavelength of 193nm with research shown to be capable of producing 20nm features[5]. From the literature, X-rays have also been seen to be used as an irradiation source with minimum attainable feature sizes of the order of 10nm. Following from the progressive trend suggested above the next trend will be extreme UV irradiation sources. All the above mentioned irradiation techniques rely on the projection of light though a master mask to produce the output pattern and there are three variations of this each having their degrees of limitation.

The variations are summarised in the *Table 3.1*;

Table 3.2 Comparison of the Advantages and Disadvantages of Lithographic Techniques.

Lithography Type	Advantages	Disadvantages
Contact Lithography – 1:1 Scaling	• Inexpensive system and relatively high resolution (~0.5µm)	• No magnification offered. • Degradation of mask with repeated contacts and dirt on the mask directly transferable to substrate
Proximity Lithography – 1:1 Scaling	• Inexpensive system and reduction of mask damage	• Lower resolution (~1-2µm) • diffraction limited • no magnification and less repeatable as a technique
Projection Lithography – 1:4 Scaling	• Really high resolution (~65nm) • no direct contact with the mask and the less chance of dirt transfer from mask to substrate	• Expensive and complicated system and limiting diffractive effects

The lithographic techniques and irradiation sources mentioned in the paragraph above are all techniques making use of a master mask for transferring the pattern to the substrate. Another avenue that can be used for patterning features with sub-micron feature sizes is direct maskless lithography.

Direct laser writing could also be used for the patterning of substrates, but in this approach the limitations are set by the size of laser spot. Laser machining using a 1,310nm laser is capable of writing structures with minimum dimensions of the order of 25µm [6].

Although the lithographic techniques and irradiance wavelengths have been shown to have beneficial effects in the final dimensions of the devices, the parallel development of higher quality, thinner resists with higher aspects ratios, lenses with higher numerical apertures (NA) reductions made in aberrations and processing have also had a major effect on the reduction of the device sizes.

In this chapter an outline of the working principles and associated difficulties encountered with E-beam lithography was presented for the fabrication of three photonic devices with feature sizes ranging from 200nm to 1000nm used for sensing and security applications later described in subsequent chapters. A description of pattern transfer through Reactive Ion Etching (RIE), the working principles and optimisation of conditions for efficient fabrication are also presented for three different substrate materials.

3.2.   E-beam Lithography

E-beam lithography uses high energy (1kV-100kV) electron beams to form patterns in a thin (50nm-1000μm) polymer film[7]. The advantages of e-beam lithography over conventional UV lithography are that the diffraction limit of light is surpassed enabling the formation of patterns with nm sizes (high resolution)[8] and the direct patterning of substrates without the need for expensive masks. The disadvantages on the other hand are that there is a high cost associated with this technique as well as associated slow speed. There have been a wide range of applications for this patterning technique in low volume semi-conductor components, high precision masks for photo lithography and other research applications. This is not a high volume manufacturing tool as the beam is required to scan across the surface in a serial manner to generate the desired patterns.
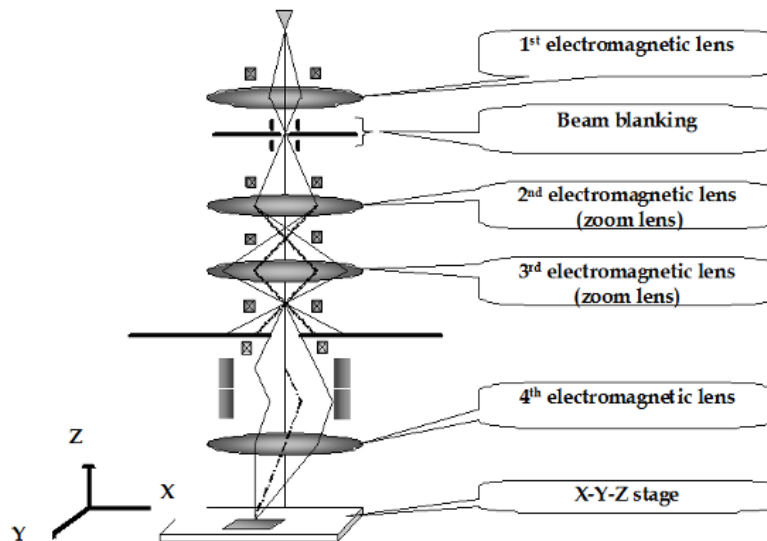
Figure 3.1. Schematic of an electron beam column[24].

There are two major problems associated with e-beam lithography, namely stitching errors[9] and proximity errors[10].

In an e-beam column as seen from **Figure 3.1.** , the electron beam is generated by a high voltage tungsten electron source which passes through a pair of magnetic coils and electrostatic elements (electromagnetic lenses). For each magnification used during the exposure process, an area called the write field exists. Inside this write field, the e-beam can cover the entire area by solely changing the electron optics and leaving the stage in the same position. Deflection of the electron beam results in some error. The write field alignment is an adjustment carried out for the electron optics inside the column to align to the translation stage at the bottom. This stage is corrected and the e-beam deflection is adjusted to it. Larger patterns most frequently require to be split into several write fields, which consequently need to be stitched together. This in turn gives rise to stitching errors since no perfect match can be found between the write fields. This error can be minimised through the careful alignment of the write fields (hence focusing and alignment is carried out on 100nm gold spheres on the surface of the sample), increasing the patterning area or overexposing the desired pattern. There is however no guarantee that this error would be eliminated. In most cases this is down to random precision errors in the laser stages. Depending on the conditions, this error can range from 10's to 100's of nanometers.

The proximity effect on the other hand is due to the scattering of the incident electrons. An electron beam incident on a material undergoes both elastic (no energy loss, angular change) and inelastic (energy loss) collisions. Consequently the electrons moving

backwards during elastic scattering are back scattered electrons. The inelastic scattered electrons on the other hand depending on the amount of energy lost lead to the generation of X-rays.

The electron beam also broadens during exposure due to the backscattering in the resist layer in a phenomena called the proximity effect. It results in the exposed features to have rounded edges and larger sizes when compared to the initial design. Optical proximity correction is required by carrying out a correction on the exposure dose in densely packed regions when compared to isolated features. There exists an automated proximity correction package in the design software, but most frequently trial and error works the best because the proximity effect is dictated by factors such as the acceleration voltage, resist nature, substrate thickness, substrate material, etc.

3.2.1. Resists, Spin Speed and Layer Thickness

There are two kinds of e-beam resists. Positive resists undergo chain scissors upon e-beam exposure and the exposed parts become soluble. Negative resists on the other hand undergo cross linking after exposure to electrons and become insoluble after exposure. The e-beam resist chosen for the patterning of the waveguides was AZ-nLof 2070 negative tone resist from Microchem. This resist provides a number of important properties such as an adjustable level of undercut which is necessary for pattern transfer through lift off as well a high degree of stability to thermal softening which occurs during thermal evaporation processes. It can be diluted with propylene glycol monomethyl ether acetate, which is also found to improve surface adhesion of the resist. Substrates are prepared by soaking in a solution of rinse aid (Neutrocon) in a heated water bath followed by an acetone bath and an increment in the surface roughness through a 5minute RF only Argon plasma at 150W. Conventional oxygen plasmas were found to have a reduction of surface adhesion of undiluted resist concurring with the adhesion of oxygen and the organic solvent. The resists are applied onto the substrate by spin coating for a duration of 90 seconds. The thickness curves are shown in *Figure 3.2.*
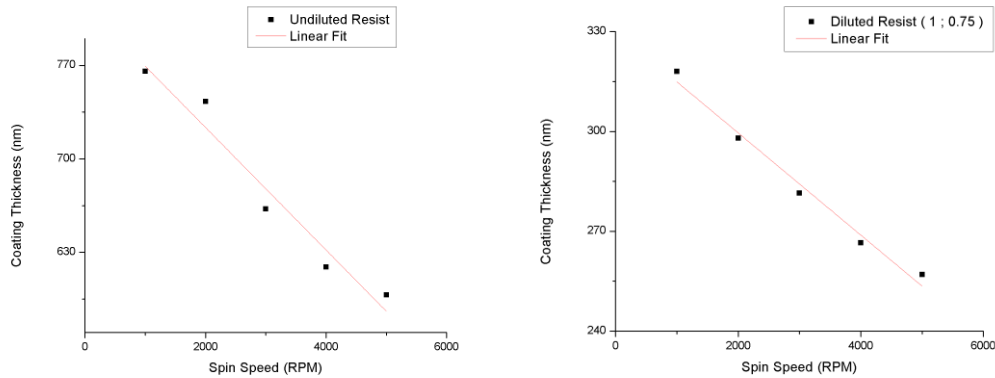
Figure 3.2. Thickness of Undiluted (LEFT) and Diluted 1:075 (RIGHT) Az-NloF 2070 Negative tone e-beam resist as a function of spin speed.

Negative metallic masks are used because they increase the selectivity and allow for cleaner, deeper etches and favours the lift off process. The thickness of the coating needs to be at least twice as thick in comparison to the metallic mask for lift off to occur. The thickness of the metal mask on the other hand is determined by the combination of etch depth and selectivity. The waveguides can also be patterned by the use of a positive tone resist such as PMMA (Poly (Methyl MethAcrelate)), however PMMA does not have the property to undercut so an additional sacrificial layer of PMGi (Polymethylglutarimide) would have to be introduced to provide the undercut nature of the bi-layer structure. The exposure of positive resists would be more time consuming when compared to the negative tone resist because the exposure dosage required is about 50 times more than that for the negative resist and hence increasing the overall writing time.

3.2.2. Write Field Size

As mentioned beforehand for each magnification used during the exposure process, there is an area called the write field. Inside the write field the e-beam can cover the entire area by solely changing the electron optics and not moving the translation stage. Therefore it is an indication of the amount that the e-beam deflects. A guideline is that the larger the write field the smaller the aperture size and the smaller the write field the larger the aperture size. A 1mm write field is usually used for patterning of structures whose dimensions are much larger than the size of the field (i.e. contact pads). A technique used for the reduction of the writing time of large structures is to increase the size of the write field which leads to a reduction in the stitching accuracy between adjacent fields and results in breaks in the pattern. Large fields are not ideal for use with fine patterns because

there is a reduction in the dwell time, hence less time exposure time which in turn leads to poor resolution of the patterns. A reduction in the write field while keeping the aperture the same leads to a significant improvement in both the stitching accuracy and the resolution of the pattern. A comparison of the same structure written with write fields of 1mm and 0.2mm while keeping the aperture size the same is shown in the *Figure 3.3* .
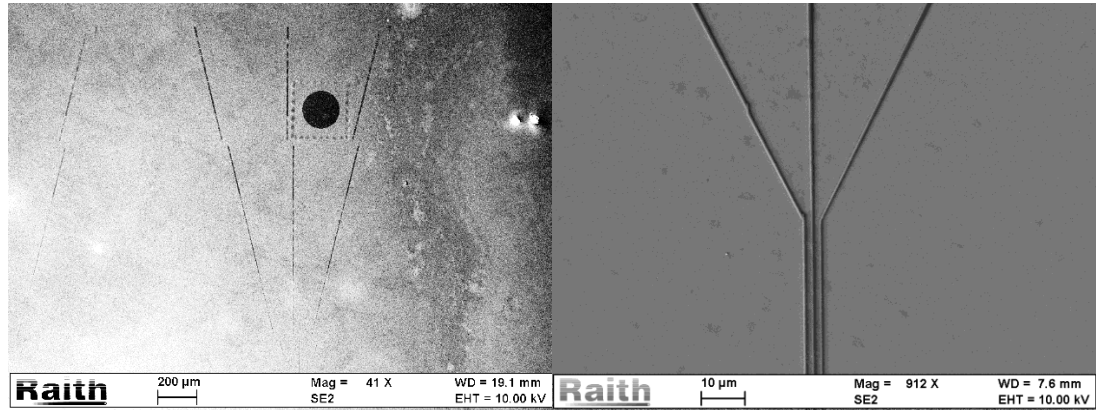
Figure 3.3. Scanning Electron Beam Micrographs of waveguides written with a write field of 1mm (LEFT) and 200µm (RIGHT).

3.2.3. Step Size

The step size defines the amount that the electron optics move the beam by with every shot of electrons. Large step sizes are ideal for patterning of large areas and lead to reduction in writing times. A 4 micron step size provides a ratio of 4:1 with respect to the minimum feature size. The step size should be about $1/10^{th}$ the size of the smallest feature to be patterned. The micrographs in *Figure 3.4* show a ratio of 4:1, 1:1 and 0.1:1 in respect of step size to minimum feature.
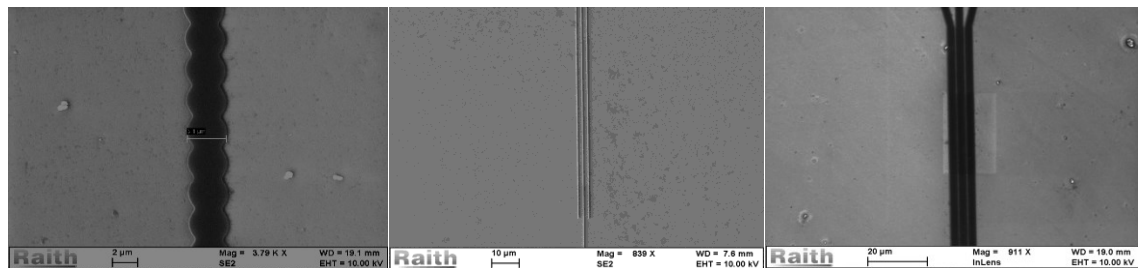
Figure 3.4. Scanning Electron Beam Micrographs of waveguides written with step sizes of 4µm (LEFT), 1µm (CENTER) and 900nm (RIGHT).

33

The region where the three adjacent waveguides rest is clearly separated. The shadows observed on either side of the waveguides indicate an undercut in the resist. The undercut is necessary in facilitating the lift off of the resist after metallisation.

3.2.4. Aperture Size

Aperture size of the e-beam affects the deflection of the electrons, larger apertures experience larger deflections and are used for patterning of large features while small apertures have smaller deflections and used for smaller feature sizes. Large apertures also have large electron beam deflection angles associated with them hence are not capable of producing vertical or undercut side wall profiles. Smaller apertures with lower beam currents are more directional and better suited in the formation of vertical sidewalls or undercut profiles. Larger apertures sizes also lack the fine alignment option. This can be seen by comparing the two images in *Figure 3.5* one written with a 120micron aperture and the latter with 20microns.
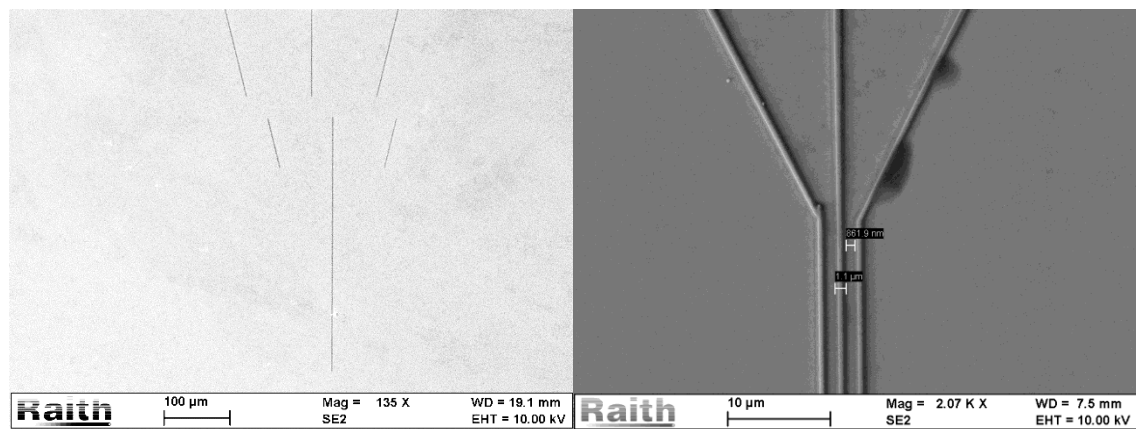
Figure 3.5. Scanning Electron Beam Micrographs showing the waveguides written with aperture sizes of 120µm (LEFT) and 20µm (RIGHT).

3.2.5. Acceleration Voltage

The acceleration voltage governs the penetration depth and backscattering of electrons from the resist. A 10kV acceleration voltage was found of being capable of forming patterns in diluted resists. In the undiluted resist 10kV was too low an acceleration voltage so the electron beam did not have enough power to penetrate through the resist leading to

the underexposure of the features. 20kV produced undercut sidewall profiles and 30kV overexposed the patterns.

3.3. Waveguides

A Raith Pioneer 150 SEM and E-beam lithography system was used for the E-beam exposure, using a Gemini column and a high precision laser interferometric stage combined with a digital to analogue converters for the e-beam deflection during lithography. The maximum acceleration voltage is 30kV. The design specified below was used for the calibration of the E-beam writer.
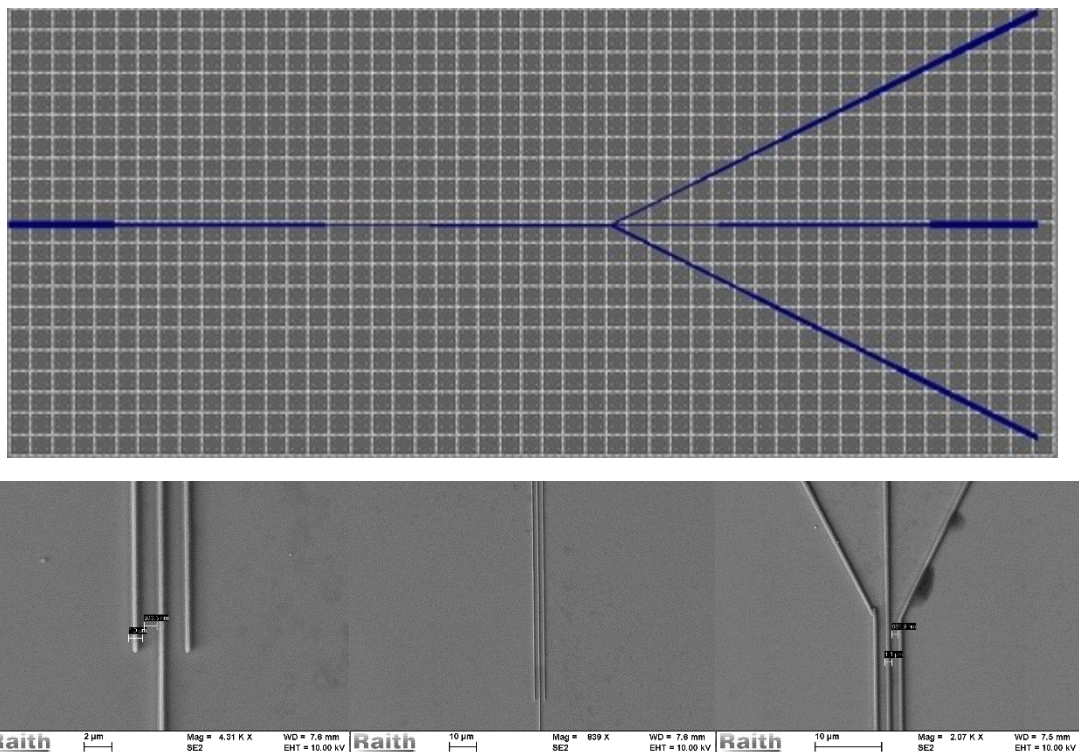
Figure3.6. GDS-II as viewed by the Pioneer Editor prior to writing (TOP) scanning electron micrographs of the input and output of the active coupling region of the fabricated device (BOTTOM).

The fabricated waveguides have dimensions as follows, the length from end to end measures 4.85mm, the width at the most extreme right measures 2.1mm. The three adjacently spaced waveguides where the evanescent coupling occurs are 1μm in width separated by 900nm between waveguides. The length of the active coupling region is 850 μm and the waveguides then expand from a width of 1 μm to 30 μm to facilitate for the butt coupling of the optical fibres. This is shown in *Figure 3.7.* The coupling of guided

light between the waveguides is based on the evanescent coupling in which if the waveguides are in sufficiently close proximity to one another then the guided light can couple from one to another. This is the underlying operation principle used in fibre based couplers, ring resonators and optical switches[11].

The checklist for exposing the waveguide devices with Az-nLof 2070 is as follows;

1. Spin coat the sample with Az-nLof 2070 resist at 2,000rpm for 90 seconds, which produces a coating thickness of 700nm.
2. Bake on a hot plate at 110°C for 60 seconds.
3. Spin coat PEDOT:PSS conducting polymer at 5,000rpm for 60 seconds, which produces a coating thickness of 50nm.
4. Bake on a hot plate at 75°C for 90 seconds.
5. Set the acceleration voltage for 10kV, adjust the stigmation for X at 3% and Y at 6.3%, focusing and aperture alignment for the 20 μm aperture.
6. Select the 200 μm write field and carry out the write field alignment for field sizes of 20μm, 10μm and finally 5μm.
7. Measure the beam current for the 20μm aperture at the Faraday cup on the sample holder and adjust the position to the middle.
8. Set the step size for 0.09μm and the area dose at 9.98μC/cm^2 the exposure dose factor at 175 times and expose the pattern.
9. Wash off the PEDOT:PSS in DI water for 90 seconds.
10. Bake on a hot plate at 110°C for 60 seconds.
11. Develop the patterns in MIF-726 neat developer for 240 seconds, followed by a rinse aid solution to remove any leftover developer from the surface of the sample.
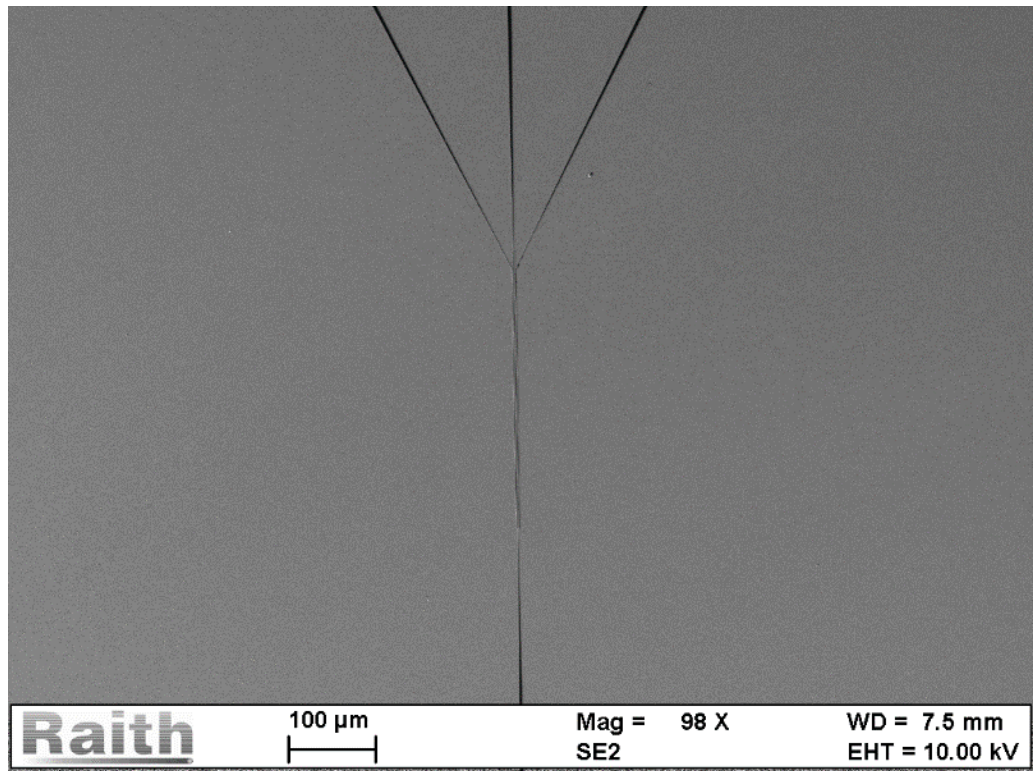
Figure 3.7. Scanning Electron Micrograph of Waveguides written with the ideal parameters listed above.

3.4. Nanoholes

The designed nanohole arrays start as being made up of 200nm wide circular pillars which have a periodic spacing of about 620nm in both dimensions. The pillars are about 390nm high and show pronounced undercut profile to aid in lift-off.

A checklist for the exposure of the nanohole arrays with Az-nLof 2070 is as follows;

1. Spin coating of the Az-nLof 2070 resist at 4000rpm for 90 seconds which produces a coating thickness of about 530nm.
2. Baking in an oven at 95°C for 10 minutes.
3. Spin coating of the PEDOT: PSS for 60 seconds with produces a coating thickness of about 50nm.
4. Hot plate bake at 75°C for 90seconds.
5. Set the acceleration voltage to 20kV, adjust the stigmation, focusing and aperture alignment for the 20μm aperture.
6. Select the 50μm write field and carry out the write field alignment for field sizes of 10μm, 5μm and finally 2μm.

7. Measure the beam current for the 20µm aperture at the Faraday cup on the sample holder and adjust the position to the middle.

8. Set the step size for 0.03µm and the area dose at 9.43µC/cm^2 the exposure dose factor at 2 times and expose the pattern.

9. Wash off the PEDOT: PSS in DI water for 90 seconds.

10. Bake in an over at 95°C for 300 seconds.

11. Develop the patterns in MIF-726 neat developer for 300 seconds, followed by a rinse aid solution to remove any leftover developer from the surface of the sample.

| Raith | 2 µm | Mag = 3.03 K X | WD = 7.6 mm |
| | | InLens | EHT = 10.00 kV |
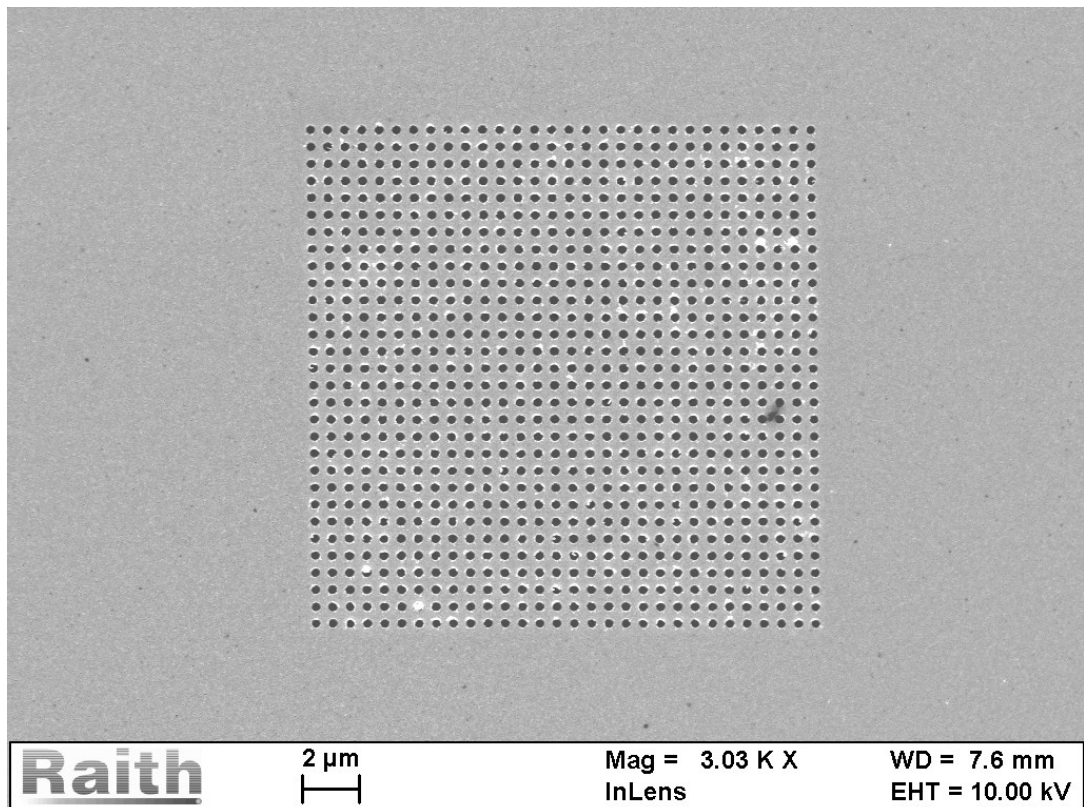
Figure 3.8. Scanning Electron Micrograph of a Nanohole array written using the parameters listed above.

3.5. Binary DOEs and Gratings

The designed surface relief grating is made up of high frequency base grating with feature sizes of width measuring 240nm on a periodicity of 520nm. This is the carrier grating which causes the dumping of the light in the -1 diffraction order.

The origin of the design comes from the pulse modulation of the base high frequency grating which was carried out by Dr Andrew Waddie and further explanations of the modulation scheme can be found in later chapters of the thesis.

A checklist for the exposure of the Binary Diffractive Optical elements with Az-nLof 2070 is as follows;

1. Spin coating of the Az-nLof 2070 resist at 4000rpm for 90seconds which produces a coating thickness of about 530nm.

2. Baking in an over at 95°C for 10minutes.

3. Spin coating of the PEDOT: PSS for 60 seconds with produces a coating thickness of about 50nm.

4. Hot plate bake at 75°C for 90seconds.

5. Set the acceleration voltage to 20kV, adjust the stigmation, focusing and aperture alignment for the 20μm aperture.

6. Select the 50μm write field and carry out the write field alignment for field sizes of 10μm, 5μm and finally 2μm.

7. Measure the beam current for the 20μm aperture at the Faraday cup on the sample holder and adjust the position to the middle.

8. Set the step size for 0.03μm and the area dose at 9.43μC/cm^2 the exposure dose factor at 2 times and expose the pattern.

9. Wash off the PEDOT: PSS in DI water for 90 seconds.

10. Bake in an over at 95°C for 30 seconds.

11. Develop the patterns in MIF-726 neat developer for 300 seconds, followed by a rinse aid solution to remove any leftover developer from the surface of the sample.

Raith   20 μm   Mag = 1.17 K X   WD = 10.2 mm
                  InLens   EHT = 10.00 kV
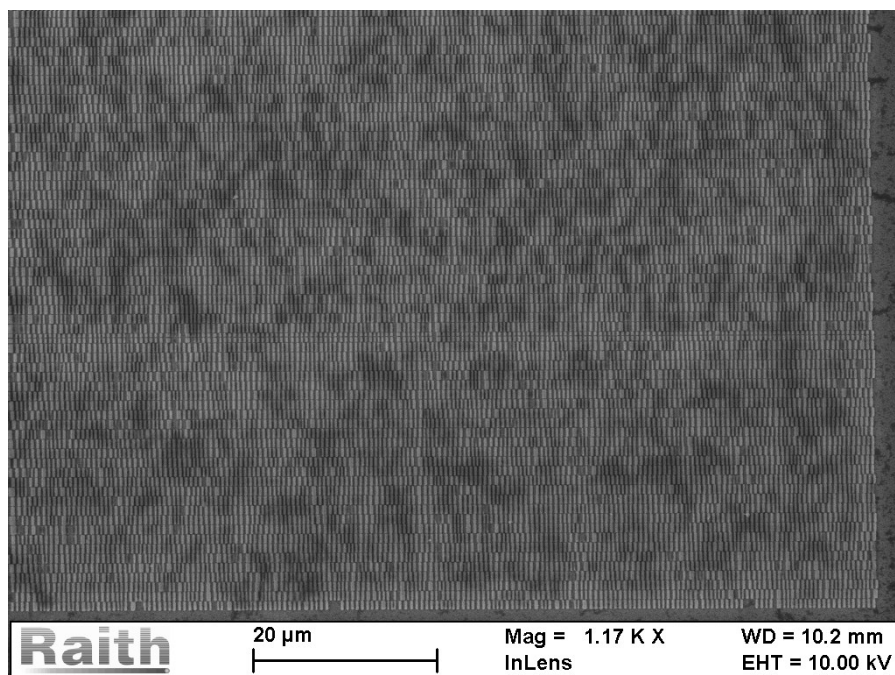
Figure 3.9. Scanning Electron Micrograph of a Pulse modulated Binary grating written using the parameters listed above.

3.6. Reactive Ion Etching
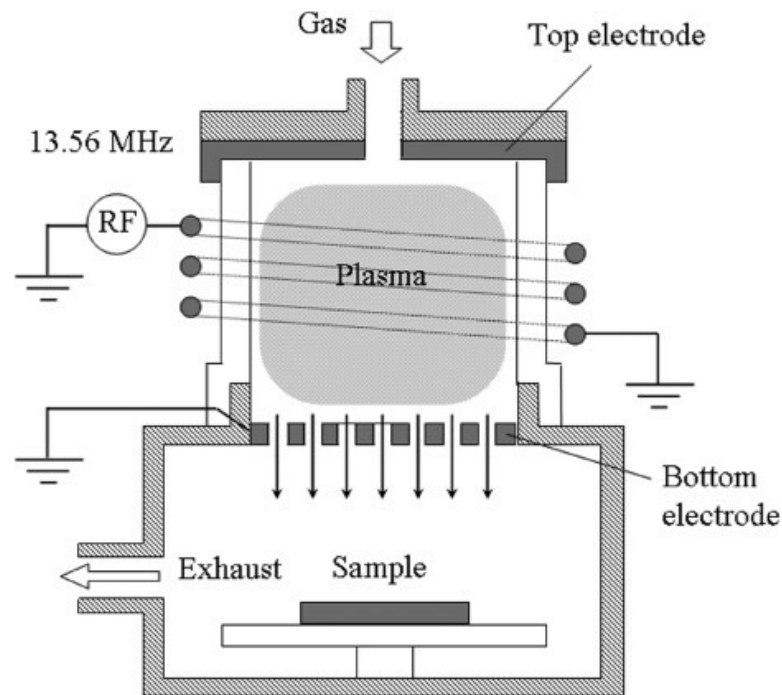
Figure 3.10. Schematic of a Reactive Ion Etcher (RIE) with an inductively coupled plasma attachment (ICP).

The dry etching is carried out in an Oxford Plasma 100 RIE-ICP etcher. It is capable of generating a maximum RF power of 300W and 600W for the ICP coil. The plasma is initiated by the application of a strong RF field to the wafer holder. This field is typically set to 13.56MHz. A schematic of the chamber can be seen from *Figure 3.10*. This field results in the ionisation of the gas by knocking out electrons from the atoms to create a plasma. The electrons get accelerated and move up and down striking both plates. The ions on the other hand are much larger in size hence showing little response to the applied field. Electrons striking the surface of the holder get absorbed and lead to the formation of a negatively charged plate. The plasma attains a slightly higher overall mean charge due to the lack of electrons. This results in an overall downwards movement of the ions which etch the sample in a highly anisotropic manner due to the straight downward delivery compared to wet etching which is isotropic. Important parameters which need to be considered include the sidewall verticality, smoothness of the etched trenches and the selectivity. The selectivity provides an indication of the ratio of substrate etched to mask etched. For deep trenches in general metal masks are favoured because of the extra resistance provided to prolonged plasmas and thermal effects when compared to organic resists. To obtain deep trenches the mask must be uniformly spread across the surface, the mask must have a lower etch rate compared to the substrate.

3.6.1. Lithium Niobate (LiNbO₃)

Lithium niobate is a man made birefringent material, with ferroelectric , pyroelectric, piezoelectric, acustooptic and electrooptic properties[12]. It is these properties that make lithium niobate the second most widely manufactured semiconductor material after silicon and has found its way into numerous applications and a wide range of devices such as photonic crystals[13], surface acoustic wave devices[14], electric field sensors[15].

Lithium Niobate crystals were first obtained by Mathias and Remeika[16] grown from a melt solution. Presently though Lithium Niobate is grown in air by the Czochralski process[17]. The process consists of pulling a cylindrical crystal from a melt with growth being initiated by a small seed crystal. The crystal and melt are made to rotate in opposing directions to ensure homogeneity and also to prevent thermal gradients at the crystal melt interface. After the growth, the boule is cooled and cut into the shapes and orientations required. The Czochralski grown single lithium niobate crystals are mutli-domained. To produce single domain material the growth must be carried out in the presence of an electric field[18].

Deep silicon etching of $LiNbO_3$, has limitations in depth, aspect ratio, verticality of side walls and smoothness of the etched surface. As $LiNbO_3$ is heated, the crystal lattice expands which causes a change in the spontaneous polarisation as a result of the movement of the lithium and niobium ions relative to the oxygen planes. This results in the build-up of charge on the positive and negative faces of the crystal and consecutive sparking.

3.6.1.1. Substrate

Two different grades of lithium niobate base wafers were used in the trial, the first being optical grade z-cut lithium niobate and the second being z-cut 'black' lithium niobate which is chemically reduced at high temperatures in the presence of nitrogen and hydrogen. This results in an improvement of the electrical conductivity and optical absorption[19], reduction of the pyroelectric discharge during heating and cooling encountered during etching and e-beam lithography. Under the same RIE parameters the

'black' lithium niobate wafers showed a reduction in the etch rate of ~3nm/min when compared the optical grade lithium niobate.

3.6.1.2.   Mask

Organic resists offer a high etch rate of about 24nm/min however suffer from poor selectivity. The best recorded selectivity is 1:3.7 with respect to the resit. This poses a further issue with regards to the aspect ratio, which is 1:1, so for a 3μm etch depth the coating has to be of the exact same order. But the selectivity acts as a hindrance limiting the maximum etch depth to about 800nm.

Metallic masks work much better compared to organic resists in energetic plasmas. Both thermally evaporated and RF sputtered chromium were tested. The best selectivity obtained from a thermally evaporated mask was about 3.14:1 with respect to the resist. This is an improvement over organic resists because the mask is etched at a lower rate compared to the substrate. This gave an etch rate of 14.2nm/min. There is also the limitation to the maximum coating thickness to 100nm which would give a maximum etch of 314nm.

RF sputtered masks offer several advantages over thermal evaporated being. Much thicker coating can be applied, the sputtered layer is much tougher and resistant to etching and it is carried out at relatively lower temperatures. The selectivity was increased from 3.14:1 to 4:1 and the etch rate was increased from 14.15nm/min to 20nm/min.

3.6.1.3.   Chemistry

Lithium niobate is etched using a fluorine chemistry[20]. Lithium Niobate being an element in the 1st group of the periodic table and fluorine being in the 7th , one being highly electronegative and the other high electropositive leading to the formation of Lithium Fluoride[21] salt as a by product of the etching process. Sulphur hexafluoride (SF_6) chemistry was investigated and produced an etch rate of 17.2nm/min with a poor selectivity with regards to organic masks standing at a ratio of 1.5:1. The dry etch recipe conditions are as follows; Pressure – 10mTorr , RF Power – 150W , ICP Power – 150W , CF_4 – 30sccm , CHF_3 – 20 sccm , Ar – 10sccm , H_2 – 3sccm. The following wet etch

SC-1 solution which is made up of 70% water, 20% Hydrogen peroxide and 10% Ammonium Hydroxide.

3.6.1.4.   Power

The radio frequency power is applied to the lower electrode of the reactor (i.e. cathode) to generate a plasma influencing the mechanical etching. An increase in the RF power mainly causes an increase in the energy of the bombarding ions.

An RF power level of 25W results in an etch rate of 3nm/min. At 100W the etch rate was 15nm/min: at 150W the etch rate was 19nm/min and at 200W it falls once again to about 16nm/min. From the data above an increase in the RF power results to an increase in the etching rate but also a reduction in the selectivity upto a certain point after which the etch rate falls but the selectivity keeps increasing. Higher RF powers also result in the formation of more energetic ions which in turn also cause the cathode to heat up.

Inductively coupled plasma increases the vertical magnetic field passing through the plasma. Which increase the number of electron gas collisions and therefore number of ions in the chamber. This increase in ion density results to more available reactive species sent to the substrate. ICP therefore increases the number of ions without an energy increase.

3.6.1.5.   Pressure

Pressure has a major role in plasma etching. A low chamber pressure leads to a longer mean free path of the ions and less reactants. A power increase would lead to a momentum increase in the ions resulting in sputter etching. A high chamber pressure leads to a shorter mean free path of the ions and more frequent collisions between the gaseous species and more released free radicals. The etching at high pressures is mainly chemical with higher ion energies and lower selectivity. Pressure also has an effect on the side walls; for vertical side walls lower pressures are better suited.

3.6.2. Silicon

Over the last 50 years Silicon has become one of the most produced , used and researched materials for the production of semiconductor devices in the semiconductor industry. With numerous applications in a variety of fields ranging from CMOS, photodetectors and photovoltaics. It is the most important elemental semiconductor. It has not been traditionally used for the fabrication of light emitters because of its indirect band gap. However some forms of silicon are viable as light emitters and silicon photonics.

For micro fabrication applications, in silicon grade used,   the crystal lattice of the entire solid is continuous, unbroken to its edges and free of any grain boundaries. Most silicon monocrystals are grown through the Chrocalski process similar to that used in the growth of lithium niobate crystals also described earlier into ingots of up to 2 meters and weighting up to a few 100 kilograms. These massive ingots are then sliced into sections which have varying thicknesses depending on their applications.

Monocrystalline silicon differs from all the other allotropic forms such as amorphous silicon, polycrystalline silicon both of which consist of small particles called crystallites[22]. It has a high thermal melting point of 1,414°C and excellent electric conductivity making it a suitable base substrate for lithographic applications.

3.6.2.1.   Chemistry

The substrates are prepared for etching through spin coating of a Az-nLof 2070 (negative tone e-beam resist), patterning through E-beam lithography and subsequent development. The gas mixture was made up of CHF_3 and SF_6 in the ratio of 7:1. The power level was maintained at 100W RF and the chamber pressure set at 10mtorr. Under the above mentioned conditions the silicon was etched at a rate of ~39nm/min and the resist was etched at ~20nm/min. This produced the best combination in terms of etch rate, selectivity and vertical sidewalls. Using the aforementioned recipe sidewalls with an angle of 89 degrees were etched indicative of a highly anisotropic etch. Using SF_6 with a gas flow of 10sccm produced an etch rate in silicon ~50nm/min, however the etch rate of the resist was >50nm/min and the highly isotropic. A comparison of the attainable grating geometries is seen in *Figure 3.11*.
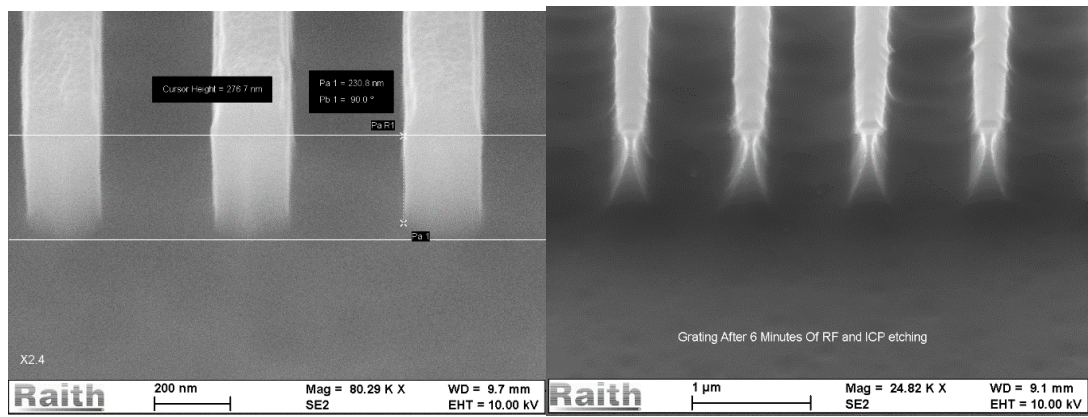
Figure 3.11. Scanning Electron Micrographs of binary gratings showing anisotropic etching of grating (LEFT) and isotropic etching of grating (RIGHT) achieved through altering the etching conditions.

3.6.2.2.   Power

Two different power levels were investigated while keeping the gas, gas flow rate and chamber pressure the same. The power levels were 100W and 200W used in combination with CHF_3 and SF_6 gases. The etch rates in silicon were ~39nm/min, and ~75nm/min respectively. The etch rates in the photo resist were ~20nm/min and ~35nm/min respectively. This leads to the conclusion that an increase in the RF power leads to an increase in the DC bias, hence leading to an enhancement in the ion energies and an increase in the etch rate. Lower chamber pressures increase the mean free path and reduce the frequency of ion to ion scattering which also results in higher etch rates.

3.6.3. Fused Silica

Fused silica is a glass containing SiO_2 in amorphous (non-crystalline) form. It differs from all traditional forms of glass in the sense that it contains no other ingredients, typically added to lower the melting temperatures. The optical properties of fused silica are superior to those of other glasses with its optical transmission properties (transparency range from UV to IR region) making it a suitable choice for lithographic masks, glass carrier plates, lenses , diffractive optical elements and other optical components. It also possesses a low thermal expansion coefficient which is useful and necessary for the fabrication of high precision mirrors. It also has a low chipping rate during dicing producing consistently clean cuts.

It is manufactured by fusing high purity silica sand consisting of quartz crystals (containing oxygen and silicon). Commercially available variations of fused silica contain

impurities which are most commonly either aluminium or titanium. The melting is carried out at 1,650°C in either an electrically powered furnace or an oxygen flamed furnace. It can be made from any silicon rich precursor, using a continuous process involving flame oxidation of volatile silicon compounds to silicon dioxide resulting in the formation of this high purity and optically wide transmission band glass.

It is an attractive material for the fabrication of optical devices, micro electro mechanical devices, stamps and micro fluidic devices due to its inertness, biocompatibility, wide transmission range, electric insulation, high thermal melting points mechanical rigidity and compactness.

3.6.3.1. Chemistry

Fused silica is etched using a fluorocarbon chemistry[23]. This breaks the Si-O bonds and leads to the formation of volatile CO and CO_2. Reports have also indicated that the etching of fused silica is due to the bombardment of carbon containing compounds rather than fluorine radicals. The two different gases used in the trials were CHF_3 and CF_4. Two identical substrates were spun coated with S1805 (positive tone resist from microchem), exposed and baked in an identical way. The RIE chamber was preconditioned with an oxygen plasma prior to the two runs. The runs were both carried out under the same power conditions which was 125W of RF only , with 25sccms of gas flow at 15mTorr chamber pressure. This chamber pressure was found to give the highest etch rate/selectivity combination in lithium niobate. Higher pressures led to lower etch rates, higher selectivity but less vertical sidewalls. The CHF3 run yielded an etch rate in fused silica of ~33nm/min and the CF_4 was ~40nm/min. The main difference between the etched arose in terms of selectivity. The CHF_3 gas produced a resist etch rate of ~10nm/min and the CF_4 gas produced ~20nm/min, nearly double hence rendering it less effective for deeper etches. Both gases produced nearly vertical side wall geometries.

3.6.3.2.   Power

The radio frequency (RF) power is applied to the lower electrode of the reactor (i.e. cathode) to generate plasma influencing the mechanical etching. An increase in the RF power mainly causes and increase in the energy of the bombarding ions.

Three different power levels were investigated while keeping the gas, gas flow rate and chamber pressure the same. The power levels were 100W, 125W and 150W with used in combination with CHF_3 gas. The etch rates in fused silica were ~26nm/min, ~33nm/min and ~41nm/min respectively. The etch rates in the photo resist were ~9nm/min, ~10nm/min and ~15nm/min. This leads to the conclusion that an increase in the RF power leads to an increase in the DC bias, hence leading to an enhancement in the ion energies and an increase in the etch rate. Lower chamber pressures increase the mean free path and reduce the frequency of ion to ion scattering which also results in higher etch rates.

3.7.   Deposition of Chromium layer

Chromium can be deposited on a substrate by a number of ways which include: thermal evaporation, RF Sputter coating and e-beam deposition. In the thermal evaporation approach a tungsten spiral is heated up to 1,200°C under vacuum at which point the chromium changes from solid to vapour through sublimation. The drawbacks to using this approach are that the deposited layer thickness is limited to about 100nm and the poor quality of the coating. RF sputtering is performed in an Edwards 306 thermal evaporator with a RF target. The vacuum is reduced to about 10^{-6}Bar and the chamber is purged with Argon to remove any leftover oxygen. The source is set to 200W resulting to a deposition rate of about 20nm/min. The deposited layer has about a third of the resist thickness in order to ease the lift off process. A graph showing the deposition thickness is shown in *Figure 3.12*.
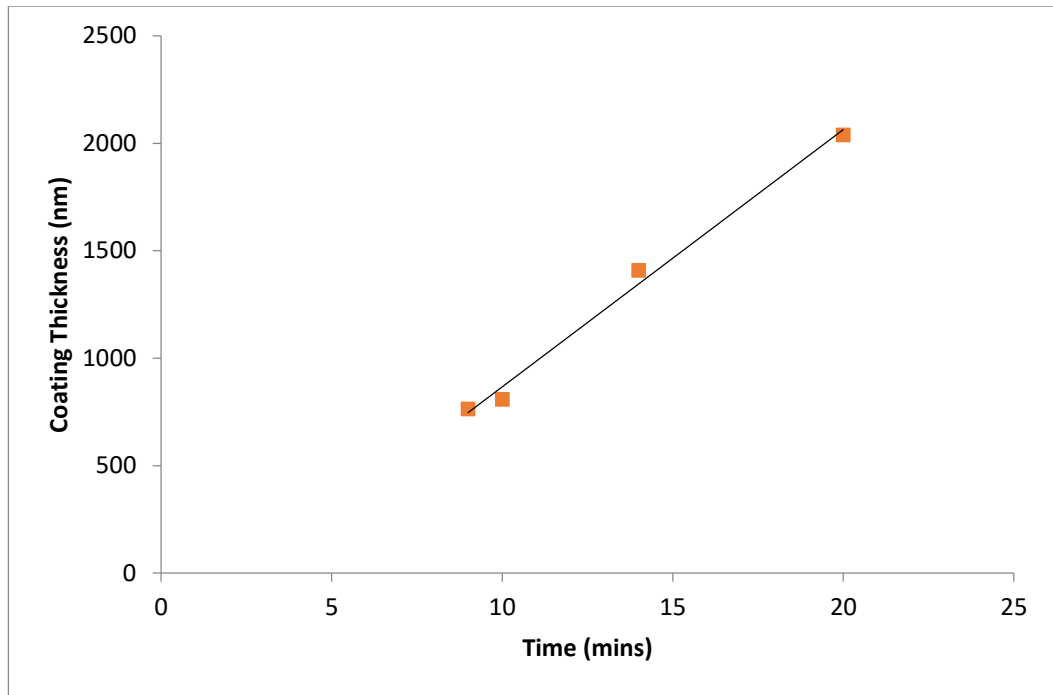
Figure 3.12. Thickness of RF sputtered Chromium as a function of deposition time.

3.7.1. Lift Off

Post etching the deposited noble metal (Au) or the hard metallic mask (Cr), has to be removed. Lift off needs to be carried out in order to facilitate the image reversal. Lift off is carried out in a bath of negative resist stripper (Technistrip NI555) which is heated to 80°C and placed in an ultrasonic bath. The structures lift off in about 2 hours post soaking with gentle agitation applied to the base substrate by the ultrasonic bath. Upon completion the substrates are soaked in a heated bath of rise aid which helps with the removal of any leftover resist on the surface.

3.8. Deposition of a-Si and influence of power on refractive index

An Edwards 306 thermal evaporator with a RF sputter add on. A crystalline silicon target with 99.9% purity is used. During sputtering the silicon changes from crystalline nature to amorphous due to its internal structure changes. The sputtering is carried out in a high vacuum of the order of 1000mBar, above which all the left over vapour on the sidewalls of the chamber could affect the quality of the coating. External heating of the sidewalls to 80°C is shown to help with this. The sputtering frequency is set to 13.56MHz and argon is used as a plasma gas to yield the highest outputs. Additionally it also reduces the potential of forming a silicon dioxide layer on the top of the surface. The measured thickness for a-Si at a power level of 250W is shown by the figure below and it is observed

that the layer thickness increases linearly with duration at a rate of 12nm/min which is invariant of the RF power seen in *Figure 3.13*. A piece of tape is stuck on a small section of the sample being coated to provide a sharp edge which can be used to measure the thickness of the coating using a DekTak 3 surface profilometer. An increase in the power of the RF source from 200W to 250W increases the refractive index of the coating from 1.87 to 2.31 @1550nm.
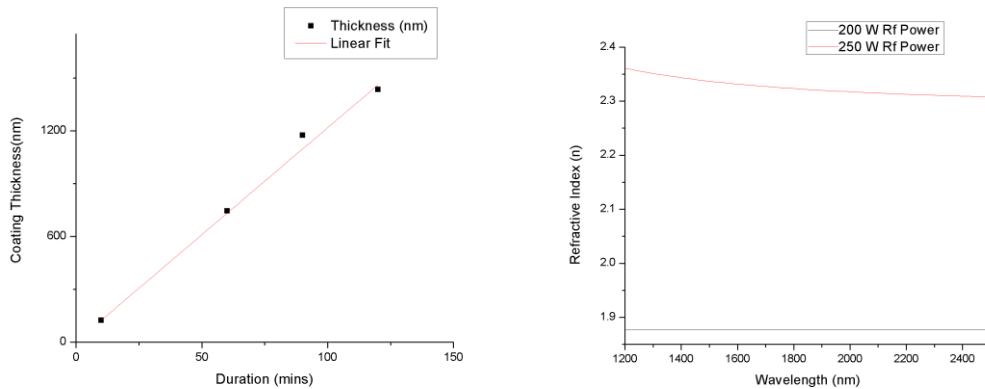
Figure 3.13. Thickness of RF sputtered a-Si as a function of time (LEFT) and ellipsometric measurement of refractive index of a-Si as a function of wavelength for two different deposition powers.

3.9. Conclusions

In conclusion, in this chapter the operating principles and associated problems encountered with E-beam lithography have been discussed in detail. The effects that acceleration voltage , write field , aperture size and step size have on photonics structures with features size ranging from 1μm all the way down to 200nm have been described and explained.

For the photonic waveguide structures where the minimum feature sizes are 1μm the optimised writing conditions for obtaining a complete structure with an adequate amount of sidewall undercut for lift off are found to be: Acceleration Voltage- 10kV, write field – 200μm, aperture size – 20μm and step size – 0.09μm. A similar study is carried out for writing large arrays of nano pillars with dimensions of 200nm on a pitch size of 600nm. A variety of different pillar sizes and periodicities were explored and the consequent effects that writing doses have on the undercut geometry of the pillars. Finally a high frequency grating structure comprising of long lines with a width of 250nm on a periodicity of 500nm was also written and the parameters optimised to obtain clean lines

with the appropriate amount of mark space ratio. The effects that the base substrates have with respect to resist adhesion and electrical conductivity have been discussed and a repeatable technique for minimising the accumulation of surface charges during e-beam lithography was developed and optimised.

In addition to e-beam lithography, the working principles of a reactive ion etch machine have been described with particular focus being made to the conditions which have the most dominant effects on etch rate, selectivity and anisotropy of the etching process. These conditions are RF power, chamber pressure and chamber chemistry. The etching recipes are developed for three materials; Lithium Niobate, Silicon and Fused Silica which were used as the base substrates for the photonic devices. For Lithium Niobate an alternating wet and dry etch recipe was introduced in order to get rid of the re-deposition of the fluoride based salt in the trenches acting as an etch stop as well as the introduction of hydrogen to smoothen the etched tranches. For silicon an etch recipe was developed which gave sufficient amount of selectivity in terms of the resist used and was also highly anisotropic yielding nearly vertical side walls. For fused silica an etch which yielded the best selectivity and etch rate in terms of the resist used was developed and optimised.

Finally the RF sputtering of both chromium and amorphous silicon were investigated. The deposition rates of material sputtered were estimated as well as the effect of the deposition power on the refractive index of the amorphous silicon deposited were investigated and tailored for the purpose of acting as the core of the waveguide photonic device.

3.10. References

[1]   J. Ma, L. Jiang, X. Pan, H. Ma, B. Lin, and J. Qin, "A simple photolithography method for microfluidic device fabrication using sunlight as UV source," *Microfluid. Nanofluidics*, vol. 9, no. 6, pp. 1247–1252, 2010.

[2]   K. Thonke, H. Klemisch, J. Weber, and R. Sauer, "New model of the irradiation-induced 0.97-eV (G) line in silicon: A CS-Si* complex," *Phys. Rev. B*, vol. 24, no. 10, pp. 5874–5886, 1981.

[3]   H. Jinbo and Y. Yamashita, "0 . 2 pm Or Less i-Line Lithography By Phase-Shifting-Mask Technology," pp. 825–828, 1990.

[4]   P. Dumon *et al.*, "Low-loss SOI photonic wires and ring resonators fabricated with deep UV lithography," *IEEE Photonics Technol. Lett.*, vol. 16, no. 5, pp. 1328–1330, 2004.

[5]   H. Fukuda, A. Imai, T. Terasawa, and S. Okazaki, "New Approach to Resolution Limit and Advanced Image Formation Techniques in 0ptical Lithography," *Interface*, vol. 38, no. I, pp. 67–75, 1991.

[6]   M. Deubel, G. von Freymann, M. Wegener, S. Pereira, K. Busch, and C. M. Soukoulis, "Direct laser writing of three-dimensional photonic-crystal templates for telecommunications.," *Nat. Mater.*, vol. 3, no. 7, pp. 444–7, 2004.

[7]   C. Vieu *et al.*, "Electron beam lithography - Resolution limits and applications," *Appl. Surf. Sci.*, vol. 164, pp. 111–117, 2000.

[8]   A. N. Broers, A. C. F. Hoole Andrew C.F, and J. M. Ryan, "Electron beam lithography - Resolution limits," *Microelectron. Eng.*, vol. 32, no. 1–4 SPEC. ISS., pp. 131–142, 1996.

[9]   R. K. Dey and B. Cui, "Stitching error reduction in electron beam lithography with in-situ feedback using self-developing resist," *J. Vac. Sci. Technol. B Microelectron. Nanom. Struct.*, vol. 31, no. 2013, p. 06F409, 2013.

[10]   G. Owen and P. Rissman, "Proximity effect correction for electron beam lithography by equalization of background dose," *J. Appl. Phys.*, vol. 54, no. 6, pp. 3573–3581, 1983.

[11]   A. Yariv, Y. Xu, R. K. Lee, and A. Scherer, "Coupled-resonator optical waveguide: a proposal and analysis," *Opt. Lett.*, vol. 24, no. 11, p. 711, 1999.

[12]   E. L. Wooten *et al.*, "A review of lithium niobate modulators for fiber-optic\ncommunications systems," *IEEE J. Sel. Top. Quantum Electron.*, vol. 6, no. 1, pp. 69–82, 2000.

[13]   A. Lecestre, S. Benchabane, L. Robert, R. Salut, G. Ulliac, and P. Blind, "Electroplated Ni mask for plasma etching of submicron-sized features in LiNbO3," *Microelectron. Eng.*, vol. 105, pp. 95–98, 2013.

[14]   T. C. Lee, J. T. Lee, M. A. Robert, S. Wang, and T. A. Rabson, "Surface acoustic wave applications of lithium niobate thin films," *Appl. Phys. Lett.*, vol. 82, no. 2, pp. 191–193, 2003.

[15]   M. Luennemann, U. Hartwig, G. Panotopoulos, and K. Buse, "Electrooptic properties of lithium niobate crystals for extremely high external electric fields," *Appl. Phys. B Lasers Opt.*, vol. 76, no. 4, pp. 403–406, 2003.

[16]   K. Nassau and H. J. Levinstein, "Ferroelectric behavior of lithium niobate," *Appl. Phys. Lett.*, vol. 7, no. 3, pp. 69–70, 1965.

[17]   K. Polgár, Á. Péter, L. Kovács, G. Corradi, and Z. Szaller, "Growth of stoichiometric LiNbO3 single crystals by top seeded solution growth method," *J. Cryst. Growth*, vol. 177, no. 3–4, pp. 211–216, 1997.

[18]   A. C. Busacca, C. L. Sones, V. Apostolopoulos, R. W. Eason, and S. Mailis, "Surface domain engineering in congruent lithium niobate single crystals: A route to submicron periodic poling," *Appl. Phys. Lett.*, vol. 81, no. 26, pp. 4946–4948, 2002.

[19]   S. Jen and R. Bobkowski, "Black Lithium niobate SAW device fabrication and performance evaluation," *Ultrason. Symp. 2000 IEEE*, pp. 269–273, 2000.

[20]   M. Tamura and S. Yoshikado, "technology and a phase composition studying Advanced Etching characteristics of LiNbO 3 crystal by fuorine gas plasma reactive ion etching," pp. 2–9.

[21]   H. Hu, a. P. Milenin, R. B. Wehrspohn, H. Hermann, and W. Sohler, "Plasma etching of proton-exchanged lithium niobate," *J. Vac. Sci. Technol. A Vacuum,*

Surfaces, Film., vol. 24, no. 4, p. 1012, 2006.

[22]   J. W. Allen and S. Oh, "E „ E)," vol. 31, no. 8, 1985.

[23]   T. Ray, H. Zhu, and D. R. Meldrum, "Deep reactive ion etching of fused silica using a single-coated soft mask layer for bio-analytical applications," *J. Micromechanics Microengineering*, vol. 20, no. 9, p. 97002, 2010.

[24]   **https://www.intechopen.com/books/lithography/high-energy-electron-beam-lithography-for-nanoscale-fabrication**

Chapter 4. Lithium Niobate Waveguides for Electric Field Sensing

4.1. Introduction

The detection of short duration electromagnetic pulses (EMP) with a double exponential temporal profile of up to a few hundred nanoseconds duration and a GHz central frequency, such as those produced by a typical lightning discharge event, is conventionally achieved by using an electrical antenna based sensor[1]. These sensors which are capable of measuring both the peak electric field strength of the EMP and the temporal profile of the pulse are macroscopic systems (with sizes comparable to several wavelengths of the central RF frequency) and can introduce a significant perturbation of the EMP during measurement.

The commercially available d-dot sensor measures the time derivative of the electric flux density on the surface of a conductor allowing the electric field profile to be calculated by integration of the measured signal. These sensors, which are capable of measuring the typical temporal electric field profiles under consideration, are subject to a number of limitations in performance and usage, most significantly in the bandwidth, sensitivity and overall sensor size. The upper frequency bandwidth of a d-dot sensor is proportional to the reciprocal of the time constant of the complete electrical circuit of the sensor. In order to have a sensor capable of high frequency operation, the low voltage capacitance of the sensor must be minimized, leading to a reduced sensitivity at lower frequencies. Hence by exploiting all-optical devices based around electro optic materials and optical detection method, a small form factor, high bandwidth sensor can be designed offering the possibility of a significantly smaller sensor package with minimal potential for EMP perturbation.

In this chapter a novel and inherently simple technique for the fabrication of leaky channel waveguides in Lithium Niobate is presented and an electro-optic sensor head is explored as an alternative to electric based antennas to measure both static and short duration electromagnetic pulses with nanosecond rise times.

4.2.   Microstructure Electric Field Sensing Geometries

In this section, a brief literature review is carried out to show possible optical based alternatives to commercially available d-dot sensors for measuring electric fields. Assuming a signal of 1mV, the commercially available d-dot sensors (Prodyn AD-20) have a sensitivity of ~5nV/Hz$^{1/2}$. The device based on the directional coupler assuming the same signal level has been reported to have a sensitivity of ~4nV/Hz$^{1/2}$ and the device based on the tapered Mach-Zender interferometer reported further on has a reported sensitivity of ~ 20nV/Hz$^{1/2}$. The field strengths indicated in the measurements are at the position of measurement. This provides not only insight in the details of the structural geometries used but also to the capabilities and associated limitations encountered in terms of both fabrication and measurements made.

4.2.1.   Directional Coupler

Che-Yun Lin et al[3] have demonstrated the sensing of electromagnetic pulses with an electrode-less, all optical, wideband, electro-optic Y directional coupler (input light comes from single channel and the output is collected from the two channels, as shown in the figure below). The results from this study suggest that the device has an effective detection range from 16.7V/m to 750kV/m at an operating frequency of 1GHz. In device arrangement one input waveguide branches into a pair of symmetric waveguides that are optically coupled with each other. Due to the device symmetry, equal optical power with the same phase is launched into the coupled waveguides, hence the operating point is set to 3dB without the need for any bias voltage. Phase modulation reversal can be realised by poling the electro optic polymer waveguides using a lumped electrode that switches between the two waveguides. A schematic of the device can be seen in *Figure 4. 1* below.
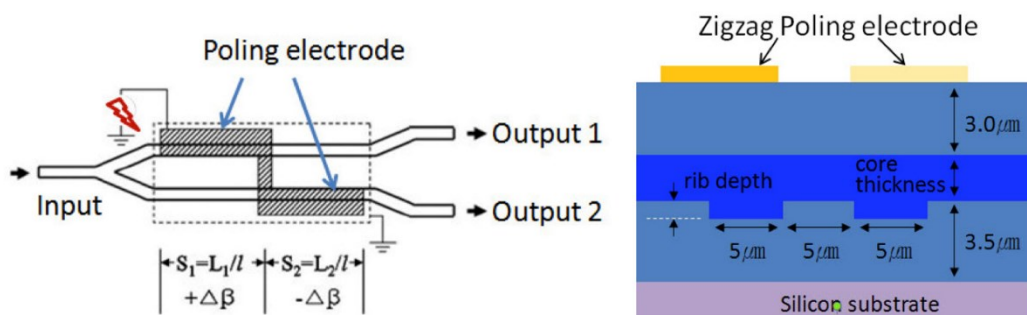
Figure 4. 1. Schematic configuration of the Y-fed directional coupler [3].

The device is fabricated on a silicon carrier wafer. The bottom cladding of the waveguides is made up of a polymer of thickness measuring 3.5μm, with the strip waveguides etched into bottom polymer through reactive ion etching leading to the formation of channels measuring 0.42μm x5μm which are in-filled with a poled electro optic polymer. This is sandwiched by another layer of polymer to act as the top cladding. The electrodes at the top of the structure are formed by conventional photolithography, metal deposition and lift off.

The device characterisation is carried out using a micro strip transmission line capable of generating RF fields in a direction perpendicular to the waveguides. The input light is supplied by a tuneable laser source to the device with TM polarisation which is butt coupled to the edge of the device. The application of the RF field generates an electric field oscillating in the vertical direction hence modulating the refractive index of the electrooptic polymer, which in turn modulates the optical output of the device and the electric field applied can be deduced from the spectrum analyser. The minimum detectable electric field using this arrangement was measured to be 16.7V/m and the maximum calculated detectable field is 750kV/m.

4.2.2. Mach-Zender Interferometer

A Lithium Niobate based photonic device with a Mach Zender optical waveguide interferometer and a tapered antenna array was designed, fabricated and investigated for the measurements of static electric fields and pulsed high power electric fields with nanosecond rise time by a Kaizin Chen et al[4]. It was shown that the device has a relatively flat frequency response in the range from 10 kHz to 5GHz with minimum detectable electric field intensity of 0.4V/m.

The configuration used in the research consisted of a 1.31μm CW laser source, which fed light into a polarisation control module consequently feeding the light into the input arm of the Mach Zender interferometer through a polarisation maintaining fibre. The output light was collected and transmitted through a single mode optical fibre to the photodiode and the transmission spectra analysed to obtain the optical signal modulated by the incident electric field.

The tapered antenna array is the travelling wave modulating electrodes of the Mach Zender optical waveguide interferometer. The array is developed in order to improve the frequency response of the sensor. This improvement comes in two ways; the resistance increases from the bottom of each pattern to the tip, hence reflection currents can be eliminated preventing the formation of standing waves and the effective capacitance of the electrodes can be reduced by using the segmented structure.
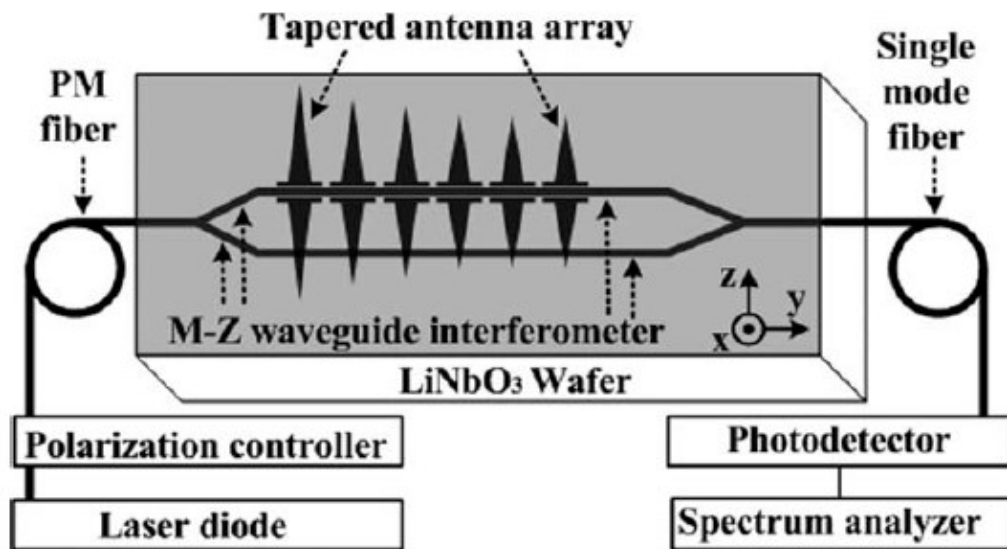
Figure 4. 2. The schematic configuration of the Lithium Niobate based photonic sensor [4].

A schematic of the described device can be seen from *Figure 4. 2* above. The waveguides of the Mach Zender interferometer were fabricated on an x-cut Lithium Niobate substrate using the Annealed Proton Exchange technique. In this technique the extraordinary optical axis is noticeably increased and the ordinary optical axis is unnoticeably decreased, hence only Transverse Electric (TE) polarisation can be used. A SiO_2 buffer layer is deposited above the waveguides through RF sputtering. Above it a Cr seed layer is used for adhesion of the Au, and the tapered antennas are then finally electroplated with Au to form the final structures, which are only placed on one arm of the interferometer.

Considering the fact that the device is designed for the measurements of EMP signals, a high sensitivity is not required. The electrodes are only added to enhance the frequency range of the device. Upon the reception of a pulsed electric field, a voltage is induced across the electrodes whose intensity depends on the magnitude of the applied pulse, consequently modulating the light guided in the waveguide and a measurement of the output extracted by a spectrum analyser which produces a measurement of the applied

pulsed electric field. The overall device dimensions are 85x15x10mm. The sensor showed a linear response for fields ranging from 0-18V/m and 1kV/m pulsed electric fields were measured by the sensor in this research.

4.2.3. Waveguides

Another sensor approach based on a high speed electro absorbance waveguide modulator was explored[5]. With the main aim of improving not only the sensitivity but also the bandwidth of optical electric field sensors, electroabsorption modulators can be used instead of lithium niobate electro optic ones. The sensor works on the principle of a change in the absorption coefficient of an optical material in response to incident electric field applied across them, which results in a modulation of the optical signal.

The magnitude of the electro absorption effect can be enhanced through the use of multiple quantum well layers with III-V materials. A schematic of such a device can been seen from *Figure 4. 3* below
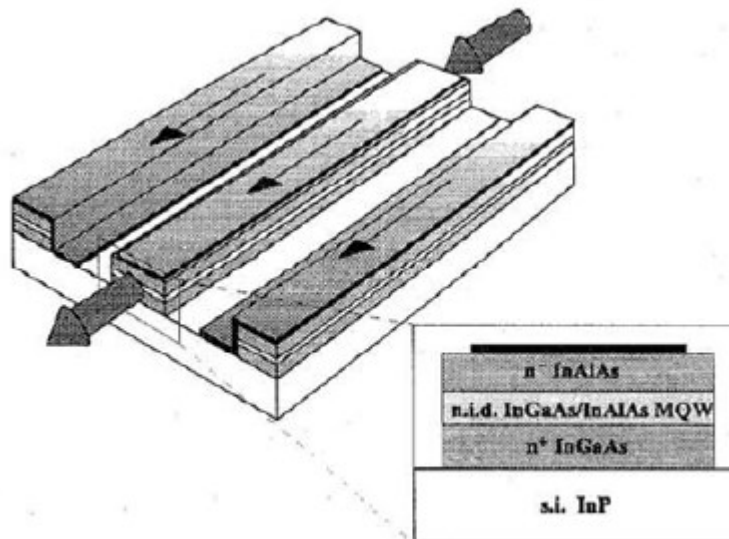
Figure 4. 3. Schematic of the coplanar waveguide modulator [5].

The setup requires the use of two laser sources. One laser source operates at 1.55um providing the optical signal to be modulated by the electro absorbance waveguide modulator, the second laser operates at 0.84μm which is used for the powering of the trans-impedance modulator, and a photo diode for the collection of the output signal. The

minimum detectable electric field using this device was 0.1V/m with a bandwidth of 6GHz.

4.2.4. Bulk Lithium Niobate Crystals

A sensor based on the electro-optic effect lithium Niobate for time domain measurements of intense electric fields was investigated[6]. The sensor head is composed of a bulk Lithium Niobate crystal. It has demonstrated to have the potential of sensing high electric fields (800kV/m) with a wide frequency response ranging from 10Hz to 10MHz. The sensor head was investigated for the measurement of lightning impulses with nanosecond rise times as well.

The principle of operation of the sensor is based on the electro-optic effect present in Lithium Niobate. It is composed of an amplitude modulator in the transverse configuration , with a polariser and an analyser at a cross polarisation with an induced phase shift of the transmitted light caused by the incident electric field applied between the two orthogonal light components. The electric field is applied in the Z-direction of the crystal across two electrodes. A block shaped Lithium Niobate crystal is placed between the polariser and analyser composed of two cross polarised beam splitters. A laser emitting at 1550nm was used as the light source, which travels through a single mode fibre, passes through a collimating lens which focuses the beam inside the crystal. Inside the sensor package the light passes through a linear polariser, a quarter wave plate, the Lithium Niobate crystal and finally out the analyser. The applied electric field modulated the polarisation state and a large diameter multimode fibre used to collect the light. The overall sensor dimensions are 65x15x15mm. A schematic of the experimental setup is shown in *Figure 4. 4* below.
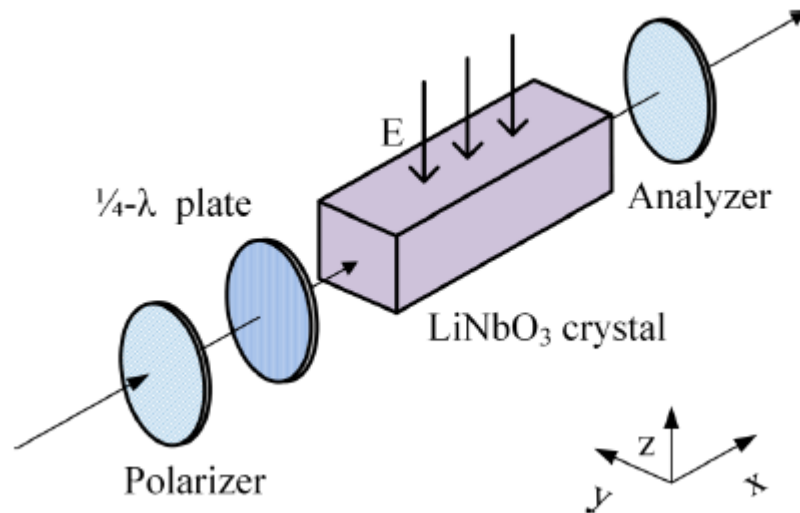
Figure 4. 4. Schematic of the electro-optic conversion unit [6].

In terms of measurements made of lightning impulses, 1.2μs and 50μs rise time pulses with durations of 250μs and 2500μs were investigated using the aforementioned sensor geometry. The sensor has demonstrated of having a flat response across a wide frequency range from 10Hz to 10 MHz. Finally a peak pulsed electric field voltage of 140kV/m was detected using this arrangement.

4.3. Device Geometry and Modelling

The basic structure used to perform the EMP sensing is based around three waveguides which are in sufficient close proximity to permit the evanescent coupling[7] between the central input waveguide and the two side waveguides and seen from *Figure 4. 5.* This evanescent coupling is highly sensitive to the refractive index of the cladding material between the waveguides and by using a material with a large electro-optically non-linear refractive index, a device with an output that is a function of the applied electric field can be created.
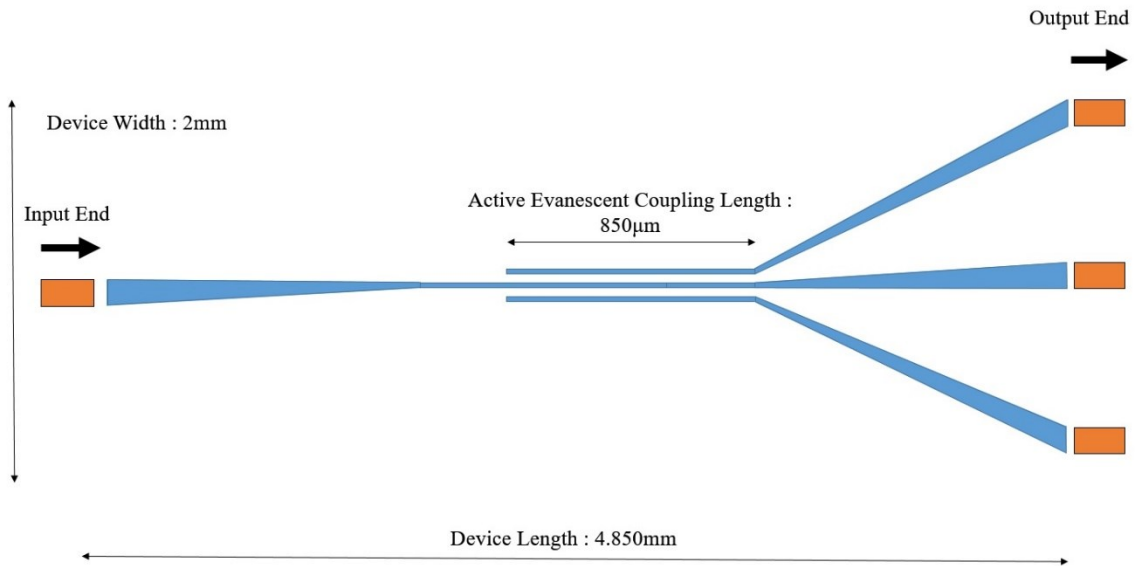
Figure 4. 5. Schematic of the Lithium Niobate Based Waveguide Sensor. (Figure not to scale)
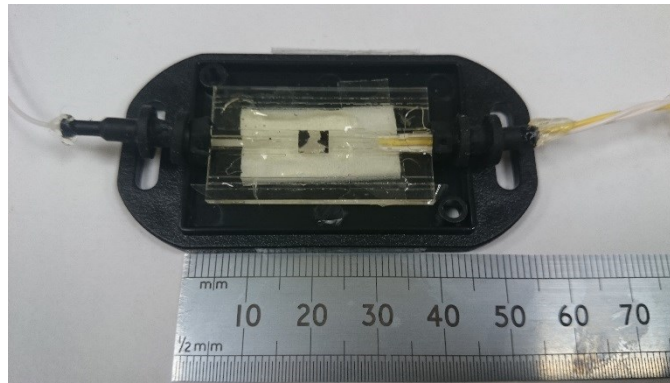
Figure 4. 6. Assembly of the complete sensor package.

Figure 4. 6 above shows a top view of the complete sensor package. The device is fabricated as per the steps mentioned in the previous chapter. The devices fabricated and tested had two different device lengths based on the lengths of the three adjacent waveguides in the active evanescent coupling region. These measured at 4.450mm and 4.850mm respectively. Each of the three adjacent waveguides in the active region has a width of 1μm and is spaced by a distance of 900nm. The waveguides are etched to a depth of 1μm. From the simulations results and the practical limitations of the e-beam writer, this separation distance demonstrated the best evanescent coupling between waveguides. Single mode fibres at an operational wavelength of 1550nm (SMF-28e) with a core diameter of 8.9μm, a mode field diameter of 9.2μm and a cladding diameter of 125μm were used to feed light into the device through butt coupling as well as collecting it. The input and output waveguides have a tapered region with dimensions of 30μm. The input and output channel tapers both measure 2mm in overall length, the output taper measures

at 30μm, which wedges down to 1μm to feed the input and output light into the active region of the device where the waveguides are 1μm in width. This was designed to ease the alignment procedure with respect to the core of the optical fibres. The central tapered output waveguide and the two adjacent tapered waveguides are separated by a distance of 1000μm and are displaced by 30° and -30° in respect to the central output tapered waveguide. The direction of light propagation is from left to right on the page and the incident applied electric field is applied into the page due to the z-cut substrate resulting in a change in the refractive index of the cladding of the waveguides, hence promoting a higher degree of evanescent coupling between the adjacently spaced waveguides in the active region of the device.

The waveguides are designed for single mode operation at 1.55μm which is the operational wavelength but go into multimode operation as the input wavelength is lowered. The light that propagates through the waveguide has most of the power concentrated within the central core of the waveguide. In the cladding region the light intensity decays exponentially with distance from the core. Placing additional waveguides on either side of the central waveguide introduces a perturbation to the mode shape of the central waveguide and vice versa[8]. Therefore, instead of having two independent modes with the same effective index, one of which is localised in the central waveguide and the other in the adjacent waveguides, the modes and their effective indices couple and two super modes (Symmetric and Antisymmetric) are created with effective indices slightly larger and slight lower than the effective index of the unperturbed central waveguide mode. These two modes are excited through a laser source passing through the central waveguide channel and exist because of the numerical solution of the differential equation used.
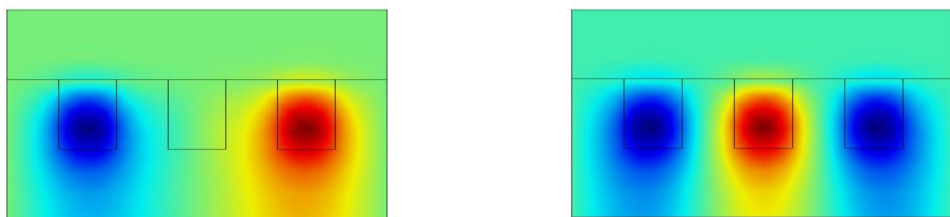
Figure 4. 7. Electric field distribution of waveguide coupling structure showing the asymmetric mode (LEFT) and the symmetric mode (RIGHT). The black lines indicate the areas filled with a-Si acting as the cores of the waveguide and the area underneath being the Lithium Niobate base substrate and the area above being a fused silica substrate.

For the precise device geometry under consideration in this chapter, the cladding of Lithium Niobate is n=2.211 and the core is made up of amorphous silicon n=2.334. The

61

cross section is a square with a total size of 1µm x 1 µm. Due to the amorphous silicon deposition method used during fabrication, a thin bridge of amorphous silicon is formed between the waveguides. From the simulations carried out this thin bridge of amorphous silicon results in an additional slight leakage of the light guided through the waveguides in the upwards direction but it has been shown to have minimal effects on the evanescent coupling between the waveguides. The magnitude of the electric field distribution in the supermodes along the direction of propagation of the symmetric and antisymmetric super modes is shown in *Figure 4. 7.*
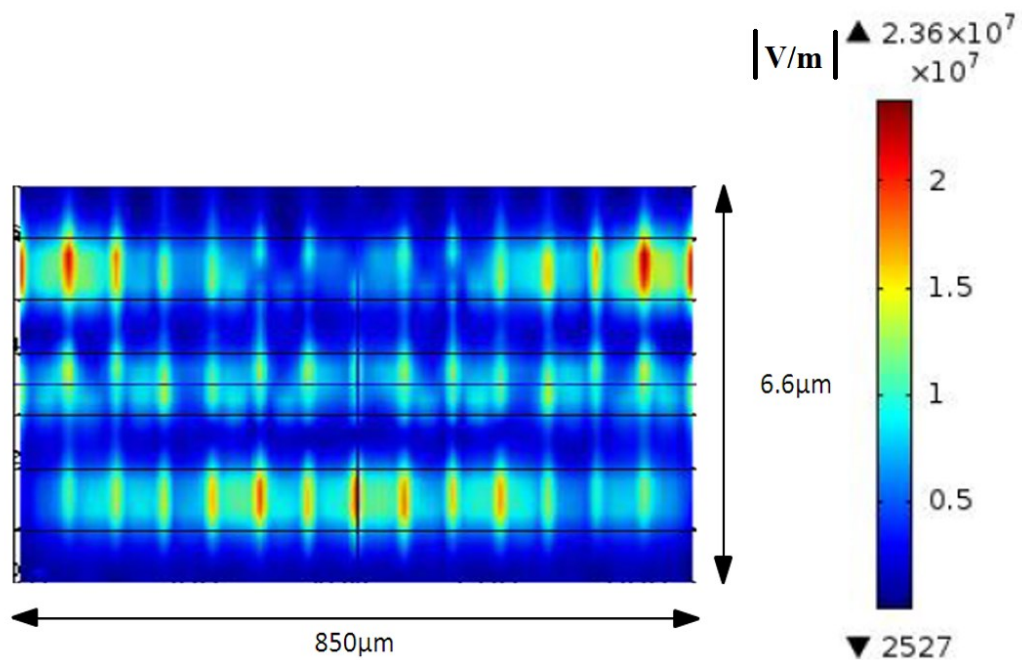
Figure 4. 8. Top view of the electric field distribution in the waveguides at an input wavelength of 1550nm propagating through the waveguides. The black lines indicate the cores of the waveguides and the mode coupling is shown at 500nm below the surface.

The supermodes are both solutions to the wave equation and upon excitation will propagate unperturbed through the waveguides. When both the symmetric and anti-symmetric modes are excited a beating effect is observed between the two modes and the power distribution between the individual waveguides changes as the incident light propagates through the structure. The length of the waveguide structure can be adjusted to ensure a specific level of coupling from the central waveguide to the adjacent waveguides. Due to the typical propagation length being much longer than the wavelength of the propagated light, the beam envelope method can be used to model the waveguide coupling as the computational mesh does not need to resolve on the wavelength scale but rather on the inter-super mode beating length scale[9].

The total electric field can be written as the sum of the electric fields of the two super modes;

$$E(r) = E_1\, exp(-i\beta_1 x) + E_2\, exp(-i\beta_2 x) \qquad (4.1)$$
$$= [E_1 + E_2\, exp(-i(\beta_2 - \beta_1)x]\, exp(-i\beta_1 x)$$

Where E1 and E2 are the amplitudes of the two supermodes (and can be assumed to be identical), β 1 and β 2 are the propagation constants of the antisymmetric and symmetric supermodes respectively and x is the propagation distance along the waveguide.

The expression within the square parenthesis can be solved for and the beat length L can be written as;

$$(\beta_2 - \beta_1)L = 2\pi \qquad (4.2)$$

Therefore;

$$L = \frac{2\pi}{(\beta_2 - \beta_1)} \qquad (4.3)$$

The result of one of the mode propagation simulations is shown in *Figure 4. 8.* The black lines show the lateral extent of the waveguide cores. For this simulation the symmetric mode was found to have an effective refractive index of 2.2248 and the antisymmetric mode has an effective refractive index of 2.2295.From this, the propagation constants β_1 and β_2 have numerical values of 0.0090186 (1/nm) and 0.0090376 (1/nm) with a beat length of ~330μm.
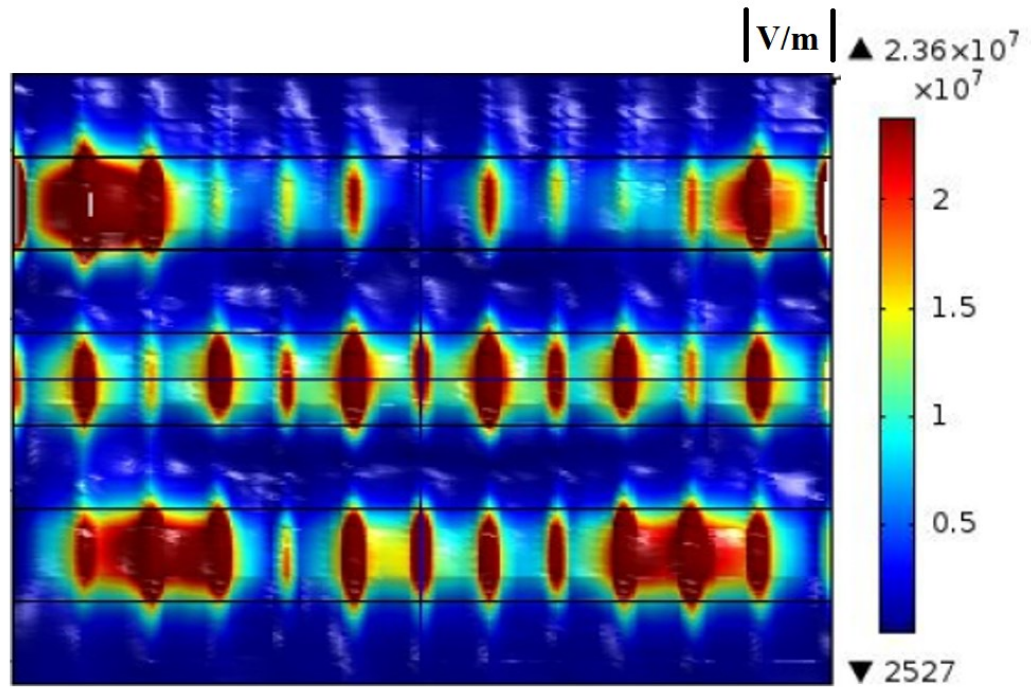
Figure 4. 9. The electric field distribution in the waveguide structure showing the mode coupling between adjacent waveguides with no applied electric field. The black lines show the core of the waveguide structure.
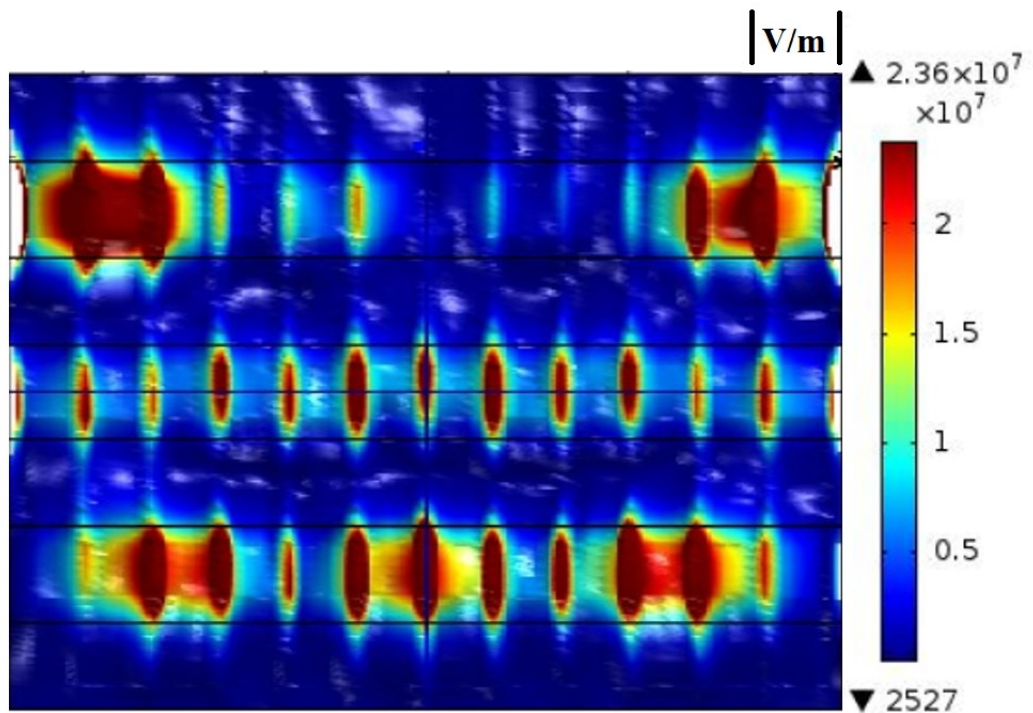
Figure 4. 10. The electric field distribution in the waveguide structure showing the mode coupling between adjacent waveguides with 500kV/m orthogonally applied electric field. The black lines show the core of the waveguide structure.

The variation of the relative propagated light intensity between the central and side waveguides as a function of the applied external electric field can be determined from a series of simulations with the cladding refractive index calculated by:

$$n(E) = n_o + \frac{1}{2} d_{33} n_o{}^3 E_z \tag{4.4}$$

Where n_0 is the ordinary refractive index of Lithium Niobate in the absence of an electric field (n_0=2.21), r_{33} is the z-field z directed component of the electro-optic tensor of Lithium Niobate (r_{33}=30.6pm/V) and E_z is the applied RF electric field (E_z= kV/m). The two images above show the total normalised electric field distribution in the three waveguides, with **Figure 4. 9** being under no applied electric field and **Figure 4. 10** with an electric field of 500kV/m. By comparing both, there is a discernable difference in the electric fields in the side channels. Under no applied electric field majority of the electric field distribution is localised in the central input waveguide channel, but upon undergoing a cladding refractive index change due to an electric field applied in the z direction changing the z electro optic tensor, light propagating from the central waveguide couples into the adjacent waveguides due to the lower confinement of the central mode caused by the refractive index drop.
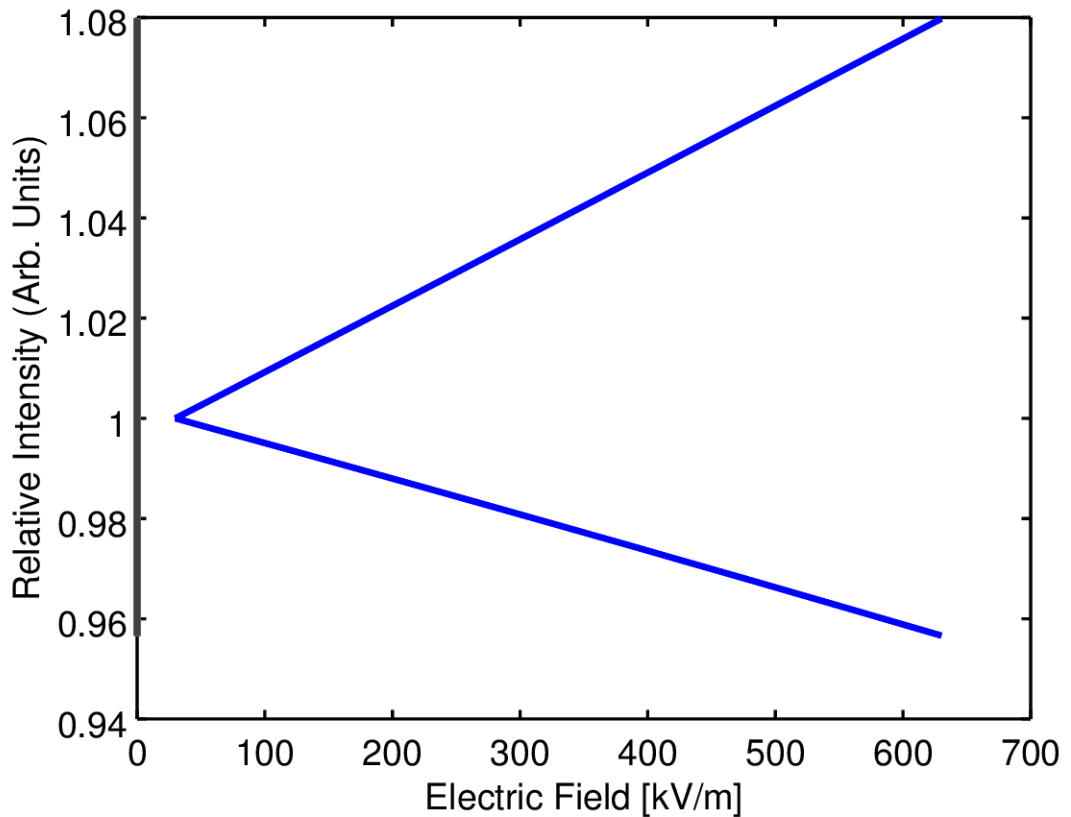
Figure 4. 11. The simulated relative intensity change from the side channels of the waveguide sensor as a function of applied electric field. The top line shows the output from the left channel and the bottom line shows the output from the right channel.

For the field strengths required to be measured (50kV/m to 500kV/m) the change of refractive index is of the order of 10^{-4} to 10^{-5}. The results of these simulations are shown in the **Figure 4. 11** above for a total coupling length of 850μm, the measured parameter is

the output intensity of both side waveguides under no applied electric field. It is seen that the sensor shows a good response to the applied electric field (of the order of 5-10%).

Table 4.1 A comparison between a commercially available d-dot sensor and the fabricated Lithium Niobate Waveguide sensor.

Sensor	AD-20 (free space d-dot)	LiNbO$_3$ waveguide
Response	>10GHz	>0.63GHz
Rise Time	<0.029ns	<1.57ns
Maximum Output	150V	1-5V
Mass	40 g	6.6g
Length	390.4mm	25mm
Breath	25.4mm	15mm
Height	10.9mm	8mm

above compares the operating parameters for a PRODYN commercially available free space d-dot electric field sensor with those for the waveguide sensor. The waveguide sensor is limited in terms of the bandwidth and rise time by the detection electronics, in particular the photodiode used to convert the optical signal into an electrical signal.

4.4. Static Field Testing

The static field testing was carried out in a controlled laboratory environment prior to the commencement of the field trials; the setup can be seen from *Figure 4. 12*. The waveguide sensor was connected to the laser and the power output from the central waveguide channel was monitored using a calibrated silicon photodiode. In order to account for any power fluctuations in the laser output, the measurements were repeated 2,000 times at a frequency of 4Hz. A DC high voltage supply was used to generate an electric field across the waveguide sensor head through two metallic plates acting as electrodes applied across the Z-axis of the sensor head. Output power measurements were taken for no applied electric field and a 312kV/m electric field. The results from this trial can be seen from *Figure 4. 13. Optical power output from Lithium Niobate waveguides for two applied electric*

field strengths. Below which shows a change of the order of 2% between the no field applied and electric field applied.
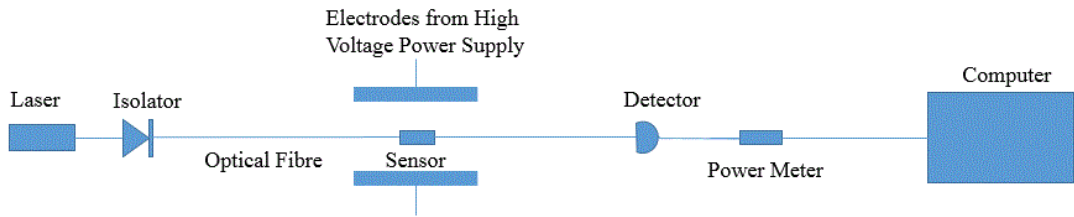
Figure 4. 12. Schematic of the experimental setup used in the static field testing.
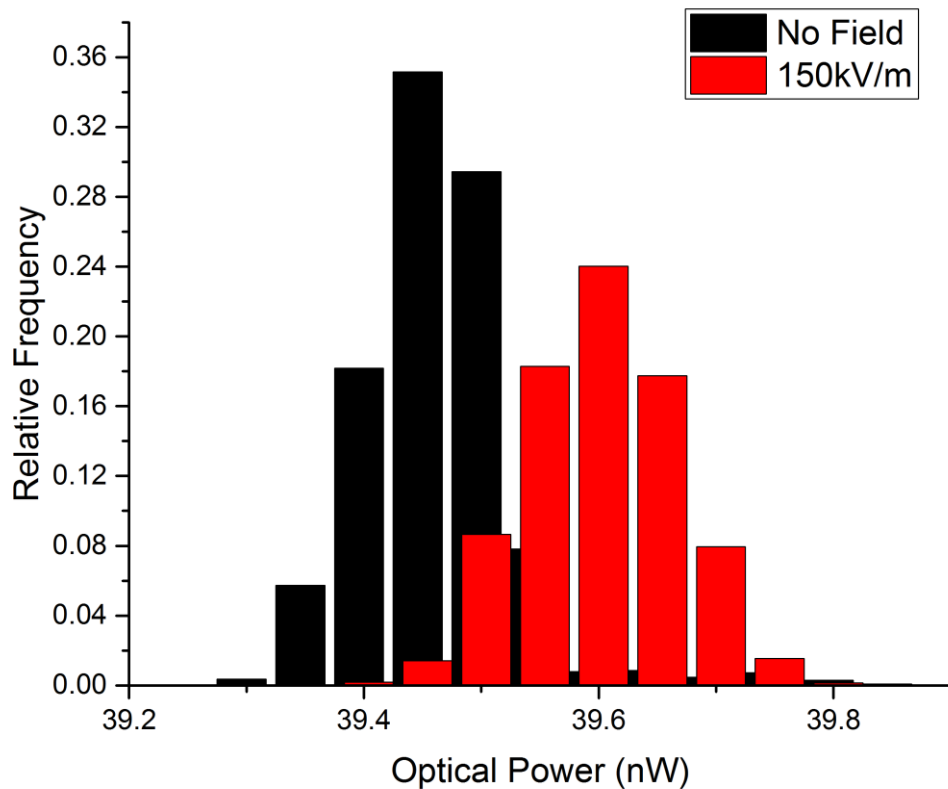
Figure 4. 13. Optical power output from Lithium Niobate waveguides for two applied electric field strengths.

The SNR figure is 1.005 with the noise equivalent power (NEP) being 11.3nW/Hz$^{1/2}$ providing a minimum detectable power of 39.2nW. The SNR can be improved by decreasing the sampling frequency (12Hz) of the power meter which should further lower the minimum detectable power. The resolution of this detector is 2nW.

4.5. Dynamic Field Testing

A schematic of the arrangement required for making pulsed measurements can be seen in *Figure 4. 14*.The completed sensors were tested using an RF pulse generation system capable of producing pulses of up to 500kV/m with a double exponential profile of 50-200ns duration. These simulated pulses are classed as nuclear electromagnetic pulses (NEMP). By placing the sensors at different locations within a tapered region of the pulse generation system, different peak field strengths were achieved and the response of the sensor to these different fields could be assessed. The sensor worked as designed although some issues regarding the amplification of the detected optical signals were addressed. The overall loss of the optical system (from laser to detector) is of the order of 60dB primarily due to the mode field mismatch between the single mode optical fibre and the amorphous silicon/Lithium Niobate waveguides. The optical signal from the waveguides was detected using an off the shelf InGaAs high speed photodiode (ThorLabs DET08CFC) with a sub-ns (<70ps) rise time and a peak responsivity of 0.9A/W, which then passes through a 50Ω termination load resistor, matching the impedance of the oscilloscope. The signal then passes through a high pass filter (Minicircuits 15542 VLF-1500+) to remove any low frequency noise. The signal is then passed through an amplifier (Minicircuits ZKL-1R5+). The amplifiers on each of the channels are powered by 9V batteries to minimise the chance of RF coupling by using an external power supply. The electric signal is carrier through RF shielded coaxial cables into an oscilloscope (Tektronic DPO 70604B, 6 GHz bandwidth, 25 Gigasamples/second). The laser used was a 1550nm Fabry-Perot laser diode with an output power of 100mW (ThorLabs FPL1009S) driven at 400mA with the Thermo-Electric Cooler (TEC) set at 15°C. This is then fed through an optical isolator in order to minimise any back reflections from the sensor which could destabilise the laser output. The signal is then guided to the waveguide sensors using 100m reels of SMF-28e single mode optical fibre terminated with FC/APC connectors on both ends to further minimise any reflections. The light feeds into the central channel of the sensor and exits through the three output waveguides into another 100m reel of SMF-28e single mode optical fibre to the detection electronics located inside the screened room. *Figure 4. 15*.
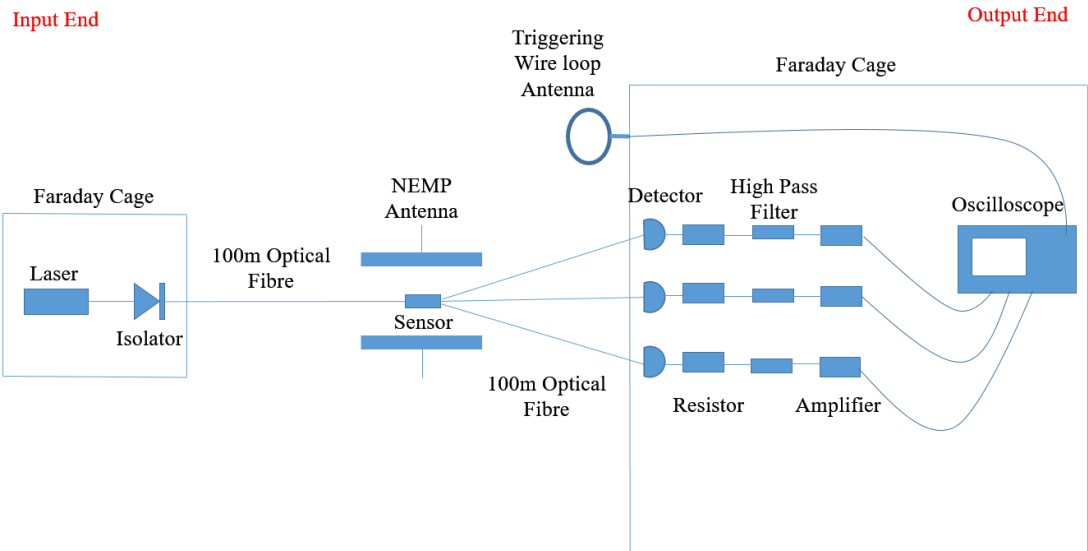
Figure 4. 14. Schematic of the experimental setup used in the dynamic field testing.
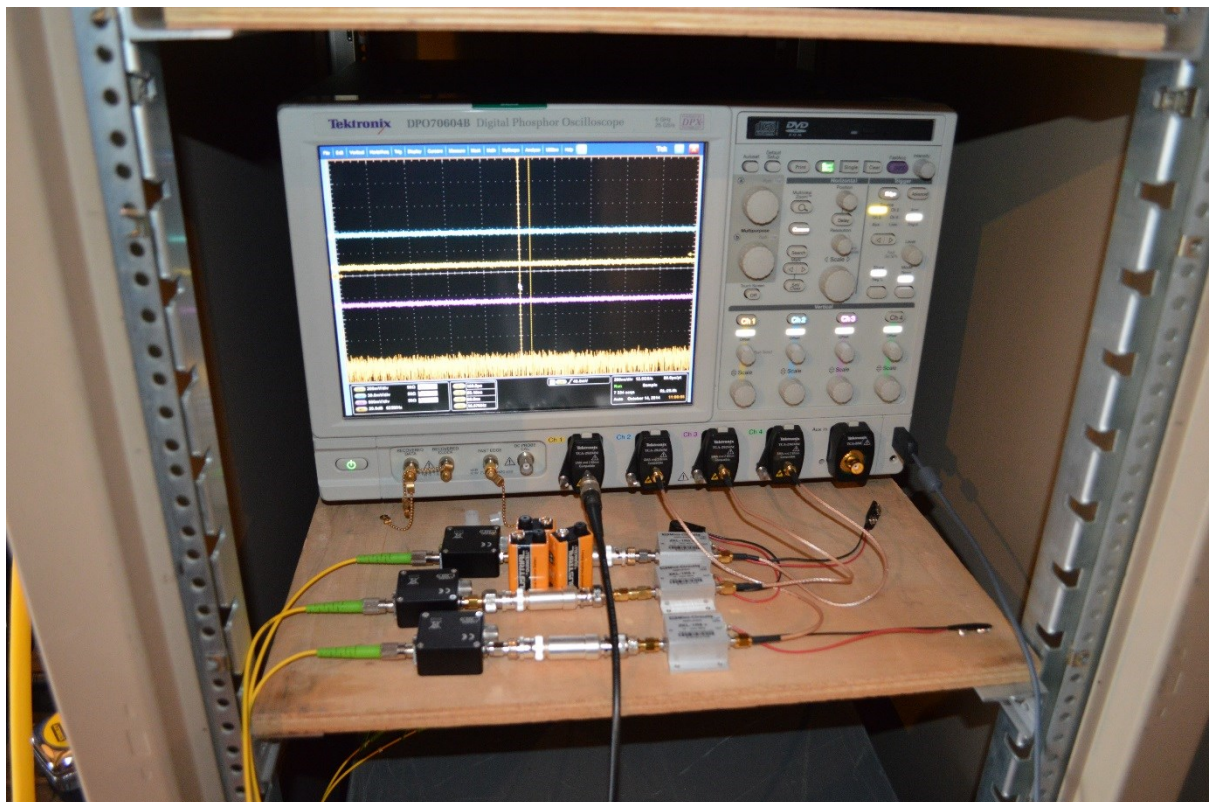
Figure 4. 15. Photograph from inside the faraday cage showing the arrangement of the detection electronics for dynamic field measurements.

69
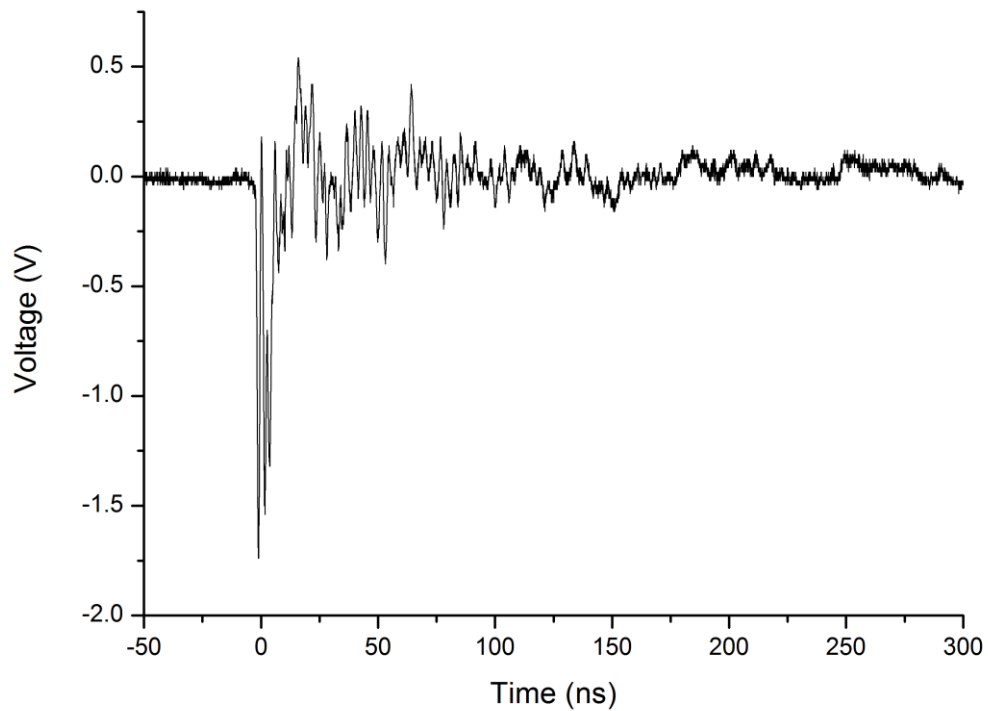
Figure 4. 16. Temporal response of the wire loop antenna at 500kV/m used to trigger the optical waveguide sensor.

The trace shown in Figure 4. 16 above shows the profile of a typical triggering EMP. This was under a peak field strength of 500kV/m. The triggering pulse is measured by a wire loop antenna placed right outside the Faraday cage. The response of the waveguide sensor to the aforementioned peak field strength can be seen from Figure 4. 17 below. The EMP was detected at each of the different peak field strengths investigated. The blue trace is shows the detected optical signal from one of the output waveguide channels. The delay between the initial triggering pulse and the observed optical signal is of the order of 60ns which corresponds to the path difference between the direct free space path of the EMP trigger and the longer guided optical path of the sensor signal. A total of 91 shots over 4 days were detected using the waveguide sensor and a typical response measured from one of the sensor side channels is shown in *Figure 4. 17* below. The blue trace shows the optical output from the central waveguide channel of the sensor as seen from the oscilloscope and the red trace is the electrical output from the wire loop antenna used for detecting the EMP, located outside the Faraday cage used as a trigger for the optical measurements. The offset between the optical and electrical traces is removed for easier visualisation of both signals on the same plot. The oscillatory behaviour in the optical signal can be

70

explained by the ring down effect of the EMP, the presence of cavity oscillations and EMP leakage into the detector electronics.
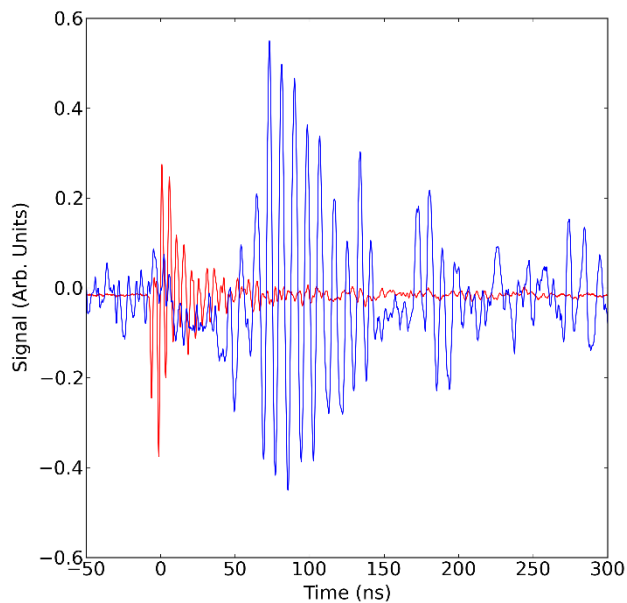
Figure 4. 17. The temporal response from the sensor under 500kV/m incident EMP. The red trace is the triggering EMP pulse measured by the wire loop antenna and the blue trace is the optical output from one of the side channels of the optical waveguide sensor.

The measured optical signal has a significant noise level which necessitated for the development of a data processing algorithm that allows the removal of most of the noise without significantly impacting the waveform produced by the sensor. The algorithm used for the noise removal is a thresholded short time Fourier transform (STFT) where a Fourier transform is applied to a moving temporal window across the duration of the signal. This method is similar in concept to the wavelet transform[10] and produces a time frequency spectrogram of the measured optical signal that shows the clear existence of the EMP induced variation separated from the background noise. The time frequency spectrogram of the optically measured EMP is shown by *Figure 4. 18.*
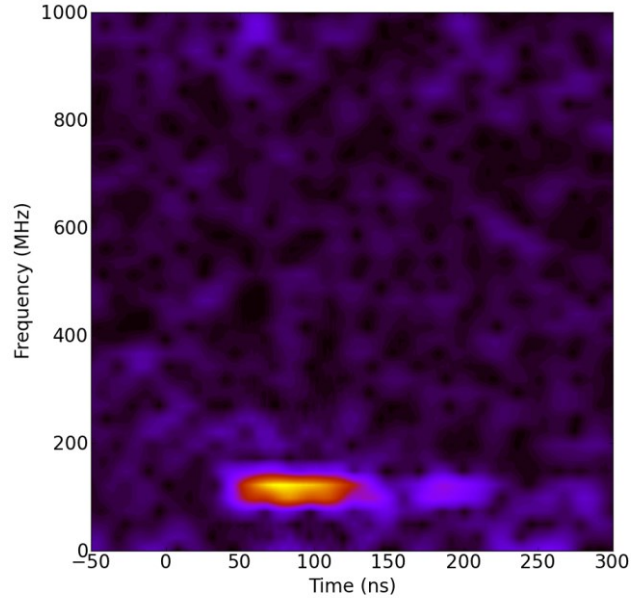
Figure 4. 18. Time Frequency spectrogram of the detected pulse measured by the waveguide sensor after noise removal by means of a thresholded STFT.

The response of the sensor to peak EMP field strength was determined by plotting the peak measured voltage of two different coupling length sensors (450μm and 850μm respectively) as a function of the nominal EMP field strength (calculated by reference to the measured pulse strength).
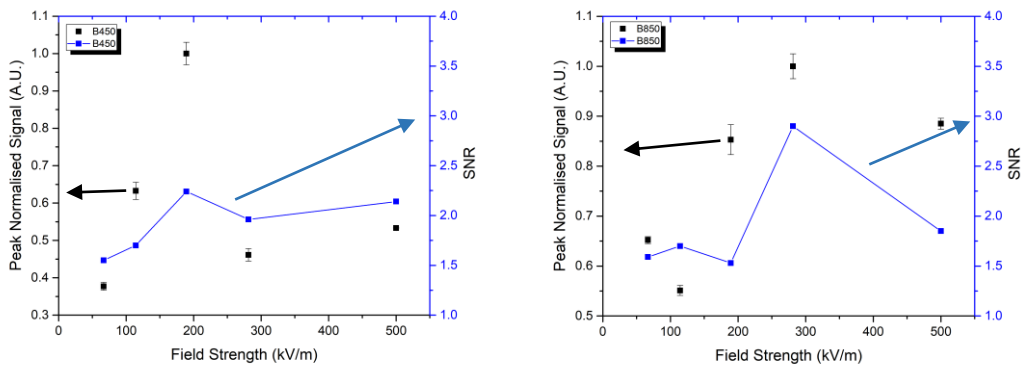
Figure 4. 19. Variation of peak measured sensor response as a function of peak EMP field strength.

As seen from *Figure 4. 19* above, the peak voltage is normalised by the detected optical power through the central sensor channel as the different sensors had different base levels of transmitted power. It can be observed that trend of the measured sensor response follows a sinusoidal like pattern, which is primarily due to the existence of a low finesse micro cavity formed between the end facets of the waveguide structure and the optical fibres used to transfer the optical signal to and from the sensor. The noise equivalent

72

voltage of the system described above is 6.8nV/Hz$^{1/2}$ giving a minimum detectable voltage of ~ 10.8mV. The best SNR produced with this configuration is around 2.9 which can further be increased by lowering the sampling frequency further or applying a sliding average. The noise equivalent of the system is also limited by the noise equivalent power of the detector used which in this case is 2×10^{-15}W/Hz$^{1/2}$ as well as the detection electronics used. There are regions of the response curves where the monotonically increasing response would allow the determination of the peak EMP field strength over a limited range of field strengths. The replacement of the orthogonal waveguide facets with angled facets is potentially a way of eliminating the effect produced by the micro cavity and hence improve the operating range of the waveguide sensor. The deployment of two sensors with different coupling lengths side by side would allow for the identification of the peak field strength over a much larger range of EMP field strengths.
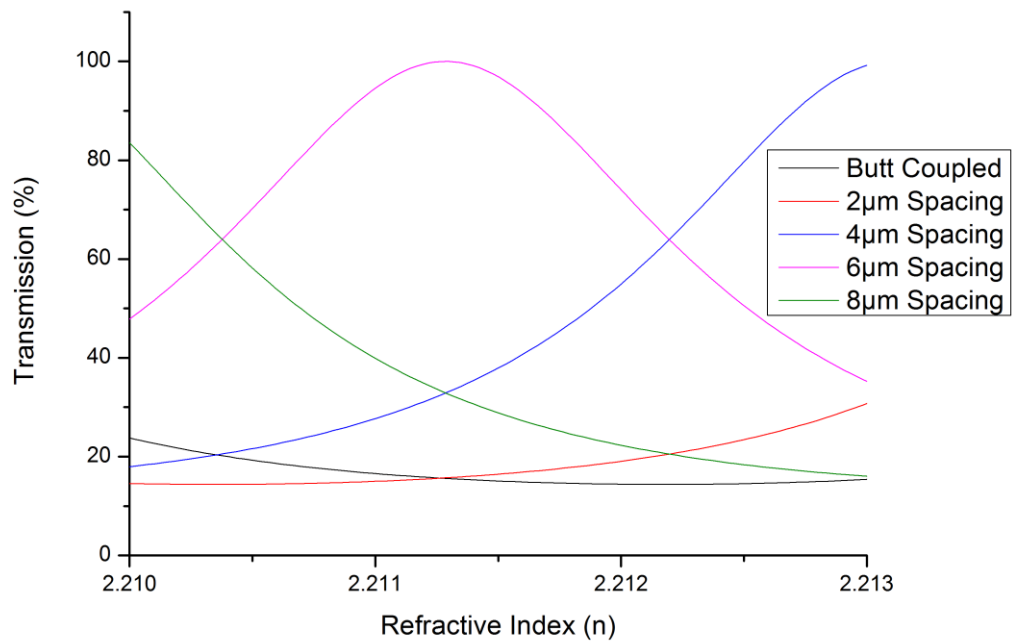
Figure 4. 20. Modelled sinusoidal variation in the peak transmissivity through the high finesse micro cavity formed between the optical fibres and the waveguide sensor showing the effects of increasing cavity length on the transmission characteristic of the device.

4.5.1. Temporal Pulse Shape

Apart from the ability of measuring the peak field strength of the incident EMP with the waveguide sensors, the measured response can also be used to provide a reconstruction of the EMP pulse shape. The optically measured signal is generally similar to that measured by the wire loop antenna used for the measurement of the triggering pulse. The triggering signal has to be integrated in order for it to be compared to the measured optical signal. There does exist a degree of temporal expansion in the features which is primarily down to the frequency response of the detection electronics used.
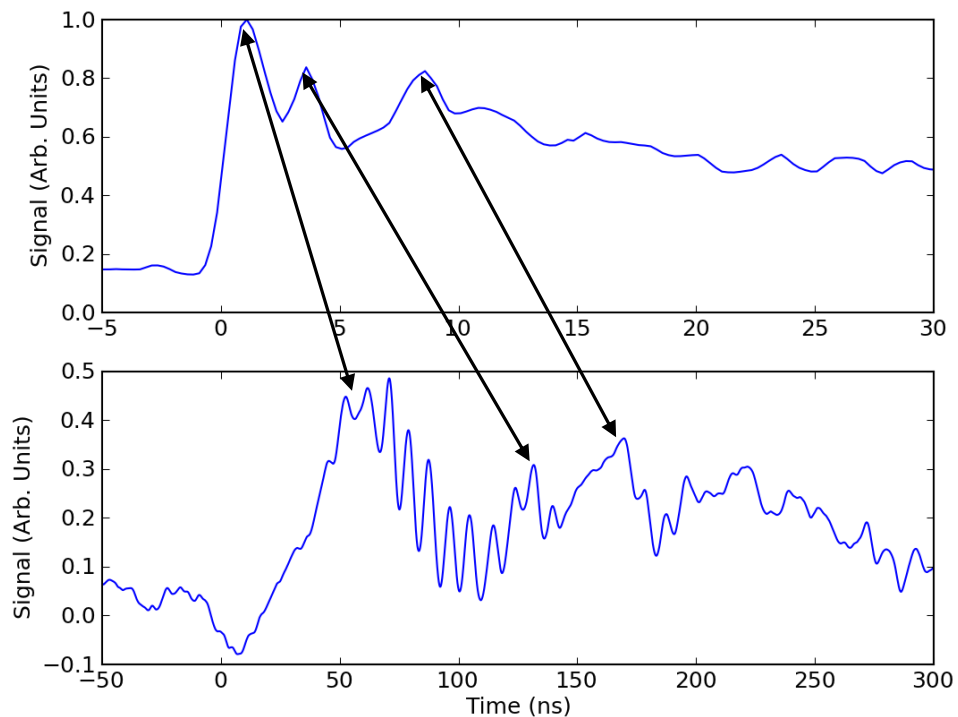
Figure 4. 21. The temporal pulse shape as measured by the wire loop antenna shown in the top figure and the optically measured response from a waveguide sensor after integration, showing a qualitatively similar pulse shape with a significant amount of temporal expansion accredited to the detection electronics.

From **Figure 4. 21** above the trace on the top is measured signal by the wire loop antenna used as the trigger of the optical system and the waveform at the bottom is as measured through one of the channels of the waveguide optical sensor. The waveform is integrated and the regions of similarity are the first, second and third peaks in the above trace.

4.6.   Field Trials at Simulateur Semi-Rhombique (SSR)

High powered electromagnetics operating in a single repetition regime, can be used to generate intense EM signals ranging from 500MHz to 5GHz, with rises times ~10's ns , pulse durations of 50-200ns and peak pulse powers of the order of MW can couple and cause damage to electronic systems and critical infrastructures in various different ways.

Hence the need for using a NEMP (Nuclear Electromagnetic Pulse) facility that creates an environment in which the vulnerability of electronic components and systems can be accurately accessed providing critical information for further hardening of systems to EMPs[11]. It is of the utmost importance to be able to; reliably simulate an environment in a limited experimental volume, measure both the magnetic and electric parts of the generated pulse with precision, accuracy and minimal sensor interference, access damage thresholds of commercial electronics and finally improve the EM hardness by shielding and surge suppression techniques. Though there are many analytical tools available which can be used to theoretically assess this vulnerability, an experimental validation to complement these theoretical predictions is required.

The bounded wave transmission line simulator is a parallel plate metal structure tapered down at both ends to a metal ground plate thereby depicting a parallel plate transmission line geometry[12]. The simulated volume is bound to the region of the two parallel plates. The EM field in the dominating transverse (EM) mode within the structure closely simulates free space EM wave propagation. The induced electric field remains perpendicular to the parallel plates with fringing occurring at the edges. The induced magnetic field on the other hand remains parallel to the parallel plates. As a result of this there exist two field vectors which are transverse to the direction of the wave propagation.

The dimensions of the SSR at Gramat are ~94m in length, ~15m in height at the tallest point, 30m wide, and the taper at the horn is angled at 18.75°. The pulses generated by the SSR have a double exponential pulse shape with a typical pulse duration of 20ns and the consistency between individual shots being high. The terminated load is carried out by means of shunt resistors at the end opposing the horn of the antenna. The antenna is powered by a 1MV Marx generator which is capable of producing single shots approximately every 10 minutes.
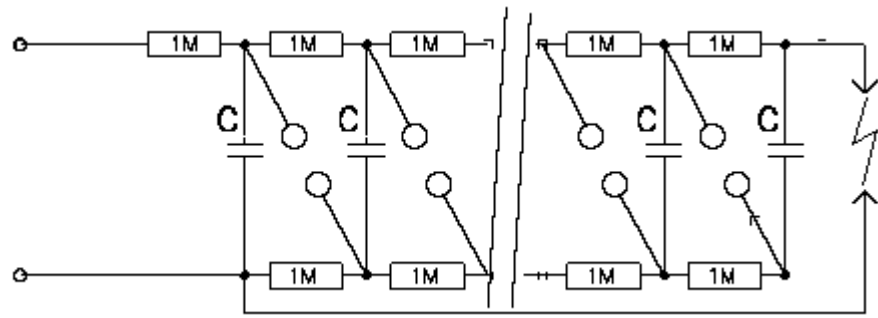
Figure 4. 22. Schematic of a MARX generator.

A Marx generator is a circuit which is capable of producing a high voltage pulsed discharge from a low voltage DC input [13]. The generator is comprised of a series of capacitors and resistors each isolated by spark gaps. The generator works based on the principle of charging a number of capacitors in parallel and discharging them in series through suddenly connecting them. The discharge is initialised though the use of spark gaps. There is a voltage across which is lower than the breakdown voltage, but as soon as the breakdown voltage is reached, the spark completes the open charging circuit and discharge occurs. A schematic of this device is shown in *Figure 4. 22*.
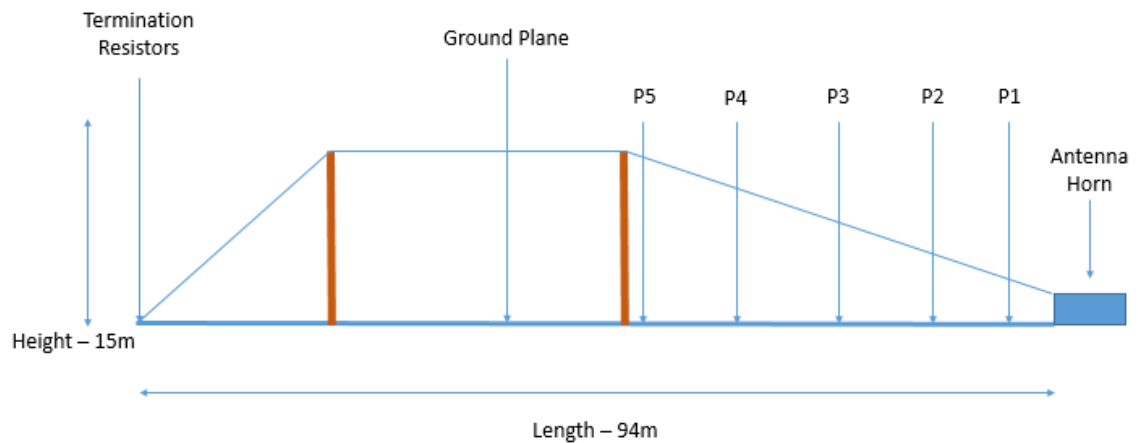
Figure 4. 23. Side profile of the SSR showing the points at which the measurements are taken of the EMP field strengths. The red sections are plastic pillars which support the antenna.

The schematic in *Figure 4. 23* above is a side view of the SSR at Gramat. On the right hand side is the horn of the antenna where the signal emanates from. P1 is a position ~1.9m

76

away from the taper of the antenna, the approximate field strength at this position is 500kV/m. P2 is a position ~6.4m away from the taper of the antenna, the approximate field strength at this position is 400kV/m. P3 is a position ~11.2m away from the taper of the antenna and this is where the D-Dot sensor located at the ground plane used for calibration measurements and the field strength at this position is 200kV/m. P4 is a position ~21.7m away from the taper of the antenna, the approximate field strength at this position is 100kV/m. P5 is a position ~42.1m away from the taper of the antenna, the approximate field strength at this position is 50kV/m. The screened room where all the sensitive detection electronics and the laser driver were located was 61.5m away from the taper of the antenna. The wire loop antenna which was used to trigger the measurements was located on the side of the screened room.

The simulator is designed to generate pulses similar to those generated by a high altitude nuclear detonation and their corresponding electrical characteristics (NEMP which is exo-atmospheric)[14]. Upon impact there is a sudden release of gamma radiation due to the detonation of the nuclear weapon, resulting to the near instant ionisation of the atmospheric gases, with the free electrons driven outwards. The free movement of these electrons, which later recombine with atmospheric atoms (Compton Recoil Effect)[15] create a pulsed EM field (Referred as NEMP), 99% of this energy is radiated in a broad spectrum from 10kHz to 100MHz, with most of the energy below 10MHz. The fast rising time (~10ns) as well as the short duration (~200ns) causes ringing in the antenna. The amplitude of the ringing depends on the amount of captured energy.

Mathematically the pulse shape can be expressed as the difference between two decaying exponentials which are time varying[16]. This pulse shape is shown in *Figure 4. 24*.The rise time is of the order of 10ns, the field intensity decays to 1/e in a couple of hundred ns, the generally agreed value of the peak field is of the order of 50kV/m. This value is used as a standard minimum threshold for damage and a standard parameter for radiated NEMP susceptibility testing of equipment (MIL-STD-461 RS105 test method).

$$E(t) = E_0\left(e^{\alpha t} - e^{\beta t}\right) V/m \qquad (4.5)$$

Where E_0 is the electric intensity constant (50kV/m), α is the decay constant (-4x10^6 /s), β is the rise time constant (-476x10^6 /s) and t is the time.
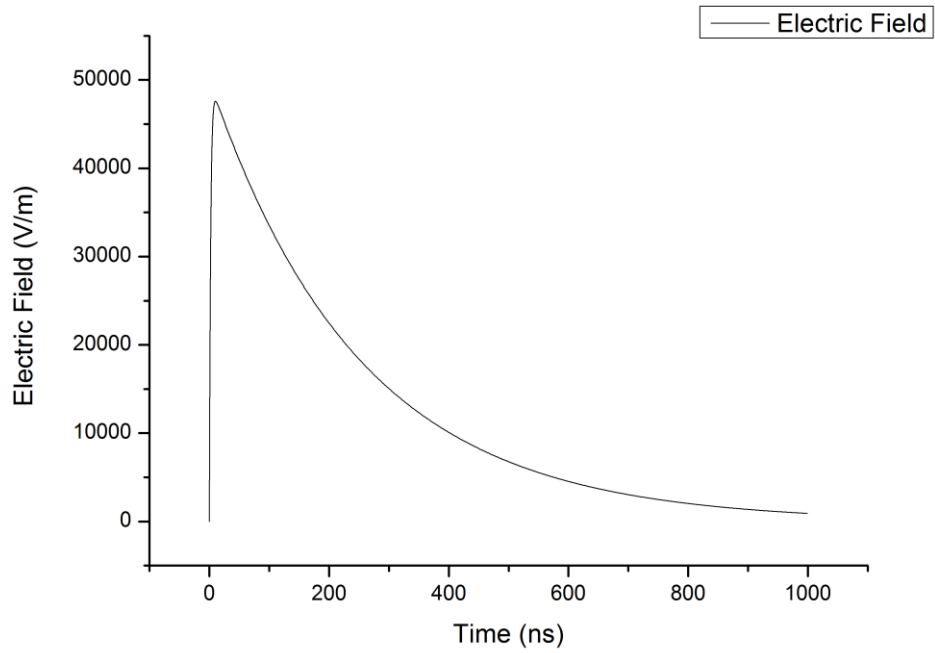
Figure 4. 24. Mathematical representation of waveform of two decaying exponentials showing an idealized EMP.
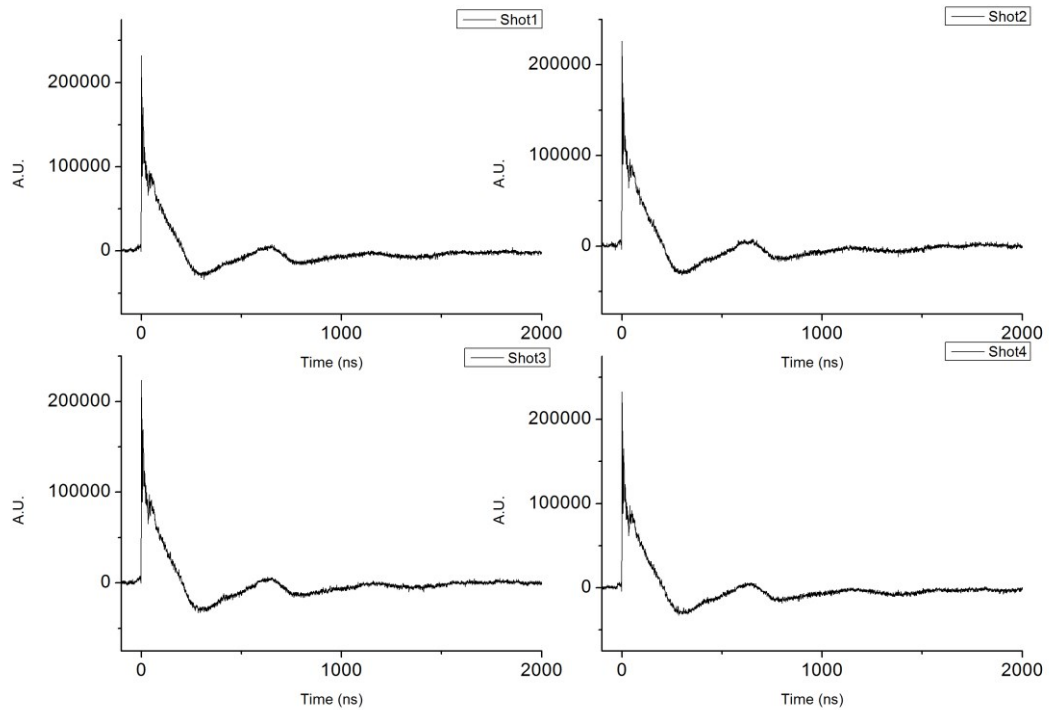
Figure 4. 25. Temporal pulse shapes of 4 EMP generated by the SSR as measured by a conventional d-dot electric field sensor showing consistency between successive pulses.

Figure 4. 25 above shows the temporal pulse shapes of the generated EMPs by the SSR as measured by a D-Dot sensor placed 11.2m away from the horn of the antenna with a

78

vertical height of ~3.3m at which position the peak EMP field strength is 200kV/m. From the graphs, it can be observed that there is a really good consistency between individual pulses with next to no variation between shots.

From transmission line theory[17], a generator with an internal impedance as well as other circuit impedances comprised of lead inductance and resistance is connected to a transmission line and terminated at the characteristic resistive impedance, which is generally resistive is generally equivalent to an RLC circuit. The terminating load also gets rid of back reflections which occur if the pulse is not fully discharged. This effect can be neglected (the termination of the load) provided that the line is effectively lossless and propagates the pulse wave shape without distortion while illuminating the object in the test volume (deemed from the dimensions). As a general rule of thumb, an acceptable low pulse wave shape distortion illumination within the test volume can be achieved if the height and width of the line are less than 1/3 of the corresponding line openings.
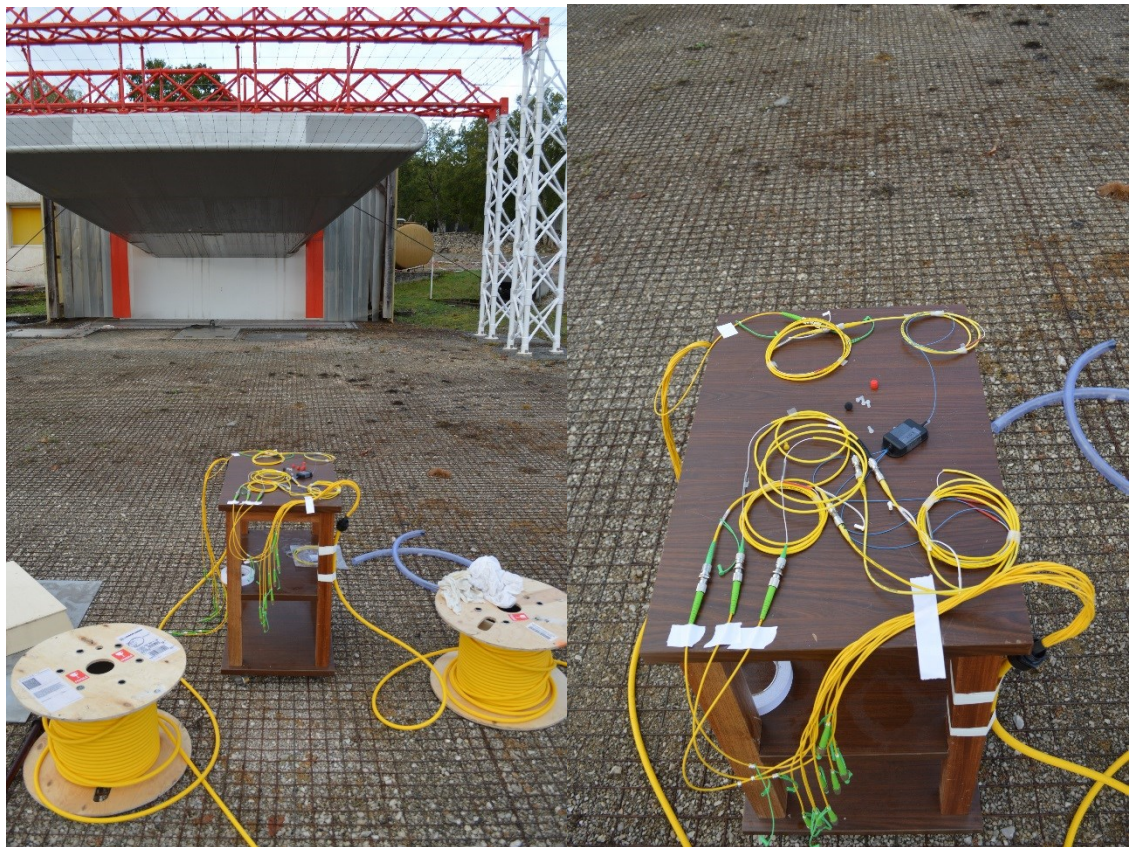
Figure 4. 26. Photographs of the waveguide sensors at position 1 under the SSR (LEFT) and a connectorized waveguide sensor (RIGHT).

4.7.   Conclusions

The design and testing of an optical EMP sensor capable of determining the both the peak EMP field strength as well as the temporal pulse shape of the incident EMP field. The use of Lithium Niobate as the substrate material has allowed for the development of a compact sensor head readily compatible with powerful readily available laser sources and optoelectronic detection hardware. The fabrication process which was needed to produce the desired waveguide structures has been characterised and fully optimised with a view of producing relative large numbers of sensors with standardized responses to the incident EMP. The integration of the sensor head with the required optical fibre equipment is still a time consuming process as each of the assemblies needs to assembled individually. The noise equivalent voltage (at a SNR of 1) of the system described in this chapter is ~ $7nV/Hz^{1/2}$, which is comparable to both the commercially available d-dot sensors and the devices described from the literature review. However due to the losses in the optical system the highest SNR measured was 2.9 for an incident EMP of field strength of ~300kV/m. From the experimental testing it has been concluded that only a single output channel needs to directly monitored and therefore only two fibres will need to be integrated with the sensor head in the future rather than the current four. Further optimisation of the fabrication and integration process will reduce the overall size of the sensor head with a view to allowing the direct fusion splicing of the sensor head with the single input/output fibre channel.

4.8.   References

[1]   H. M. Shen, R. W. P. King, and T. T. Wu, "New Sensors for Measuring Very Short Electromagnetic Pulses," *IEEE Trans. Antennas Propag.*, vol. 38, no. 6, pp. 838–846, 1990.

[2]   M. S. Smith *et al.*, "Modified 1x2 Directional Coupler Waveguide Modulator",*Electronics Letters*, vol. 22, no. 18, pp. 4–5, 1986.

[3]   C.-Y. Lin, A. X. Wang, B. S. Lee, X. Zhang, and R. T. Chen, "High dynamic range electric field sensor for electromagnetic pulse detection," *Opt. Express*, vol. 19, no. 18, pp. 17372–17377, 2011.

[4]   A. Danideh and R. A. Sadeghzadeh, "Cpw-fed slot antenna for mimo system applications," *Indian J. Sci. Technol.*, vol. 6, no. 1, pp. 3872–3875, 2013.

[5]   R.Heinzelmann *et al*"Optically Powered Remote Optical Field Sensor System Using an Electroabsorbtion-Modulator, ", *Selected Hot Topics in Optoelectronics,* vol.1, pp.1225-1228,1998.

[6]   Q. Yang, S. Sun, R. Han, W. Sima, and T. Liu, "Intense transient electric field sensor based on the electro-optic effect of LiNbO3," *AIP Adv.*, vol. 5, no. 10, pp. 0–10, 2015.

[7]   W.-P. Huang, "Coupled-mode theory for optical waveguides: an overview," *Josa a*, vol. 11, no. 3, pp. 963–983, 1994.

[8]   M. Lohmeyer, "Wave-matching method for mode analysis of dielectric waveguides," *Opt. Quantum Electron.*, vol. 29, no. 9, pp. 907–922, 1997.

[9]   S. Somekh, E. Garmire, A. Yariv, H. L. Garvin, and R. G. Hunsperger, "Channel Optical Waveguides and Directional Couplers in GaAs-lmbedded and Ridged.," *Appl. Opt.*, vol. 13, no. 2, pp. 327–30, 1974.

[10]   S. Qian, *Introduction to Time-frequency and Wavelet Transforms*. Prentice Hall PTR, 2002.

[11]   K.P.Gowd, "Parameters For Validation of a NEMP Hardended Facility.", *10 th International Conference on Electromagnetic Interference & Compatibility,* pp.645-649,2008.

[12]   M. Bushell, R. Manriquez, G. Merkel, W. Scharf, and D. Spohn, "beams.1," no. 6, pp. 1834–1838, 1980.

[13]   A. D. Andreev, M. I. Fuks, M. Roybal, and E. Schamiloglu, "Design and optimization of a low-impedance pulsed-power marx generator to drive high-power relativistic X-band magnetron," *Dig. Tech. Pap. Int. Pulsed Power Conf.*, pp. 214–217, 2007.

[14]   P. L. Rustan, "Description of an Aircraft Lightning And Simulated Nuclear Electromagnetic Pulse (NEMP) Threat Based on Experimental Data," *Electromagn. Compat. IEEE Trans.*, vol. EMC-29, no. 1, pp. 49–63, 1987.

[15]   A. H. Compton and J. C. Hubbard, "The recoil of electrons from scattered x-rays," *Phys. Rev.*, vol. 23, no. 4, pp. 439–449, 1924.

[16]   M. Camp and H. Garbe, "Parameter estimation of double exponential pulses (EMP, UWB) with least squares and Nelder Mead algorithm," *IEEE Trans. Electromagn. Compat.*, vol. 46, no. 4, pp. 675–678, 2004.

[17]   M. lanoz, C. A. Nucci, and F. M. Tesche, "Transmission Line Theory for Field-to-Transmission Line Coupling Calculations," *Electromagnetics*, vol. 8, no. 2–4, pp. 171–211, 1988.

Chapter 5. Nanostructured Plasmonic Surfaces for Electric Field Sensing.

5.1.   Introduction

The field of plasmonics has received a significant level of research interest over the last two decades with numerous applications of plasmonic based devices found in the literature with bio sensing, high resolution imaging and spectroscopy being the fields mostly exploiting their inherent advantages. The application of plasmonic devices to the detection of static and dynamic electric fields relies on the tunability of the plasmonic response ensuring a high sensitivity as well as a high speed effect. The sensing of electric fields is of particular importance in electromagnetic compatibility (EMC) studies[1], the detection of partial discharges from high voltage equipment[2] and accurate measurements of naturally occurring phenomena such as lightning discharges[3]. Conventionally electric fields are sensed using electric based sensors (such as the d-dot sensor) which are large bulky metallic devices which are capable of introducing a significant amount of perturbation to measured field as well as preventing the measurement of fields in enclosed spaces. The use of micro- and nano-structured electro-optic materials has demonstrated the potential for the development of sensors with multiple orders of magnitude less electric field distortion as well as occupying significantly less space, facilitating the measurements of fields in enclosed spaces.

Surface Plasmons (SP) are a class of electromagnetic surface waves that can propagate along the surface boundary between a thin metallic layer and an underlying base substrate. In this chapter, the surface plasmons generated due to the interaction of an incident optical frequency electromagnetic wave with a thin noble metallic surface containing a periodic array of sub micrometre holes are investigated. The aforementioned surface waves provide a coupling mechanism for the extraordinary transmission (EOT) of energy above that supported by the classical scattering theory[4]. Extraordinary transmission (EOT) has been exploited in many applications such as Surface Enhanced Raman spectroscopy[5], surface enhanced fluorescence spectroscopy[6] and biological sensing[7] which all rely on the sensitivity of the extraordinary transmission to small changes in the refractive index of the substrate material.

In this chapter, the design and experimental verification of an extraordinary transmission based sensor fabricated by forming a periodic array of nanoholes on an optically non-

linear z-cut Lithium Niobate substrate is presented. The nanostructured surface was fabricated using electron beam lithography and lift-off to form the periodic arrays of nanoholes on the surface of Lithium Niobate. An applied electromagnetic field incident of the sensor head induces a change in the refractive index of the Lithium Niobate through the largest electro-optic tensor component. The sensing mechanism is based on the detection of a change in the transmitted amplitude through the sub wavelength holes in the optically opaque thin metallic film due to the Surface Plasmon enhancement when the refractive index of the base substrate is modified by the applied electric field.

5.2. Surface Plasmons

Surface plasmons are a coherent electron oscillation that can be supported across the interface between two materials in which the real parts of the dielectric constants have different signs. This condition is however not sufficient to guarantee a true Surface Plasmon mode that can propagate over a substantial distance as well as interacting resonantly with the incident optical wave. For a true Surface Plasmon mode excitation, one of the chosen materials must possess a sufficiently large negative real dielectric constant to ensure the propagation of the surface wave along the interface. In general this condition is satisfied by most of the noble metals. Additionally, the momentum of the incident optical wave must be modified to match that of the Surface Plasmon mode by means of an external structure, being either a prism or some sort of a surface grating. Once all the necessary conditions are satisfied, energy can be transferred between the optical wave and the Surface Plasmon wave with the resonant wavelengths determined by the substrate refractive index. The propagation constant of the Surface Plasmon wave and conditions for resonance are very sensitive to changes in the optical properties of the dielectric substrate adjacent to the thin metallic layer supporting the Surface Plasmons. The surface wave excited propagates at an angle perpendicular to the direction of the incoming incident optical wave.
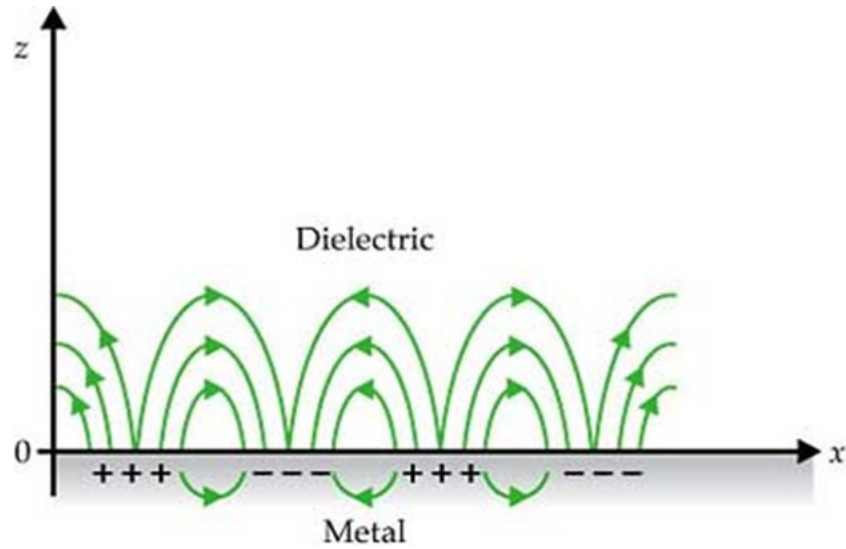
Figure 5.1. The propagation of surface waves at the metal dielectric interface[23].

5.3.   FDTD Modelling

The plasmonic device was modelled using a 3 dimensional finite difference time domain (FDTD) code with periodic boundary conditions and a perfectly matched layer in z-direction, the propagation direction seen from *Figure 5. 2*. The unit cell periodicity was 620nm, with a gold coating thickness of 100nm and circular hole diameters ranging from 250nm to 350nm. The wavelength dependence of the Surface Plasmon resonance modes of a square-packed array of circular nanoholes with the incident light incident at an angle normal to the plane of incidence of the nanohole array is given by[8]

$$\lambda_{max} = \frac{a_0}{\sqrt{m^2 + n^2}} \sqrt{\frac{\varepsilon_m \varepsilon_d}{\varepsilon_m + \varepsilon_d}}$$

(5.1)

Where λ_{max} is the resonant wavelength, a_0 is the nanohole period, ε_d is the dielectric constant of the substrate and ε_m is the dielectric constant of the metal and m and n are the integers expressing the scattering mode indices. A transmission minimum is observed before each Surface Plasmon peak due to Woods anomaly[9]. In the diagram below a thin chromium adhesion layer is added to improve the bonding between the Lithium Niobate substrate and the gold thin film.
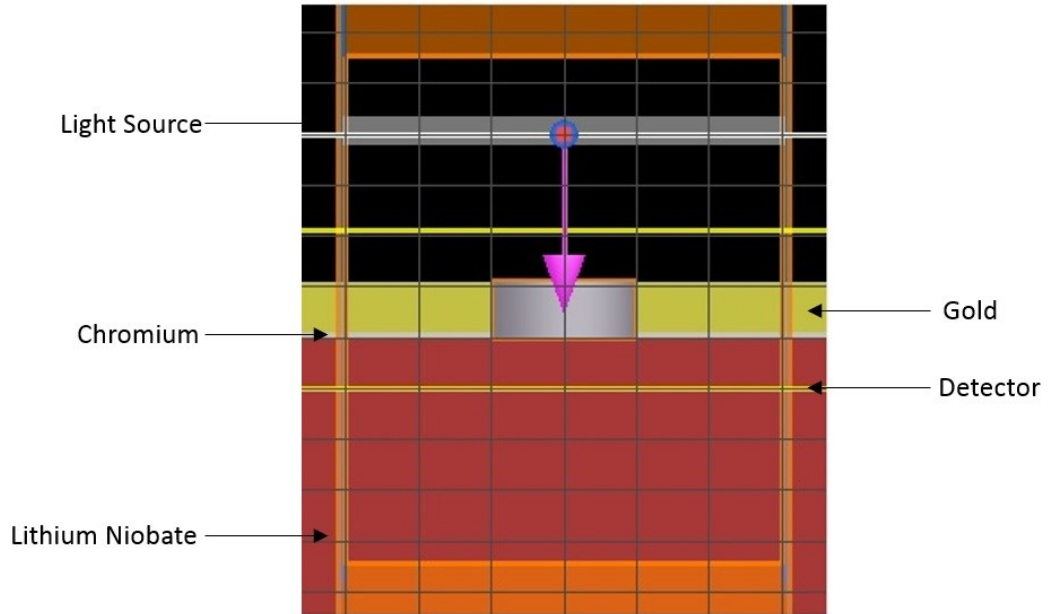
Figure 5. 2. Side view of the FDTD simulation window used for the simulation of the optical transmission and reflection spectra of the nanoholes.

The transmission spectra for the nanostructure for different hole diameters are shown in the *Figure 5. 13* below.
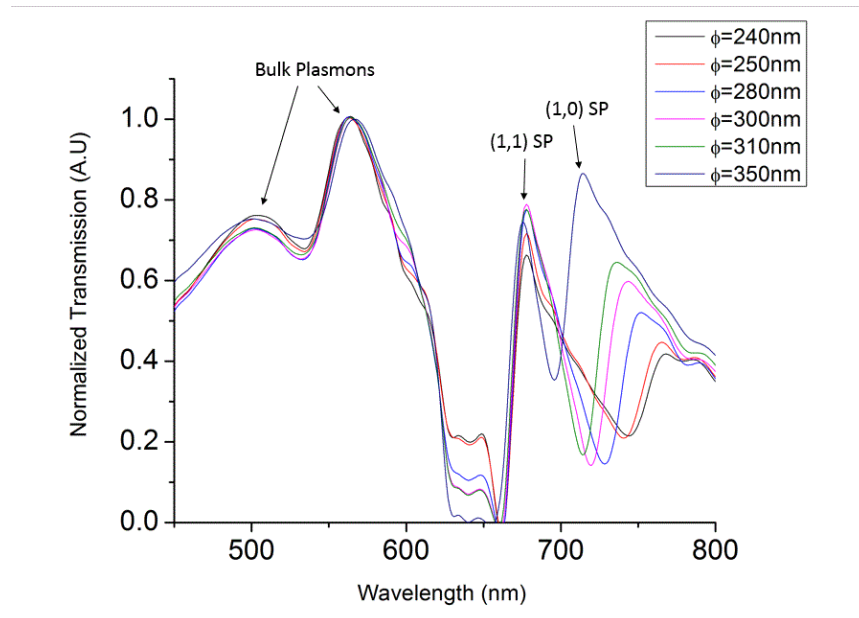
Figure 5. 1.Modelled transmission spectra of the nanostructured surface with varying hole diameter on a periodicity of 620nm.

A number of distinct transmission peaks can be observed from the transmission spectra in the figure above. The transmission peaks at 500nm and 560nm, which show no variation with hole diameter, correspond to the bulk plasmons from the thin optically opaque layer of gold. From the simulated results the transmission efficiency of the bulk plasmons, the (1, 1) SP peak and bandwidth as well as the positions and bandwidths of the (1, 0) SP peaks can be estimated. The increase in hole size has little effect on the position of the bulk Plasmon wavelength. It can be observed that an increase in the hole size of the array on a fixed periodicity results in an overall increase of the transmission efficiency through the array. This can be explained by the fact that the amount of light passing through the array is increased with increasing hole size and a larger exposed area is opened up. This increase is observed in both the transmission efficiencies of the bulk plasmons and the surface plasmons. The (1, 1) SP peak is slightly red shifted with an increase in hole size and the (1, 0) SP is blue shifted with an increase in hole size. For a 110nm increment in hole size the (1, 1) SP peak red shifted by 0.23nm and the (1, 0) SP blue shifted by 66nm. The bandwidth of the (1, 1) SP is observed to become narrower while the bandwidth of the (1, 0) SP is observed to become wider with increasing hole size. The observed change in bandwidth of the (1, 1) SP peak is 49nm for a hole size increment of 110nm. The (1, 0) SP peak is also observed to increase in transmission efficiency with an increase in hole size. The transmission minimum between the (1, 1) and (1, 0) Surface Plasmons corresponds to Woods anomaly.

By matching the refractive indices at the bottom and top interfaces of the gold film, the surface plasmon resonance peaks still exist due to the free standing nanohole array in the gold film. The positions of the bulk plasmons are in relatively the same positions when compared to the transmission spectrum with Lithium Niobate as the base substrate. The surface plasmon peaks on the other hand are observed to experience a red shift of about 30nm as well as a much larger resonance peak transmission when comparing the aspect ratios of the bulk plasmonic peaks and the surface plasmon resonance peaks. So, just having a free standing gold film perforated with nano holes will propagate surface plasmon resonances when illuminated by electromagnetic radiation. Studies have shown that by introducing a cavity[10] below the film or creating cones[11] beneath the nano hole arrays one can generate this effect but this makes the fabrication much harder and also removes the desired electro-optic effect of the base substrate. A comparison between the two transmission spectra can be seen in *Figure 5. 4*. The spectra labelled air is produced by illuminating a nanohole array on a free standing 100nm gold film surrounded by an

envelope of air while the spectra labelled Lithium Niobate is produced by illuminating the same array on a Lithium Niobate substrate.
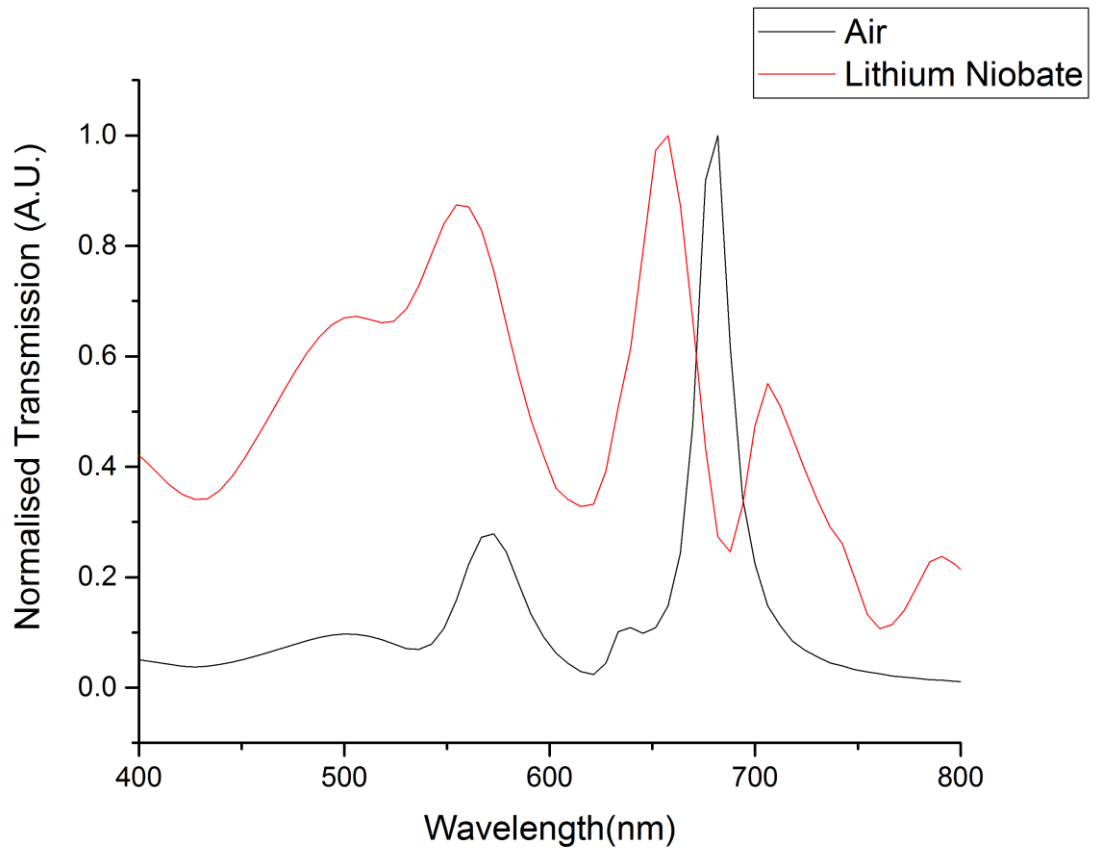
Figure 5. 4. Modelled transmission spectra of the nanostructured surface with hole diameters of 200nm on a periodicity of 620nm for two different base refractive indices.

Figure 5. 5 below show the electric field distribution around a nano hole at 675nm which corresponds to the (1, 1) SP peak. The first figure shows a top view of the transmitted electric field intensity, the second figure shows a bottom view of the reflected electric field intensity and the third figure shows an XY view of the nano hole, and the electric field distribution when the incident EM radiation wavelength corresponds to the surface plasmon wavelength.
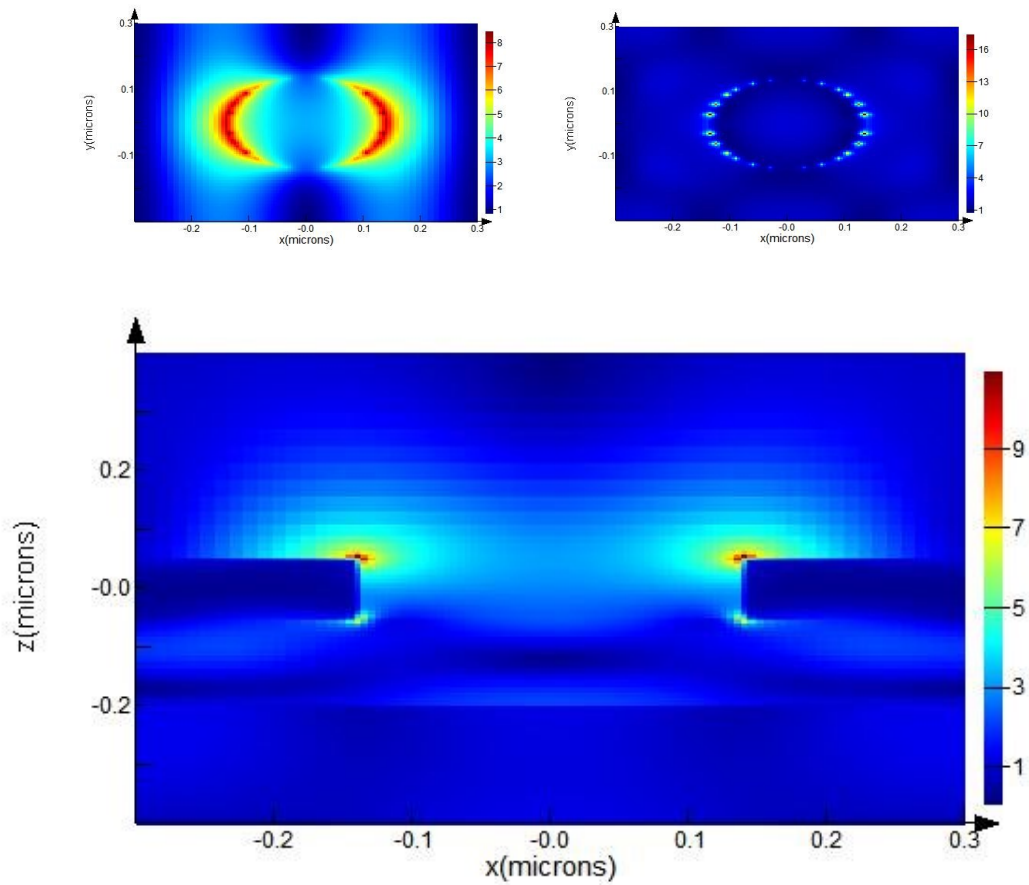
Figure 5. 5. Electric field distribution through an Au on LiNbO3 substrate nanohole illuminated at the dip of the transmission spectrum due to woods anomaly top view (LEFT), bottom view (RIGHT) and side view (BOTTOM). Au layer lies between -0.05μm and +0.05μm.

Figure 5. 6 below shows the electric field distribution around a nano hole at 630nm which corresponds to a dip in the transmission spectrum due to Woods anomaly. The first figure shows a top view of the transmitted electric field intensity, the second figure shows a bottom view of the reflected electric field intensity and the third figure shows an XY view of the nano hole, and the electric field distribution when the incident EM radiation wavelength not corresponding to any identifiable plasmonic peaks.
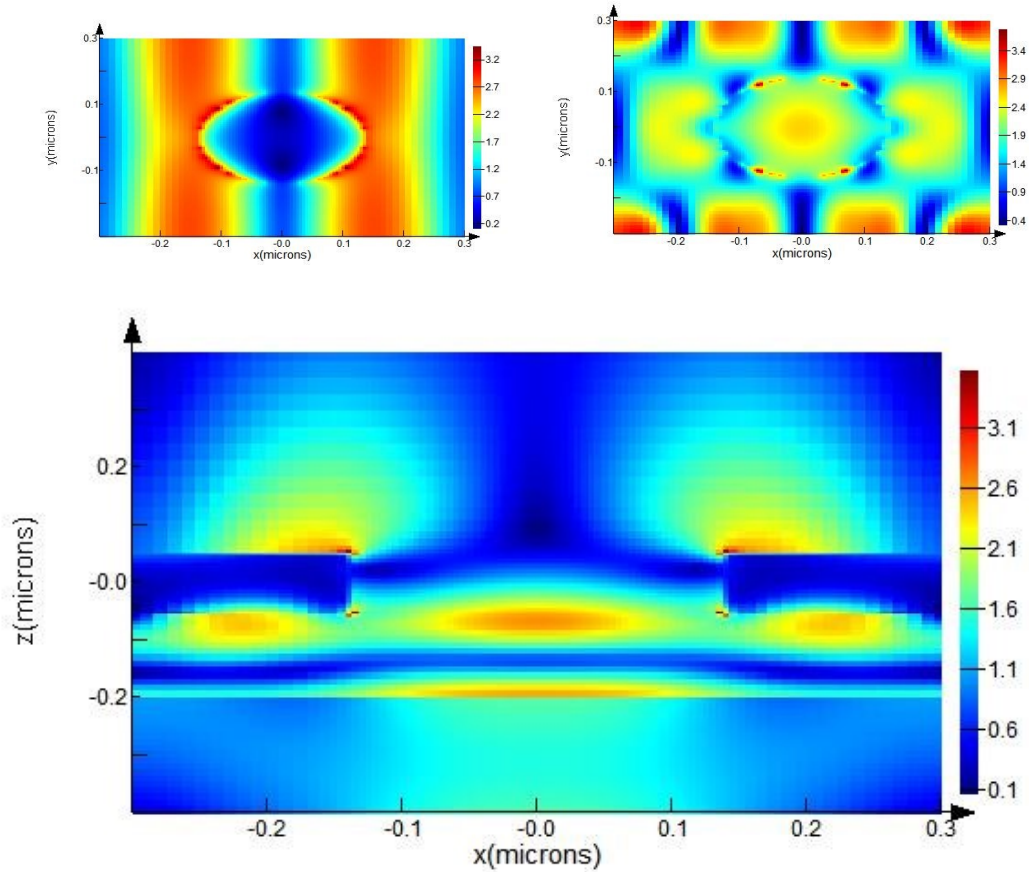
Figure 5. 6. Electric field distribution through an Au on LiNbO3 substrate nanohole illuminated at the resonant wavelength top view (LEFT), bottom view (RIGHT) and side view (BOTTOM). Au layer lies between -0.05μm and +0.05μm.

The surface plasmons are a collective excitation of free electrons at the interface between a metal and a dielectric. These surface plasmons can couple to the photons incident on the interface of the metal and insulating material if there exists a periodic grating structure on the metallic surface. The coupling between the incident photon and surface plasmons is what forms the surface plasmon modes at the interface which can clearly be seen from the X-Y electric field distribution profiles from the images above for the two conditions where excitation and no excitation occurs. If both sides of the metallic film have the same periodic structure, the surface plasmon modes on the input side and the exit side could transfer energy between the two. This energy transferred by the resonant coupling of the surface plasmons on the two sides is a tunnelling process through sub-wavelength apertures.
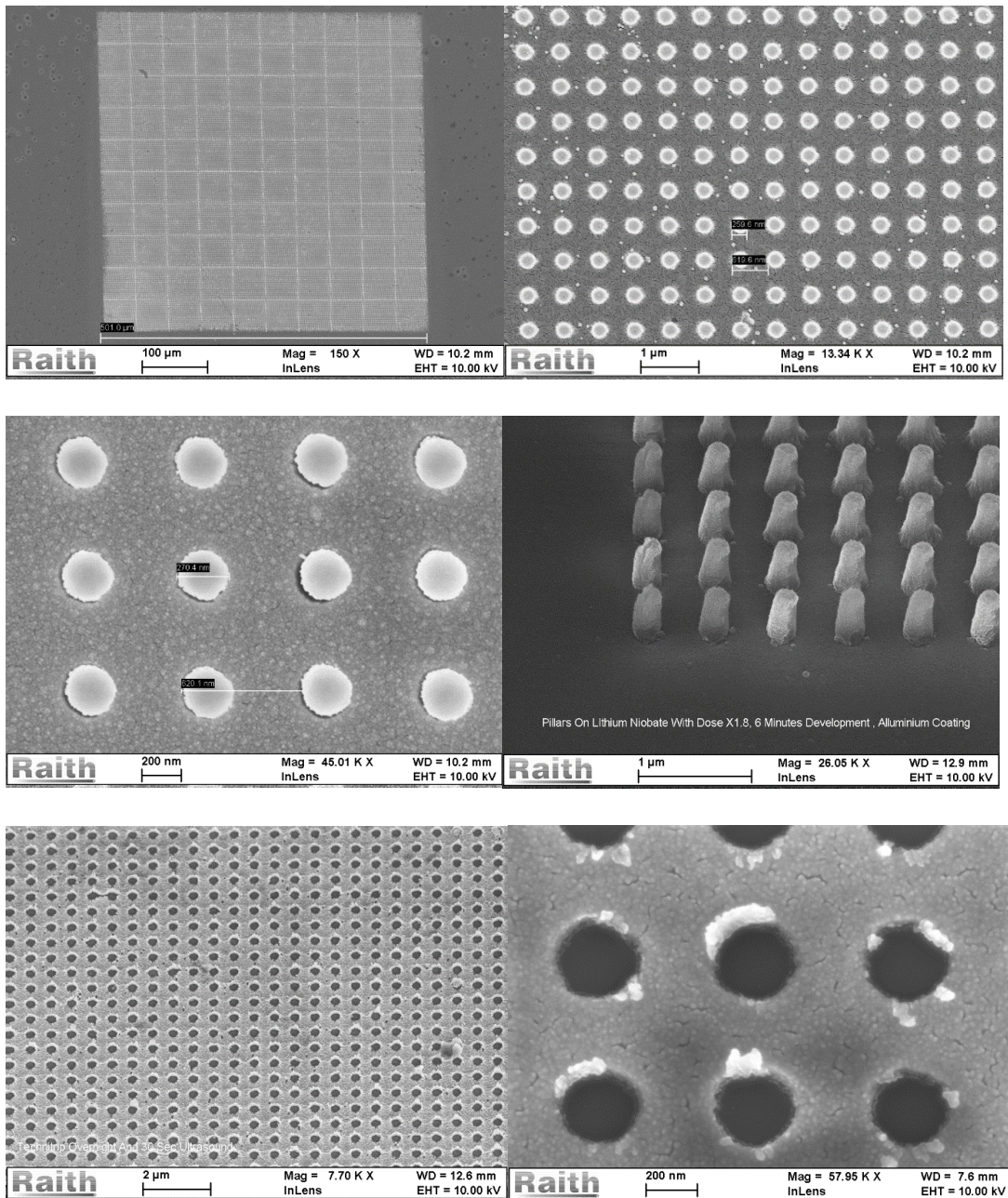
Figure 5. 7. Scanning Electron Micrographs of 500µm² nanohole array coated with Au (Top Left), Au coated array magnified (Top Right), Au coated array under further magnification (MIDDLE LEFT), 45 degree view of the pillars on the array (MIDDLE RIGHT), Nanohole array after lift-off (BOTTOM LEFT) and magnified nanoholes (BOTTOM RIGHT).

5.4.   Geometric Effects

In this section the effects of the change of various geometric parameters such as seed layer, metallic coating, thickness of metallic coating, hole size, periodicity, hole shape and polarisation dependence of the nano arrays have on the spectral position of the plasmonic peaks will be explored. The major motivation behind the design of this device arises from its high degree of tunability. Tunability in this case is driven by factors such

as matching surface plasmon resonance peaks to commercially available laser sources, negating the need for expensive and complex super continuum lasers. Another goal is to find detectors which can cope with the power levels without burning out the diodes as well as fibres which are already connectorized and readily available.

5.4.1. Seed Layer

As shown from the simulation, nano hole arrays fabricated in a gold film have demonstrated to have been the highest optical resonance transmission when compared to nano holes fabricated in other noble metals such as silver, copper and aluminium, as well as having well resolved surface plasmon peaks in the visible and near infra-red region of the spectrum. Gold does not undergo oxidation and is chemically unreactive, making it an excellent candidate for the above mentioned application when combined with a suitable electro-optic base substrate. However due to its poor adhesion properties, the need for a thin metallic adhesion layer between the gold film and the lithium niobate base substrate exists. There are a number of suitable metals that can be used as adhesion layers namely; Chromium, Titanium, Aluminium. Literature reviews[12] on similar work done in the past suggest that there is an observable red shift in the position of the plasmonic resonance peaks with the introduction of an adhesion layer. The resonance wavelength and bandwidth of the plasmonic resonances are strongly dependant on the composition and thickness of the adhesion layers. The bandwidths of the resonance peaks are generally increasing as a function of increasing adhesion layer thickness as well as showing a noticeable red shift when compared to arrays with no adhesion layers. Adhesion layer thickness increments are also shown to have a reduction in the magnitude of the transmission peaks. For example using a titanium adhesion layer introduces on average a 30nm further red shift in the position of the plasmonic resonance peak when compared to using a chromium adhesion layer.
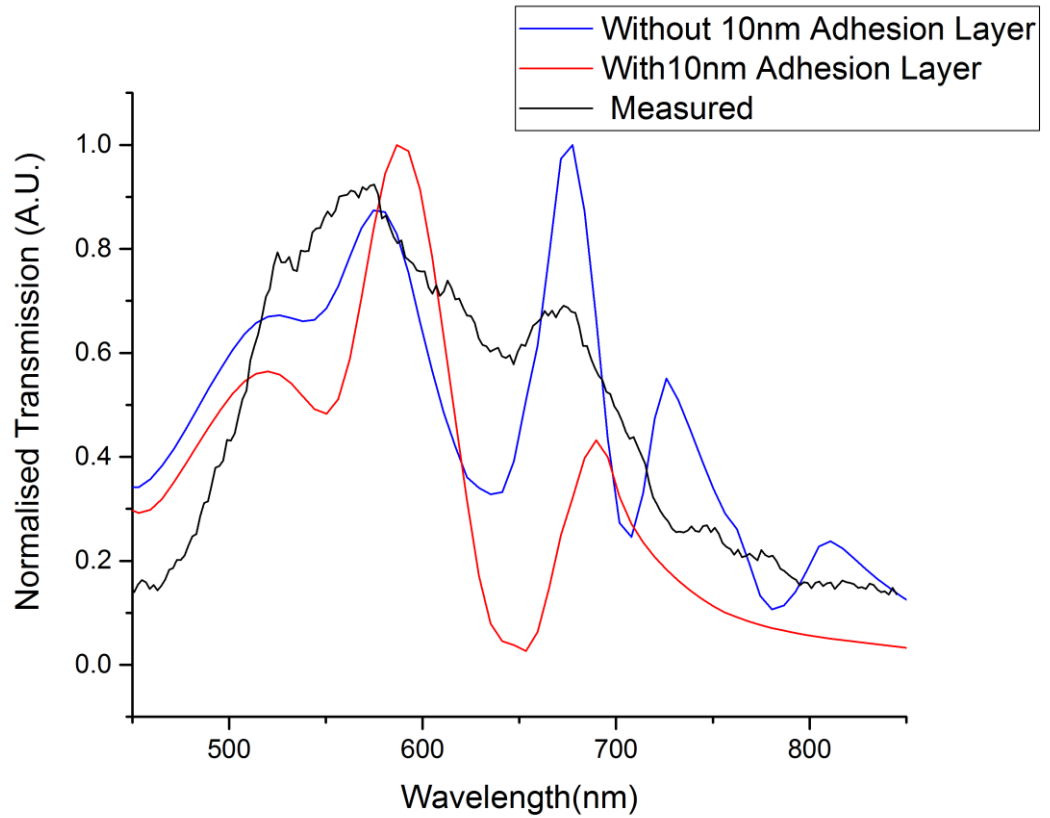
Figure 5. 8. Modelled transmission spectra of the nanostructured surface with hole diameters of 200nm on a periodicity of 620nm with and without adhesion layers, and the measured spectra.

For the above mentioned reasons as well as fabrication constraints experienced during the deposition of titanium, chromium was chosen as the adhesion layer for the nano hole arrays. A 10nm chromium layer was thermally evaporated prior to the thermal evaporation of the gold layer. A simulation was carried out to show what the effects of the deposited chromium adhesion layer would have on the transmission spectra and the positions of the spectral peaks. An array with hole sizes of 280nm on a periodicity of 620nm was used with a fully dispersive model for Lithium Niobate. From the simulation results from *Figure 5. 8* the positions of the bulk plasmons fall in the same position for both adhesion layer and no adhesion layer spectra. With regards to the (1, 0) SP peak for simulated no adhesion layer, adhesion layer and measured the peak positions are as follows: 676nm, 688nm and 673nm. The simulations show a red shift of about 12 nm in the position of the peak but the measured spectra agrees better with the no adhesion layer model. With the 10nm modelled adhesion layer the (1, 1) SP peak tends to be shifted into the infrared. The (1, 1) SP peaks for the simulated no adhesion layer, adhesion layer and measured spectra the speak positions are as follows; 727nm, N/A and 748nm. The no adhesion layer model once again agrees better with the measured results. The adhesion

layer model exhibits a 12nm red shift in spectral peak positions as well as the disappearance of the (1,1) SP peak and the increase in spectral bandwidth of the (1,0) SP peak. For the remaining simulations the model without an adhesion layer is used due to it's better conformity to the experimentally measured spectra. The results from this section would imply that the adhesion layer deposited could be less than 10nm, which was measured with a thickness monitor mounted inside the coating chamber.

5.4.2. Deposited Metal

Surface plasmons have the ability to exist at any interface between a dielectric and a material (noble metals) with a negative real part of the dielectric constant[13]. The above mentioned condition is however insufficient in guaranteeing a true surface plasmon mode capable of propagating over a substantial distance or alternatively interacting with an incident electromagnetic wave. In order to achieve a resonant interaction, the imaginary part of the dielectric constant of the material must be relatively small. In *Figure 5. 9* below the real and imaginary parts of the dielectric constants of 4 noble metals are shown.It is clear that the absolute value of the imaginary part of the dielectric constant must be much larger than the real part in order for the resonant interaction of SPs with incident electromagnetic radiation as well as propagation over substantial distances.
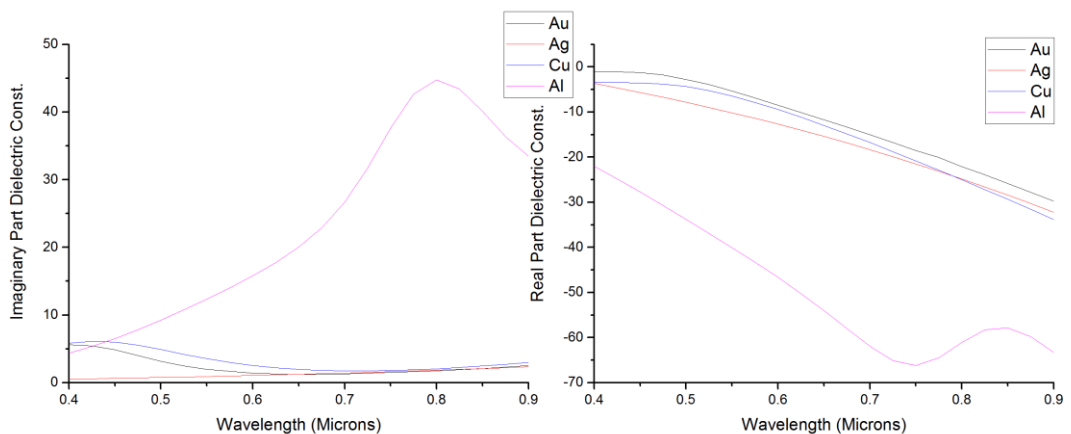
Figure 5. 9. The imaginary part of the dielectric constant (LEFT) and the real part of the dielectric constant (RIGHT) as a function of wavelength for 4 of the most commonly used plasmonic metals[13].

Further building on the conditions stated above, a simulation of the optical transmission properties of 4 nano hole arrays with hole diameters of 200nm and a periodicity of 600nm was carried out. All the metallic models are taken from Palik[14] and a fully dispersive model for Lithium Niobate was provided by Zelmon[15]. Copper and gold are seen to show identical positions of the plasmonic resonance peaks but the degree of enhancement offered by copper is much lower than that shown by gold. Aluminium tends to show resonance peaks which are closer to the ultra violet part of the spectrum and is also a special case with optical properties at an intermediate ground between noble metals and other metals. Silver has comparable optical transmission properties to gold but suffers from oxidation on exposure to air, hence making gold the most suitable candidate. These can be seen from *Figure 5. 10*.
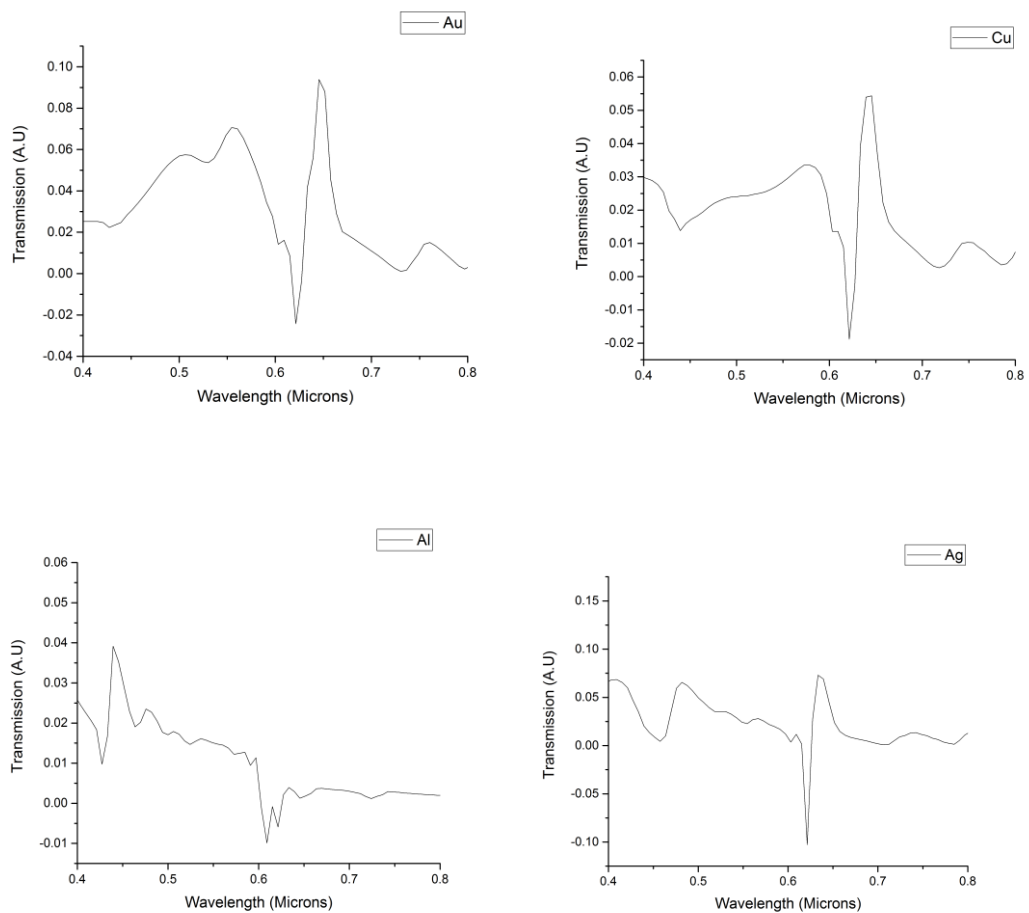
Figure 5. 10. Modelled transmission spectra of the nanostructured surface with hole diameters of 200nm on a periodicity of 600nm for gold (TOP LEFT), copper (TOP RIGHT), aluminium (BOTTOM LEFT) and silver (BOTTOM RIGHT).

5.4.3. Metal Thickness

A characterisation of the effect of thickness that the metal layer has on the transmission spectra and transmission efficiency was carried out. From literature[16], it is shown that the thickness is a determining factor but also show that the periodicity of the array is mainly responsible for determining the position of the peaks as well as the lattice type. They show a slight red shift in the SP peaks as a function of increasing thickness.

The transmission spectrum of a square array of circular nano holes of hole size of 200nm on a periodicity of 600nm with a silver metallic layer with metal thicknesses ranging from 100 to 130nm simulated. From *Figure 5. 1* below, the maximum transmission is dependent on the film thickness as well as a slight red shift observed in the plasmonic resonance peaks and no shift in the bulk plasmonic peaks. They are the only spatial features remaining unchanged as a function of parameter changes.
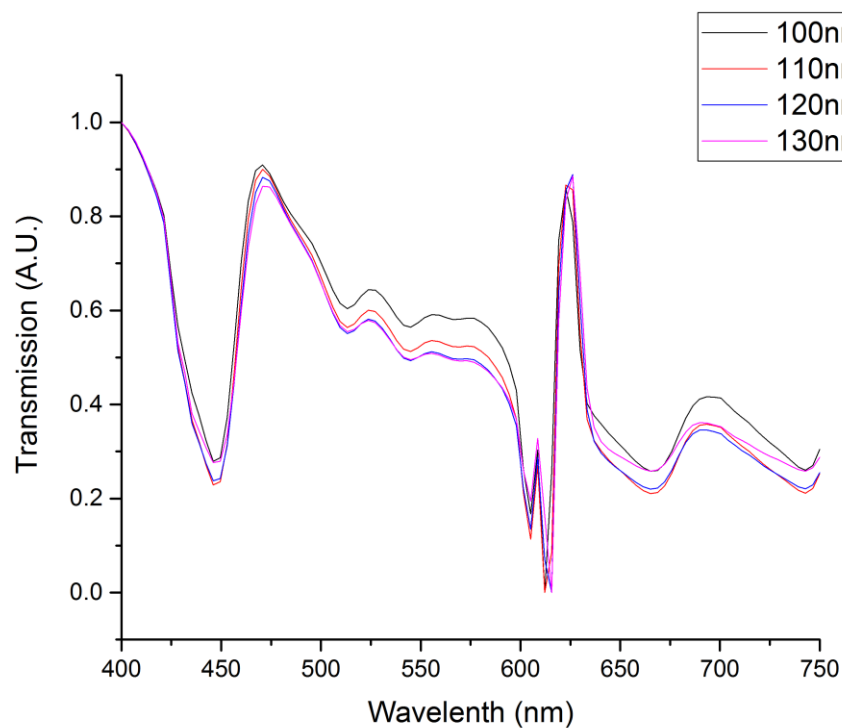
Figure 5. 21. Modelled transmission spectra of the nanostructured surface with increasing metal thickness as a function of wavelength on a periodicity of 600nm on a silver coated substrate.

In keeping the hole size, hole shape and periodicity fixed a change in the metal layer thickness was shown to have little changes on the transmission spectra as well as the resonance peak positions. Therefore in the final design used a gold layer of 100nm thickness was used.

5.4.4. Hole Size

Presented earlier in the simulated results, the transmission efficiency of the bulk plasmons, the (1, 1) SP peak and bandwidth as well as the positions and bandwidths of the (1, 0) SP peaks can be estimated. The increase in hole size has little effect on the position of the bulk plasmon wavelength[17].
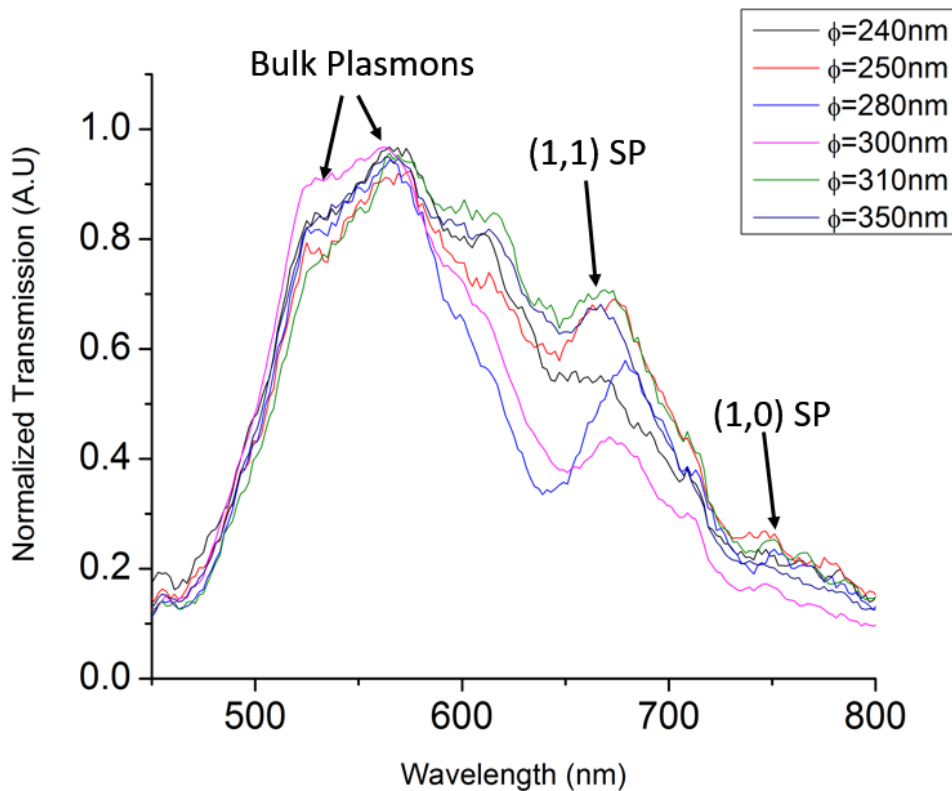
Figure 5. 3. Experimentally measured transmission spectra of the nanostructured surface with increasing hole diameters as a function of wavelength on a periodicity of 600nm on a silver coated substrate.

In *Figure 5. 3* the experimental results show the efficiency of the bulk plasmon peak, the (1, 1) SP peak, the (1, 1) SP bandwidth and the positions of the (1, 1) and (1, 0) SP peaks are estimated in much the same way as in the simulation results. The bulk plasmon (1, 0) transmission efficiency and the (1, 1) SP transmission efficiencies are seen to follow an increasing trend which is supported by the simulation results. The increase in the whole size seems to have little effect on the position of the bulk plasmon (1, 0) wavelength. However it can be observed that the transmission efficiency of the nano hole array of the same periodicity increases as the whole size increases. From the experimental results it

can be seen that the (1, 1) SP peak stays around the 670nm mark without experiencing a slight red shift as the simulation results suggested. For the array with a hole size of 280nm the peak is 678nm. The (1, 0) SP peak on the other hand is blue shifted as the hole size increases which concurs with the simulated results. For a 110 nm increase in hole size the (1, 0) SP peak shifts by 39nm into the blue. The bandwidth of the (1, 1) SP peak is also observed to become narrower as the hole size increases. The observed change in the bandwidth is 36nm for a whole size increase of 110nm. The increase in efficiency of the (1, 0) SP peak observed from the simulations cannot be observed from the experimental results. A transmission minimum is observed between the (1, 1) SP and (1, 0) SP resonances due to Woods anomaly as well. A graphical representation of the positions of both plasmonic peaks comparing the simulated results and the experimental results can be seen in *Figure 5. 4*.
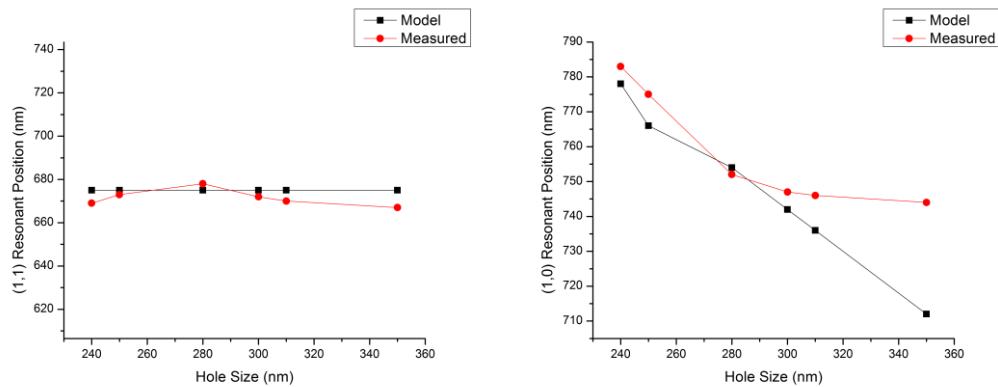
Figure 5. 4. Comparison of the modelled and measured position of the (1, 1) Surface Plasmon Peak (LEFT) and the (1, 0) Surface Plasmon peak (RIGHT) as a function of increasing hole size.

5.4.5. Hole Shape

The effects that hole shapes have on the transmission spectra through a square array have been extensively investigated in literature[18]. A simulation of the transmission spectra through a square array with periodicity of 600nm and different shapes was carried out. The shapes include holes with a diameter of 200nm, squares with sides 200x200nm and ellipses with dimensions of 200x150nm. The angle of incidence of the light was normal to the array and the simulations were carried out with a 2nm mesh size. The results from this simulation can be seen in the *Figure 5. 5* below.
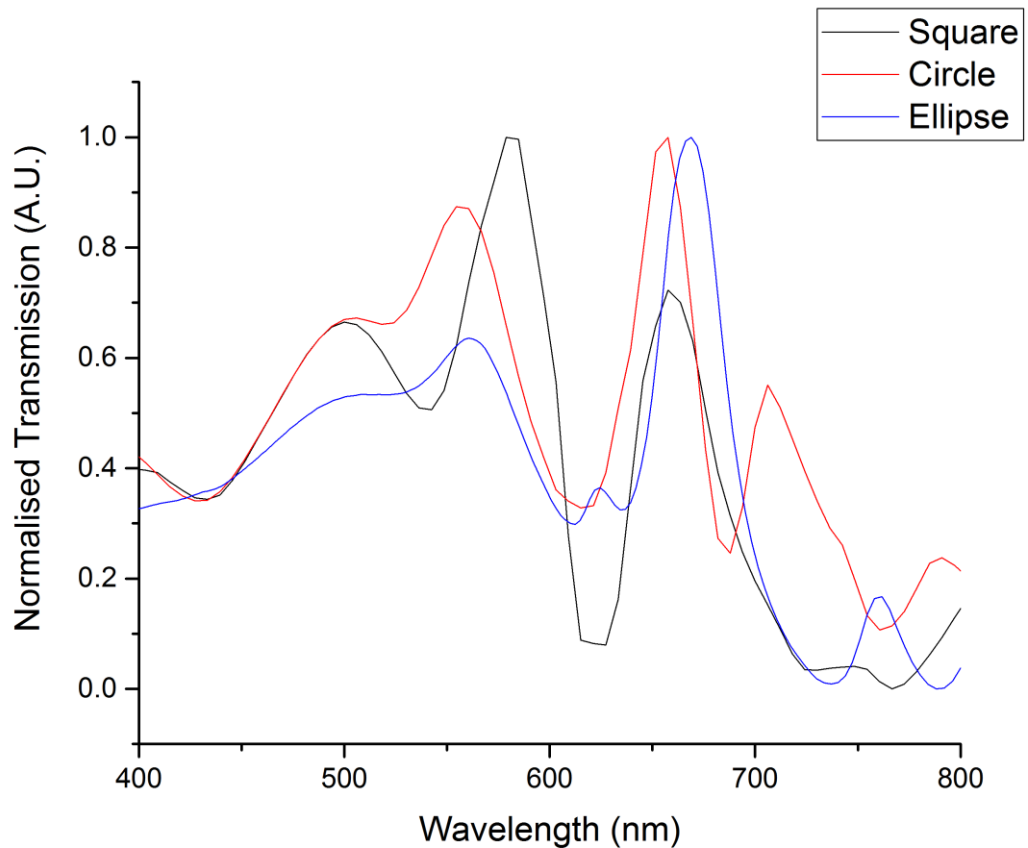
Figure 5. 5. Modelled transmission spectra of the nanostructured surfaces with different hole shapes on a periodicity of 600nm as a function of wavelength.

The position of the bulk plasmons around 500nm remains unchanged irrespective of the hole shape. For circular holes the (1, 0) surface plasmon resonance peak is at 657nm and the (1, 1) surface plasmon resonance peak is at 730nm. For square holes the (1, 0) surface plasmon resonance peak is at 658nm and the (1, 1) surface plasmon resonance peak is at 825nm. For elliptical holes the (1, 0) surface plasmon resonance peak is at 669nm and the (1, 1) surface plasmon resonance peak is at 760nm. For circular and square holes the (1, 0) SP peak falls in roughly the same position where as for the elliptical holes the peak is red shifted by 10nm. The (1,1) SP peak is where the largest difference between shapes occurs being pushed out further into the near IR for square holes compared to circular and elliptical holes.

5.4.6. Periodicity

A simulation of the transmitted intensity through the nano hole arrays was carried out. The hole size was fixed at 280 nm, the angle of incidence was perpendicular to the surface of the array, the periodicity was set to 600nm and increased by 10nm after every run, the

mesh size was set to 2nm and a fully dispersive model for Lithium Niobate was used. The results from this study are shown in ***Figure 5. 6*** below. Firstly the position of the bulk plasmons at 500nm does not change in spectral position with an increase in periodicity of the array. The positions of the (1, 0) surface plasmon resonance peak undergoes a red shift with increasing array periodicity. The positions of the peak for periodicities ranging from 600nm to 650nm with 10 nm increments are as follows: 657nm, 664nm, 672nm, 676nm, 681nm and 688nm. There is on average about a 7nm redshift in the plasmonic resonance peak position for a 10nm change in periodicity. The positions of the (1, 1) surface plasmon resonance peak is seen to experience much the same red shift change as the (1, 0) SP. The positions of the peak for the periodicities ranging from 600nm to 650nm with 10nm increments are as follows: 722nm, 730nm, 736nm, 748nm, 755nm and 766nm. This shows that on average a red shift of about 8nm is experienced for a 10 nm increment in the periodicity. The simulated results using a fully dispersive model for Lithium Niobate and no adhesion layer closely agree with the measured spectral results from an array of holes with a diameter of 280nm on a periodicity of 620nn which are 678nm for the (1,0)SP and 749 for the (1,1)SP peaks.
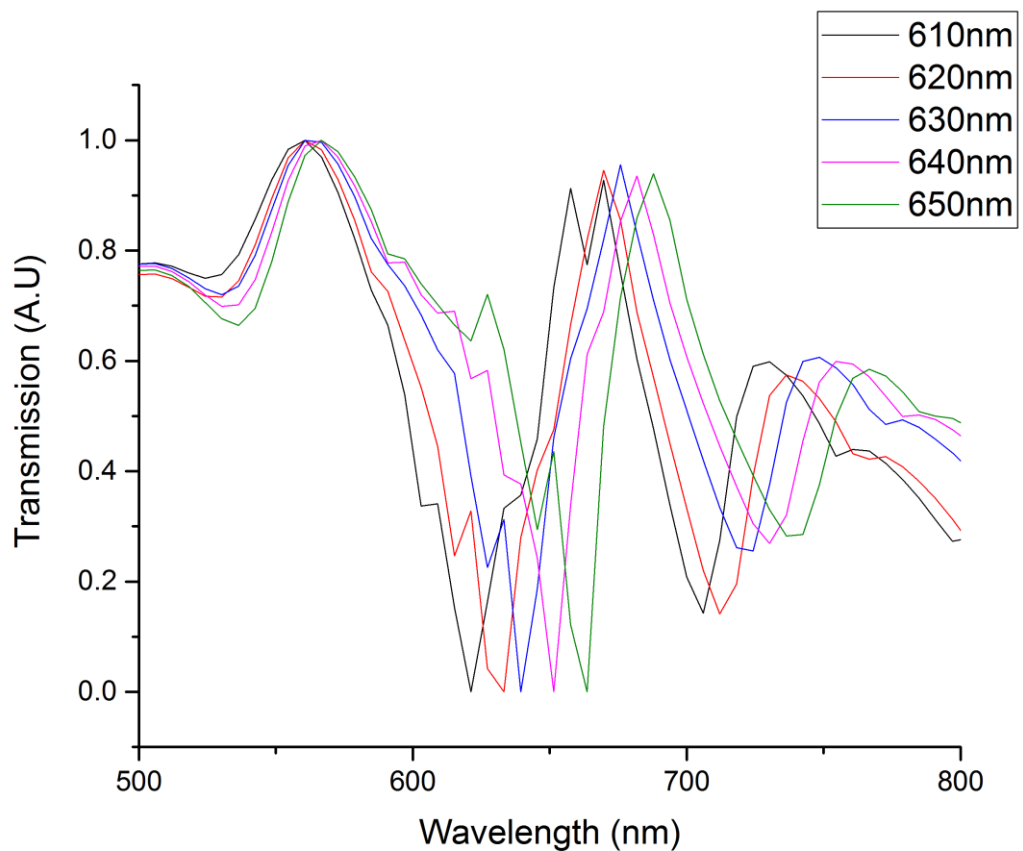
Figure 5. 6.Modelled transmission spectra of the nanostructured surfaces with small periodicity changes (~10nm) and a hole size of 200nm as a function of wavelength.

The effects that much larger periodicity changes have on the transmission spectra as well as the positions of the plasmonic resonance peak positions were also investigated. The simulation parameters are the same as mentioned above but the periodicities are 500nm, 600nm and 700nm. It is observed that the position of the bulk plasmons existing due to the gold layer around 500nm do not undergo a change in their position with increasing periodicity. The (1, 0) surface plasmon resonance peak undergoes a red shift with increasing periodicity. For array periodicities of 500nm, 600nm and 700nm the spectral position of the (1, 0) SP peaks are as follows 598nm, 672nm and 749nm and can be seen from *Figure 5. 7*. There is on average a 70nm red shift for every 100nm increment in periodicity. From the experimentally measured transmission spectra for the same periodicities, the spectral positions of the peaks are: 615nm, 678nm and 668nm. There is a 60nm red shift between 500 and 600 nm arrays and a 10nm blue shift in the 700nm array. The reason for this is due down to the spectral profile of the light source used and the drop in light intensity after 700nm, hence not permitting a clear visualisation past that wavelength. The positons of the (1, 1) surface plasmon resonance peaks from the simulations are as follows: 681nm, 748nm and 826nm. The experimentally measured transmission spectra of the arrays shows the peaks at 666nm, 750nm and the peak of the array with a periodicity of 700nm cannot be made out. The results show a similar trend of a 70nm average red shift for the simulated results and a 60nm red shift for the measured results for a 100nm increase in periodicity of the array.
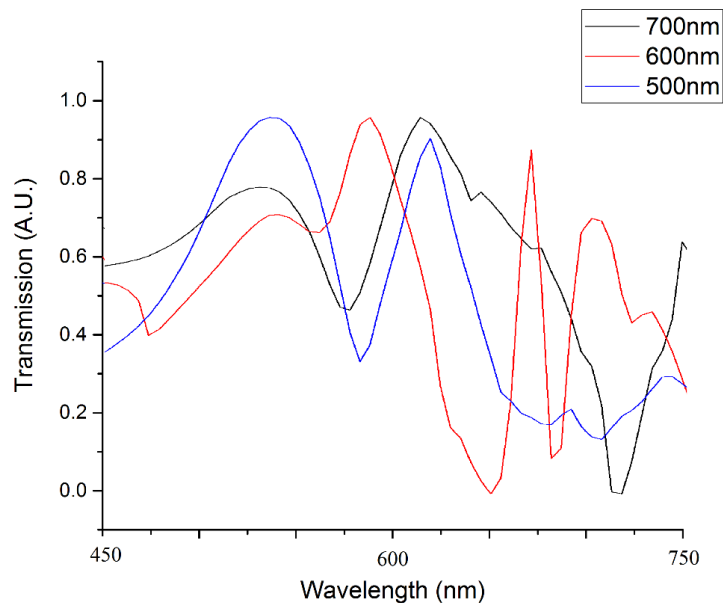
Figure 5. 7. Modelled transmission spectra of the nanostructured surfaces with large periodicity changes (~100nm) and a hole size of 200nm as a function of wavelength.

5.4.7. Incidence Angle

In this section the effect that the incidence angle of the illumination has on the transmission spectra through the nano hole array is investigated. The groove in the fused silica holder described in the appendix which holds the substrate with the nano holes has a width of 623μm. The substrate on which the nano hole arrays lie has a thickness of about 510μm. This gives a difference of about 113μm which can be accounted as a potential source for an incidence angle change of the light striking the nano hole array of 0.001°. Albeit this can be considered as nearly normal incidence, S.Balakrishnan et al[19] have reported that at higher angles of incidence of the order of 5° there is an observable red shift in the surface plasmon resonance peak as well as peak splitting. Simulations were carried out to investigate the effect that small incidence angle changes have on the transmission spectra through an array of nanoholes. For this simulation the chosen hole size diameter was 200nm on a periodicity of 600nm in a square array with 100nm of gold metal on a Lithium Niobate substrate using a fully dispersive refractive index model and the incidence angle of the light source was varied from normal incidence to 2° incidence. The results in *Figure 5. 8* show that for small changes in the angle of incidence (up to 2°) the positions of the plasmonic resonance peaks remain the same and the only observable change comes in the form of a reduction of the maximum transmitted intensity through the array as a function of increasing angle of incidence. There is ~1.8% change in the normalised transmission intensity for a 0.5° change in the angle of incidence and ~6.5% change in the normalised transmission intensity for a 2° change in the angle of incidence.
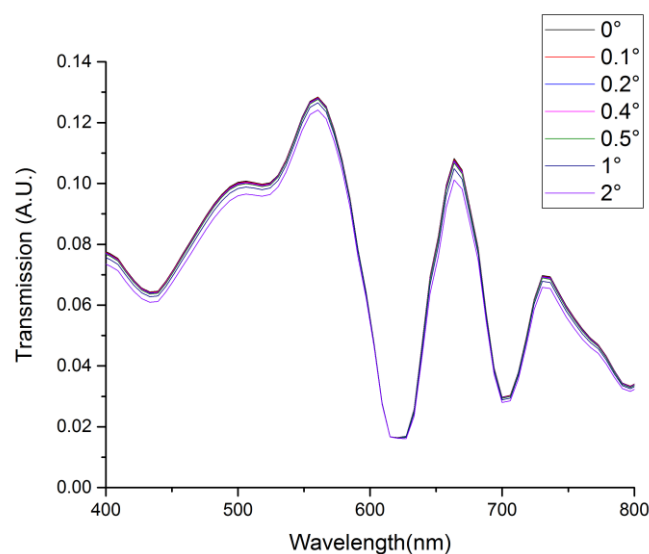
Figure 5. 8. Modelled transmission spectra of the nanostructured surfaces with changes in the incidence angle on a periodicity of 600nm and a hole size of 200nm as a function of wavelength.

5.4.8. Polarisation

Prior to fabricating an integrated optical device, the effect that polarisation has on the measurements of static and dynamic fields was carried out using a free space optical system. The experimental setup consisted of a laser source (ThorLabs HL6748MG) red light emitting laser with a central wavelength of 675nm and peak optical power of 10mW. The laser was connected to a thermo electric cooler unit (TEC) and the temperature was set at 20°C. The light was launched into a multimode optical fibre (GIF-625) through a 10X objective lens and the output of the fibre was connected to a collimating package (Thorlabs F280FC-B) with a beam diameter of 3.4mm at the focus point and a focal length of 18.24mm. The light then passed through a pair of polarisers which could separate the Transverse Electric (TE) and Transverse Magnetic (TM) polarisations. The collimated light beam coming from the optical fiber is made up of a mixture of both polarisations due to the optical fiber not being polarisation maintaining. The first polariser is set at an angle (α) where the measured intensity in each detector after the polarising beam splitter is equal. The second polariser then is rotated by $\pm 45°$ to the angle α, producing either TE or TM polarisation in the sensor arm. After this, the polarising beam splitter was replaced by a 50:50 non polarising beam splitter cube (ThorLabs BS010) which split the entirely TE or TM beam with the side channel acting as a reference signal for monitoring the laser stability. The light was then passed through a condenser lens with focal distance of ~10cm through the nanohole arrays and collected by a Silicon Photo detector. A high voltage supply was used to provide the field for the static field measurements and was later replaced with a Pockels cell driver circuit for dynamic field measurements. A diagram of the experimental setup can be seen from *Figure 5. 9* below.
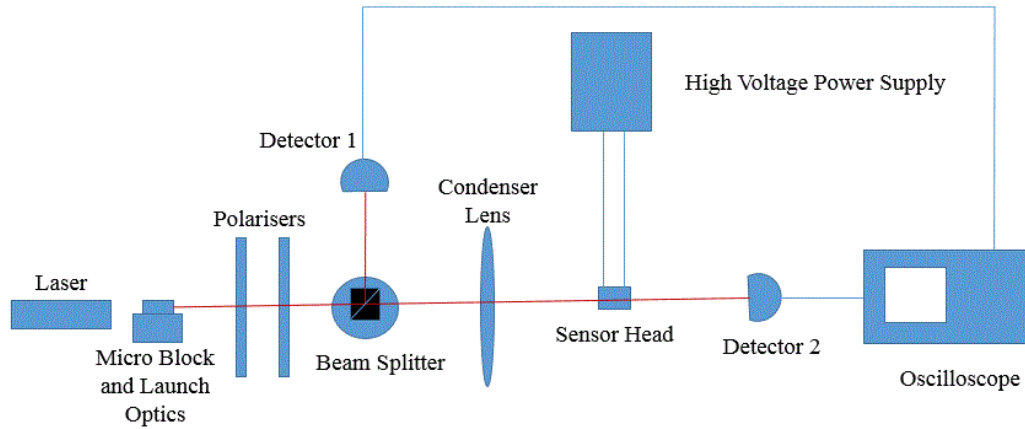
Figure 5. 9. Schematic of the experimental setup used for the free space measurements and polarisation dependence of the transmission spectra.

Upon clearly identifying both light polarisations by rotating the polarisers a study of the optical transmitted power through the nano hole array was carried out. The result obtained from the experimental measurements showed that there was a power difference of about 3.9±0.1% between the two polarisations, with the slight difference occurring due to the slight non uniformity of the fabricated nanoholes as well as the differences in the refractive indices of the lithium niobate wafer used. The transmission spectra for an array of circular nanoholes with a periodicity of ~620nm on an isotropic non birefringent base material is independent of the polarisation of light. Lithium niobate on the other hand is an anisotropic material with refractive indices n_x=2.286, n_y=2.203 and n_z=2.2 at 632nm. The simulations show that for a 90 degree rotation in the polarisation of the incident light (i.e from TE to TM) a change of 3.6% can be observed in the transmission intensity at a wavelength of 675nm. From the simulation results it is also observed that the position of the (1,0) SP peak does not undergo a wavelength shift and remains in the same position[20]. This change in optical transmission output can be seen from *Figure 5. 10* below.
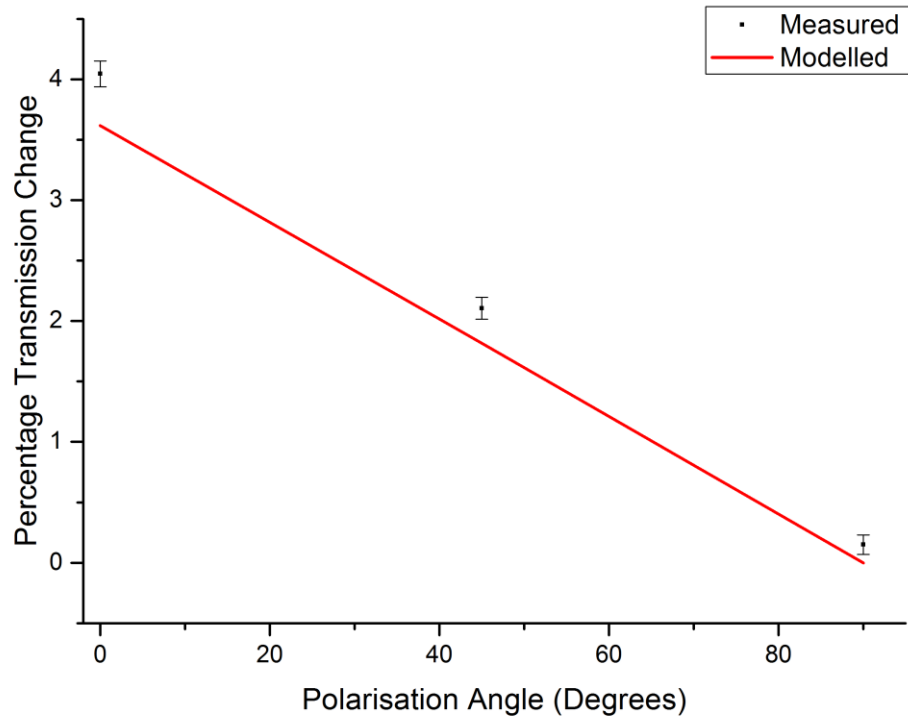
Figure 5. 10. Comparison of the modelled and experimentally measured transmission spectra change of the nanohole arrays as a function of polarisation angle.

Elliptical nanoholes were also considered with the major axis measuring 200nm and the minor axis measuring 150nm on a 620nm period with the major axis aligned to the n_x axis of the Lithium Niobate substrate. Light with polarisations parallel and perpendicular to the major axis of the ellipse were used for illumination resulting in a change of about 7.7% in transmission intensity the (1,0) SP peak. This can be observed from the simulated spectra below. The positions of the bulk plasmons remains at relatively the same position but there is an observable red shift in the peak of the (1, 0) SP of about 14nm on switching polarisations by 90°. This same trend is present in the (1, 1) SP. This can be seen from *Figure 5. 11* below.

The transmission spectra obtained from the elliptical holes at different light polarisation orientations suggests that there could be an improvement in the sensitivity of the sensor and the overall power detected power levels. There also exist a certain degree of wavelength detuning with the (1,1) SP seen as a blue shift as the polarisation is changed from TE to TM which is not present with circular holes[21].
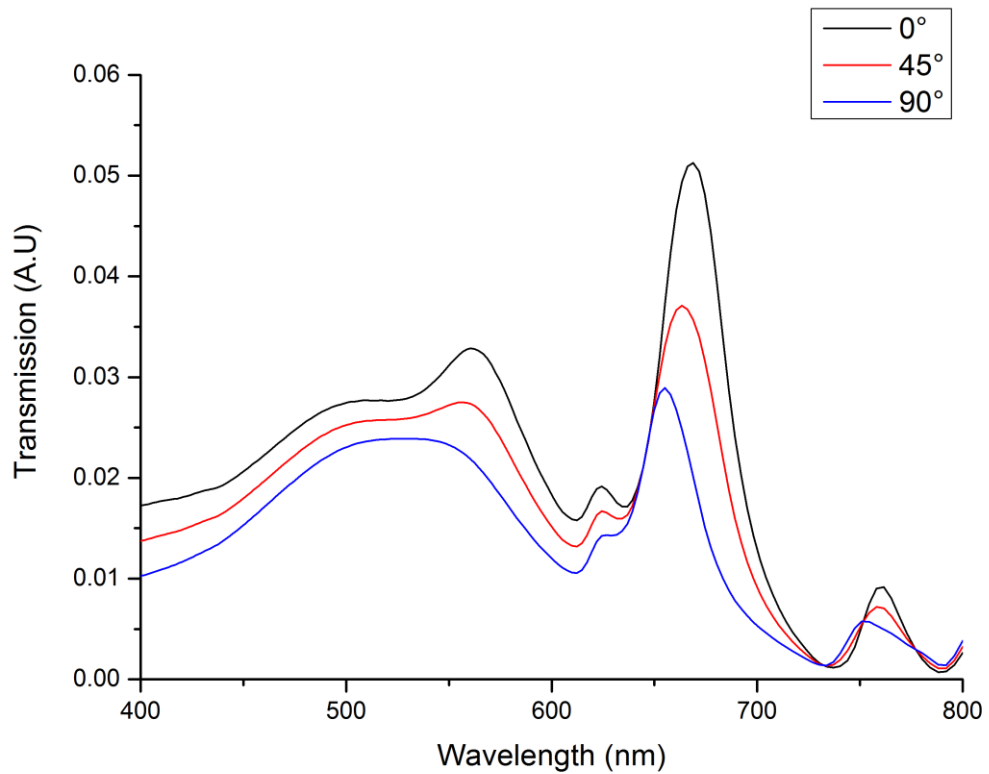
Figure 5. 11. Modelled transmission spectra of the nanostructured surface with elliptical nanoholes as a function of polarisation orientation.

Nano holes with circular holes with diameters ranging from 280nm to 350nm on a periodicity of 620nm were illuminated by the laser and the transmission measured at TE, TM and an even mixture of both polarisations. The results of this analysis are shown in *Figure 5. 12* below. It can be seen that as the optical transmission increases as a function of increasing hole size which confirms the sub section studying the effects of hole sizes on the transmission spectra. And there is a difference of about 3.1% between the two polarisations.
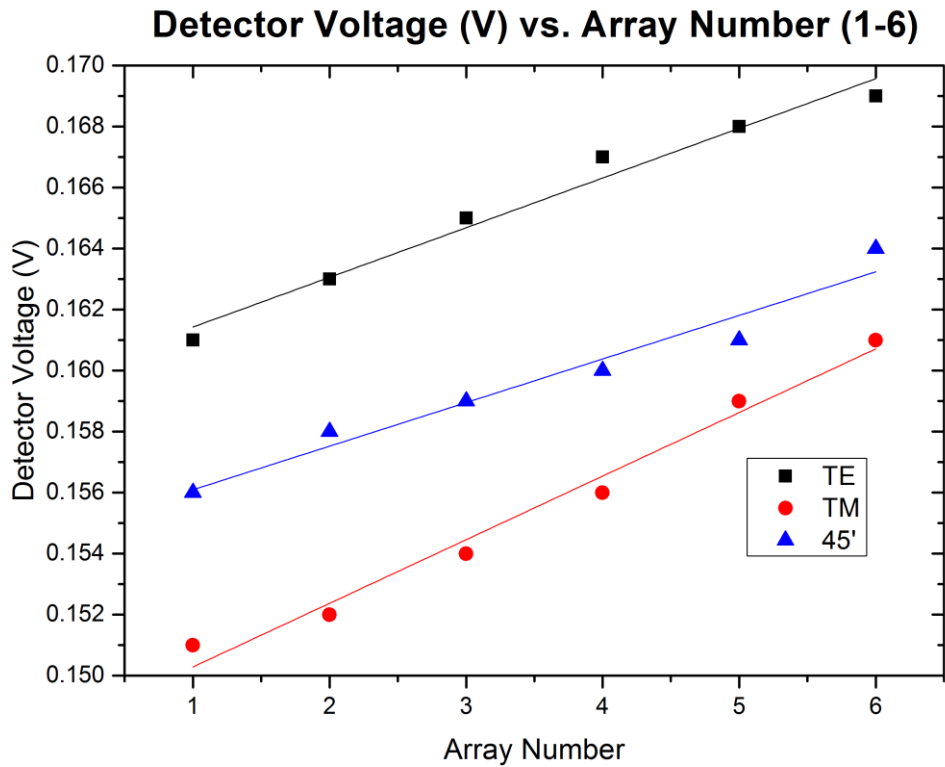
Figure 5. 12. Measured output optical power through increasing hole size nanostructured surfaces for 3 different polarisation orientations.

A high voltage supply was used to power a Pockels cell driver which was used to supply the pulses measured. The pulses produced by the Pockels cell had a pulse duration of ~2μs, a rise time of ~200ns and the estimated peak field strength was about 500kV/m. This was estimated from the spacing between the electrodes and the charging voltage supplied to the cell. The electrodes were spaced by a distance of 10mm apart and the Pockels cell driver was charged by 5kV. The triggering pulse as measured by a wire loop antenna can be seen from ***Figure 5. 13*** below. There is a high degree of inconsistency between individual shots because of the nature as well as age of the Pockels cell driver. The pulses were set to trigger at a repetition rate of 1 pulse every 10 seconds.
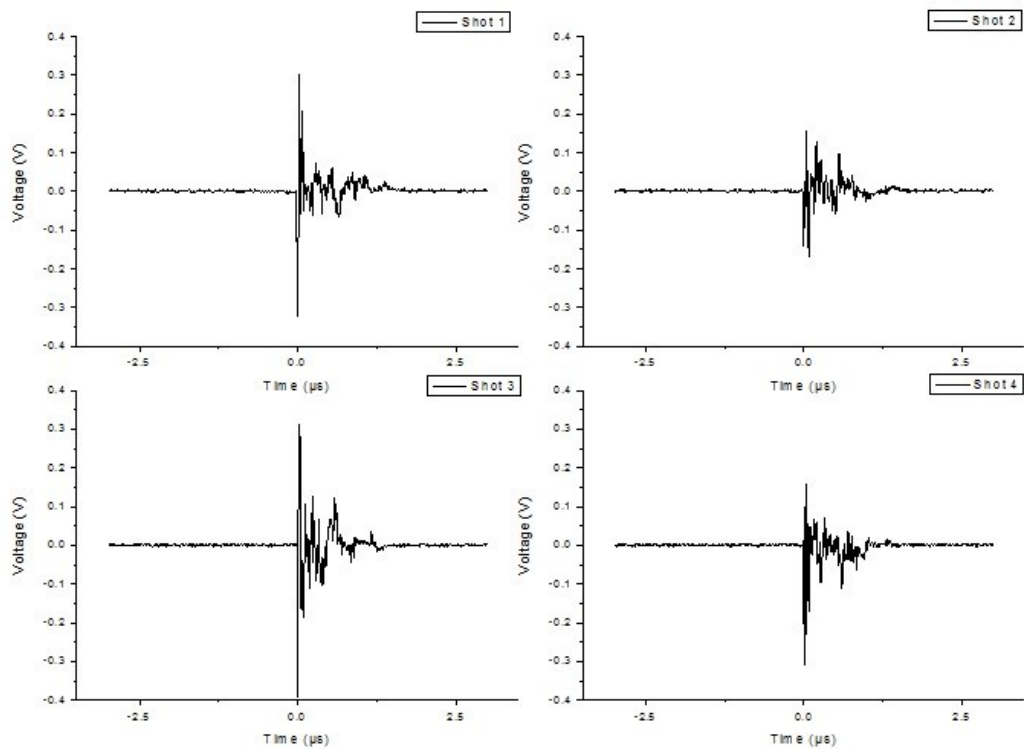
Figure 5. 13. Temporal pulse shapes of 4 EMP generated by the Pockels Cell driver as measured by a wire loop antenna showing inconsistency between successive pulses.

Figure 5. 14 below shows the TE response of the nano hole array sensor to an incident electromagnetic pulse and *Figure 5. 15* shows the TM response. In order to make sure that there was no stray RF coupling into the detection electronics, a measurement was taken with both laser switched on and no laser. There is a DC offset between the two response traces. In the one with the laser there is a clearly observable pulse about 10ns after the measurement was triggered by the reception of the incident electromagnetic pulse by the wire loop antenna. The measurements below were carried out for a transverse electric polarisation. The peak to peak voltage with laser passing through the nano hole array for this polarisation was measured to be approximately 3mV and the peak to peak voltage for the same measurement made with the transverse magnetic polarisation was approximately 2.1mV. From these measurements a difference of about 30% is found in the measurements using the two different polarisations. The large difference could be account for by the inconsistency of pulses provided by the Pockels cell driver as well as drifts in the laser power.
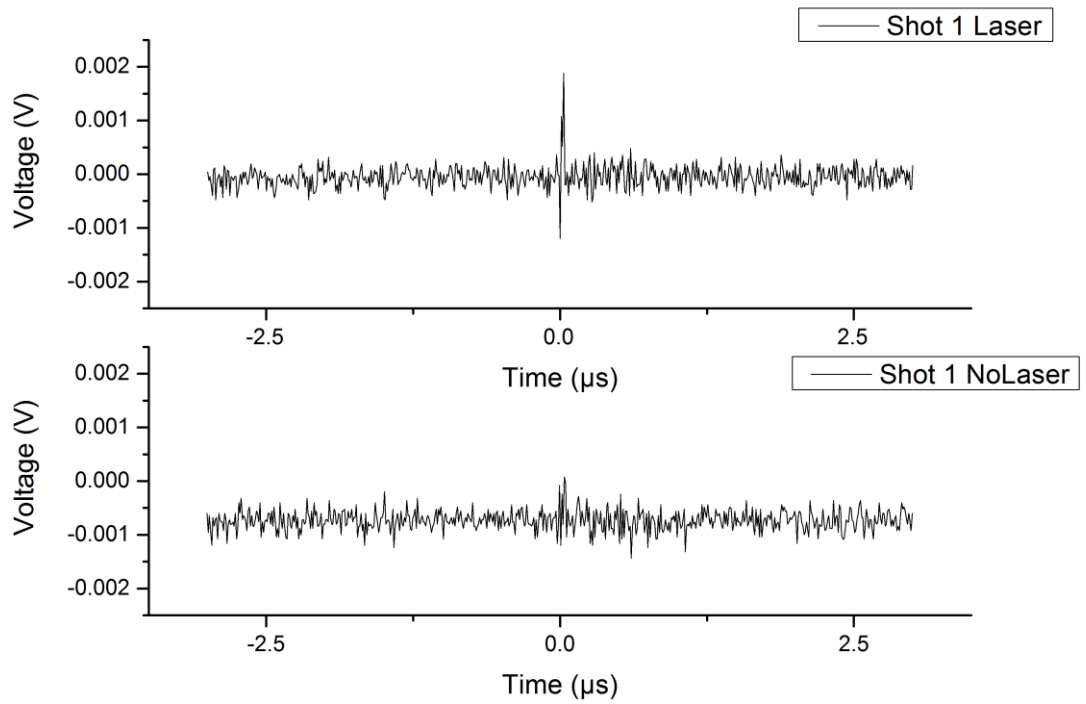
Figure 5. 14. The EMP induced variation in the output optical signal for TE incident light polarisation with light propagating through the sensor (TOP) and no light propagating through the system (BOTTOM).
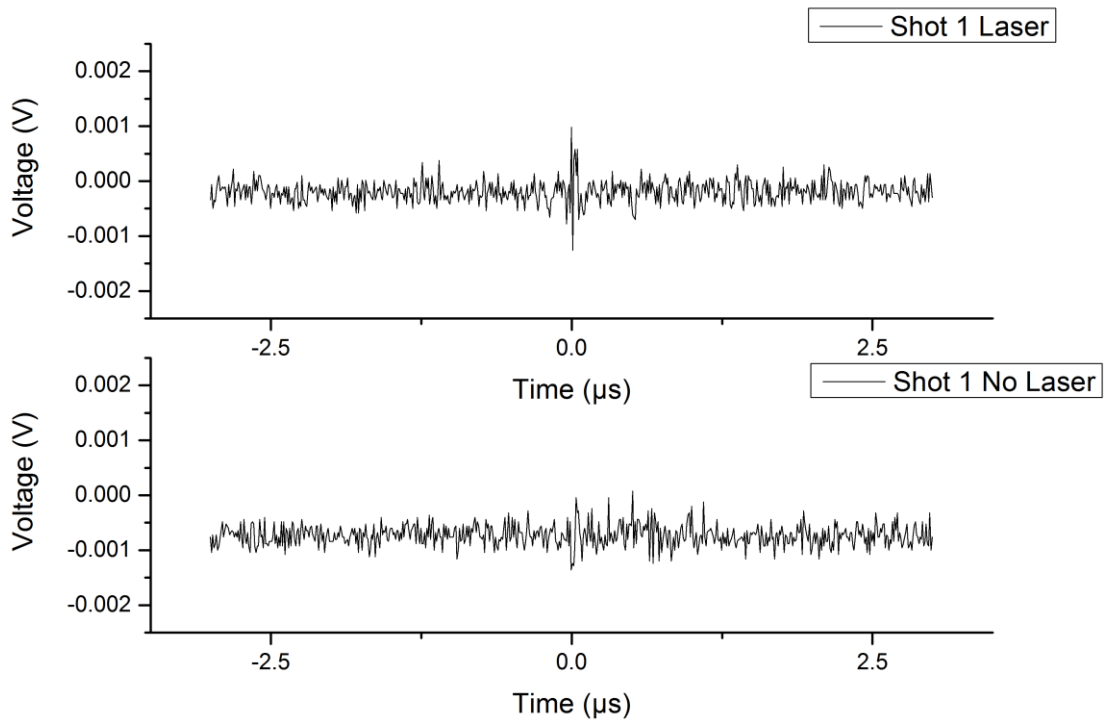
Figure 5. 15. The EMP induced variation in the output optical signal for TM incident light polarisation with light propagating through the sensor (TOP) and no light propagating through the system (BOTTOM).

5.4.9. Spectroscopic Scans

The transmission spectra from the nanohole arrays is obtained by using a tungsten light source (Olympus) with a spectrum ranging from 300nm to 1000nm which was focused through a 10X magnification condenser lens which focuses the incoming light into the multimode (ThorLabs GIF-625) which focuses the light onto the nano hole arrays. A fibre coupled spectrometer (Armedus) is used to collect the light from the nanohole arrays and produce the output spectrum.

The fabricated nano holes show a good uniformity across a total area of $500\mu m^2$ with an overall optically opaque gold layer thickness of 100nm. The transmission spectrum obtained from the fabricated nano holes is shown in *Figure 5.2.*;

5.5. Experimental Setup

The plasmon transmission results from show a good general agreement with the simulation results. From the spectroscopic scans the efficiency of the bulk plasmon peak, the (1, 1) SP peak and bandwidth as well as the positions of the (1, 1) and (1, 0) SP peaks are estimated.

The nanostructured plasmonic device was integrated with a multimode fibre (ThorLabs GIF-625) and illuminated by a 10mW 670nm red light laser diode (ThorLabs HL6748MG). The total losses of the integrated optical system were of the order of 80-90dB. The losses are so high due to the fact that a multimode fiber was used which has a large range of angles formed, misalignments and milling accuracy during formation of the grooves on the carrier, Fresenel reflections from the substrate as well as losses from passing through an optically opaque film of gold. In order to induce a change in the substrate refractive index the sensor was placed between a pair of 5mm diameter circular electrodes separated by 8mm. The optical transmission through the system was measured by a fibre-coupled Silicon photodiode with a maximum bandwidth of 2GHz (ThorLabs DET025AFC). The set up can be seen from *Figure 5. 16* below.
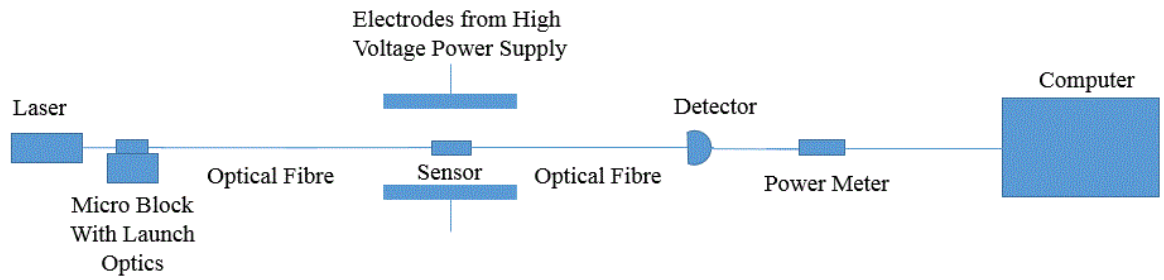
Figure 5. 16. Schematic of the experimental setup used for the measurements of static electric field changes.

5.6. Static Fields

Three different levels of static fields were applied to the device, (0kV/m, 312.5kV/m and 625kV/m) with the resultant output power being measured by the calibrated silicon photodiode. In order to account for any power fluctuations in the laser output, the measurements were repeated 2,000 times at a frequency of 4Hz. The results from the static field measurements can be seen in *Figure 5. 17* below where the peak measured power has been normalised to the peak measured power under no applied electric field. The simulated curve shows a similar gradient to the experimental data but has a different intercept, which could be explained by the difference in the actual value of the refractive index of the Lithium Niobate from the value used in the model.
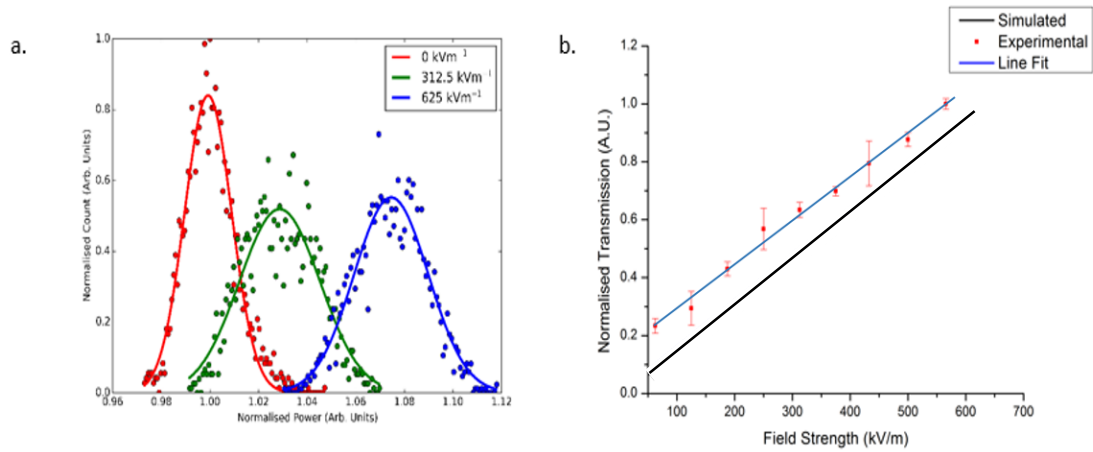
Figure 5. 17. Optical power output for 280nm diameter nanohole array for 3 different applied electric field strengths (LEFT) and a comparison to the modelled changes (RIGHT).

5.7. EMP Sensing

The response of the plasmonic device to a pulsed RF electromagnetic field was measured by applying the output from a 5kV Pockels cell driver across two plane parallel electrodes within a Faraday cage. The Pockels cell driver is capable of producing pulses up to 400kV/m with a double exponential profile of 1-2µs pulse duration. In the experimental setup a high voltage power supply is used to charge the Pockels cell driver. After the Pockels cell driver is fully charged, the discharge is induced by the leading edge of a pulse from the signal generator switching on a Field Effect Transistor and lowering the breakdown voltage in the first stage of the Marx generator. The peak field strength of the pulse was modified by changing the spacing between the electrodes and the response of the sensor to these different field strengths can be assessed. The sensor worked as designed, and the low power issues (such as; losses due to change in the modal shape going from a circular waveguide to a rectangular waveguide, Fresnel losses from the interfaces, chipping in Lithium Niobate during dicing hence reflections, transmission through lossy waveguides, misalignments in fibers) which were experienced during the testing of the waveguide sensors were addressed and rectified. The overall loss of the optical system from detector to laser was minimised by using larger core multi-mode fibres and the previously encountered issues of mode field mismatching were minimised to about 30dB. The optical signal from the plasmonic device was detected using an off the shelf Si high speed photo-diode (ThorLabs DET025AFC) with a sub-ns (<150ps) rise time, which then passes through a 50Ω termination load resistor, matching the impedance of the oscilloscope. The signal is then passed through an amplifier (Minicircuits ZRC

111

1R5+) powered by a 12V power supply. The electrical signal is carried through RF shielded coaxial cables minimising the chance of incident RF coupling into an oscilloscope (Tektronic TDS 744A 500MHz bandwidth and 2 Gigasamples/second). The laser used was a 675nm laser diode with an output power of 10mW (ThorLabs HL6748MG) driven at 30mA with a Thermo-electric cooler (TEC) set at 25°C. The optical signal is then guided to the plasmonic device using ~30m reels of GIF-625 multimode optical fibres terminated with FC/PC connectors. It should noted that the range of angle for this multimode fiber will be large. Based on the specifications of the manufacturer, the normalised frequency or V-number of this fiber is calculated to be ~ 80. Due to the large number of modes and modal dispersion the transmission will be both length and bandwidth limited in comparison to single mode fibers. In addition, the limited clear area of the plasmonic sensor (~10% of the area); the angular spread from the multimode fiber and the Fresnel reflections from the LiNbO3 limit the optical power that can be transmitted through the sensor. The input light illuminates the nano hole arrays causing the excitation of the surface plasmon peak which is highly sensitive to refractive index changes in the base substrate induced by the incident RF electromagnetic field. The output is then gathered by another GIF-625 multimode fibre which is then fed back to the detection electronics. The plasmonic device, high voltage supply powering the Pockels cell driver, the triggering wire loop antenna and the signal generator which sets the repetition rate (set to produce a shot every minute) of the pockels cell driver, are placed in a RF shielded Faraday cage ~30m away from the laser light source and the detection electronics. This minimises the RF coupling into the detection electronics and pick up of stray signals. A figure of the experimental setup can be seen from *Figure 5. 18* below.
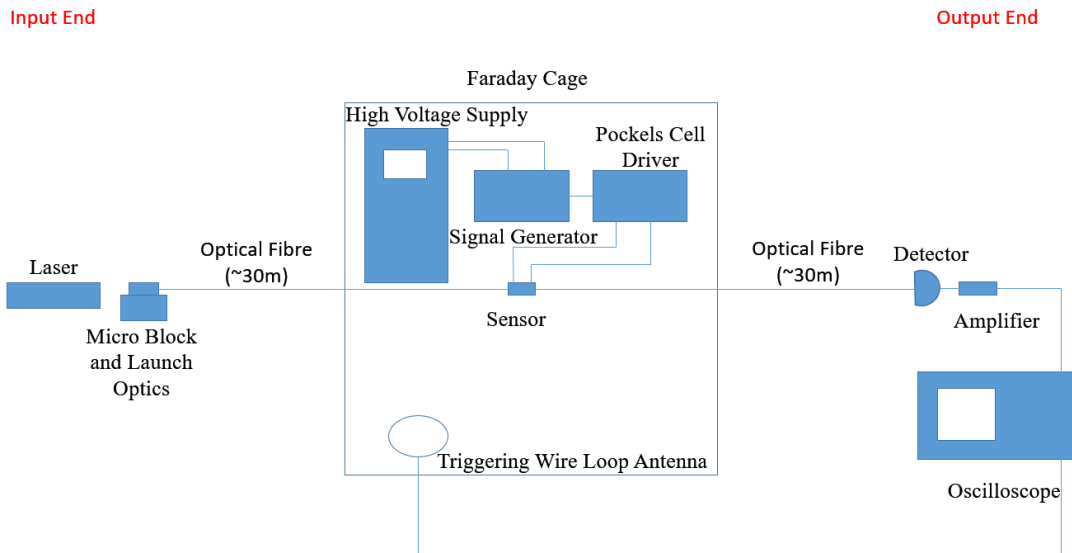
Figure 5. 18. Schematic of the experimental setup used for the detection of incident EMPs.
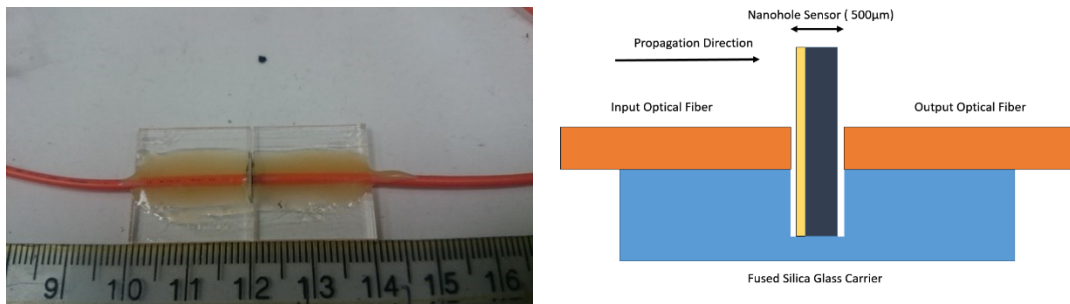
Figure 5. 19. Assembly of the complete sensor package.

The trace shown in ***Figure 5. 20*** below shows the profile of a typical triggering EMP as measured by the wire loop antenna in the Faraday cage. This was measured under a peak field strength of ~400kV/m. There is an observed mode hopping from the Pockels cell driver which is shown by the presence of two modes at slightly different frequencies suggesting that the output of the cell is not consistent. The second diagram shows the time-frequency spectrogram of the triggering EMP pulse shape and provides information about the frequency content of the triggering pulse. The triggering pulse has a duration of ~2μs and a central frequency of ~19MHz. The third diagram is the triggering pulse after integration. This provides the necessary information about the pulse shape as well as the rise time of the triggering pulse which was measured at about 200ns.
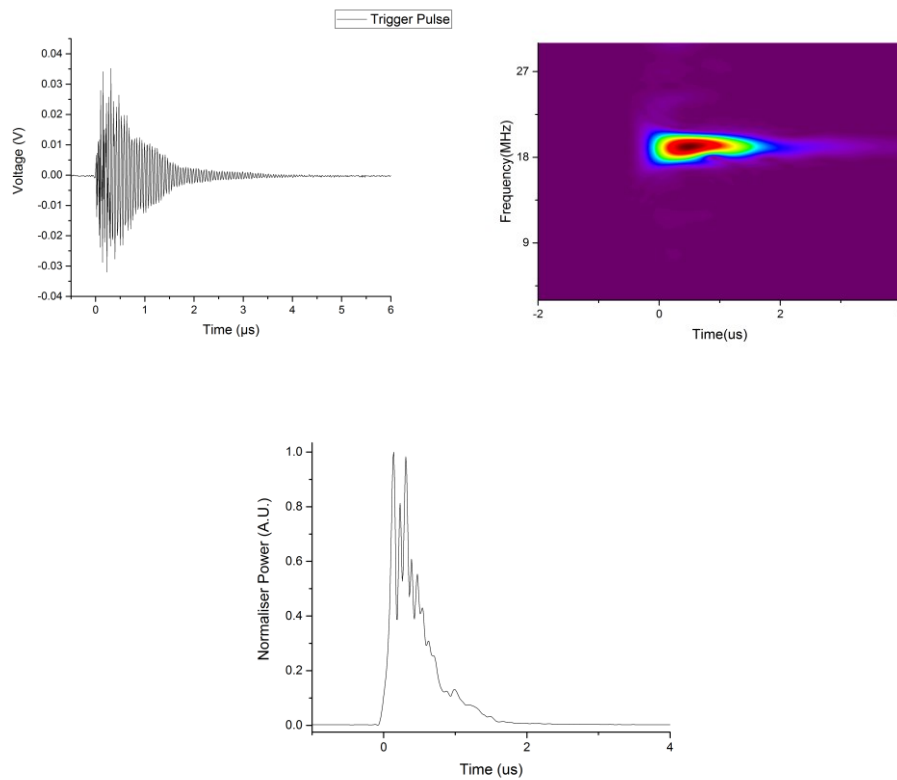
Figure 5. 20. Trace of the triggering pulse as measured by a wire loop antenna inside the faraday cage (TOP LEFT), Time-Frequency spectrogram of the trigger pulse (TOP RIGHT) and temporal pulse shape of triggering pulse (BOTTOM).

A typical response of the plasmonic device to peak field strengths of ~ 50, 100, 200 and 400kV/m can be seen from *Figure 5. 21* below. The EMP detected at different peak field strengths was investigated. There exists a delay between the the initial triggering pulse and the detected optical signal of the the order of 10ns which corresponds to the path difference between the direct free space path of the EMP trigger and the guided optical path of the sensor signal. A total of 40 shots at different field strengths were detected using the plasmonic device and the optical signal outputs at the different estimated field strengths shown.

114
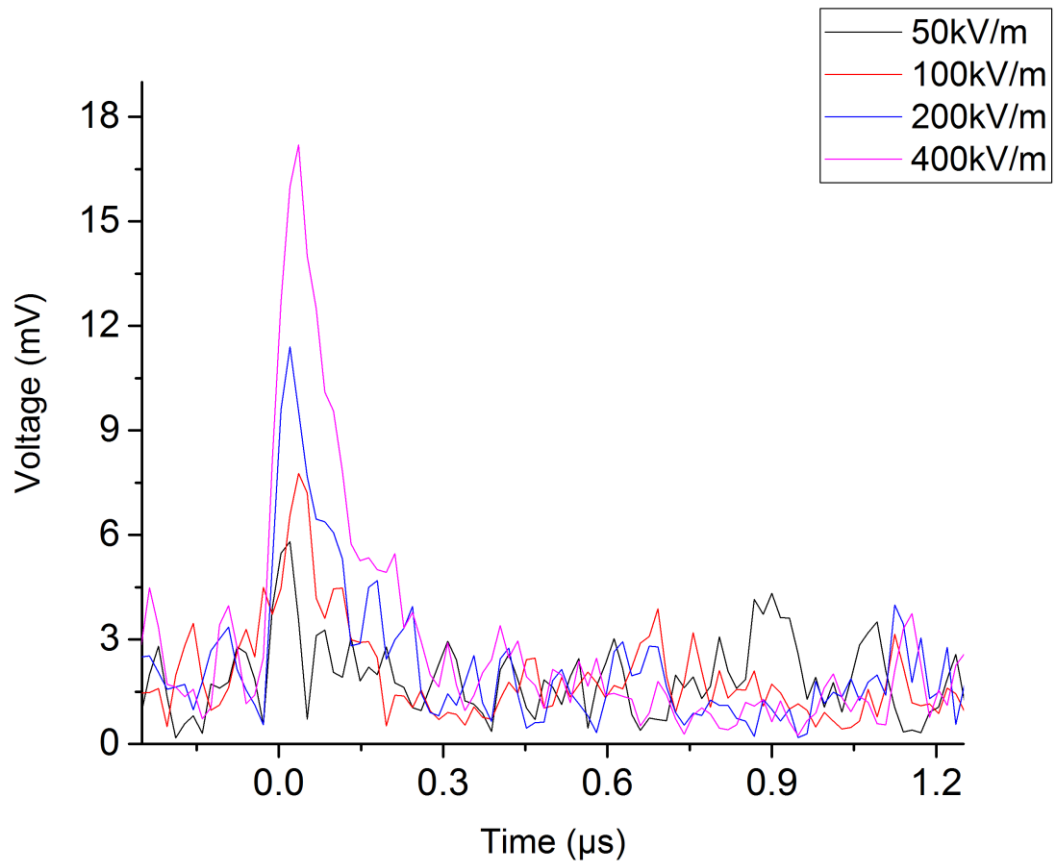
Figure 5. 21. Traces of the optical output of the nanohole sensor as a function of increasing EMP field strength.

The measured optical signal has a significant noise level which necessitated for the development of a data processing algorithm that allows for the removal of most of the noise without significantly impacting the waveform produced by the plasmonic device. The algorithm used for noise removal is thresholded short time Fourier transform (STFT). The short time Fourier transform is used to show the sinusoidal frequency as well as the phase content of a time varying signal. The first step is to carry out the thresholding at the 90th percentile of the data removing most of the noise and then window the signal so that the important part of the signal holding the information about the pulse shape, frequency and duration is not lost. The long signal is broken up into shorter segments all of equal length, and a Fourier transform is carried out separately on each of those equal length segments. This method is similar in concept to the wavelet transform and produces a time-frequency spectrogram of the measured optical signal that shows the clear existence of the EMP induced variation separated from the background noise. *Figure 5. 22* below show the time-frequency spectrograms of the measured optical signal for EMP field strengths of 50, 100, 200 and 400kV/m and it can be clearly seen that the measured power of the detected optical signal increases as a function of increasing field strength.
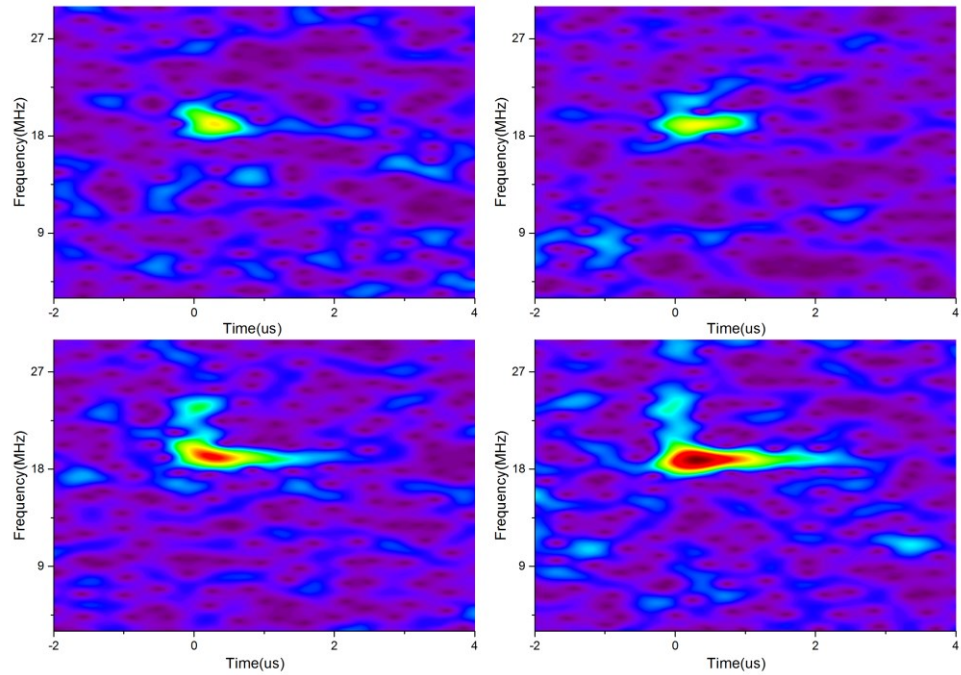
Figure 5. 22. Time-frequency spectrogram of 280nm hole array for EMP peak field strengths of 50kV/m (TOP LEFT), 100 kV/m (TOP RIGHT), 200kV/m (BOTTOM LEFT) and 400kV/m (BOTTOM RIGHT).

The peak response of the sensor increases with increasing EMP field strength as anticipated by the static field measurements shown in the previous section. The response of the sensor to peak EMP field strengths was determined by plotting the peak measured voltage as a function of the nominal EMP filed strength (calculated by dividing the Pockels cell driver charging voltage by the spacing between the electrodes) can be seen from **Figure 5. 23** below. The pulse shape can be determined by the study of the time-frequency spectrograms[22] of both the incident EMP and the measured sensor response. As seen from the figure below, the peak voltage is normalised by the detected optical power through the plasmonic device without any incident EMP. It can be observed that the trend of the measured sensor response follows a generally linear pattern. The existence of a low finesse micro cavity between the end facets of the fibres used to transfer the optical signal to and from the plasmonic device showed that, response follows a linear trend, with the cavity length being 600μm about 8 times less in comparison to the waveguide sensors , the maximum transmission peaks are much further apart as a function of refractive index change and for the induced refractive index changes due to the incident EMP field the response of the device follows a near linear trend line. The noise equivalent voltage of the system described above is $140\text{nV/Hz}^{1/2}$ giving a minimum detectable

116

voltage of ~ 1.4mV. The best SNR produced with this configuration is around 3.4 which can further be increased by lowering the sampling frequency further or applying a sliding average. The noise equivalent of the system is also limited by the noise equivalent power of the detector used which in this case is $9.5 \times 10^{-15} W/Hz^{1/2}$ as well as the detection electronics used.
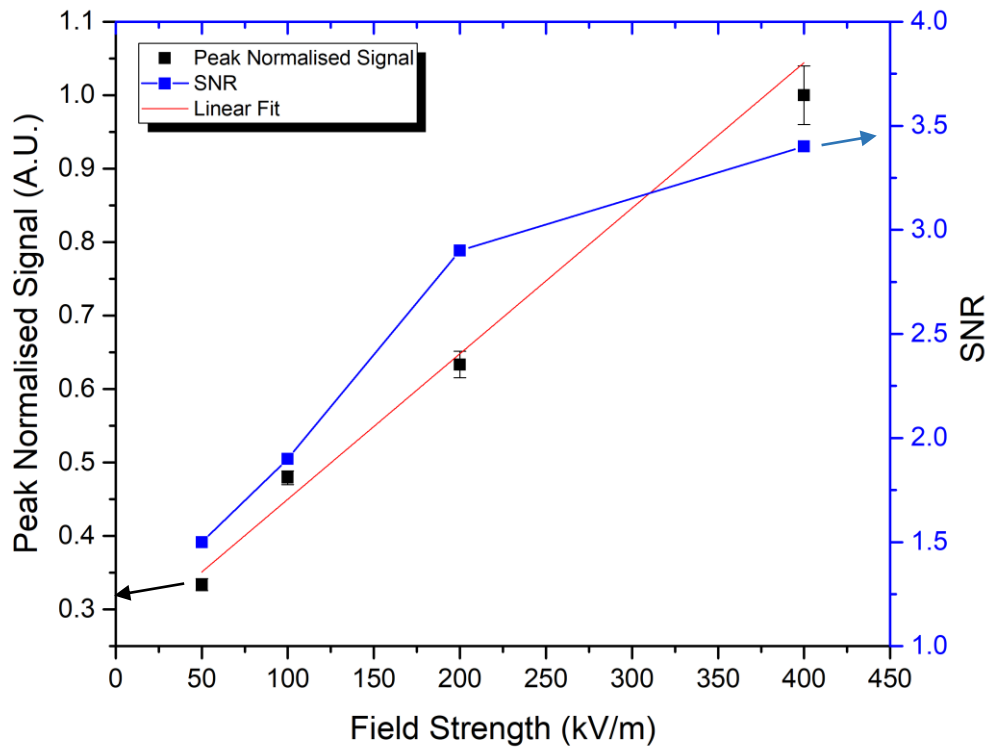
Figure 5. 23. Peak response curve of sensor as function of increasing field strength.

The measured pulse shape at the primary EMP frequency of 19.11MHz is qualitatively similar to the incident EM pulse. The full duration of the pulse is not visible due to the significant losses in the optical system dropping the light through the sensor below the noise floor of the photo detector. Improvements to both the optical system (by,for example, decreasing the overall losses of the system through micrometre scale launch and collection optics) and the optoelectronics (by for example improving the shielding of the detector) should improve the signal to noise ratio allowing more definitive measurements of the full pulse duration to be made. *Figure 5. 24* below shows the modelled transmission behaviour through a low finesse micro cavity formed between the end facets of the optical fibres transporting light to and from the plasmonic device. The cavity length is set to 600μm which is the Lithium Niobate substrate thickness. The refractive index of the fibre

is 1.46 and the refractive index of Lithium Niobate is 2.27 at 675nm. This forms the reflection coefficients at both ends of the cavity. The operational wavelength of the cavity is set to 675nm and the refractive index change is set to correspond to an EMP induced refractive index change from 0kV/m to 1000kV/m. The model shows that for that range of refractive index change the transmission increase is near linear which is a marked improvement over the waveguide sensors described in the previous chapter which followed a roughly sinusoidal trend with regions of monotonically increasing response.
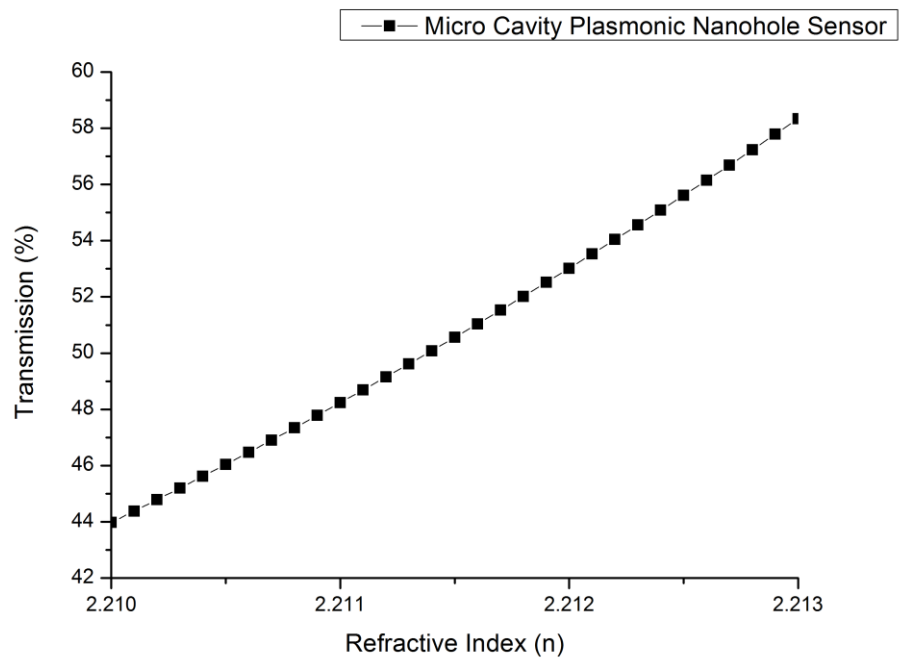
Figure 5. 24. Variation in the peak transmissivity as a function of increasing refractive index of the base substrate through the high finesse micro cavity formed between the optical fibres and the nanohole sensor showing the effects of the high finesse cavity on the transmission characteristic of the device.

5.8. Conclusions

In conclusion, the details of the design, fabrication and testing of a novel electro-optic nanostructured device that provides a simple and efficient sensor for the detection of both static and dynamic electric fields has been described. The nanostructured device demonstrates a high degree of tunability in terms of operational wavelengths coinciding with plasmonic peaks by altering the periodicity, hole size and metal layer. The device has been shown to have a high sensitivity and broadband response mainly limited by the detection electronics used. A square array of nanoholes of 280nm size on a periodicity of 620nm with a Gold metallic layer on a Lithium Niobate base substrate gave a surface Plasmon peak identified by simulations and confirmed through experimental

measurements at 675nm which coincides with readily available commercial laser sources 675nm and fast detection electronics. The nanostructured device was capable of detecting EMP pulses with a duration ~ 2μs, rise times of ~200ns and peak field strengths ranging from 50kV/m to 400kV/m. The device described in this chapter has a noise equivalent voltage of ~140nV/Hz$^{1/2}$, which is much higher in comparison to that of the waveguides described in the previous chapter with figure of merit of ~6.8nV/Hz$^{1/2}$. This is however due to the sampling frequency used for this experiment. If the sampling frequency were to be increased then the noise equivalent voltage would be lower. The highest signal to noise ratio of this device was measured to be ~3.4 for an incident EMP of field strength of 400kV/m which demonstrates an improvement over the waveguides where the highest SNR was ~2.9 at a field strength of 300kV/m. When compared to the commercially available d-dot sensors which have a noise equivalent voltage of ~ 5nV/Hz$^{1/2}$ and optical devices described in the literature review (noise equivalent voltage ~4-20nV/Hz$^{1/2}$), the figure of merit is much larger but can be further reduced by increasing the sampling frequency. The device has a small form factor and shown to be capable of measuring EM fields in enclosed spaces with introducing a minimal amount of perturbation of the measured signal. The device has about 9 orders less metallic volume when compared to conventional electric based d-dot sensors. It has shown to respond linearly to applied external electric fields for both static and dynamic fields. The measured pulse shape of the triggering EMP at a frequency of ~19MHz is qualitatively similar to the optically measured pulse. Further improvements to the optical system and the detection optoelectronics will allow the overall sensitivity of the device to be further improved.

5.9. References

[1] F. Álvarez, F. Garnacho, J. Ortego, and M. Á. Sánchez-Urán, "Application of HFCT and UHF sensors in on-line partial discharge measurements for insulation diagnosis of high voltage equipment," *Sensors (Switzerland)*, vol. 15, no. 4, pp. 7360–7387, 2015.

[2] H. S. Jung, "Electro-optic electric field sensor utilizing Ti:LiNbO 3 symmetric Mach-Zehnder interferometers," *J. Opt. Soc. Korea*, vol. 16, no. 1, pp. 47–52, 2012.

[3] J. E. Toney, A. G. Tarditi, P. Pontius, A. Pollick, S. Sriram, and S. A. Kingsley, "Detection of energized structures with an electro-optic electric field sensor," *IEEE Sens. J.*, vol. 14, no. 5, pp. 1364–1369, 2014.

[4] T. W. Ebbesen *et al.*, "Extraordinary optical transmission through sub-wavelength hole arrays," *Nature*, vol. 86, no. 6, pp. 1114–7, 1998.

[5] A. G. Brolo, S. C. Kwok, M. G. Moffitt, R. Gordon, J. Riordon, and K. L. Kavanagh, "Enhanced Fluorescence from Arrays of Nanoholes in a Gold Film

Enhanced Fluorescence from Arrays of Nanoholes in a Gold Film," no. 10, pp. 14936–14941, 2005.

[6]   Y. B. Zheng, B. K. Juluri, X. Mao, T. R. Walker, and T. J. Huang, "Systematic investigation of localized surface plasmon resonance of long-range ordered Au nanodisk arrays," *J. Appl. Phys.*, vol. 103, no. 1, 2008.

[7]   E. H. Mullen and Y. Fainman, "Plasmonic Sensing of Biological Analytes Through Nanoholes," *IEEE Sens. J.*, vol. 8, no. 12, pp. 2074–2079, 2008.

[8]   D. E. Grupp, H. J. Lezec, T. Thio, and T. W. Ebbesen, "Beyond the Bethe Limit: Tunable Enhanced Light Transmission Through a Single Sub-Wavelength Aperture," *Adv. Mater.*, vol. 11, no. 10, pp. 860–862, 1999.

[9]   R. Gordon, A. G. Brolo, D. Sinton, and K. L. Kavanagh, "Resonant optical transmission through hole-arrays in metal films: Physics and applications," *Laser Photonics Rev.*, vol. 4, no. 2, pp. 311–335, 2010.

[10]   M. Najiminaini, F. Vasefi, B. Kaminska, and J. J. L. Carson, "Effect of surface plasmon energy matching on the sensing capability of metallic nano-hole arrays," *Appl. Phys. Lett.*, vol. 100, no. 6, 2012.

[11]   M. Najiminaini, E. Ertorer, B. Kaminska, S. Mittler, and J. J. L. Carson, "Surface plasmon resonance sensing properties of a 3D nanostructure consisting of aligned nanohole and nanocone arrays," *Analyst*, vol. 139, no. 8, p. 1876, 2014.

[12]   M. Najiminaini, F. Vasefi, B. Kaminska, and J. J. L. Carson, "Optical resonance transmission properties of nano-hole arrays in a gold film: effect of adhesion layer," *Opt. Express*, vol. 19, no. 27, p. 26186, 2011.

[13]   A. R. Hajiaboli, B. Cui, M. Kahrizi, and V.-V. Truong, "Optical properties of thick metal nanohole arrays fabricated by electron-beam and nanosphere lithography," *Phys. Status Solidi*, vol. 206, no. 5, pp. 976–979, 2009.

[14]   A. D. Rakic, A. B. Djurisic, J. M. Elazar, and M. L. Majewski, "Optical properties of metallic films for vertical-cavity optoelectronic devices.," *Appl. Opt.*, vol. 37, no. 22, pp. 5271–5283, 1998.

[15]   D. E. Zelmon, D. L. Small, and D. Jundt, "Infrared corrected Sellmeier coefficients for congruently grown lithium niobate and 5 mol.% magnesium oxide –doped lithium niobate," *J. Opt. Soc. Am. B*, vol. 14, no. 12, p. 3319, 1997.

[16]   F. Przybilla *et al.*, "Efficiency and finite size effects in enhanced transmission through subwavelength apertures," *Opt. Express*, vol. 16, no. 13, pp. 9571–9579, 2008.

[17]   M. Najiminaini, F. Vasefi, B. Kaminska, and J. J. L. Carson, "Experimental and numerical analysis on the optical resonance transmission properties of nano-hole arrays," *Opt. Express*, vol. 18, no. 21, pp. 22255–22270, 2010.

[18]   B. Sepúlveda, Y. Alaverdyan, J. Alegret, M. Käll, and P. Johansson, "Shape effects in the localized surface plasmon resonance of single nanoholes in thin metal films.," *Opt. Express*, vol. 16, no. 8, pp. 5609–5616, 2008.

[19]   S. Balakrishnan, M. Najiminaini, M. R. Singh, and J. J. L. Carson, "A study of angle dependent surface plasmon polaritons in nano-hole array structures," *J. Appl. Phys.*, vol. 120, no. 3, 2016.

[20]   N. Sedoglavich, J. C. Sharpe, R. Künnemeyer, and S. Rubanov, "Polarisation and

wavelength selective transmission through nanohole structures with multiple grating geometry.," *Opt. Express*, vol. 16, no. 8, pp. 5832–7, 2008.

[21]   J. Elliott, I. I. Smolyaninov, N. I. Zheludev, and A. V Zayats, "Polarization control of optical transmission of a periodic array of elliptical nanoholes in a metal film.," *Opt. Lett.*, vol. 29, no. 12, pp. 1414–1416, 2004.

[22]   S. Time, F. Transform, and D. F. Transform, "B3. Short Time Fourier Transform (STFT)."

[23]   **https://reu.uoregon.edu/research-projects/miriam-deutsch/.**

Chapter 6. Hologram Generation via Binary Surface Relief Profiles (Pulse Position Modulation)

6.1. Introduction

Conventionally Diffractive Phase Elements (DPE) are designed using the paraxial scalar theory and fabricated by photolithography or moulding of a polymer onto a hard shim. DPE which are multilevel (z>2) involved the use of several optically aligned masks. At each and every stage of alignment and etching a small level of fabrication error is introduced which cumulatively adds as the levels are built up leading to effects such as increment in the zeroth order scatter, reduction of diffraction efficiency, increased levels of cross talk for two coloured images and a general deterioration of the optical output.

An alternative to photolithography can be sought after in the form of electron beam lithography or direct laser writing. In both of these techniques the structures are directly written on the resist on the substrate. Electron beam lithography has demonstrated of being capable of fabricating features down to 25nm[1] with a positional accuracy of ±10nm. However for the feature sizes and positional accuracy mentioned, the process becomes very difficult, time consuming, expensive and requires a lot of calibration runs. In this chapter of the thesis, a modulation scheme based on Bragg incidence combined with the high frequency modulation of a binary grating is displayed. The optical outputs are high resolution single colour images and are designed to viewed by the naked eye and appear catching. The theoretical diffraction efficiencies of binary gratings with a high frequency modulation are comparable to those of multilevel structures >80%. Through the use of electron beam lithography, the advantages of having sub-micron features and great positional accuracies can be exploited. The fabrication only involves one writing stage, the scatter and zeroth order contributions are minimised and the feature depths can be tuned to suit the designed operational wavelengths by adjusting the spin speeds of the resist used. The effects that the geometry of the structure has on the optical outputs has been analysed and devices that function in both reflection and transmission operational modes have been fabricated with the experimental results shown. Lastly the insensitivity of these devices to the illumination wavelengths has also been demonstrated.

6.2. Modelling of Reflection and Transmission Spectra of Nanostructured Gratings

A schematic of the Bragg incidence from a subwavelength grating is shown in *Figure 6. 1*. In order to satisfy the Bragg condition, a monochromatic plane wave of wavelength λ incident at an angle θ, will be given as

$$\sin(\theta) = \lambda / 2nd \qquad (6.1)$$

Where n is the refractive index of the substrate and d is the periodicity of the grating. Here all but the 0th and -1st diffraction orders are evanescently decaying, if the condition below is satisfied.

$$\frac{1}{2} < \frac{d}{\lambda} < \frac{3}{2} \qquad (6.2)$$

The modulation is carried out by shifts in the grating pulse in both x and y directions by an amount a and b. The -1st diffraction order is split into a signal window corresponding to this shift. The modulation of gratings using this scheme has previously been described by [2][3].
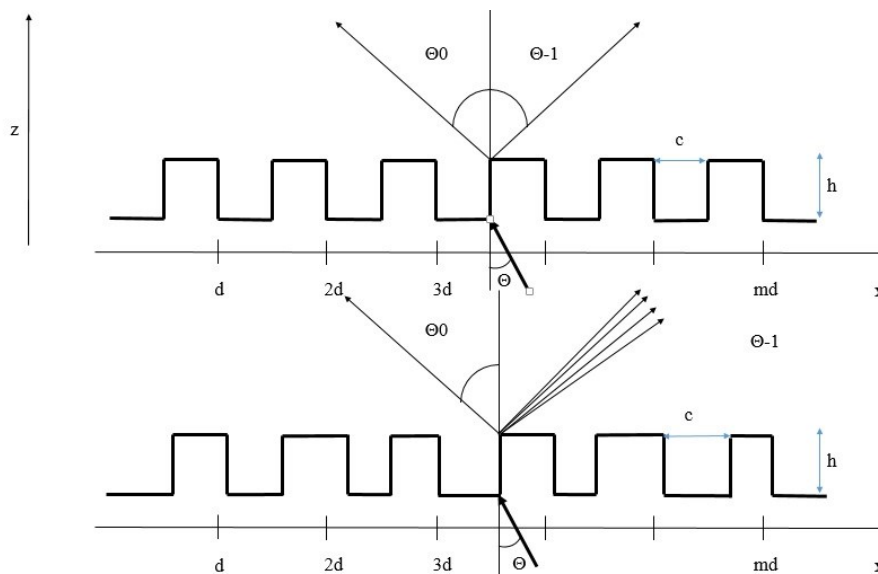
Figure 6. 1.Side profile of a binary high frequency grating illuminated at the Bragg incidence angle (TOP) and a pulse modulated binary grating (BOTTOM).

This had led to an optimisation with the aim of increasing the diffraction efficiencies of binary elements to levels comparable to those of multilevel DPE. The major benefits of this scheme are that the structures are binary, alleviating the need for complex multilevel writing, the diffracted image appears in the -1st order, hence negating the scattering due to the 0th order, the surface relief profiles are quite shallow (<1μm) making it easier for writing and replication (limitations of which are described in the next chapter), insensitive to operational wavelength which just results to a change in the viewing angle of the element.

Previous work carried out by [4] and [5] has shown a pulse width binary grating in which all but the 0th orders are evanescent. The drawback to this approach comes in the form of large ratios of groove depth to feature size much larger that 10 to 1, and with the selectivity and aspect ratio limitations of resists this requires for the use of an even more complex system. The technology require the use of deep X ray lithography, multiple etches making it complex and time consuming. By reducing this ratio to 1, electron beam lithography can be used for the fabrication of these devices to generate -1st order images off axis and nearly all 0th order on axis.

The integration of the diffraction pattern through the modulation of the base grating structure has been shown[6] and an outline is presented below. It starts with the formation of a continuous phase profile, in which the magnitude of the reflectance or transmittance phase profile in the Fourier plane is the required intensity. This is formed based on techniques from the scalar diffraction theory framework. In order to ensure that the feature sizes in the grating are not too small, the use of a continuous phase structure is preferable. To end the parameterisation, the continuous phase structure is used. The angular power spectrum is extended to two dimensions for a continuous phase profile in the x direction only. A high frequency carrier grating is added the phase profile and the result binarised. The image is then encoded in the signal window appearing about the -1st order of the grating. The choice of characteristics of the carrier grating in terms of periodicity(d), pulse width(C) and pulse height(h)allow to maximise the efficiency going into the -1st order when the grating is illuminated at the Bragg incident angle. Assuming that the periodicity is similar to the illumination wavelength, then the carrier grating characteristics can be predicted correctly through the use of the rigorous electromagnetic diffraction theory of gratings[7] used further on for looking at grating geometries. For

reflection based devices a diffraction efficiency of 100% is obtainable for TM polarised light but TE polarised light requires a much higher ratio of h/λ making it unfeasible from a fabrication point of view. Having optimised the carrier grating, the encoding of the high frequency grating is carried out next. The carrier is always added in the direction of the continuous profile. The structure has to be hard clipped to yield the modulated surface relief profile. In this scheme the lateral translational accuracy of the fabrication process is important, being at least an order of magnitude smaller than the wavelength. This is in contrast to the DPE described in the next chapter where the accuracy of the played pulse is dominated by the phase of the diffracted light rather than the lateral translational accuracy. To ensure a good image fidelity the 600-800nm range, the positional accuracy must be less than 30nm. An incorrect pulse height leads to a drop in the diffraction efficiency of the grating. A diffraction efficiency of ~90% is maintained if the accuracy of the pulse height is within 100nm for the fused silica and polymer based gratings.

6.3.   Reflection Devices

The device used for operation in reflection is also suitable for use as the master for the shim formation and subsequent replication. The grating is optimised for operation at 532nm, has a periodicity of 520nm, feature size of 250nm and a height of 717nm producing a (d/λ=0.98) and a (c/d=0.48) and a refractive index of 4.152. The fabricated element measures 5mm by 5mm. The in-depth fabrication procedure is covered in chapter 3 of this thesis. The diffraction efficiency of the -1st diffraction order where the optical output produced has a 95% efficiency at an angle of incidence of 24° for a perfectly rectangular grating. A simulation was carried out using COMSOL to find out the effects that geometry changes in the base carrier grating have on the efficiencies and incidence angles of the -1st diffraction order and to determine whether or not a further increase in the diffraction efficiency can be attained through these alterations. The geometric changes seen from *Figure 6.2* in the grating are carried out by expanding or contracting the base of the grating, which can be closely achieved by altering either the development parameters or the etching parameters. In this simulation a grating of 250nm features on a periodicity of 520nm is considered. The reflection efficiencies and angles of the 1st, -1st and 0th orders are calculated as a function of change of incidence angle ranging from 0° to 90°.
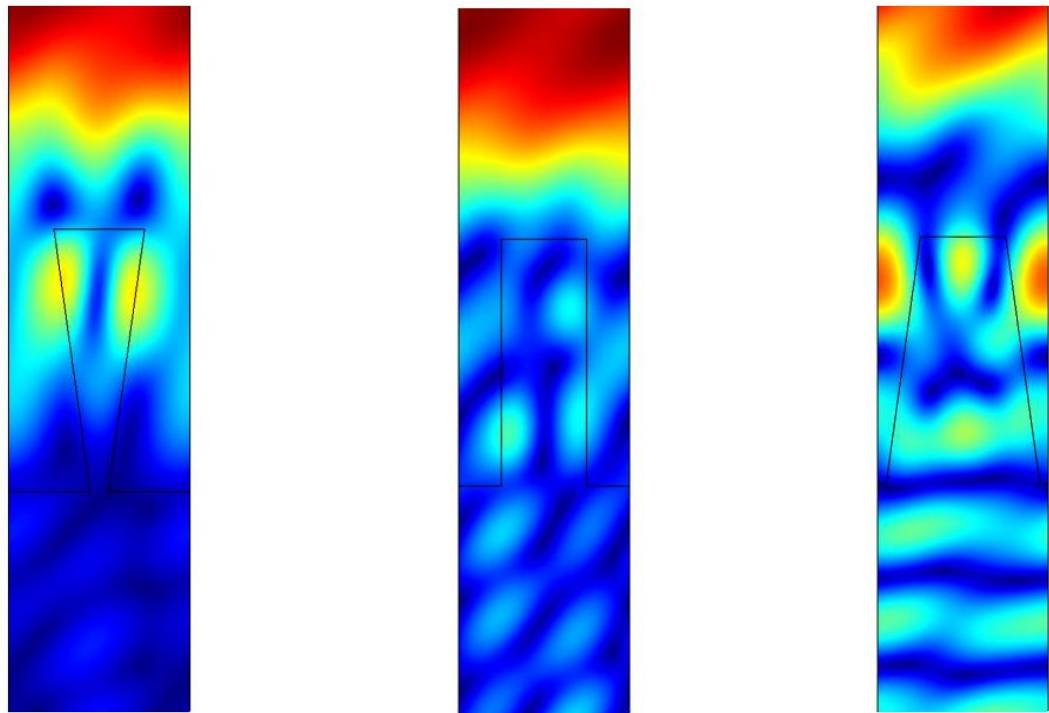
Figure 6.2. The design window in COMSOL showing an undercut grating (LEFT) a perfect grating (CENTER) and an over exposed Grating (RIGHT).

In *Figure 6.3* below show the diffraction efficiency and diffraction angles for the -1st diffraction order as a function of undercut or overcut of the grating. Undercut is defined when the base of the grating is smaller than the top and overcut is defined when the base of the grating is larger than the top. From the efficiency plot, on fitting a line fit a trend can be observed in which as the grating changes from undercut to overcut the efficiency of the -1st reflection order decreases by about 20%, the highest efficiency is for a standard rectangular grating while the position of the reflection angle of the same order remains at 30° to 40° with no observable trend.
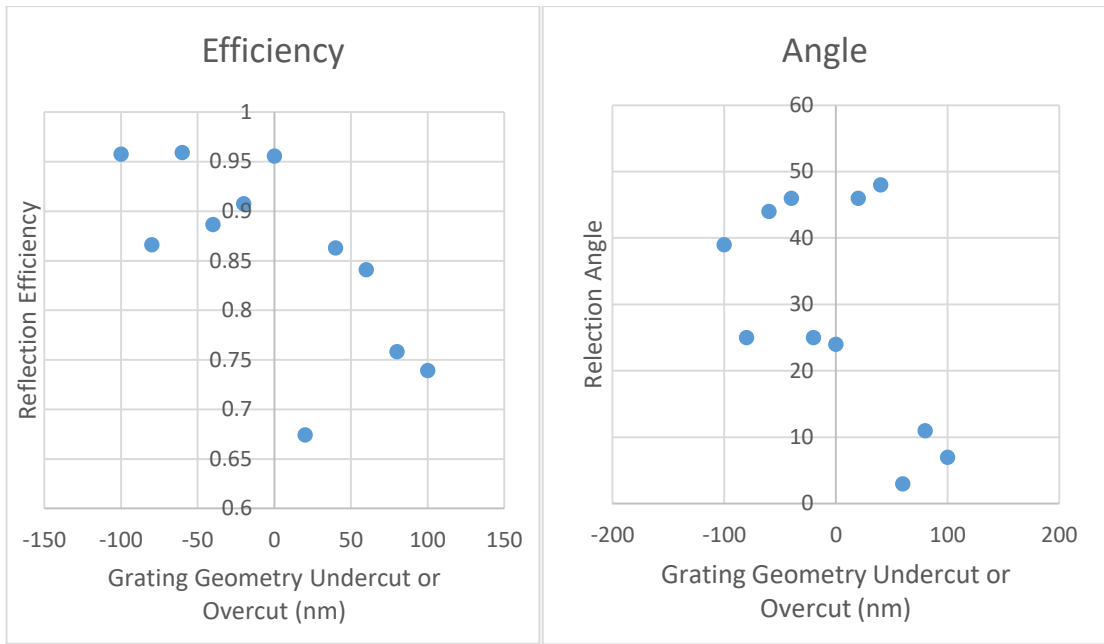
Figure 6.3. Showing the reflection efficiency from the -1st diffraction order as a function of grating geometry (LEFT) and the Bragg angle of the -1st diffraction order as a function of grating geometry (RIGHT).

Below in *Figure6.4* is an SEM image of the of the high frequency grating fabricated, the existence of small gaps in between the individual pulses can be accounted for by an over development of the grating after exposure which could explain the slightly lower optical output.
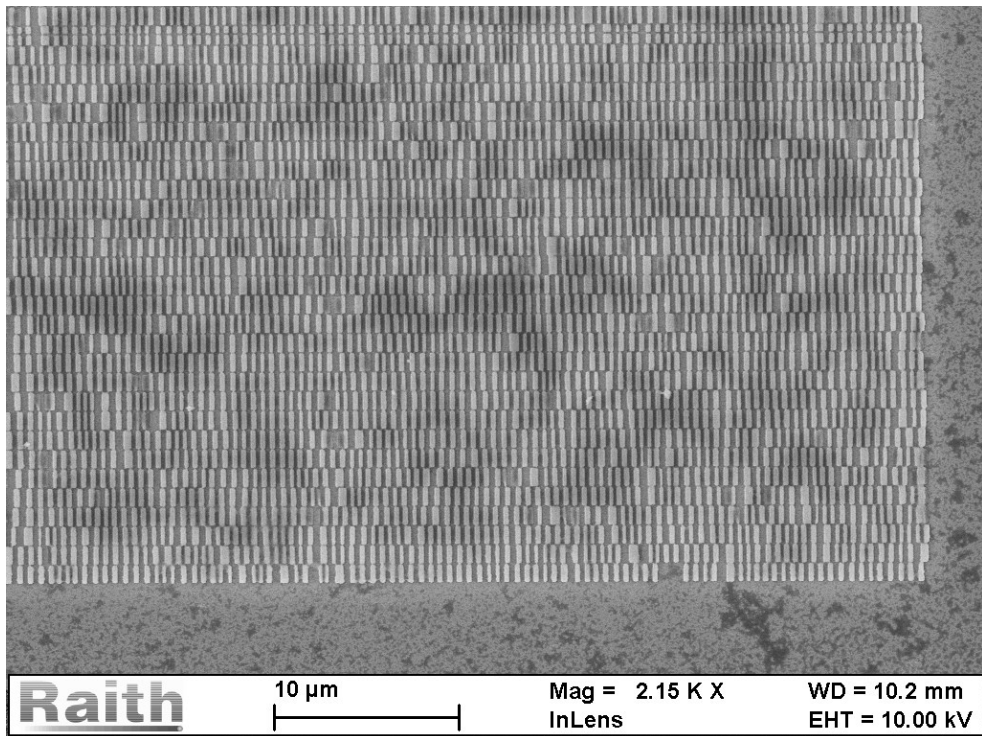
Figure6.4. Scanning Electron Micrograph of the pulse modulated reflection grating.

Figure 6.5 below shows the optical output from the reflection based device, the -1st order is observed at an angle of incidence of 12°, whereas the theory predicts that it should occur at 24°. The diffraction efficiency of the element was measured to be 71% whereas the theoretical model suggests that it should be 90%. Both of these drops can be accounted for by the fact that the grating is over etched to compensate for the shrinkage which would occur during the replication process. The pulse height difference and breaks between pulses can be a source of drop in efficiency as well as lateral positioning fabrication errors.

Figure 6.5. Optical output from the -1st diffraction order produced by illuminating the grating at the Bragg incidence angle and projected on a screen. The image appears distorted being captured and projected at an angle.

6.4.   Transmission Devices

The device used for operation in the transmission mode copy on the polymer film replicated from the shim of the reflection based device. The grating is optimised for operation at 532nm, has a periodicity of 520nm, feature size of 250nm and a height of 520nm which is estimated from the pre compensation curves and shrinkage analysis introduced in the last chapter producing a (d/λ=0.98) and a (c/d=0.48) and a refractive index of 1.54. The device now works in transmission with a calculated diffraction efficiency of 90%, occurring at an incidence angle of 30 degrees. The diffraction efficiency of the -1st diffraction order and the Bragg angle can be seen from *Figure 6.6*.
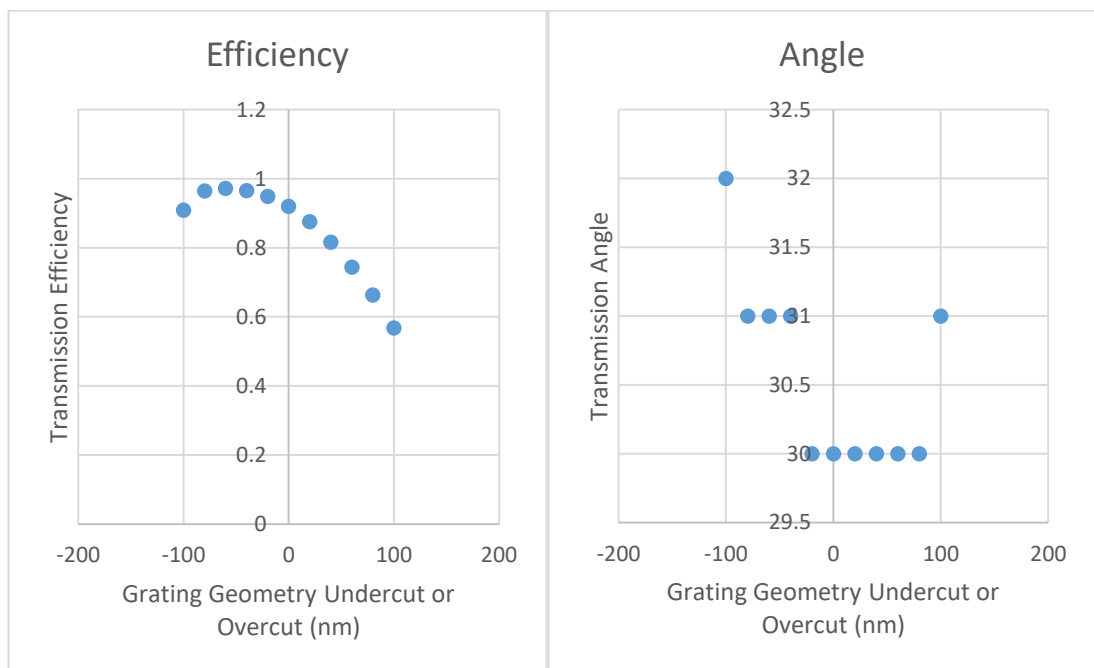
Figure 6.6. Showing the transmission efficiency from the -1st diffraction order as a function of grating geometry (LEFT) and the Bragg angle of the -1st diffraction order as a function of grating geometry (RIGHT).

6.5.   Experimental Verification of Optical Outputs and Efficiencies of Elements.

In order to carry out an experimental verification from the optical outputs of the high frequency modulated Bragg gratings, the patterns are imprinted on a transmissive and electrically conducting substrate. Fused silica with a coating of FTO and BK7 with a coating of ITO were used for the e-beam lithography. A schematic of the experimental

setup is shown in **Figure 6.7** below. A green laser emitting at 532nm is used for illuminating the gratings. The laser light is focused through a short focal length lens (~15cm) to converge the spot size in order to illuminate on period. The substrate with the gratings is secured on an optical turn table which allows a translation through 360 °. The optical output from the -1st diffraction order is viewed on a screen. Two phase profiles were chosen for encoding with the pulse position modulation, the first was the number 100 and the second is a line art of a portrait.
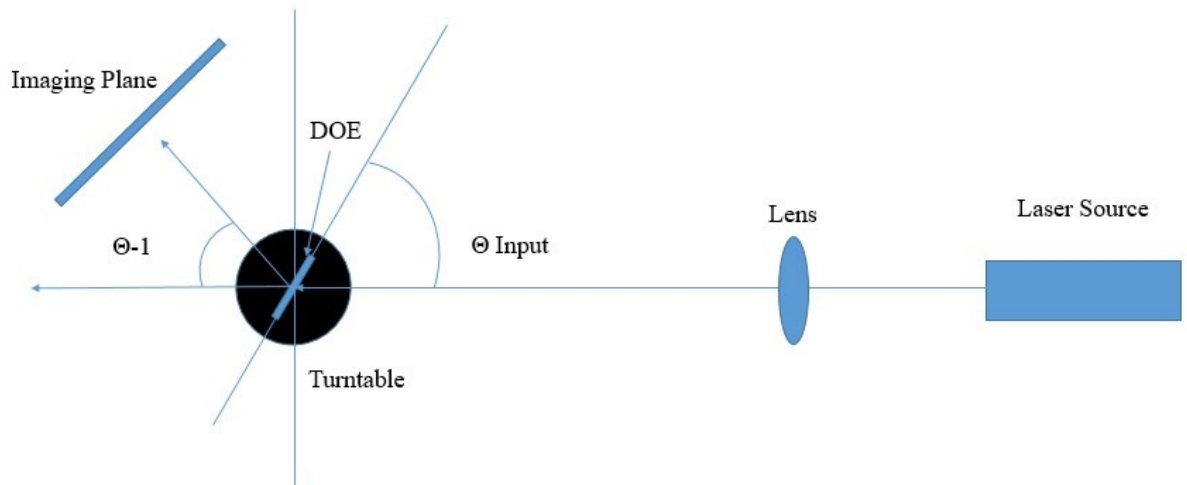
Figure 6.7. Schematic of the experimental setup used for capturing images from the pulse modulated gratings.

Figure6.9 below shows the optical output from the aforementioned device and the image shows a high fidelity rate, and no zeroth order scatter because they appear in the -1st diffraction order. The image on the left hand side shows the optical output at normal incidence, a faint outline of a 0 is observed but engulfed by the scatter from the 0th order diffraction. The image on the right hand side shows the optical output from the grating when illuminated at the Bragg angle. The measured Bragg incidence angle is 31°, which closely follows the prediction made by the model with predicted 30°. The diffraction efficiency on the other hand is ~69%, lower than the predicted 90% which can be explained firstly the Fresnel losses that occur at the interfaces (~4% at normal incidence), the Fresnel losses of the two light polarisations emerging from the laser for non-normal incidences) which increases as a function of angle and by fabrication errors from the design. The image starts appearing from shallow angles in the range from 10° all the way up to 70° but is significantly distorted unless at the Bragg angle. A change in the illumination wavelength from 532nm to 405nm reduces the incidence angle to 21° with

the pattern still made out despite appearing slightly fuzzier and at 650nm the incidence angle is increased to 51° with the image still appearing.
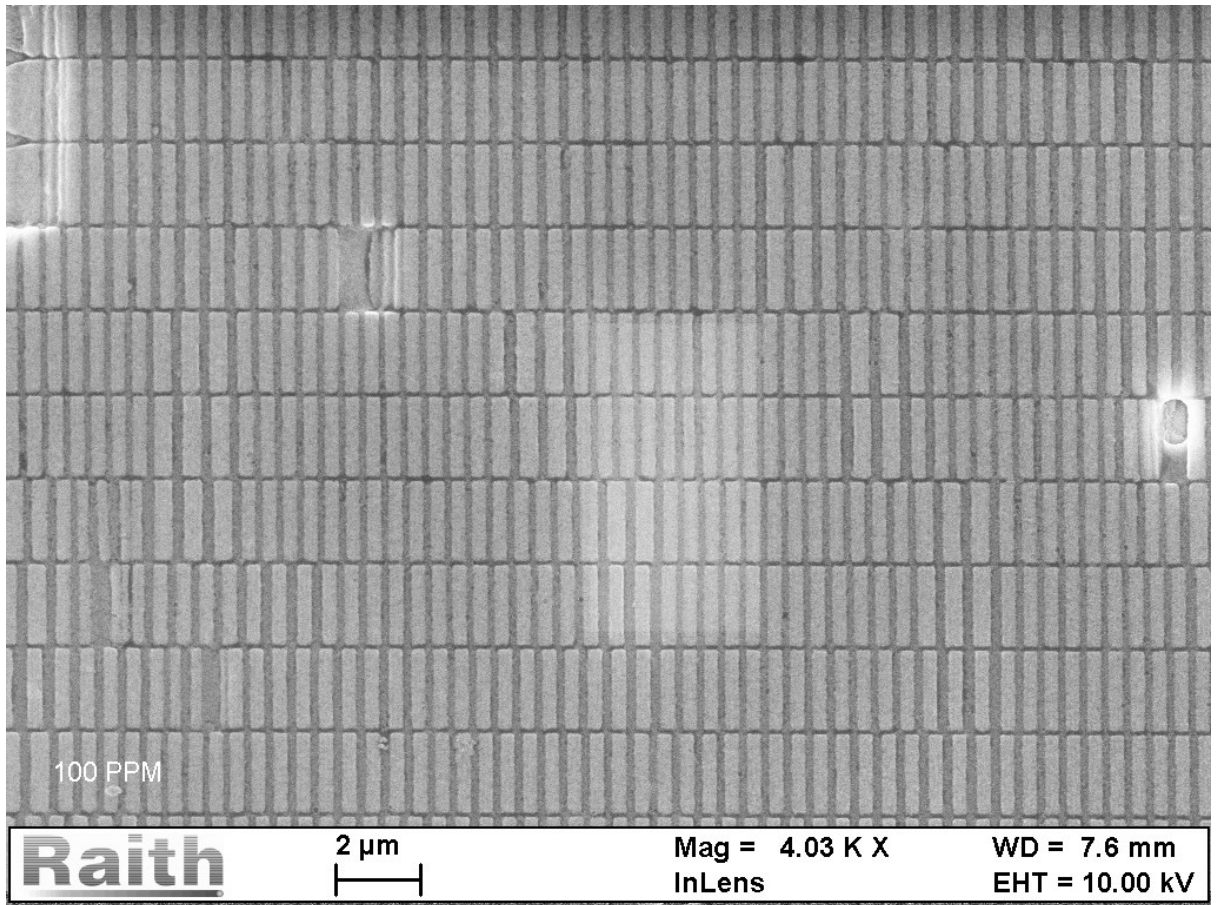
Figure 6.8.Scanning Electron Micrograph of the pulse modulated reflection grating.

Figure 6.8 above is a SEM image of the high frequency modulated grating producing the output described above and shown below. Once again the reduction in efficiency is due to a combination of pulse height errors, fabrication errors in which the pulses are separated as well as lateral translation errors.

	Normal Incidence	Bragg Angle
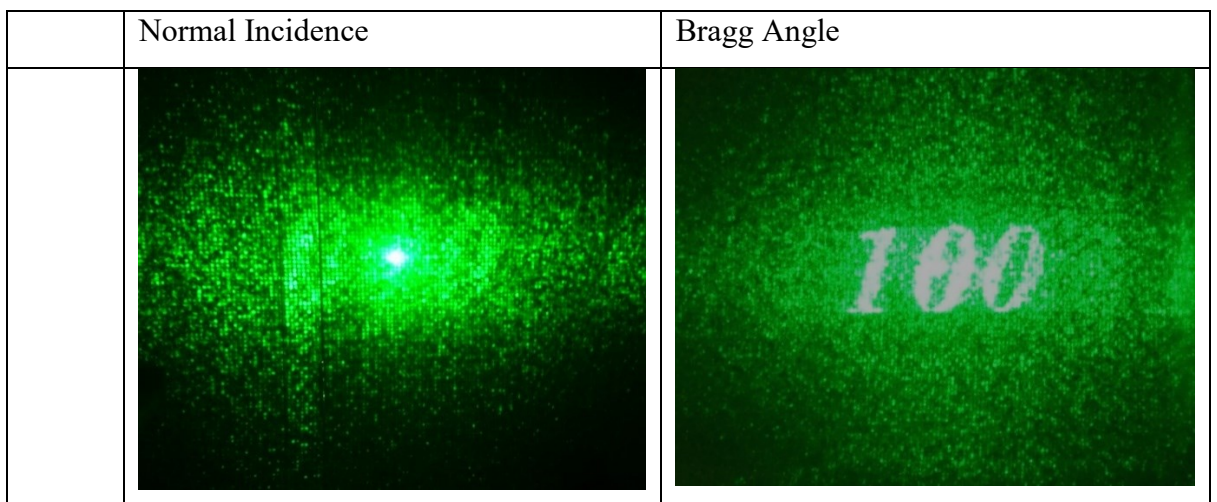
Figure6.9. Comparison between the optical outputs at normal incidence and the the Bragg angle.

Apart from the trial in which the phase pattern consists of simple numericals, a more complicated line art drawing was also tested. *Figure 6.10* below is a SEM micrograph of the modulated high frequency grating producing the optical output of the line art.
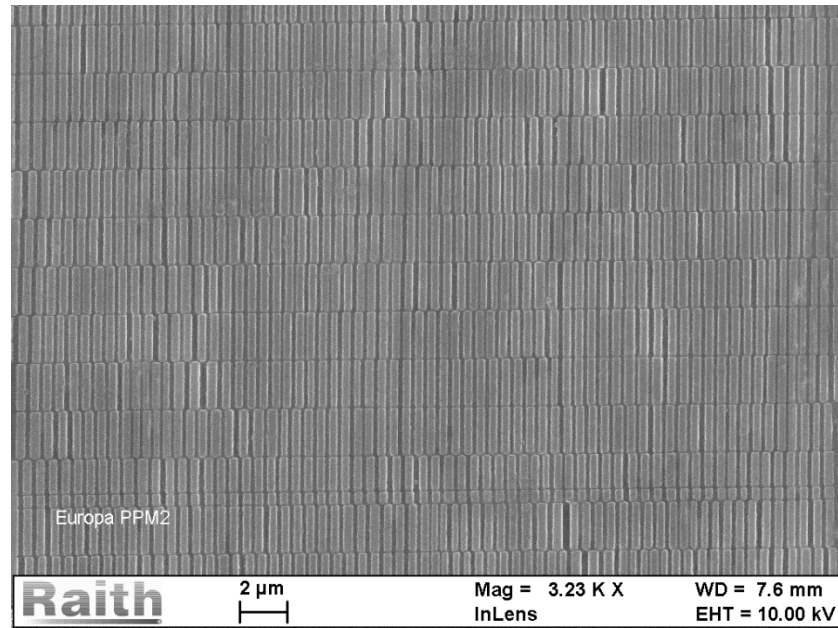
Figure 6.10.Scanning Electron Micrograph of the pulse modulated transmission grating.

Figure 6.11 below is the image produced at an incidence angle of 31° with a diffraction efficiency of 70% of the line art.
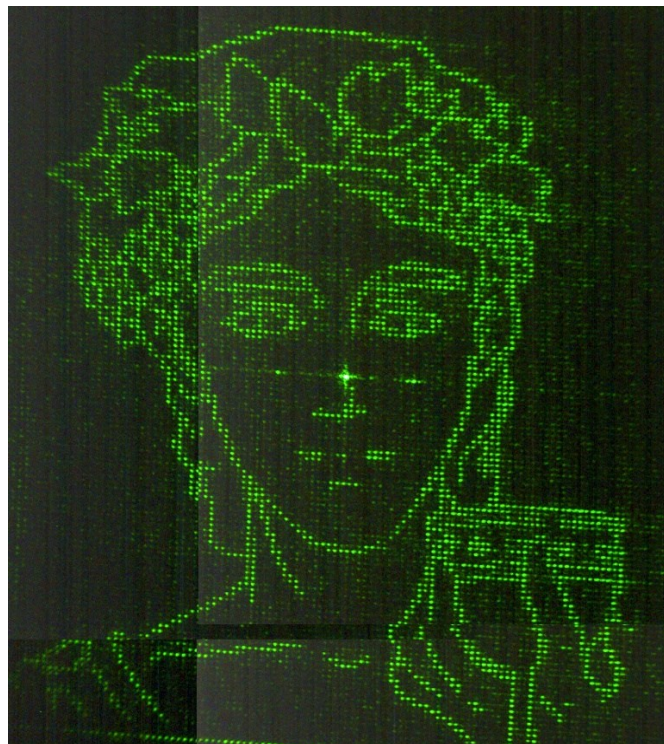
Figure 6.11. Optical output from the -1st diffraction order produced by illuminating the grating at the Bragg incidence angle and projected on a screen.

6.6. Conclusions

In conclusion, in this chapter high frequency carrier gratings were encoded with three different two dimensional signals. Elements have been fabricated for 532nm operation with and diffraction efficiency of 70% for transmission and reflection operation which could double up as a hard shim for the replication process. The generalised process for encoding the carrier grating was described. An investigation into the effects that achievable grating geometries through the advancements in fabrication techniques have on both the diffraction efficiency and angle of incidence of the gratings. The phase depth mismatch due to fabrications and replication errors commonly encountered with deep multilevel DPE (described in Chapter 7) have been solved by having a shallower etch depth of the elements, the zeroth order scattering is minimised by locating the image in the -1st order, producing diffracted images with a high fidelity as well as the addition of an extra degree of security through the operation of the element at the Bragg angle of incidence. The added value of the work described in this chapter comes from the development of much more complex diffraction patterns in comparison to previously reported work in the field, accredited to both the improvements in the fabrication of the devices with regards to attainable feature sizes and fabrication accuracy.

6.7. References

[1]   H. Duan, V. R. Manfrinato, J. K. W. Yang, D. Winston, B. M. Cord, and K. K. Berggren, "Metrology for electron-beam lithography and resist contrast at the sub-10 nm scale," *J. Vac. Sci. Technol. B Microelectron. Nanom. Struct.*, vol. 28, p. C6H11, 2010.

[2]   J. Turunen, P. Blair, J. M. Miller, M. R. Taghizadeh, and E. Noponen, "Bragg Holograms With Binary Synthetic Surface-Relief Profile," *Opt. Lett.*, vol. 18, no. 12, pp. 1022–1024, 1993.

[3]   P. Blair, M. R. Taghizadeh, W. Parkes, and C. D. W. Wilkinson, "High-efficiency binary fan-out gratings by modulation of a high-frequency carrier grating," *Appl. Opt.*, vol. 34, no. 14, p. 2406, 1995.

[4]   W. Stork, N. Streibl, H. Haidner, and P. Kipfer, "Artificial distributed-index media fabricated by zero-order gratings.," *Opt. Lett.*, vol. 16, no. 24, pp. 1921–3, 1991.

[5]   M. W. Farn, "Binary gratings with increased efficiency.," *Appl. Opt.*, vol. 31, no. 22, pp. 4453–4458, 1992.

[6]   A. Vasara *et al.*, "Binary surface-relief gratings for array illumination in digital optics.," *Appl. Opt.*, vol. 31 17, pp. 3320–3336, 1992.

[7]   R. Petit and M. Cadilhac, "Electromagnetic theory of gratings: some advances and some comments on the use of the operator formalism: errata," *J. Opt. Soc. Am. A*, vol. 8, no. 3, p. 596, 1991.

Chapter 7. Novel Polymer Based Diffractive Optical Elements for Anti-Counterfeiting Applications.

7.1. Introduction

Diffractive phase elements are high efficiency optical devices that have numerous applications but are mainly used for the manipulation of the far field intensity pattern of laser beams.

They are made up of multilevel micron scale features etched or imprinted into an optically transmissive substrate for operational wavelengths ranging from the Ultra–Violet to the Infra-Red. There are numerous classes of diffractive phase elements, but the class under consideration is pattern formation elements, which are periodic far field elements capable of generating intensity patterns made up of many diffraction orders. The large number of diffraction orders can be accurately manipulated by these elements to form complex patterns.

A major disadvantage associated with pattern formation elements is the single operational wavelength. Illumination with a different wavelength other than the specified one will result in a reduction of the diffraction efficiency, an increase in the zeroth order as well as a distortion of the image.

Two colour diffractive phase elements phase elements have been used in a variety of applications ranging from laser displays[1], spectroscopy[2], medical applications where one of the wavelengths is used for alignment and the second for incision, Their application for the purpose in this thesis is in security printing.

The design process used for the formation of the two coloured diffractive phase elements is based on the iterative Fourier transform algorithm (IFTA)[3]. This approach helps with the reduction of the quantisation errors arising from the use of a limited number of discrete phase levels in the optical element. The phase delay from a diffractive phase structure is given by;

$$\phi = 2\pi(n_\lambda - 1)\frac{h}{\lambda} \tag{7.1}$$

Where n is the refractive index as a function of wavelength, h is the height of the structure and λ is the operating wavelength.

An alteration in the input wavelength to a new value will alter the associated phase delay of the structure by an amount proportional to the ratio of the two desired wavelengths. The resulting change being linear, a surface profile cannot be built up that produces a phase profile for one wavelength and a different one for the second wavelength. Therefore the phase profiles for the two illumination wavelengths are constrained to each other by the physical dimensions of the structure.

An approach to solving this problem would be going to deeper surface relief structures previously demonstrated by Noach et al[4]. Deep surface relief structures represent phase delays greater than 2π for the specified wavelength. Increasing the height of the surface relief structure by an amount of 2π phase delay for the first illumination wavelength has no effect on the effective total phase delay. A further increase in the height alters the phase delay for the second wavelength, as the phase difference does not represent 2π. Meaning that the deep structures do not constrain the phase profile for the new wavelength as the shallow ones do. 2π blocks are added to the structure until the phase profile for the first wavelength reaches close to the desired effective phase profile for the second wavelength.

The benefits of going to deeper structures (up to 8π) come in the form of increments in the diffraction efficiencies for the images in both colours, reduction of quantisation noise and reduction of non-uniformity.

In this chapter of the thesis, a systematic study of pattern formation elements designed for operation under illumination by both one and two wavelengths is carried out. The single coloured elements are designed for illumination by 532nm and have 8 phase levels, while the two coloured elements are designed for illumination by 450nm and 650nm and have 16 phase levels. The images produced are a lot more appealing to the eye in two colours when compared to their single colour counterparts. An outline of the embossing process used for the mass replication of these elements will be presented, limitations of depth in the final embossed surface profiles as well as an analysis of the overall effect of the replication process dependence into the major sources of both lateral and transverse feature shrinkage during replication. The necessary compensation for the replication of the surface relief profiles making up the DOEs is developed to account for the shrinkage and a thorough investigation into the planarization through the use of polymer based overcoats is demonstrated. The effects that the fill factor, refractive index difference and surface roughness of the overcoats have on the final far field intensity patterns is also shown.

7.2. Security Printing

Security printing is a field of industrial printing which deals with the printing of passports, cheques, identity cards and banknotes. It is mainly aimed at preventing forgery, tampering and counterfeiting. In recent times, with many of the techniques used being made more readily available, the need for incorporating newer and more sophisticated security platforms has emerged.

The most common bank notes nowadays are made from heavy paper cotton fibres to ensure strength and durability. The American dollar for example has additional special fibres (coloured forensics) enhance security.

Countries with a high level of humidity and adverse weather conditions have switched to using polymer (plastic banknotes) with the aim of increasing the circulation life time between batches with the inclusion of a clear transparent window (of the order of a few square mm's) as an additional security feature, making it especially difficult to reproduce using conventional counterfeiting techniques. The environmental conditions are not the only driving factor behind the switch, because the United Kingdom has also introduced them to incorporate additional security features.

The first set of polymer bank notes were printed by the Bank of Australia in 1988[5] using polypropylene polymers. These notes incorporated a diffractively optical variable device of Capt. James Cook in the clear aforementioned transparent window.

Figure 7. 1. A picture of the first bank note made entirely from polymer produced by the bank of Australia with a picture of James Cook [21].

This is seen on the top right corner of the note from *Figure 7. 1*, which is an iridescent image exhibiting various optical effects such as movement or colour changes. These cannot be photocopied or scanned, neither can they be accurately and precisely reproduced and replicated. They are fabricated through a combination of printing and embossing. Problems did exist with the first set of bank notes issued with the security holographic feature detaching from the note.

Twenty seven countries in the world have switched from paper to printing in polymer as a testament to the security and ecological benefits from polymer notes[6].

Some of the advantages of using polymer banknotes include;

- Being more environmentally friendly, because of their long lasting nature.
- Less energy being used in the printing process and transportation as well as recycling the notes at the end of their lifetime into newer polymer plastic products.
- They are also inherently waterproof.

Better security features, like single coloured diffractive optical elements as seen in the 50 pesos note from the bank of Mexico which has shown a remarkable drop in counterfeiting rates to about <<0.1% in 2015.

Figure 7. 2. A picture of the first polymer banknote incorporated with a diffractive phase element released by the bank of Mexico. The image on the right is the optical output produced from the diffractive phase element illuminated by white light as viewed by the human eye[22].

Upon illuminating the clear transparent window outlined by the wing of the butterfly in the top right corner of the banknote with a white light source, a projection of the 50 numerical can be observed, this can be seen in *Figure 7. 2*.

Strength being the last advantage, the polymer notes are expected to last at least 2.5 times longer than the current paper bank notes and they can also withstand repeated folding in wallets and crunching in pockets.

7.3. Mass Replication Techniques of Photonic devices in industry

Imprint lithography is a well-developed mass fabrication technique which has a high throughput, low cost and high resolution capabilities. Through the formation of a 3 dimensional pattern in a polymer, achieved by the mechanical displacement of the material a wide range of applications for patterning of polymers becomes possible.

The polymer patterns are generate through the moulding of a viscous material and fixing it in place by UV curing or cooling. In comparison to photolithography where the photo resist undergoes a selective chemical modification through exposure and development. This technique, which was first pioneered in the 1970's, is capable of replicating structures well into the nm regions. The surface topologies can be replicated with a high fidelity and the smallest demonstrated features are 5nm lines on a pitch of 14nm replicated by nano imprinting[7]. There are two imprinting processes.

7.3.1. Hot Embossing

Hot embossing or thermoplastic moulding, first developed in the early 1960's[8], is the first process. This process has the advantage that the viscosity of the material used can be altered to a large extent by thermal heating. The first step is the fabrication of a master, the masters used are fabricated in fused silica through a multi-step mask and etch photolithographic process. Next comes the formation of the shim which is a negative copy of the surface relief profile in the fused silica master. The shims are usually made out of metals such as nickel. The moulding of the thin film by using the shim is carried out next. The thermoplastic film is first softened through heating, and shaped to the desired phase profile by the application of pressure on the shim. The pressures used are of the order of 80kPa which forces the polymer to fill the cavities of the shim, conforming to the surface relief profile of the shim. Once the cavities are filled, the temperature is lowered in order to set the film while the pressure is still applied, hence setting it to the desired profile. Once fully set the polymer film is then demoulded from the shim. An outline of this process is shown in *Figure 7. 3* below.
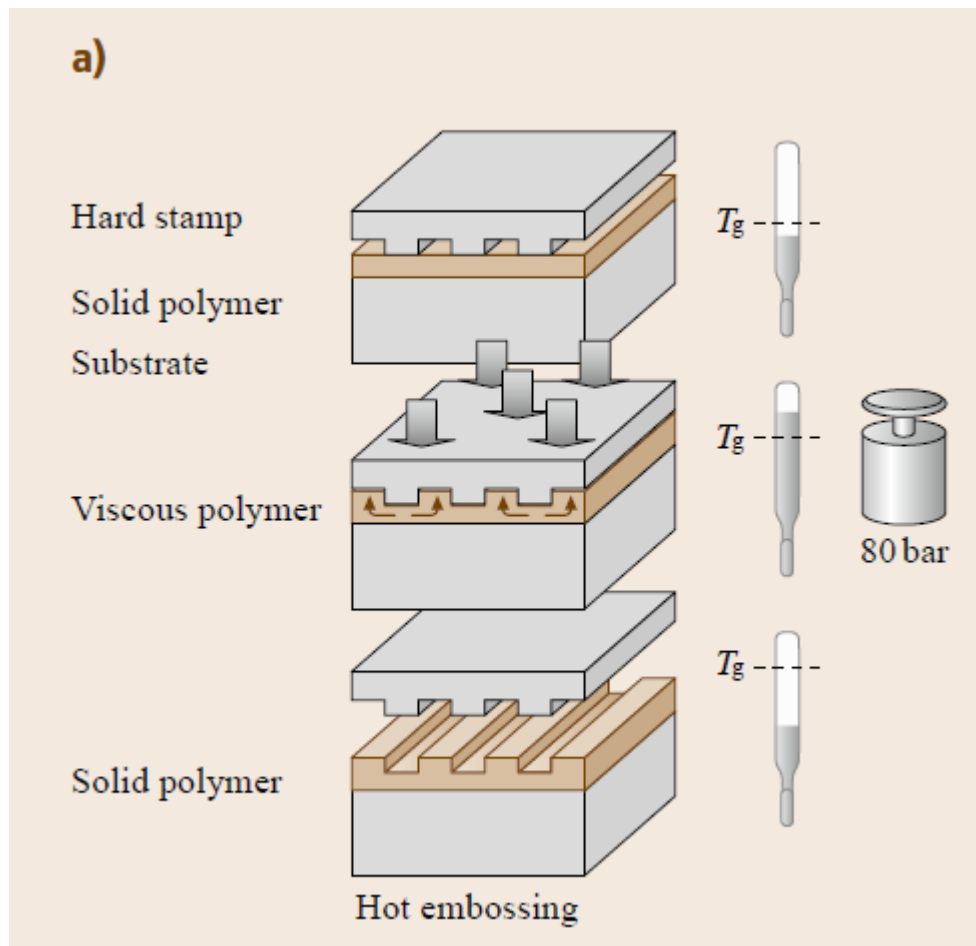
Figure 7. 3. Schematic of the workflow used in thermal Nano imprint lithography (Hot Embossing)[23].

7.3.2. UV Embossing

The second imprinting process is UV moulding[9]. In this process unlike hot embossing the polymer thin film is kept at room temperature and moulded to the desired profile at much lower pressures of the order of 1kPa , or even just through capillary action. In most cases the polymers are transparent in the UV–Visible range. The fabrication steps are outlined in the previous section and are shared between the two processes. On exposing the transparent polymer to UV illumination it gets cross-linked and hardened. The shims used must be kept at a constant distance from the base polymer for setting in place due to the low viscosity. This is the process used in the replication of the diffractive phase elements in this thesis. A schematic of this imprinting process is shown in *Figure 7. 4* below.
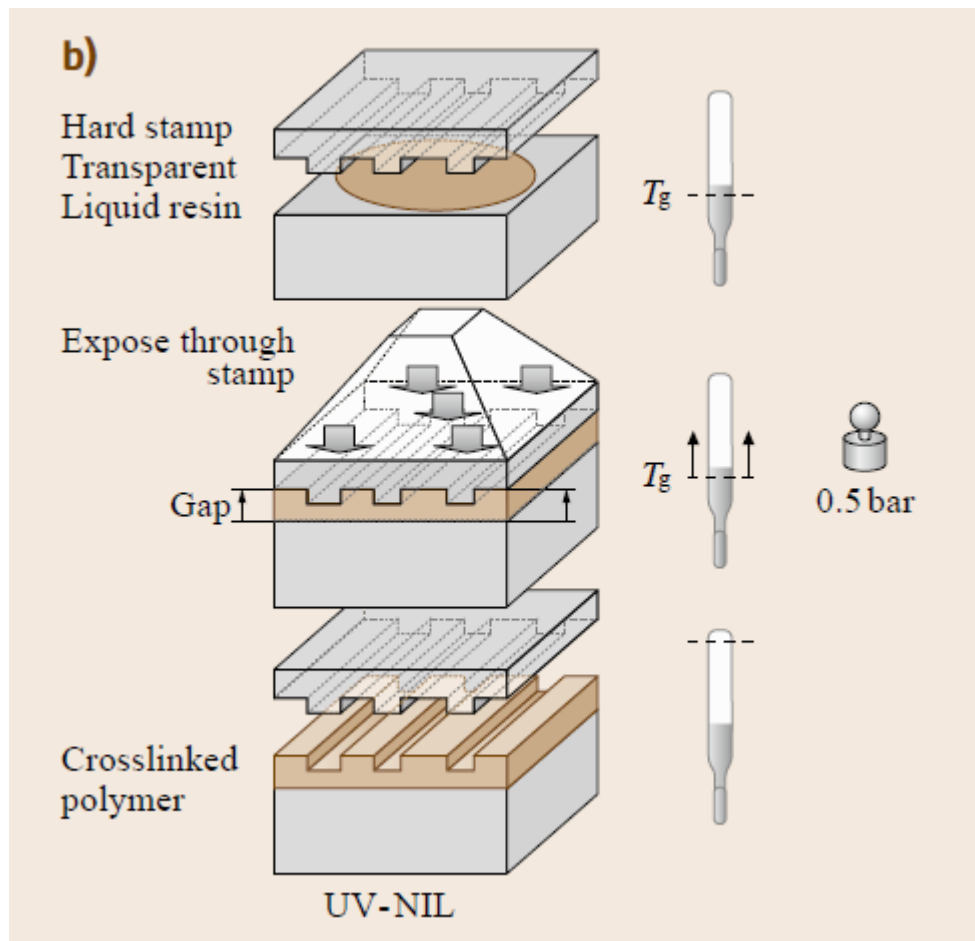
Figure 7. 4.Schematic of the workflow used in UV Nano imprint lithography (UV Embossing)[23].

7.4. Process Work Flow

The replication process starts with the design and fabrication of a fused silica glass master. This glass master is then made into a metallic flexible shim[10], which is a negative copy of the surface relief profile of the glass master, the negative fused silica masters are designed for replication onto polymer at this stage. The shim copy then gets copied once again inverting the surface relief profile into the mother copy, the positive fused silica masters are designed for replication onto the polymer at this stage.

The shim and mother are made by electroplating copies of the glass master. This process is carried out by first depositing a 5nm adhesion layer of either titanium or nickel, masters then get moved into an electroplating bath where the rest of the nickel layer conforming to the outlines of the surface relief profile of the glass masters is deposited. Once the electroplating has been successfully completed, the metallic moulds of the imprinted surface are recombined with a flexible metal base. Depending on the extent of this process

the structures in the surface relief profile can either shrink or extend in size which is based on the thermal expansion coefficient of the metal used.
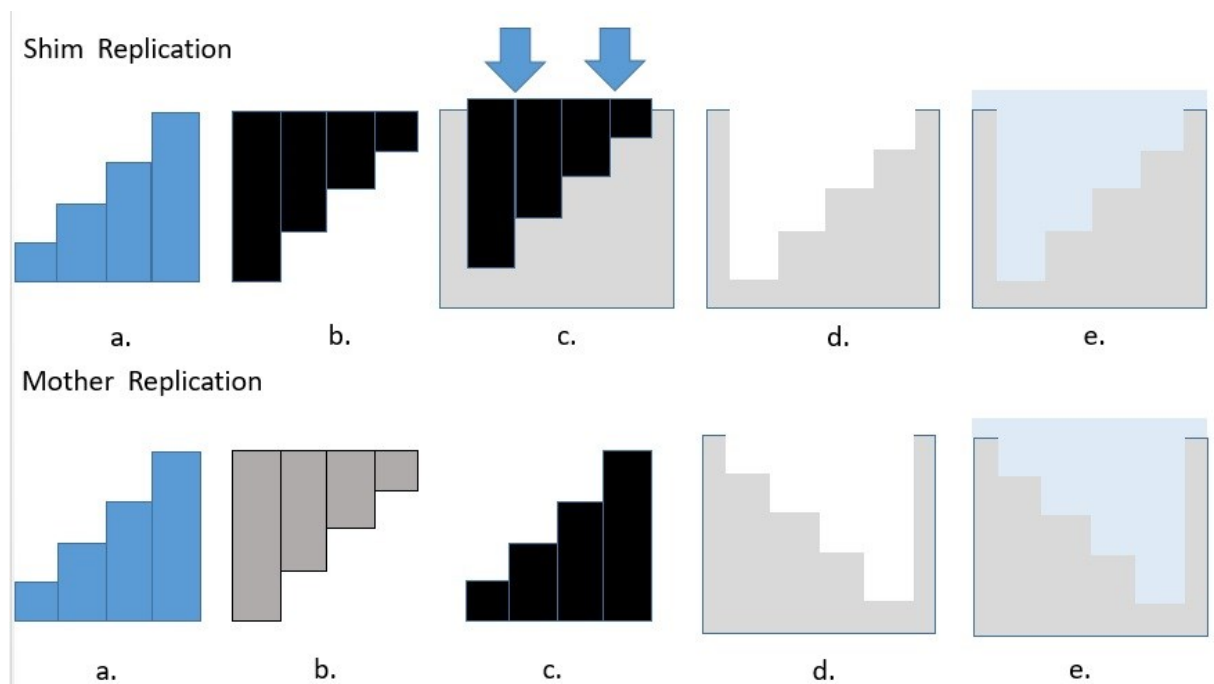

Figure 7. 5. Process workflow showing the different stages involved in the replication process for copying from the Shim (TOP) and copying from the Mother (BOTTOM).

The metallic shim or mother copies of the fused silica masters are then pressed onto the polymer and the polymer conforms to the relief of the shim/mother, which is then fixed in place by illumination by UV. Because UV curing involves a change in the physical conformation of the polymer[11], the process is always associated with a volumetric shrinkage of the polymer. The base polymer used in this thesis is a biaxially orientated polypropylene[12] which has a refractive index of ~1.54. The shim/mother then needs to get demoulded from the moulded polymer copy. When fully moulded the thickness profile imprinted on the polymer has an inverse in polarity of the shim/mother. This process is carried out in the frozen/set state[13]. There are a few conditions which are required for a clean release of the polymer copy from the shim copy: the side walls on the surface relief have to be vertical for a demould without distortions[14], the shim needs to be prepared with an adequate anti adhesive in order to reduce the Van der Waals forces[15] and hydrogen bridges in the polymer and no high aspect ratio structures should be used because they make the polymer more prone to ripping[16].

The over coating polymer which has a higher refractive index when compared to the base polymer is then spray coated onto the replicated polymer copies with the aim of

planarizing the final DOE. A systematic outline of the above mentioned work flow can be seen from *Figure 7. 5*.

7.5. Diffractive Optical Element Design.

The phase profiles of the two colour diffractive optical elements used in thesis were generated by Dr. Andrew Waddie. The element are made up of periodic (768 µm), 128x128 pixels multilevel (16 Phase Levels, minimum feature sizes of 6µm and 8 µm with a designed maximum etch depth of 3750nm. The phase profiles can be seen from the images below.
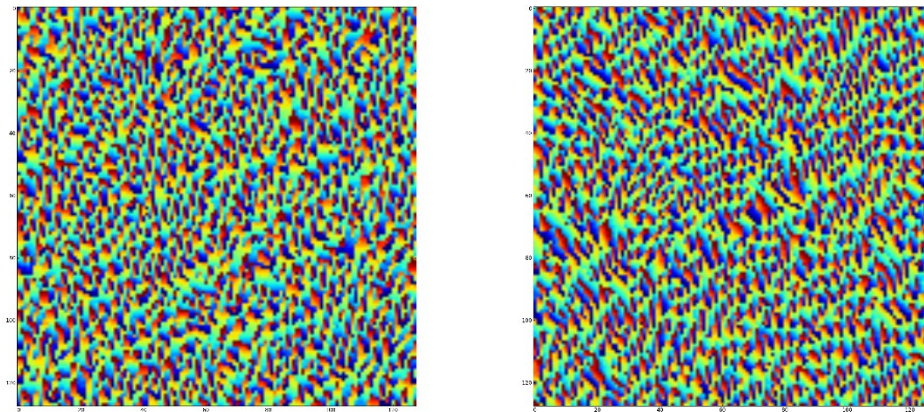

Figure7. 6. Computed phase profiles using IFTA algorithm

The designed operating wavelengths are 450nm and 650nm and the expected optical outputs at those wavelengths generated by the IFTA algorithm are shown below for the two colours.
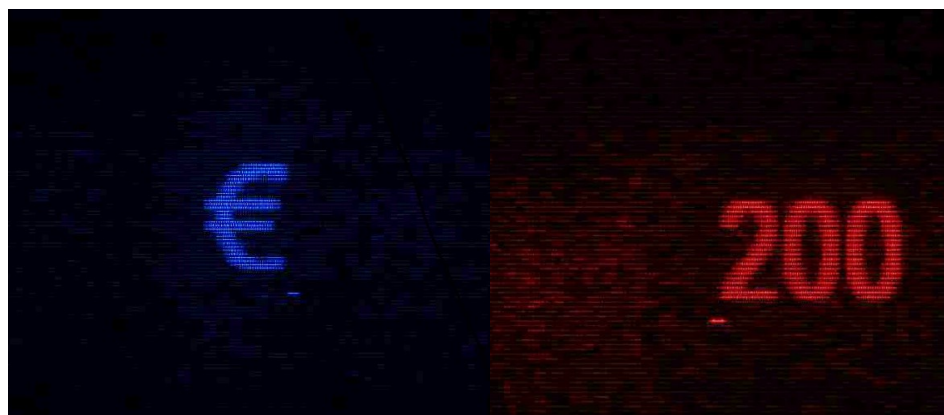

Figure7. 7. Computer Optical output for 450nm illumination (Left) and 650nm illumination (Right).

7.6. Characterisation of Polymer Shrinkage during Replication

The rationale behind the work carried out on the shrinkage occurring during replication from the fused silica master to the polymer copies comes from the deviation experienced in the desired phase profile of the DOE. Shrinkages in the surface relief profile of the replicated profiles result in changes to the phase profile of the DOE leading to deterioration in image sharpness, reduction in diffraction efficiency, increased cross talk and increase in the zeroth order scattering. The thermal and volumetric changes[17] that take place during the formation of the metallic shim as well as during moulding of the polymer introduce a degree of shrinkage to the final replicated relief profiles when compared to the fused silica glass masters. A corner which is easily identifiable is picked on the glass masters and line scans of the surface relief profile of the first 10 rows are carried out. The measurements are carried out using a Zygo white light interferometer and the measurements are made at a 40µm bilateral scan speed. The same corner measured on the fused silica master is then measured on the shim and mother metallic copies used for replication. The vertical height of each feature on the master in a 50µm long scan is measured and compared the same feature on the shim, master, and respective polymer copies of each. The heights are then allocated bin spaces with a 250nm between constituting the individual levels of the DOE. The largest amount of shrinkage during the replication process occurs at the shim stage. *Figure 7. 6* below shows the shrinkage grouped as function of DOE level for the shim copy. The graph on the left is a comparison between an uncompensated fused silica master and its shim counterpart while the graph on the right is that for a compensated counterpart. The application of a linear fit produces an average value across the levels which stands at about 18% feature height reduction. But in terms of shrinkage in respect to etch level, the shallower levels show larger amounts of shrinkage when compared to the deeper ones. Levels 1-4 stand at ~35 %, 5-9 at ~ 28 %, 9-12 at ~ 20% and 13-16 at ~14%, exhibiting a non-linear behaviour. From the graphs below, B1 refers to an uncompensated polymer copy and B2 is the compensated polymer copy. V2 are polymer copies from the mother and V4 are polymer copies from the shim.
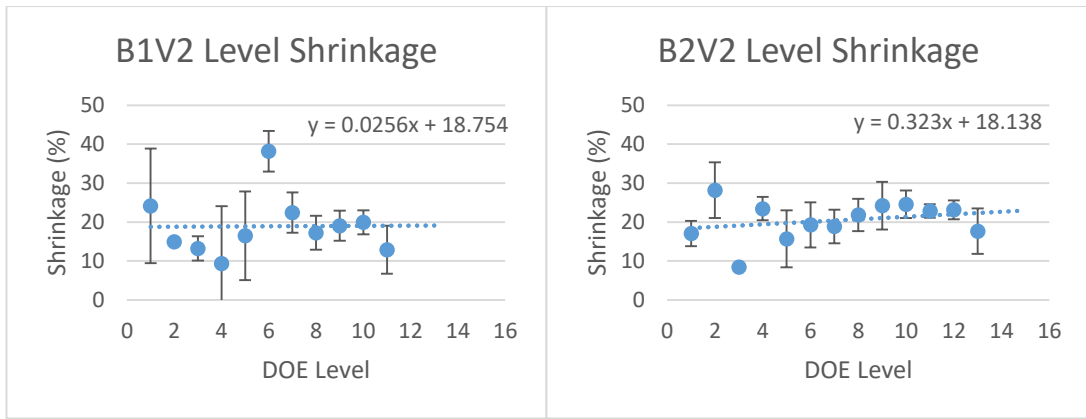
Figure 7. 6. Measured shrinkage in polymer based replicated elements for copies made by embossing with the Mother. The shrinkage is grouped according to phase levels. The graph on the left shows the uncompensated copy and the graph on the right shows the precompensated copy.

Figure 7. 7 below show the shrinkage grouped as function of DOE level for the mother copy. The graph on the left is a comparison between an uncompensated Fused Silica master and its mother counterpart while the graph on the right is that for a compensated counterpart. The application of a linear fit produces an average value across the levels which stands at about 21% feature height reduction. But in terms shrinkage in respect to etch level, the shallower levels show larger amounts of shrinkage when compared to the deeper ones. Levels 1-4 stand at ~45 %, 5-9 at ~ 35 %, 9-12 at ~ 25% and 13-16 at ~19%, also exhibiting a non-linear behaviour.
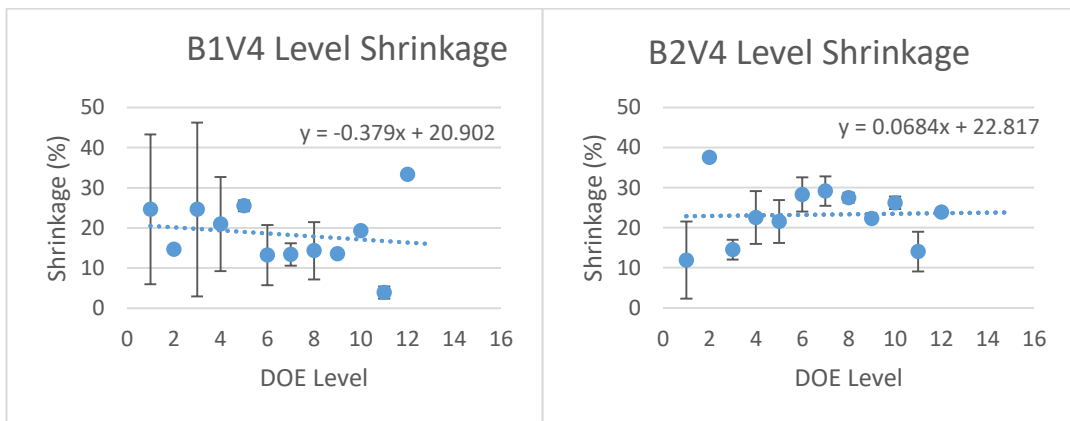

Figure 7. 7.Measured shrinkage in polymer based replicated elements for copies made by embossing with the Shim. The shrinkage is grouped according to phase levels. The graph on the left shows the uncompensated copy and the graph on the right shows the precompensated copy.

The shrinkage occurring during the replication between shim and polymer copy is of the order of 20nm uniformly occurring across all the levels, whilst that for mother and

145

polymer copy is of the order of 40nm occurring across all the levels. With the largest difference being feature height dependent, across the DOE levels in the shim.

The shrinkage does not only occur in the lateral dimension, it is also present in the transverse. The shim copy is identical to the fused silica master in width and breadth but the polymer shim copy shows a shrinkage of 0.2µm in each and the polymer mother copy shows a shrinkage of 0.4µm.
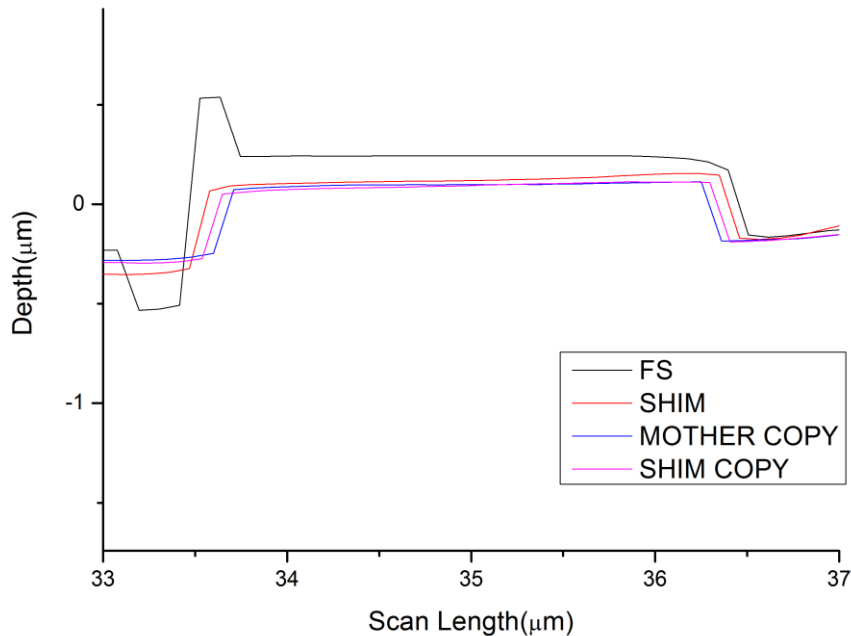

Figure 7. 8. A feature showing the transverse shrinkage occurring during replication between the Shim, the Shim copy and the Mother Copy.

The line scan from ***Figure 7. 9*** shows a comparison of the same feature as replicated from the shim to polymer shim copy and the mother shim copy. The transverse dimensional shrinkage occurring has a less detrimental effect on the optical output at close viewing distances such as those as observed by the human eye. The effect becomes more prominent at longer projection distances where the diffracted image will be projected at a wider projection angle. The lateral shrinkage has a much greater impact on the optical performance, which will be blue shifted as the surface relief profile becomes shallower. There will be more observable zeroth order as well a reduction in the diffraction efficiency of the diffraction orders.
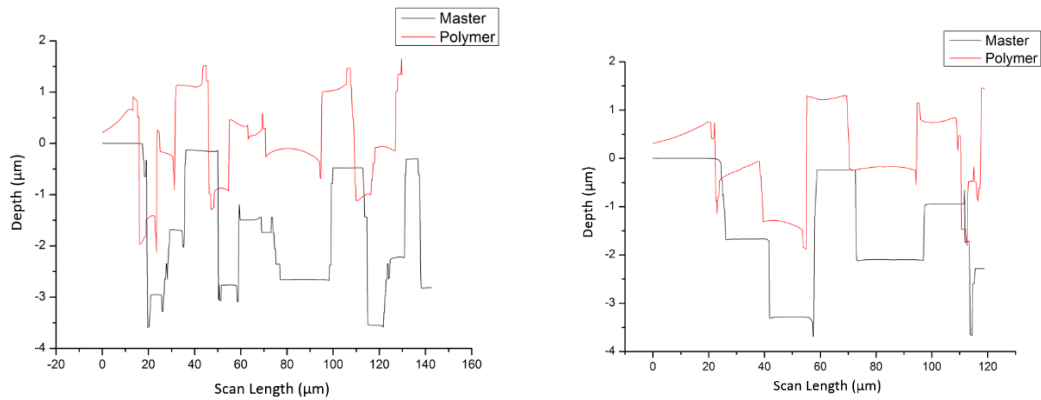
Figure 7. 9. Line scans comparing the surface profile between the fused silica master and a polymer copy replicated using the mother (LEFT) and using the shim (RIGHT).

Figure 7. 9 above show a comparison between the fused silica master and the respective polymer shim copy and polymer mother copy. Apart from the measured reduced shrinkage in the shim copy (~3%) due to 1 less replication step when compared to the mother copy, the surface relief profile of the geometry is less conformal to the shim. The curving at the bottom of the trenches can be explained by either a ripping effect in when the polymer is ripped from the substrate or relaxation of frozen strain both of which are common during demoulding from shim and the formation of rims at the top of the features which is inherent to processes using rollers (speed of process). These could all be associated as sources of noise, scatter, zeroth order contributions, reduction in efficiency, operational colour shifts as well as twin imaging. The polymer shim copy on the other hand is much cleaner and more conformal to the master, also expressed in the form of an improved optical output.

7.7. Development of a Compensation Techniques for Application to Polymer Replication

Having identified the source of shrinkage (volumetric contraction) in the replication process and proving a quantifiable estimate of the amount of shrinkage from the previous section, the development of a technique to account for the shrinkage and compensate it was developed. Observing that the shim polymer copies show 3% less shrinkage comparing to the mother copies, as well as observing that the shallower levels exhibit more shrinkage than the deeper ones. In principle the shallower levels of the DOE control the clarity of the image and the deeper levels control the efficiency. Two compensation techniques were developed and tested.

147

7.7.1. Linear Compensation

The first compensation technique is designed to precompensate for the shrinkage in the polymer by applying the average level of shrinkage measured across all the etched phase levels. For the shim polymer copies it was observed that the average shrinkage across the levels stands between about 18% and 21% for the master polymer copies. For the positive elements to be replicated from the mother, all the etch levels are over etched by about 20%. For the negative elements to be replicated from the shim copy it was observed that the deeper levels have a shrinkage of about 12 %, hence over etching the phase levels by 12%.

From **Figure 7. 10** below, the 20% pre compensated fused silica master is compared to the uncompensated master. Line scans of the first 10 rows are carried out using the Zygo white light interferometer and the feature heights in the former and latter directly compared. They are then binned in accordance to etch level. The x axis indicates the actual etch depth and the y axis shows the percentage over etch. It can be seen that the first 8 levels are clustered together at a maximum of about 17 % and the second 8 at a maximum of about 19%. There are a few points that do not agree with the general trend and can be deemed as outliers. The reasons for these outliers could be spurious measurements and dust particles on the sample as well as fabrication errors.
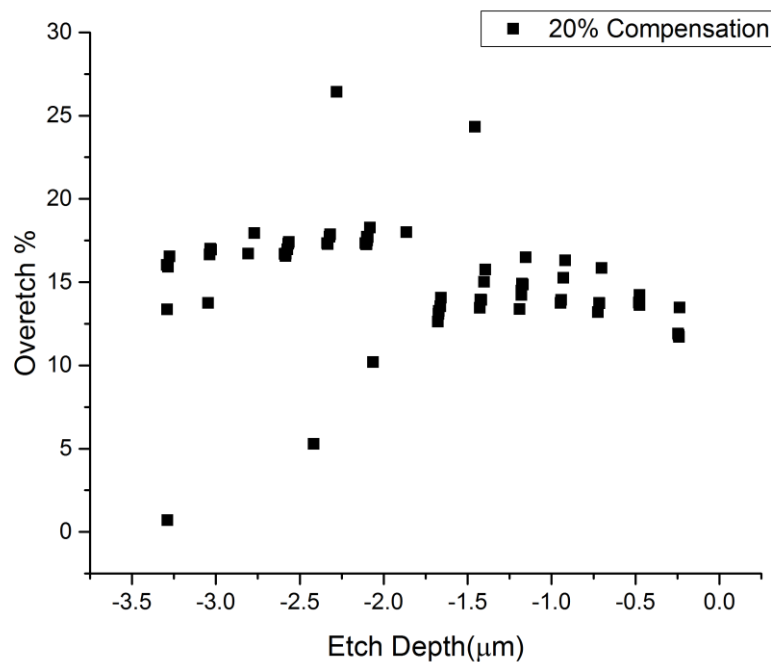
Figure 7. 10. Comparison between the uncompensated fused silica master and the linearly compensated fused silica master showing the percentage over etch as a function of etch depth.

7.7.2. Non- Linear Compensation

The second compensation technique is designed to pre compensate for the shrinkage in the polymer by applying the shrinkage values averaged out across the levels grouped in sets of 4 (Therefore phase levels 0-3, 4-7, 8-11 and 12-15). The difference in lateral feature shrinkage between shim copy and master is still accounted for and stands at 3%. From the shim polymer copies which are replicated from the negative master a compensation of 40%, 29%, 19%, 14% is applied hence once again over etching each of the levels by those amounts. For the mother polymer copies which are replicated from the positive master a compensation of 45%, 35%, 26% and 19 % is applied and the levels are over etched by those amounts. From the *Figure 7. 11* below, the non-linear precompensated positive fused silica master is compared to the uncompensated master. Line scans of the first 10 rows are carried out using the Zygo white light interferometer and the feature heights in the former and latter directly compared. They are then binned in accordance to etch level. The x axis indicates the actual etch depth and the y axis shows the percentage over etch. The shallower levels stand at about 30% and the deeper levels at about 10%. The clustering as a function of etch level can be observed from this graph as well.
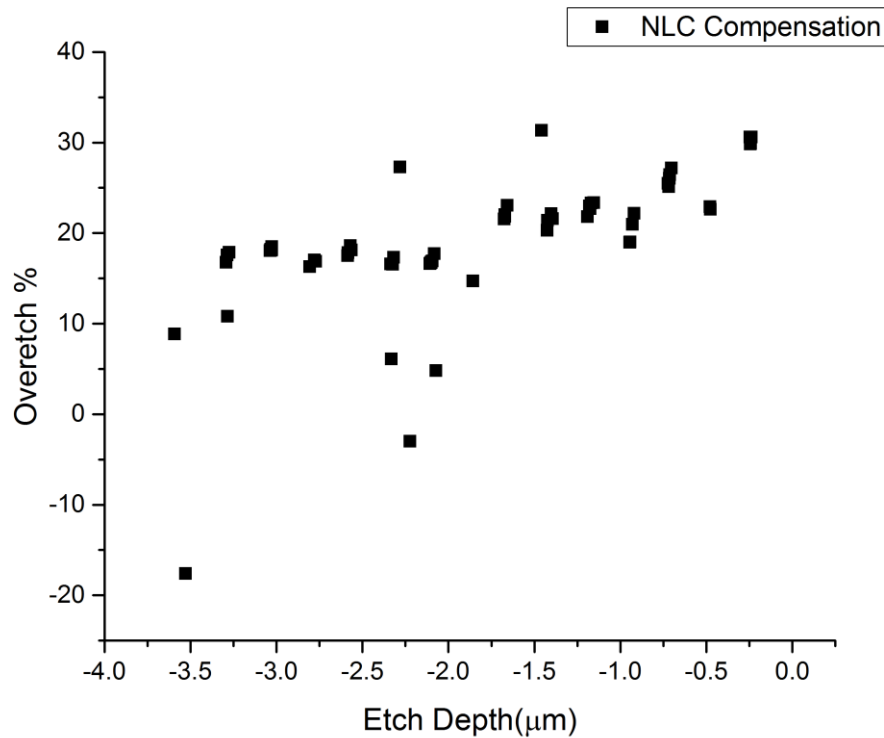
Figure 7. 11. Comparison between the uncompensated fused silica master and the non-linearly compensated fused silica master showing the percentage over etch as a function of etch depth.

7.8.   Fabrication of Single Colour Multilevel Elements for Replication

To carry out a proof of concept a single coloured diffractive phase element was designed and fabricated for replication into the polymer with an operational wavelength set to 532nm. The design process for single coloured elements make use of the Gerchberg Saxton algorithm which is capable of producing diffraction efficiencies of the order of 80%[18].

Through the application of a thin, transparent overcoat the surface relief profile of the DPE can be planarised, providing an obstacle for further replication in counterfeiting. The effects such as refractive index difference, fill factor and film scattering have on the final optical output of the device have will be looked at in depth further in the thesis.

Element A is a positive 8 level element with 8μm feature sizes. The element is uncompensated. This element is designed for replication with the mother. In this design

the position of the zeroth order is placed between rights in the middle of the diffraction pattern.

Level	Etch Target (nm)	Etch Actual (nm)	% Over Etch
1	255	253	-0.57
2	509	547	7.5
3	1019	1012	-0.69
Total	1783	1812	0.02

In *Figure 7. 12* photographs are taken from the optical outputs of the replicated element. On the left hand side is a photograph of the element without an overcoat and the presence of the zeroth order is indicative of a shrinkage causing the detuning of the phase profiles from the specified operational wavelength. On the right hand side is the same element with an overcoat applied to it, there is a significant increase in the zeroth order scatter as well as a drop in the diffraction efficiency, which is accredited to the combination of both replication shrinkage and the partial filling in the overcoat. But the element does produce an optical output and the proof of concept can be deemed successful.

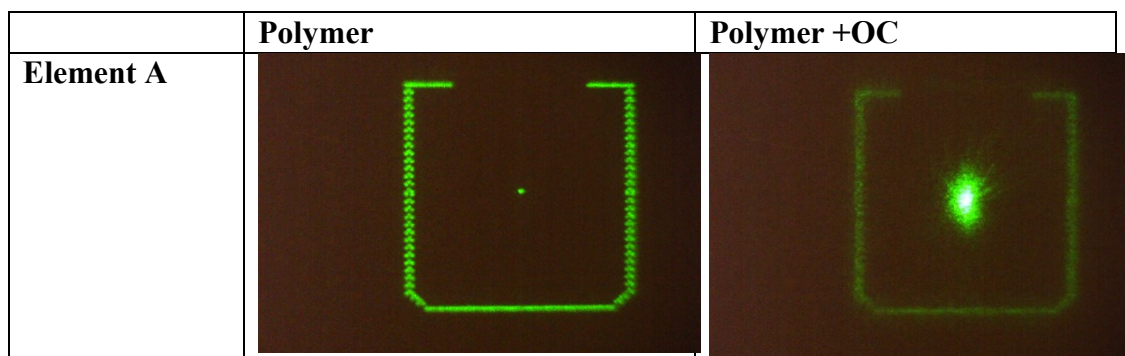|	**Polymer**	**Polymer +OC**
Element A		

Figure 7. 12. Optical output from a 8 level single coloured diffractive optical element replicated on a polymer designed for illumination with 532nm, the image on the left is the output from an uncoated element and the image on the right is from an over coated element showing a significant deterioration due to scattering.

7.9.   Fabrication of Two Colour Multilevel Elements for Replication

In general the fabrication of the fused silica masters is carried out using a multistep, mask and etch photolithographic process. This process should not be carried out on surface

relief profiles with more than 16 phase levels due to tolerances in terms of mask alignment. The alignment between mask levels has been shown to have the biggest impact on the optical performance of the diffractive phase elements[19], because the errors are cumulative and lead to degradation in the output with every additional level. Furthermore, the fabrication of deep multistructures using photolithography becomes challenging in terms of aspect ratios of the resists used as well as the limitations imposed by the replication process.

The conditions that must be satisfied are that the overall etch depths have to be kept under 5 μm because the production line facilities are incapable or replicating structures deeper than that and that the master have to be no more than 16 levels in order to keep the fabrications errors to a minimum. An issue arising by using a shallower structures (2π and multiples) is that the quantisation noise during the design process is increased when compared to deeper structures as well as a drop in the diffraction efficiency of the images and an increase in the non-uniformity. Trials have been carried out using irregular phase levels but the errors are too high and the optical output is severely compromised. For this reason, regular phase levels have been used.

7.9.1. Master 1

Master 1 is a negative 16 level element with a periodicity of 768μm and 4μm feature sizes. A pre-compensation of 12% has been applied to every level during etching. This element is designed for replication with the shim. In this design the position of the zeroth order is placed between right in between the two symbols.

Level	Etch Target (nm)	Etch Actual (nm)	% Over Etch
1	280	285	1.8
2	560	564	0.7
3	1120	1120	0
4	2240	2273	1.5
Total	4200	4242	1

The fabrication was carried out on a fused silica substrate with a thickness of 1.52mm. The substrate was cut to have a dimension of 50mm in order to fit under the chuck of the mask aligner. The substrate are cleaned in a rise aid solution for 10 minutes followed by

a 2 minute oxygen plasma. The surfaces are primed with Hexamethyldisilazane (HMDS) in order to prevent the washing off the features during development. The photoresist used is S1805 positive tone resist which is spun coated at 2000rpm for 60 seconds which yields a coating of about 700nm and soft baked on a hot plate at 95°C for 10 minutes. The photolithography is carried out using a Karl Suss MJB-3 mask aligner. The resist is exposed for 4 seconds and then developed for 35 seconds in 1:4 ratio of 326 developer to water. Finally hard baked on a hot plate at 110°C for 10 minutes. The etching is carried out in an Oxford plasma RIE-ICP machine parameters as follows; 125W RF only plasma, 25sccm of CHF_3 at 20mtorr. These parameters consistently produce an etch rate of ~33nm/min as well as smooth trenches. Once the etching of the level is completed the etch depth is measured using the DekTak 3 surface profile-meter to determine the etch depth. Once the target depth is reached the photoresist is washed off with acetone and a 2 minute RF only oxygen plasma at 200W is carried out in order to remove any leftover resist from the cavities, prior to the start of the application of the next level. The first three etch levels were carried out with S1805 resist and the last used the S1813 resist.
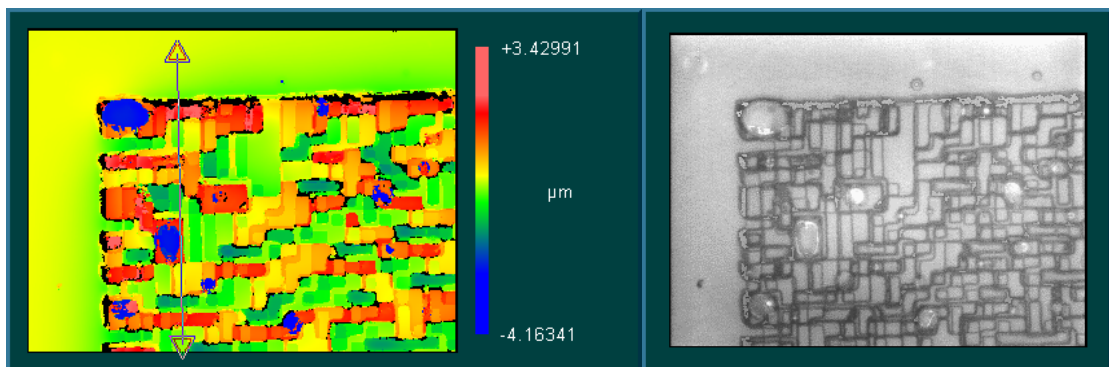

Figure 7. 13. Surface relief profile of one of the corners of the polymer copy of Master 1 with height in the z-axis (LEFT) and a microscope image of the same corner under 50X magnification (RIGHT).

From *Figure 7. 13* on the left is a 2 dimensional image of the surface profile of the shim with the height being assigned colour maps while the image on the right is a microscope image at 50X magnification and a further 1.3X addition on the eye piece. There is an observable residual layer on the outer perimeter of the structure due to stamp protrusions left behind after de moulding. All the masters are designed to have an easily identifiable feature marking the corner that the measurements are carried out on. A 40μm biaxial scan is selected and the first 5 rows in x and y directions are measured.
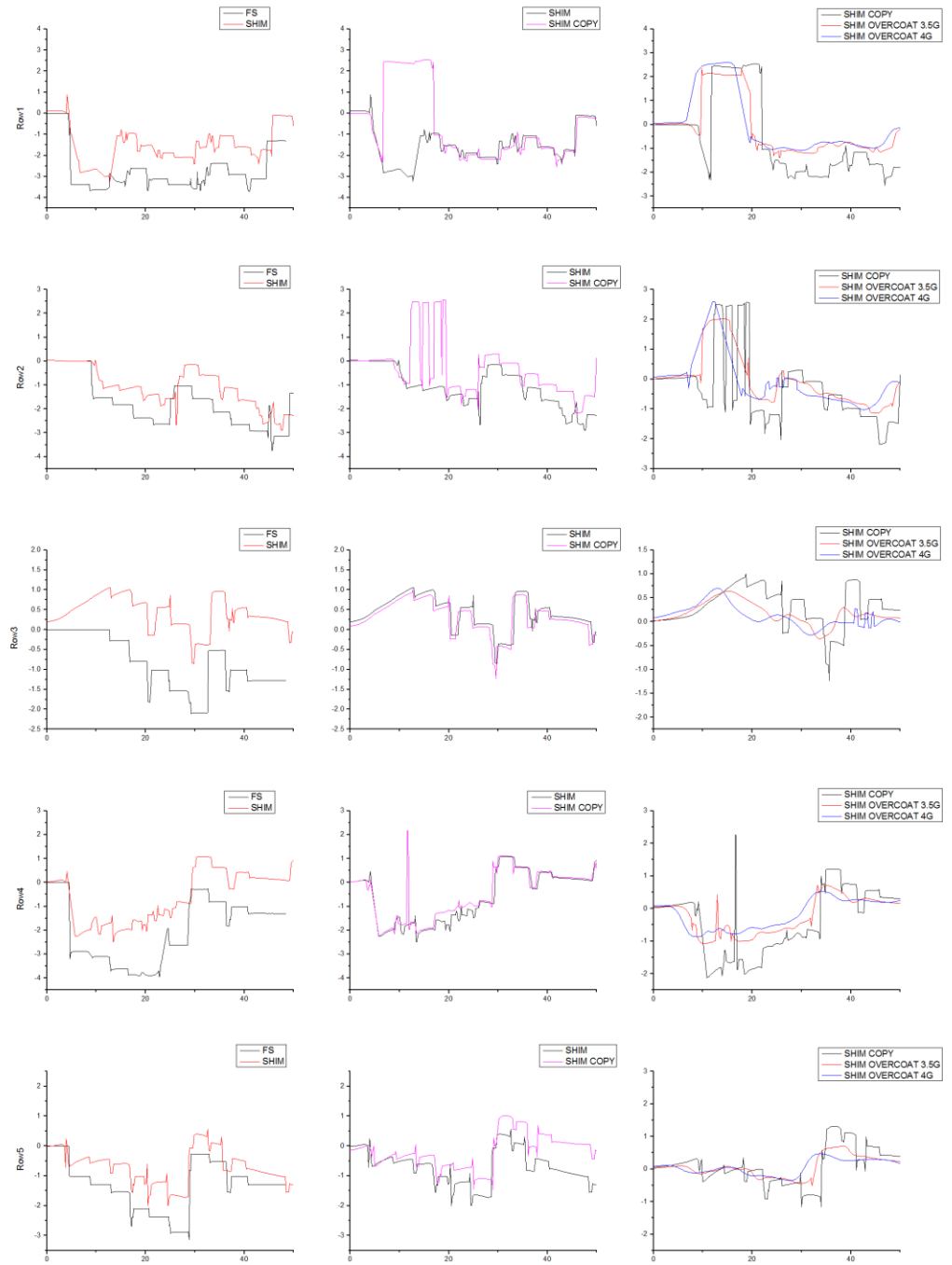
Figure 7. 14. Line scans carried out using the ZYGO white light interferometer of the first 5 rows (descending) on master 1. The scans on the left hand side show a comparison between the fused silica master and the shim, the middle column shows a comparison between the shim and the shim copy and the right column compares the shim copies and the two commercially produced overcoats.

The results of these measurements are seen from the ***Figure 7. 14***. The scan length is 50μm and the first 5 rows are measured. The first column shows a comparison between the fused silica master and the shim used for replication. This is the source of the largest amount of lateral feature shrinkage identified and compensated for by over etching. The second column shows the shim and the polymer shim copy, the polymer copy is seen to conform closely to the surface profile of the shim with minimal lateral feature shrinkage (~20nm) but a 0.2μm transverse feature shrinkage. The third column then shows a comparison between the shim polymer copy and the over-coated polymer copy showing that the surface relief is insufficiently filled and the polymer conforms to the underlying structure.

Figure 7. 15. Linearization of the etch depths from the replication process of Master 1. The x axis indicates the designed etch depth prior the compensation and the y axis is the measured etch depth on the polymer copy.

The analysis of the success of the replication process is shown by ***Figure 7. 15*** above, on the x axis the design depth is indicated and the y axis indicated the actual depth measured on the shim. A linear fit is carried out and the R squared value of the fit is 99.2%. The slope of the line is 0.958±0.012 and its intercept is -0.012±0.013. Ideally the slope should be 1 and the intercept should be 0. For the shim polymer copy the slope of the line is the same but the intercept is moved to -0.032±0.013. The straight line fit and linearization of the depth indicates that the applied precompensation has successfully worked and the

replicated surface relief profile is significantly close to the designed surface relief profile for the elements to work as designed.

7.9.2. Master 2

Master 2 is a positive 16 level element with a periodicity of 768µm and 4µm feature sizes. A compensation of 20% has been applied to every level during etching. This element is designed for replication with the mother. In this design the position of the zeroth order is placed between right in between the two symbols.

Level	Etch Target (nm)	Etch Actual (nm)	% Over Etch
1	300	298	-0.7
2	600	608	1.3
3	1200	1221	1.7
4	2400	2480	3.2
Total	4500	4607	2.3

The fabrication process for the master is much the same as the one described in the previous sub section with the differences arising in the form of increments in the etching times of the fused silica master because of required deeper features.
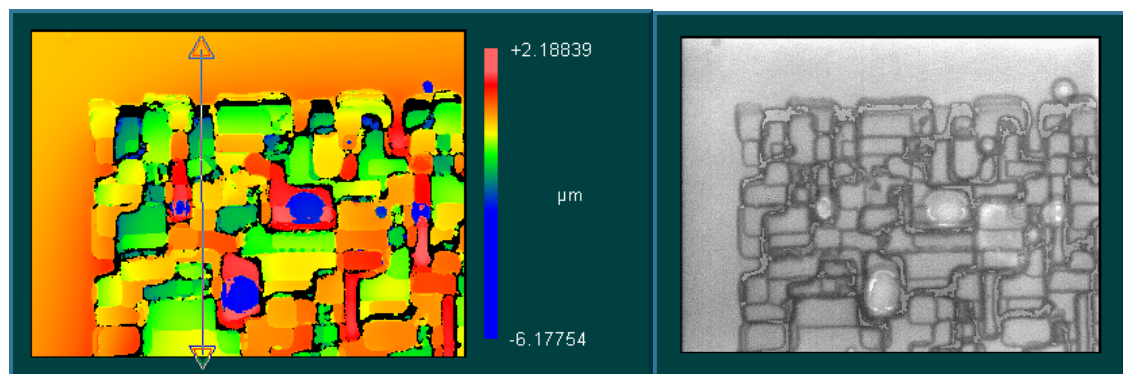
Figure 7. 16.Surface relief profile of one of the corners of the polymer copy of Master 2 with height in the z-axis (LEFT) and a microscope image of the same corner under 50X magnification (RIGHT).

From *Figure 7. 16* on the left is a 2 dimensional image of the surface profile of the mother with the height being assigned colour maps while the image on the right is a microscope image at 50X magnification and a further 1.3X addition on the eye piece. There is an observable residual layer on the outer perimeter of the structure due to stamp protrusions left behind after de moulding. All the masters are designed to have an easily identifiable

feature marking the corner that the measurements are carried out on. A 40μm biaxial scan is selected and the first 5 rows in x and y directions are measured.
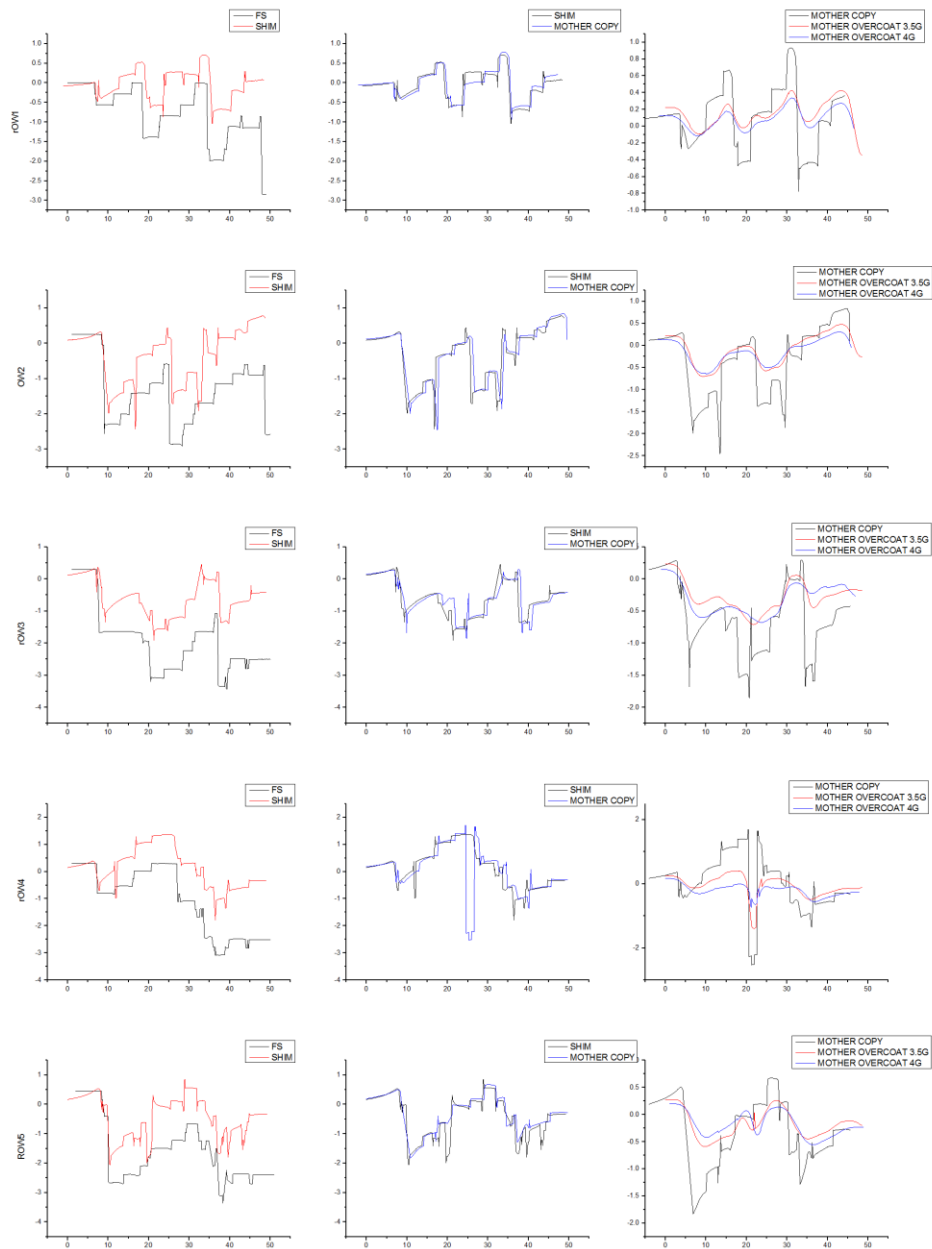

Figure 7. 17. Line scans carried out using the ZYGO white light interferometer of the first 5 rows (descending) on master 2. The scans on the left hand side show a comparison between the fused silica master and the shim, the middle column shows a comparison between the shim and the mother copy and the right column compares the mother copies and the two commercially produced overcoats.

The results of these measurements are seen from *Figure 7. 17*. The scan length is 50μm and the first 5 rows are measured. The first column shows a comparison between the fused silica master and the shim used for replication. This is the source of the largest amount of lateral feature shrinkage identified and compensated for by over etching. The second column shows the mother and the polymer mother copy, the polymer copy is seen to conform closely to the surface profile of the shim with minimal lateral feature shrinkage (~40nm) but a 0.4μm transverse feature shrinkage. The third column then shows a comparison between the shim polymer copy and the over-coated polymer copy showing that the surface relief is insufficiently filled and the polymer conforms to the underlying structure.

Figure 7. 18. Linearization of the etch depths from the replication process of Master 2. The x axis indicates the designed etch depth prior the compensation and the y axis is the measured etch depth on the polymer copy.

The analysis of the success of the replication process is shown by *Figure 7. 18* above, on the x axis the design depth is indicated and the y axis indicated the actual depth measured on the shim.

7.9.3. Master 4

Master 4 is a negative 16 level element with a periodicity of 768μm and 6μm feature sizes. A compensation of 40%, 29%, 19% and 14% (in ascending order as a function of level) has been applied to the four level during etching. This element is designed for replication with the shim. In this design the position of the zeroth order is placed beneath the middle numerical with the aim of reducing the scatter.

Level	Etch Target (nm)	Etch Actual (nm)	% Over Etch
1	350	351	0.3
2	645	660	2.3
3	1190	1212	1.8
4	2280	2330	2.1
Total	4465	4553	1.9
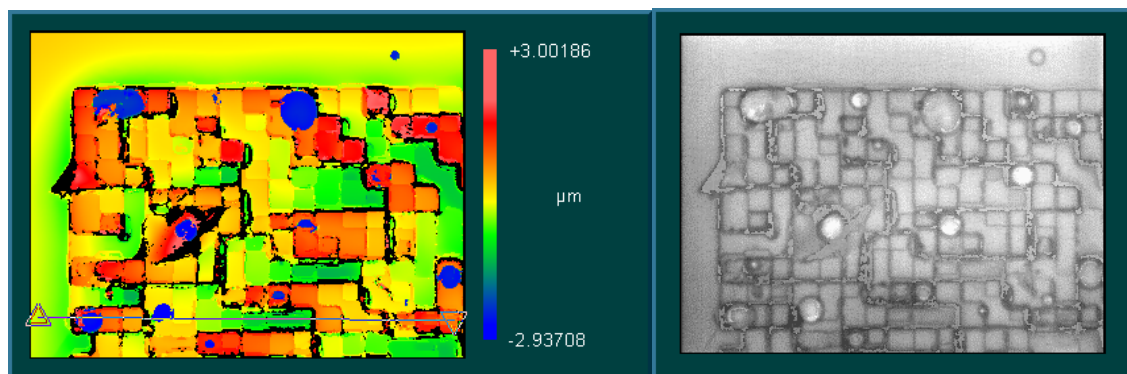
Figure 7. 19.Surface relief profile of one of the corners of the polymer copy of Master 4 with height in the z-axis (LEFT) and a microscope image of the same corner under 50X magnification (RIGHT).

From *Figure 7. 19* on the left is a 2 dimensional image of the surface profile of the mother with the height being assigned colour maps while the image on the right is a microscope image at 50X magnification and a further 1.3X addition on the eye piece. There is an observable residual layer on the outer perimeter of the structure due to stamp protrusions left behind after de moulding. All the masters are designed to have an easily identifiable feature marking the corner that the measurements are carried out on. A 40μm biaxial scan is selected and the first 5 rows in x and y directions are measured.
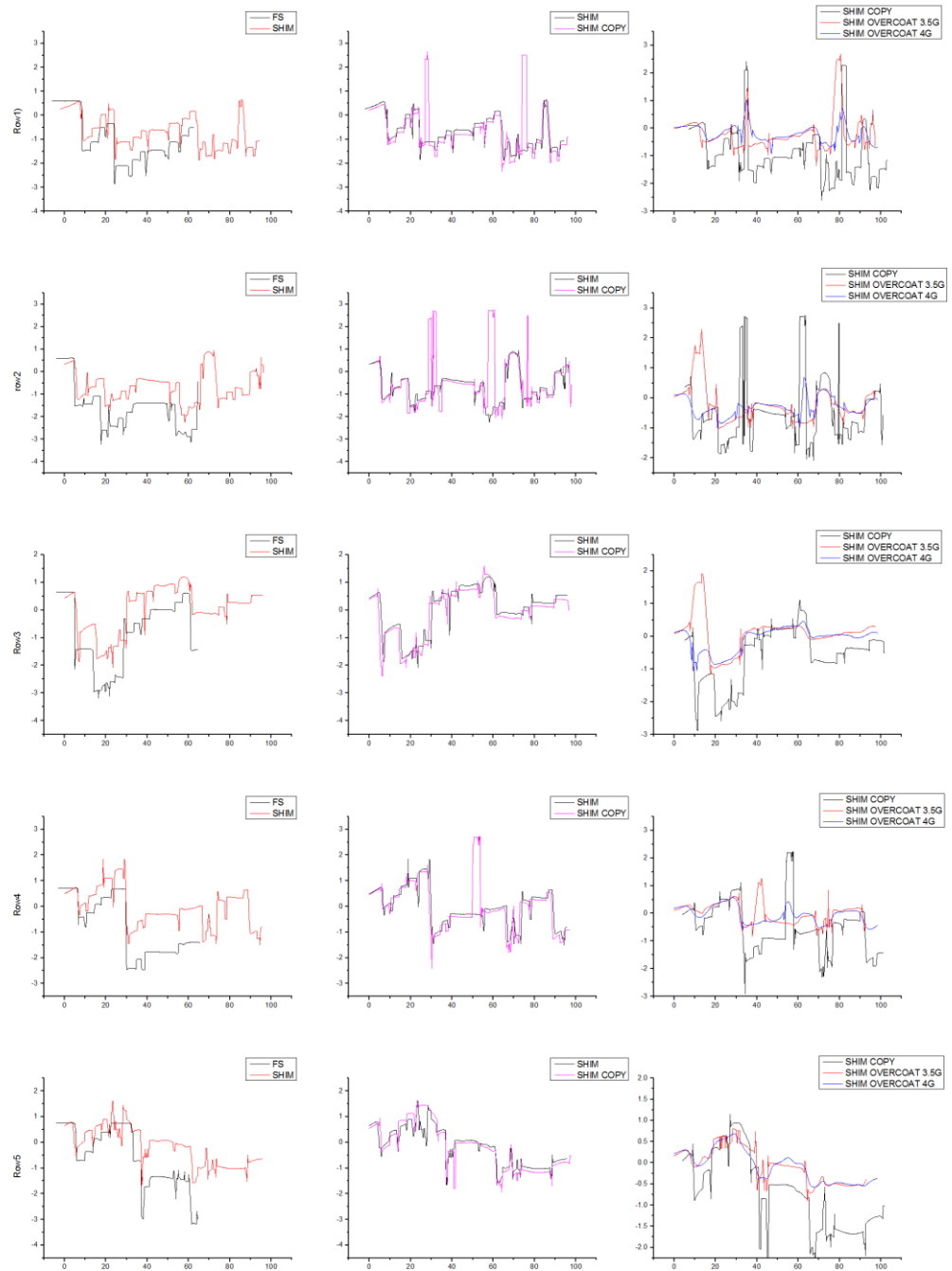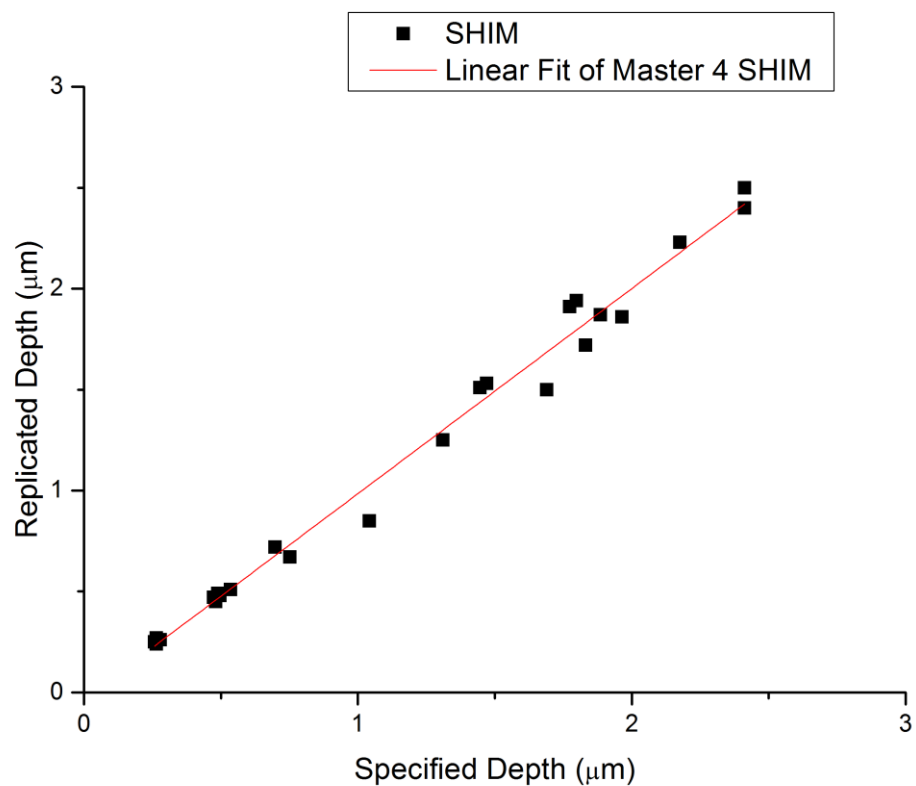
Figure 7. 20. Line scans carried out using the ZYGO white light interferometer of the first 5 rows (descending) on master 4. The scans on the left hand side show a comparison between the fused silica master and the shim, the middle column shows a comparison between the shim and the shim copy and the right column compares the shim copies and the two commercially produced overcoats.

The results of these measurements are seen from *Figure 7. 20* . The scan length is 50μm and the first 5 rows are measured. The first column shows a comparison between the fused silica master and the shim used for replication. This is the source of the largest amount of lateral feature shrinkage identified and compensated for by over etching. The second column shows the shim and the polymer shim copy, the polymer copy is seen to conform closely to the surface profile of the shim with minimal lateral feature shrinkage (~20nm) but a 0.2μm transverse feature shrinkage. The third column then shows a comparison between the shim polymer copy and the over-coated polymer copy showing that the surface relief is insufficiently filled and the polymer conforms to the underlying structure.

Figure 7. 21.Linearization of the etch depths from the replication process of Master 2. The x axis indicates the designed etch depth prior the compensation and the y axis is the measured etch depth on the polymer copy.

The analysis of the success of the replication process is shown by *Figure 7. 21* above, on the x axis the design depth is indicated and the y axis indicated the actual depth measured on the shim.

7.9.4. Master 5

Master 5 is a positive 16 level element with a periodicity of 768μm and 4μm feature sizes. A compensation of 45%, 35%, 26% and 19% (in ascending order as a function of level) has been applied to the four level during etching.. This element is designed for replication with the mother. In this design the position of the zeroth order is placed between right in between the two symbols.

Level	Etch Target (nm)	Etch Actual (nm)	% Over Etch
1	362.5	378	4.1
2	675	680	0.7
3	1260	1280	1.6
4	2380	2384	0.2
Total	4677.5	4722	0.9
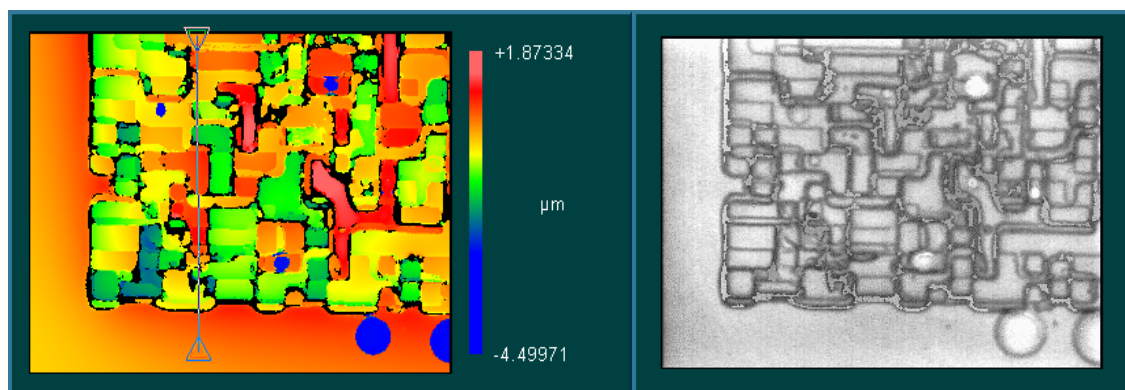
Figure 7. 22.Surface relief profile of one of the corners of the polymer copy of Master 5 with height in the z-axis (LEFT) and a microscope image of the same corner under 50X magnification (RIGHT).

From *Figure 7. 22* on the left is a 2 dimensional image of the surface profile of the mother with the height being assigned colour maps while the image on the right is a microscope image at 50X magnification and a further 1.3X addition on the eye piece. There is an observable residual layer on the outer perimeter of the structure due to stamp protrusions left behind after de moulding. All the masters are designed to have an easily identifiable feature marking the corner that the measurements are carried out on. A 40μm biaxial scan is selected and the first 5 rows in x and y directions are measured.
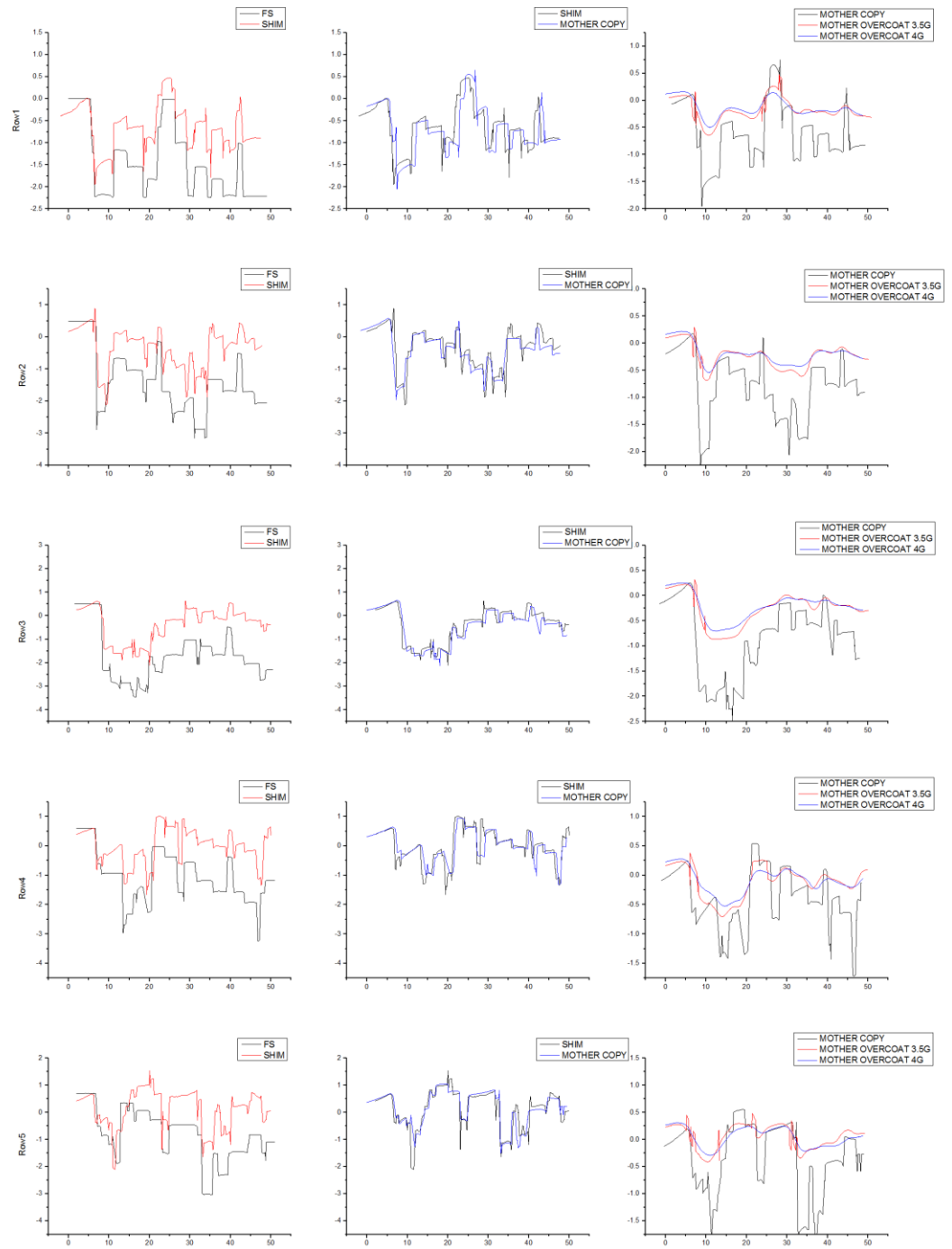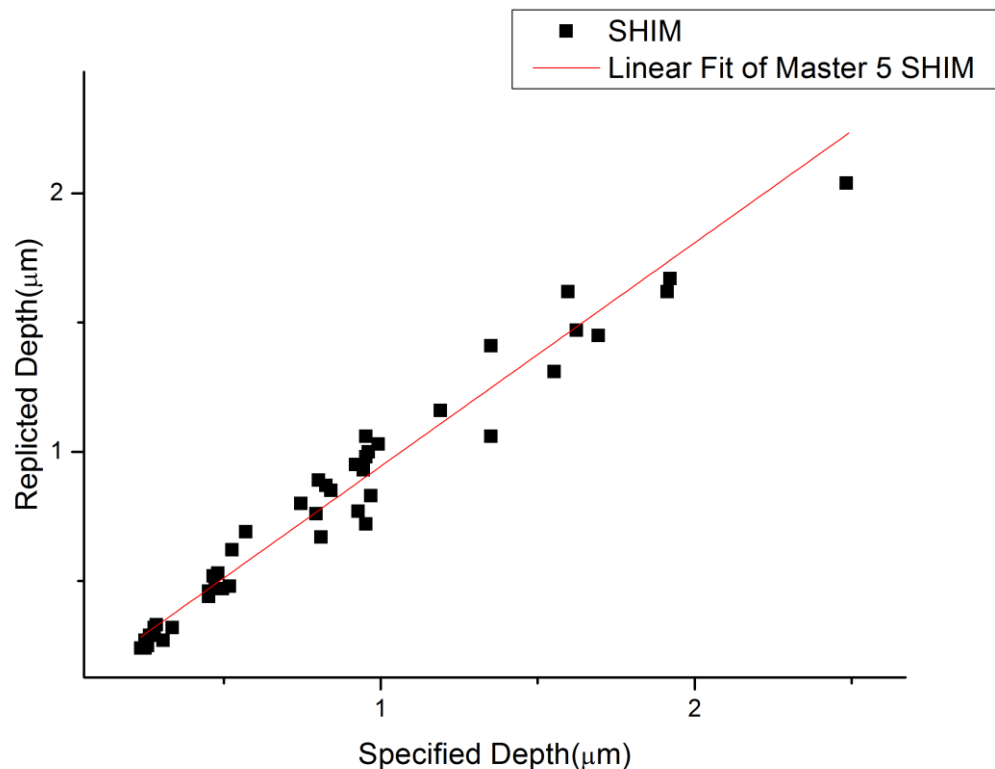
Figure 7. 23. Line scans carried out using the ZYGO white light interferometer of the first 5 rows (descending) on master 5. The scans on the left hand side show a comparison between the fused silica master and the shim, the middle column shows a comparison between the shim and the mother copy and the right column compares the mother copies and the two commercially produced overcoats.

The results of these measurements are seen from *Figure 7. 23*. The scan length is 50μm and the first 5 rows are measured. The first column shows a comparison between the fused silica master and the shim used for replication. This is the source of the largest amount of lateral feature shrinkage identified and compensated for by over etching. The second column shows the mother and the polymer mother copy, the polymer copy is seen to conform closely to the surface profile of the shim with minimal lateral feature shrinkage (~40nm) but a 0.4μm transverse feature shrinkage. The third column then shows a comparison between the shim polymer copy and the over-coated polymer copy showing that the surface relief is insufficiently filled and the polymer conforms to the underlying structure.

Figure 7. 24.Linearization of the etch depths from the replication process of Master 2. The x axis indicates the designed etch depth prior the compensation and the y axis is the measured etch depth on the polymer copy.

The analysis of the success of the replication process is shown by *Figure 7. 24* above, on the x axis the design depth is indicated and the y axis indicated the actual depth measured on the shim.

7.9.5. Replication Analysis

A table summarising the results from the fits on all 4 Master copies is presented below. The R^2 fitting parameter as well as the slope of the line and its intercept is shown. In an ideal situation the fitting parameter should be as close as possible to 100%, the slope of the graph should be 1 and the intercept should be 0.

Table 7. 1 Comparison of the success of the replication process for polymer copies.

	R^2 (%)	Slope	Intercept
Master 1	99.2	0.958±0.012	-0.012±0.013
Master 2	97.7	0.964±0.022	-0.002±0.020
Master 4	98.8	1.015±0.022	-0.133±0.033
Master 5	96.3	0.846±0.025	0.039±0.027

From the results above based on the slope, Master 4 should have the best pre compensation out of the set. Based on the intercept Master 2 should be the best and on fitting parameter Master 1 should be the best. On comparing the numerical fitting values to the optical outputs presented in the next section Master 1 has the least amount of scattering and shows the clearest dual colour operation of the set.

7.10. Optical Outputs of Uncoated Polymer DOES

The optical outputs from the polymer copies are obtained using the setup shown in *Figure 7. 25*. A camera with a short focal length lens is used to focus on the end of an optical fibre. The distance between the camera lens and the optical fibre end is ~50mm. The optical fibre used is a multimode optical fibre with a core diameter of 62.5µm and cladding diameter of 125µm (ThorLabs GIF-625). This acts as the point source of illumination. The fibre is fixed onto a micro block allowing for alignment to the focal plane of the light source. The light source used an LED with a cold emission spectrum (ThorLabs LEDWE-15) driven at 5V. The light from the LED is collected using a 10X objective and launched into the fibre. The diffractive phase element is positioned right in front of the camera lens to simulated viewing as observed by the human eye. The distance between the lens and the DPE is around 10mm.
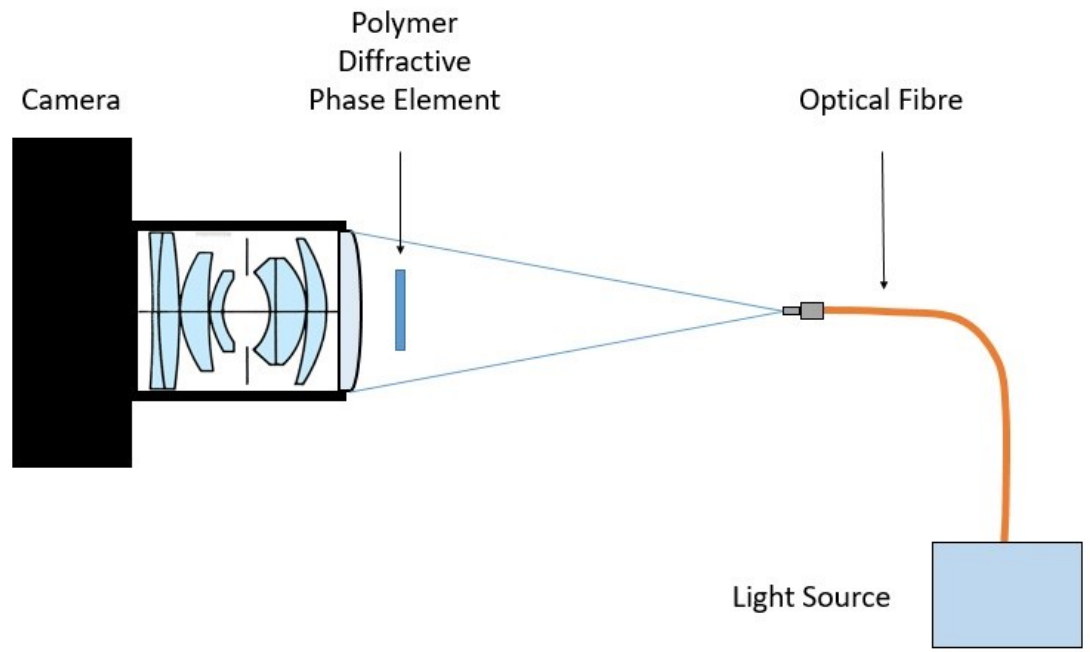
Figure 7. 25. Schematic of the experimental arrangement used to capture the optical outputs from the DPEs.

The diffractive phase element is also viewed with the 2 designed laser wavelengths of 450nm and 650nm respectively. A spectrum of the light emitted by the LED and the two lasers was measured using an ocean optics usb2000 spectrometer and shown in *Figure 7. 26* below.
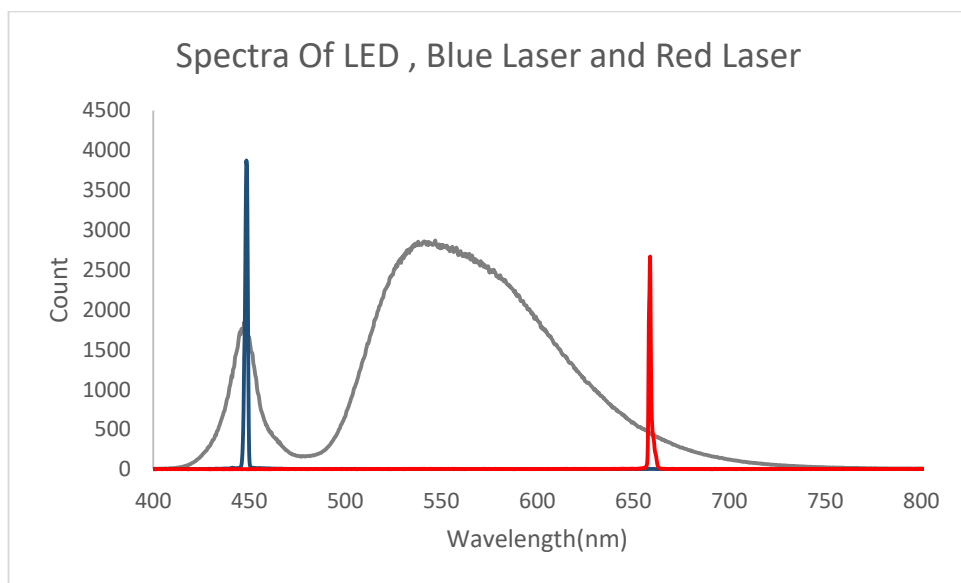

Figure 7. 26. Comparison of optical spectra from a mobile phone flash light to the blue and red designed laser wavelengths.

The wavelength of the blue laser diode falls around 450nm and the red laser diode is at 660nm. However since these elements are mainly designed for viewing by the naked eye and appearing catching, all the images captured are post processes with a photopic colour correction to look as though seen by the eye. The response between different human eyes has a certain level of variance and has been corrected for the vision of the author.

From the **Figure 7. 27** below under white light illumination it appears that element 4 produces the best optical output, but whenever the outputs from the laser sources are captured, it appears that element 1 shows the highest diffraction efficiency and lowest scatter. Elements 1 and 4 are both negative masters which were designed for replication by the shim. The difference comes in the form of the compensation used, element 1 had a 12% linear compensation across the levels and element 4 had a non-linear compensation. Elements 2 and 5 are the positive master which also do produce an optical output but seem to be swarmed by a bit more noise when compared to the negatives, which could come down to excessive compensation, fabrication errors and replication errors.
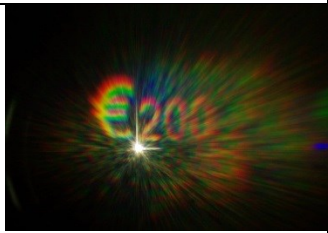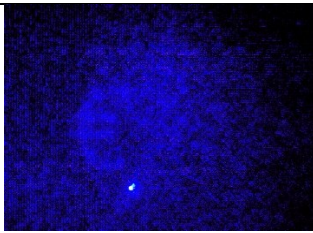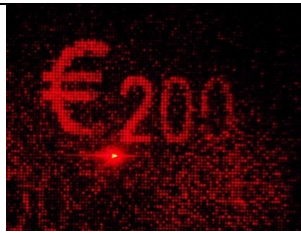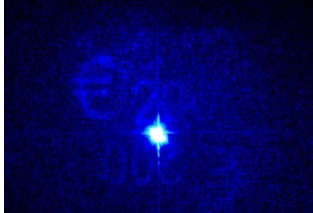
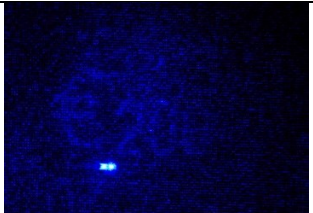| Element	White Light	Blue	Red
1			
2			
4			
5			

Figure 7. 27. The optical outputs from the uncoated polymer DPE. The left column shows the output upon illumination with white light, the middle column shows the output upon illumination with a blue laser and the right shows the output upon illumination with a red laser.

7.11. Overcoats on DOEs

Through the application of a thin, transparent over coat the surface relief profile of the DPE can be planarised, providing an obstacle for further replication in counterfeiting. In this subsection of the thesis the effects such as refractive index difference, fill factor and film scattering have on the final optical output of the device have will be looked at in depth.

7.11.1. Effects of Refractive Index

The DPE is designed to produce a dual colour operation under illumination by the designed wavelengths and a refractive index difference of 0.26, between the base and the overcoat for wavelengths of 450nm and 650nm. The testing was carried out on a fused silica master which was etched to the modelled depths, taking into account the dispersion coefficient of fused silica, designing for the above mentioned wavelengths and refractive index difference. This is carried out in order to carry out a proof of concept, the DPE can function in with the presence of an overcoat with a higher refractive index.
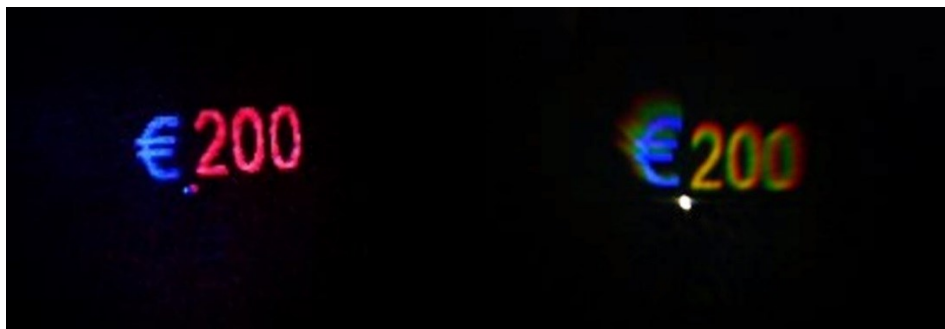

Figure 7. 28. The optical outputs from an uncoated fused silica DPE. The image on the left shows the optical output upon illumination with the two designed laser wavelengths and the image on the right shows the optical output upon illumination with a white light source.

In *Figure 7. 28* above show the operation of an uncoated DPE on fused silica. The image on the left hand side displays the optical output when illuminated by both operational wavelengths at the same time, quite clearly showing the two images appearing in their desired colour with no cross talk between them. The image on the right shows the output under white light illumination, the '€' appears blue but the '200' appears yellowish red. This can be explained by the high refractive index difference pushing the colour of the second image into the green. Both of these images show next to no scatter when compared to the polymer copies, showing the near perfect fabrication.

The **Figure 7. 29** below shows the optical output of the DPE at illumination wavelengths of 450nm, 532nm and 650nm respectively.

Overcoat	Blue	Green	Red
No Fill			
NOA 170			
S1805			
S1813			

Figure 7. 29. Optical outputs from over coated fused silica DPE with different refractive refractive index differences. The left column shows the output upon illumination with a blue laser, the middle column shows the outputs upon illumination with a green laser and the right column shows the outputs upon illumination with a red laser.

From the first image, the refractive index difference is ~0.46. The '€' symbol solely appears in blue, there is an observable cross talk with the '200' appearing marginally brighter in green and the '200' solely appears in red.

$$Pixel\ Count\ Intensity = \left(\frac{(\frac{P_{I1} + P_{I2} + P_{In}}{\sum P_N})}{Area} \right) x\ {P_{I(\lambda)}}\Big/{P_{I\ Max\ (\lambda)}} \qquad (7.2)$$

By carrying out a pixel count, obtaining an average of the pixels in the image, dividing by the area of the image and multiplying that by the ratio of the maximum pixel value on the image for the a set of known laser wavelengths a ratio of intensities of the two images is carried out. This is shown in the graph below, where the x axis is wavelength and the y axis is ratio of images. From the *Figure 7. 30* below the cross talk wavelength at which both images have an equal amount of intensity is estimated to occur at about 540nm.
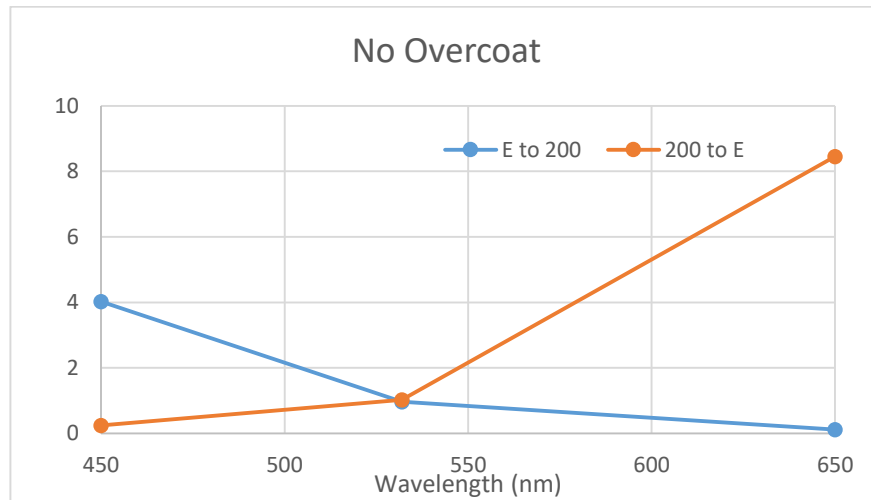

Figure 7. 30. The ratios of the intensity of the two images as a function of illumination wavelength for the uncoated fused silica DPE.

From the second set of images, NOA 170 is used as an over coat. This is an optical cement with a high refractive index of 1.7. The refractive index difference in this case is 0.24, which is close to the desired 0.26. In blue the '€' is a lot more intense compared to the '200', in green the '€' is a less intense compared to '200', and in red the '200' is has a little bit of the '€' showing. Assuming that the structure is perfect with no fabrication errors, the cross talk at the operational wavelengths can be justified by the 0.02 refractive index difference from the designed value. This is shown in the *Figure 7. 31* , where the x axis is wavelength and the y axis is ratio of images.
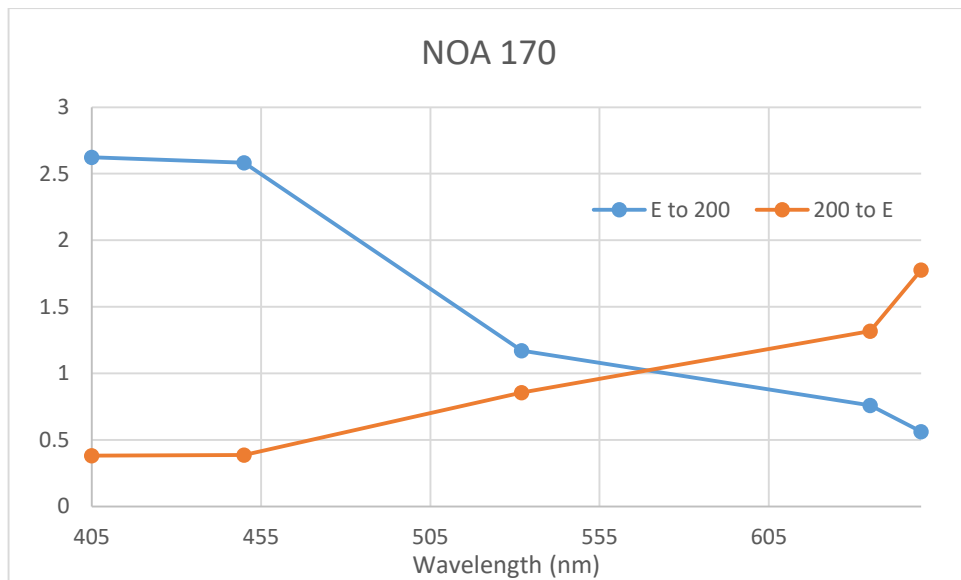
Figure 7. 31.The ratios of the intensity of the two images as a function of illumination wavelength for the NOA 170 over coated fused silica DPE.

From the third set of images, a positive tone photoresist, S1805 is used as the overcoat, it has a refractive index of about 1.66 and this gives a refractive index difference of 0.2. In blue both images appear with the '200' being more intense than the '€', in green the much the same is observed with both images appearing and the '200' exhibiting a high intensity and in red the '200' is the dominant image with a tiny amount of the '€' sipping through. This is shown in the **Figure 7. 32**, where the x axis is wavelength and the y axis is ratio of images.
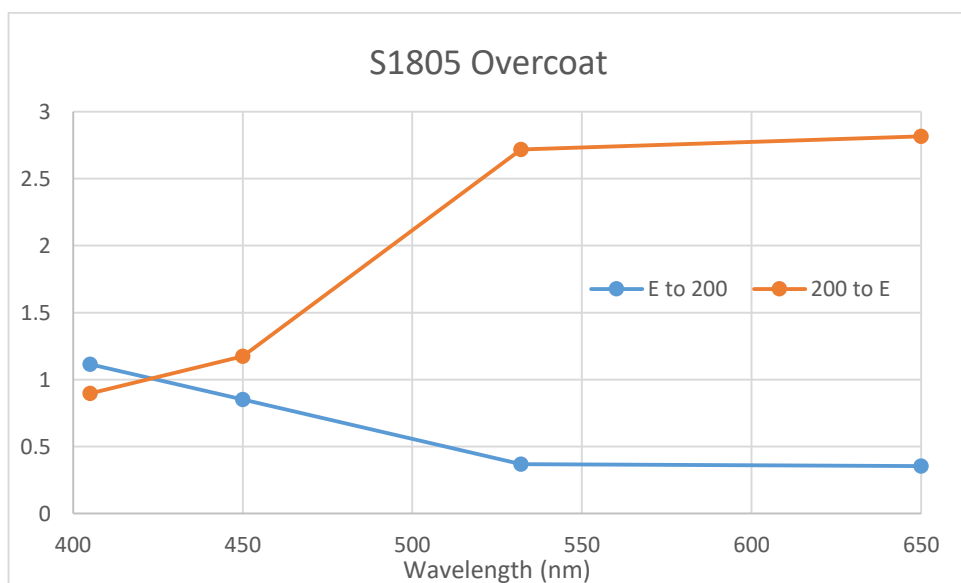
Figure 7. 32.The ratios of the intensity of the two images as a function of illumination wavelength for the S1805 photoresist over coated fused silica DPE.

From the fourth set of images, a positive tone photoresist, S1813 is used as the overcoat, it has a refractive index of about 1.67 and this gives a refractive index difference of 0.21.

In blue both images appear with the '€' being more intense than the '200', in green both images appear and the '200' exhibiting a high intensity and in red the '200' is the dominant image with a tiny amount of the '€' sipping through. This is shown in the **Figure 7. 33**, where the x axis is wavelength and the y axis is ratio of images. From the graphs above generated by the procedure using pixel counting a table summarising the refractive index differences and effect it has on the cross talk wavelength is presented below.

On comparison of the optical outputs of from this refractive index difference and the fully coated polymer copy the, outputs look nearly identical indicating that the refractive index difference between the base polymer and the overcoat lies at a similar level.
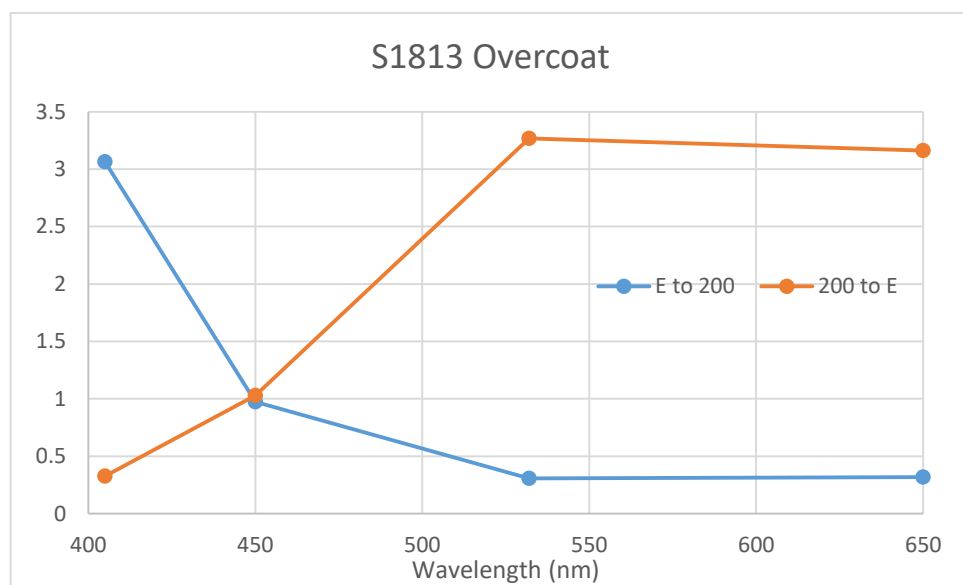
Figure 7. 33.The ratios of the intensity of the two images as a function of illumination wavelength for the S1813 photoresist over coated fused silica DPE.

As a further test NOA 170 was used to coat the polymer copies, which provides a refractive index difference of 0.16. From the measurements made the cross talk wavelength at which both images had equal intensity was pushed into the UV making sources difficult to obtain and not safe for viewing by the naked eye.

Table 7.2 summarising the results from the analysis carried out on the optical outputs from the over coated glass masters.

Overcoat	Refractive Index Difference	Cross Talk Wavelength.
N/A	0.46	540nm
NOA170	0.24	567nm
S1805	0.2	420nm
S1813	0.21	448nm

7.11.2. Effects of Fill Factor

Through the application of an overcoat the surface relief profiles of the diffractive phase element can be planarised, hence making it difficult for counterfeiting. The polymer used as an overcoat during the replication process is a transparent, UV curable polymer which contains titanium dioxide nano particles. The polymer is synthesized by Keira Chemicals, Netherlands and a specification sheet can be found attached in the appendix. This will be called Coating A for simplicity in the remainder of this section. Coating A was measured to have a refractive index of ~1.8 and a density of ~1.18±0.02g/ml. During the replication process, coating A is applied after de moulding of the structures through spray coating and cured by exposure to UV. It was applied at two rates of 3.5g/m^2 and 4 g/m^2.

The optical outputs on illumination with a white light source from all the elements with the application of coating A as an overcoat is shown in *Figure 7. 34* below. All the images have been post processed and a correction factor to account for the viewing conditions as by the human eye is carried out. From the images it is observed that there exists a lot of noise and scattering which is explained by the partial filling of the surface relief profile. The light passing through only sees a partial phase difference which leads to a deterioration in the quality of the diffracted image. The first element is the only one in which the 200 can be made out while the euro symbol is engulfed in noise. The elements are designed to have a 100% fill factor in order to function.
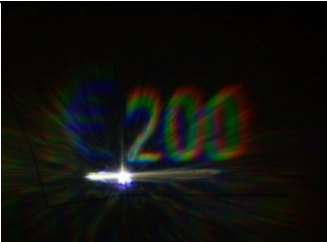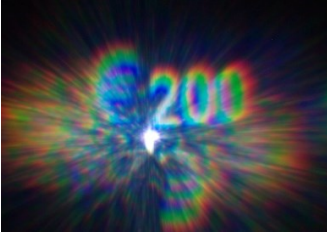
Figure 7. 34. The optical outputs from the over coated polymer DPE upon illumination with a white light source. The left column shows the output from the commercial coating process with a deposition rate of 3.5g/m² , the centre column shows the output from the commercial coating process with a deposition rate of 4g/m² and the right column shows the output from the in house developed coating process achieving a complete over fill.

On further analysis the infill factor is measured by comparing the depth on the polymer copy across 5 features with the depth of the over coated sample across the same range. The results are shown in the *Figure 7. 35* below, the x axis shows the depth of the polymer copy and the y axis shows the fill factor percentage for both coating rates. For the 3.5g/m² coating the average infill factor stands at about 65 % and for the 4g/m² coating the average infill factor stands at about 72%. The desired depth of the polymer surface relief profile is 3.75μm, assuming that Coating A does not undergo any volumetric change on application then with the measured density the maximum layer thickness at 3.5g/m² would be 2.9μm and at 4g/m² would be 3.35μm. These suggest fill factors of about 80% and 90% respectively, both insufficient to produce a 100% fill factor without accounting for volumetric shrinkage or conformity of the polymer to the base surface relief profile.

In order to achieve the 100 percent fill factor the coating rate would have to be increased to $\sim 5g/m^2$.
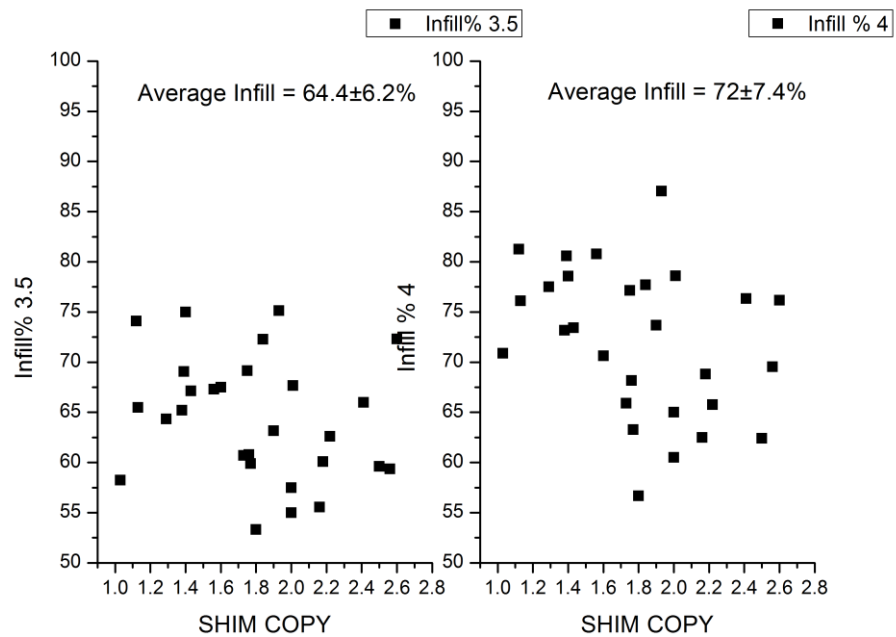
Figure 7. 35. A scatter of the over coat infill percentage in the polymer DPE from the commercial process. The graph on the left shows the infill for a deposition rate of 3.5g/m2 and the graph on the right shows the infill for a deposition rate of 4g/m2.

With partially filled surface relief profiles, an in-house techniques was developed in order to achieve a full filling. The techniques comprises of the addition of multiple layers of Coating A on top of the polymer copy until completely in filled. An optical inspection is carried out after the addition of each successive layer. The steps involved in the technique are as follows;

1. Spin coating of Coating A at 500rpm for 30 seconds.
2. Air drying of the deposited layer for 45 seconds.
3. UV curing the layer for 3 minutes.

The procedure above is repeated 5 times. Each layer has a thickness of $\sim$ 6µm and the overall thickness of the multilayer coating is measured at ~30µm. Carrying out the optical inspection before curing each layer displayed a marked improvement in the optical output of the diffractive phase structures. After the addition of the first layer the Euro symbol starts appearing despite the noise surrounding it and it becomes a lot clearer with successive layers. The most insignificant change is observed between layers 4 and 5. The images above show a comparison of the optical outputs from the commercially filled and laboratory filled DPE and the difference is remarkable. Both images can be seen by using the above mentioned approach and the DPE shows dual colour operation as well, because

the Euro symbol appears in blue and the 200 appears in reddish. Also observed with the above mentioned process is that there is an associated volumetric shrinkage associate with each of the processes. After air drying the Coating A, a 20% reduction in volume was measured. After UV curing there is a further 10% reduction in volume of coating A, yielding an overall volumetric reduction of ~30% after carrying out both processes.
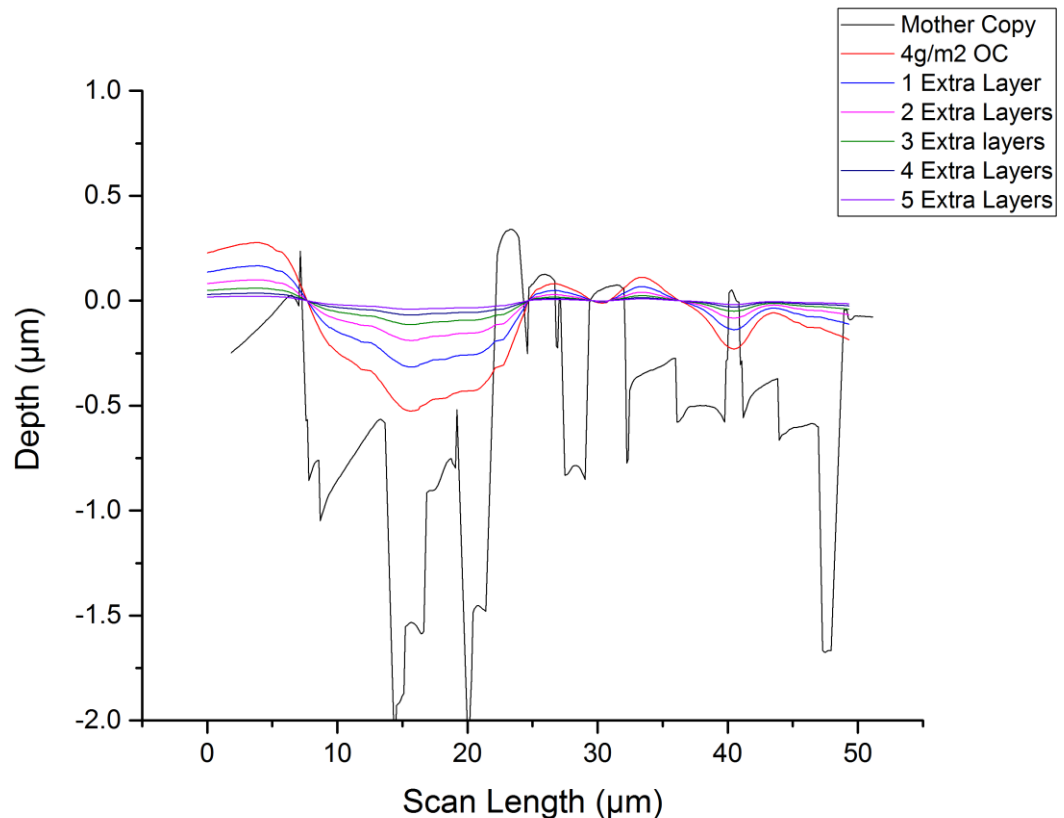
Figure 7. 36. Line scan of the surface profile of a polymer DPE uncoated and the effects that the addition of successive layers of over coat have on the surface relief profile.

Figure 7. 36 above shows the effect of addition of successive layers of Coating A to the surface relief profile until a fully planarized structure is obtained. The x axis shows the line scan length and the y axis shows the lateral height difference between successive layers. Assuming that during the coating process the polymer conforms to the underlying structure due to its physical nature (viscosity) as well as surface tension effects[20] and each layer only fills ~70% of the structure. The next successive layer would fill a further 70 % and so on and so forth, after the application of the fourth layer the structure would be ~99% filled. This is confirmed by the optical checks carried out between successive layers and the lack of change in output between the 4th and the 5[Th] layers.
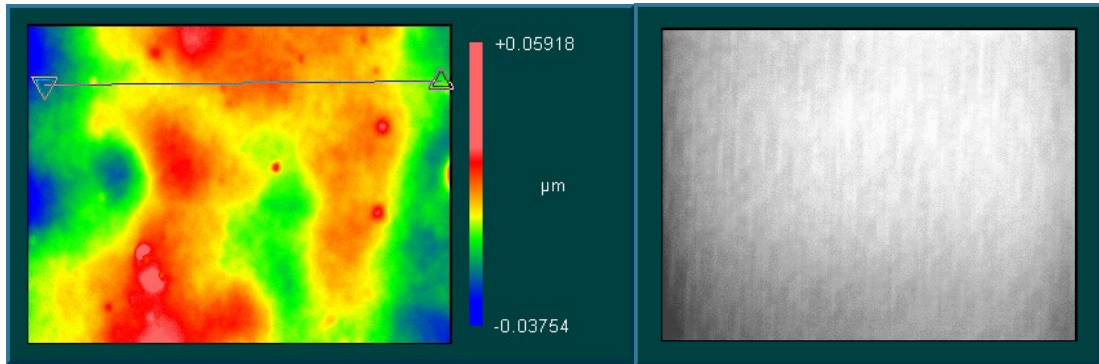
Figure 7. 37.Surface relief profile of one of the corners of an in house over coated polymer DPE with height in the z-axis (LEFT) and a microscope image of the same corner under 50X magnification (RIGHT).

From **Figure 7. 37** the image on the left is a 2 dimensional image of the surface profile of the fully filled polymer copy with the height being assigned colour maps while the image on the right is a microscope image at 50X magnification and a further 1X addition on the eye piece. From the scans it can be observed that there exist peaks which are about 36nm in dimension but the features of the underlying structure cannot be seen anymore and the surface appears linear.

In **Figure 7. 38** below are line scans of the of the first 5 rows of a polymer copy of an element and the line scan of the surface of a fully filled element with the multilayer deposition technique that was previously described. They show that the structures have been fully planarised.
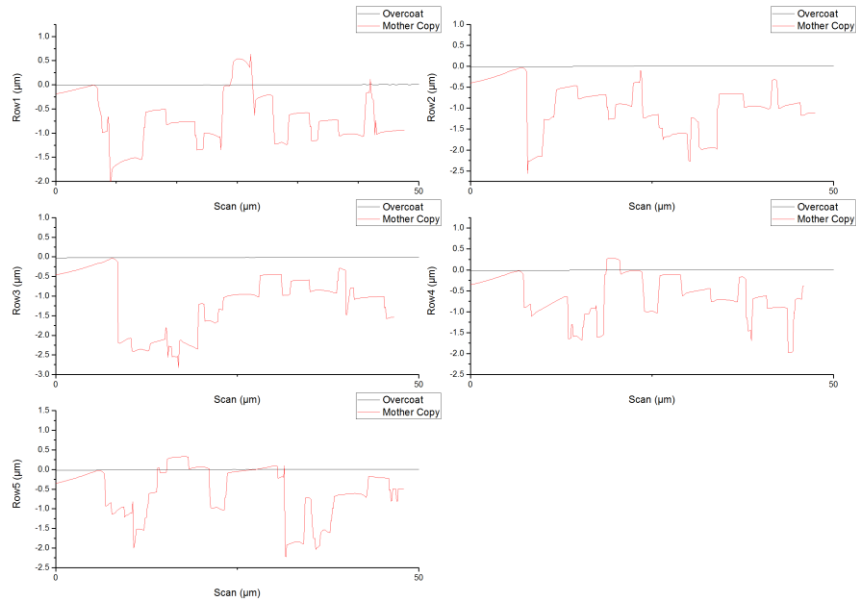
Figure 7. 38. Line scans carried out using the ZYGO white light interferometer of the first 5 lines comparing an uncoated polymer copy and an in house filled polymer copy.

Line scans from the first 5 rows are taken and from *Figure 7. 39* below it can be observed that after the application of 5 layers of Coating A with the method described above the peak to peak height differences are of the order of 40nm and the average surface roughness (Ra) is measured to be of the order of 9nm. In comparison to the over coating carried out at the replication stage, for which the fill factor stands at 80 % at best the fill factor of the coating carried out in house is of the order of 99%. This is not only shown by the surface analysis carried out, but also confirmed by the quality of the optical output from the DPE. The graph below shows the line from the fully filled element.
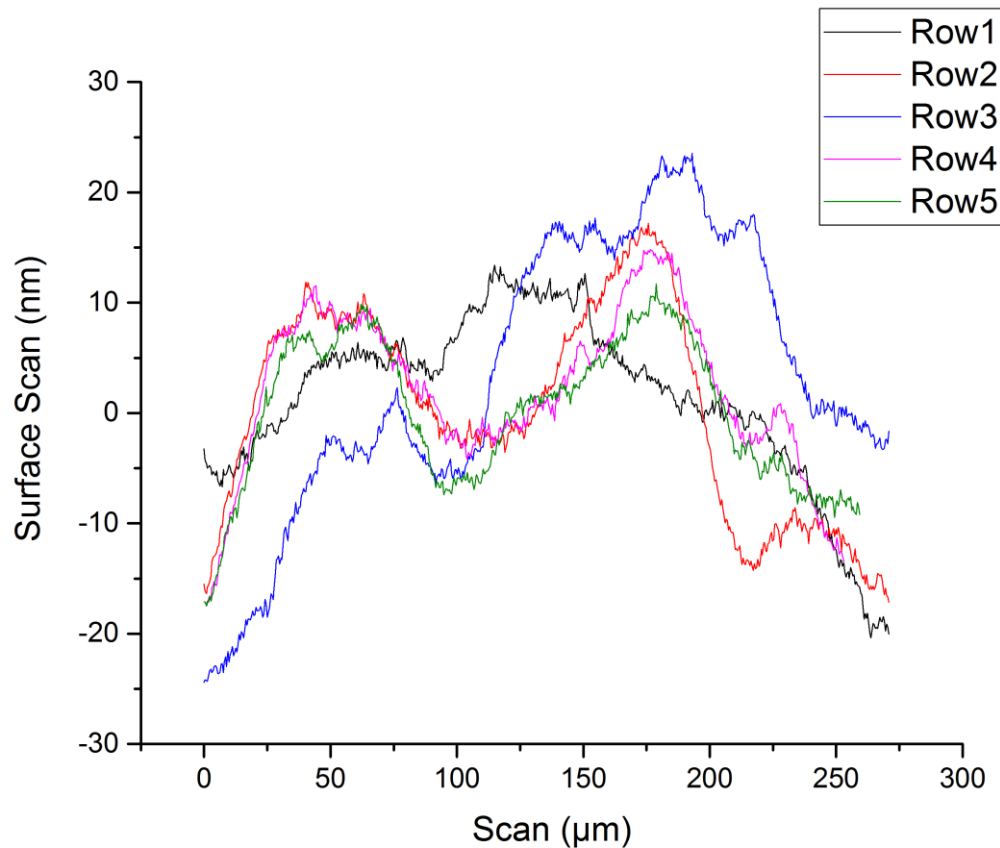
Figure 7. 39. Line scans carried out using the ZYGO white light interferometer of the first 5 lines of the in house filled polymer copy showing surface roughness.

7.11.3. Film Scattering

A source of optical output deterioration of the DPE arises as an intrinsic property of the surface roughness of the polymer film used. In comparison to fused silica, which possesses an atomically smooth surface profile, the polymer film does not. The surface roughness was measured on 4 corners of both a coated and an uncoated polymer film. The results from these measurements are shown in the **Figure 7. 40** below. The uncoated film has a surface roughness of the order of 30nm which should have an insignificant effect on the optical output as it is equal to less than 10 percent of the shallowest level. The commercial coated sample on the other hand has a surface roughness of about 200nm which is quite close to the value of the shallowest level. This could arise either due to conformity of the coating to the base polymer, surface tension effects or even the rollers used during the replication process due to the observable low frequency undulations.
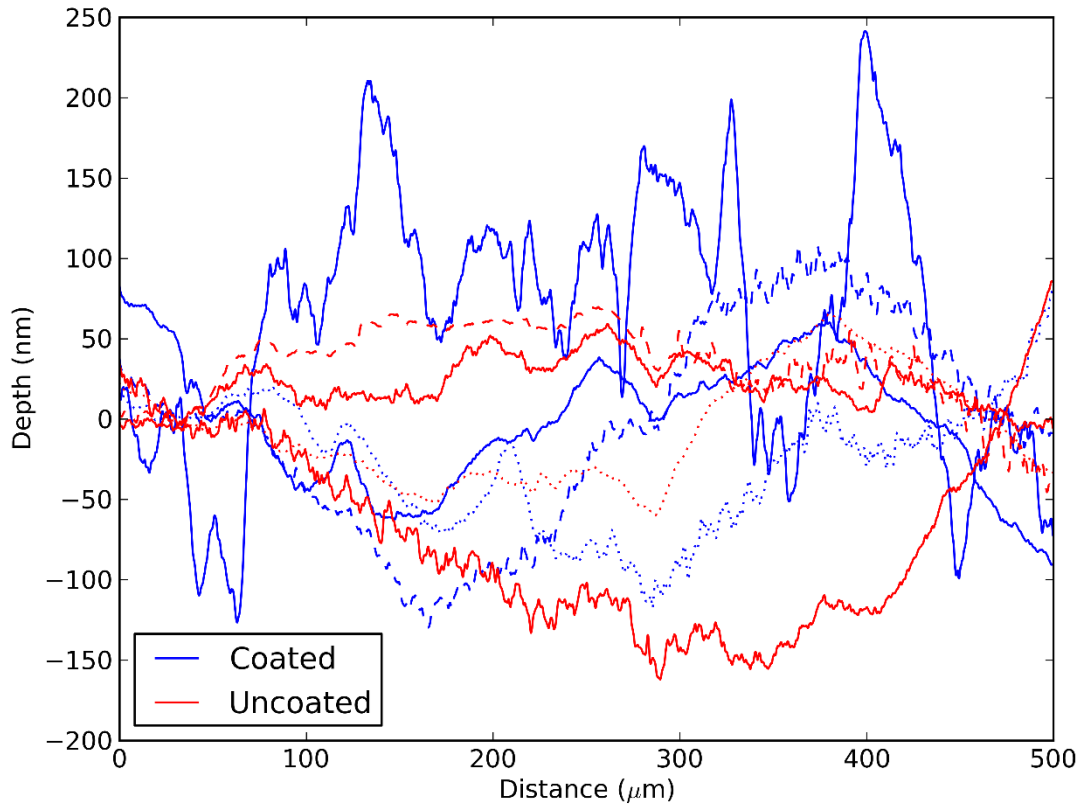
Figure 7. 40. Line scans carried out at 4 different locations comparing the surface roughness of an uncoated polymer film (Red Trace) and a commercially over coated polymer film (Blue Trace).

Subsequently statistical analysis carried out on the data showed that the mean normalised surface roughness for the uncoated was 9.8 nm and for the commercially coated sample 19.3nm from *Figure 7. 41*. There also exists further clustering of data at 50nm, 80nm and 160nm all of which will add to the amount of scatter. Both the base polymer and coating A are UV curable so there would be no softening and remoulding occurring at temperatures in excess of 80°C, where the polymer starts to thermally shrink and fracture.
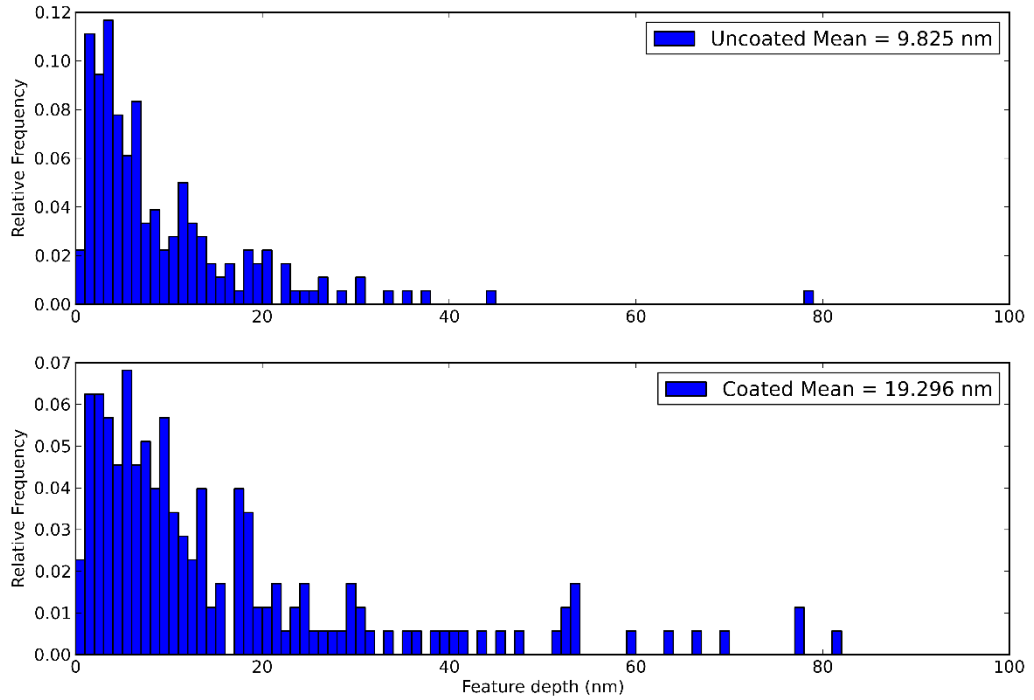
Figure 7. 41. Histograms showing the surface roughness of the uncoated polymer (TOP) and the commercially coated polymer (BOTTOM).

In **Figure 7. 42** below are images of the scattering due to the surface roughness on a commercially coated and uncoated polymer film. In the images all the zeroth order of the optical system is removed and this is the reason why there is a dark spot in the middle. In this way the scattering due to the surface roughness can be visualised more clearly. The coated sample has a significantly higher amount of scatter which further reduces the diffraction efficiency and deteriorates the image quality. In order to overcome this problem, the addition of multiple layers in order to further reduce the surface roughness or development of a new application process.
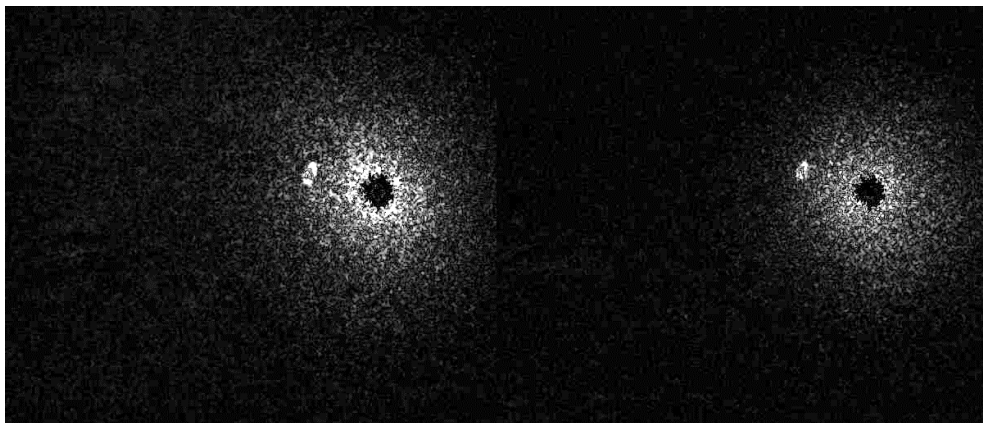
Figure 7. 42. Optical outputs from a plain polymer film showing the effect of scattering, image on the left is the optical output from the commercially over coated polymer and the image on the right is the optical output from the plain polymer film.

181

The technique developed in-house, in which the coating is applied in multiple layers (5) through successive spin coating, drying and UV curing. The average surface roughness here is around 9nm which is a significant improvement over the original coating. This is shown in the *Figure 7. 43* below.
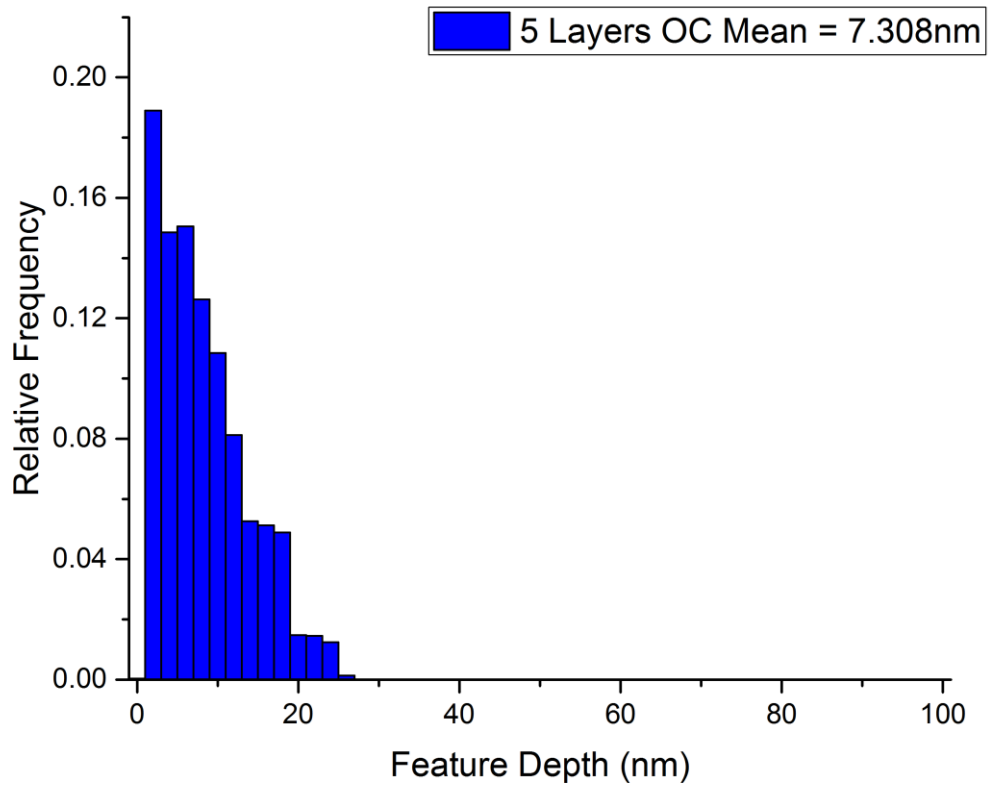
Figure 7. 43. Histogram showing the surface roughness of the in house filled polymer DPE.

7.12. Experimental Verification

The optical outputs from the fully coated polymer copies of Master 1, which is linearly pre compensated element with 12% compensation across the levels were taken to confirm the optical performance of the element can be seen in *Figure 7. 44* below. In regards to linearization of the moulding depths, the polymer copy has a gradient of 0.958 ± 0.012 and an intercept of -0.032 ± 0.013. The fitting is carried out with a 99.2% accuracy. This

indicates that there do still exist errors in the depths of the replicated copies of the order of 5%. An introduction of random noise of a 10% level for example would contribute to cross talk between the images of the two colours as well as zeroth order contributions. The optical output of the element under white light illumination clearly shows a dual colour operation, in which the '€' symbol appears in blue and the '200' appears in greenish red. Under blue, both the '€' and the '200' appear but the intensity of the '€' is greater than that for '200'. Finally under red light illumination, the '€' symbol has completely disappeared and the only visible image is '200'. All the images below have been corrected to simulate as viewed by the human eye.

	White Light	Blue	Red
Master 1			

Figure 7. 44.The optical outputs from in house filled polymer copy of Master 1. The left column shows the optical output upon illumination with white light, the middle column shows the optical output upon illumination with a blue laser and the right column shows the optical output upon illumination with a red laser.
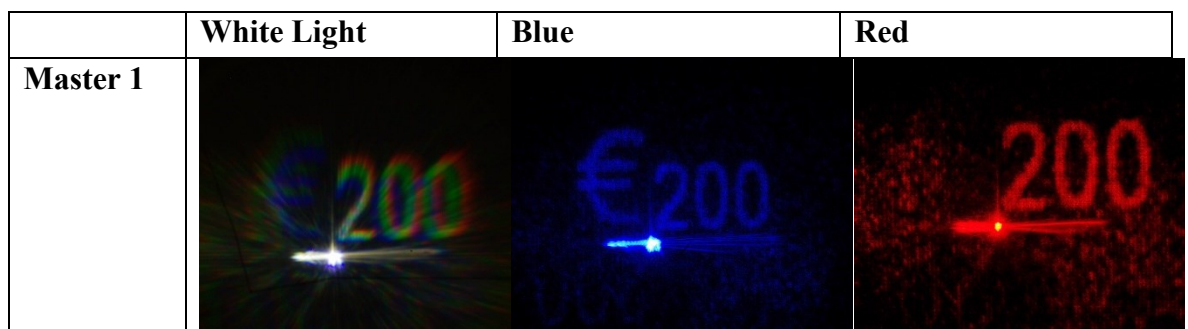
In terms of diffraction efficiency which is not critical when the main objective is the generation of an esthetically pleasing image to the naked eye, for the uncoated copy of Master 1 the blue stands at 47% and the red is 56%. On completely filling the relief profile with coating A, the efficiency for the blue falls to 37% while the red stays at 55%. This can be explained by the existing fabrication errors which will increase the amount of cross talk, especially at the lower wavelength, but not as much as observed in the image above. The next source comes from the refractive index difference between the base polymer and the overcoat. The base polymer used has a refractive index of 1.54 and Coating A was measured to have a refractive index of about 1.8. This gives a difference of 0.26 which is what the elements are designed for. By carrying out a pixel count, obtaining an average of the pixels in the image, dividing by the area of the image and multiplying that by the ratio of the maximum pixel value on the image for the a set of known laser wavelengths a ratio of intensities of the two images is carried out. This is shown in *Figure 7. 45* below, where the x axis is wavelength and the y axis is ratio of images.
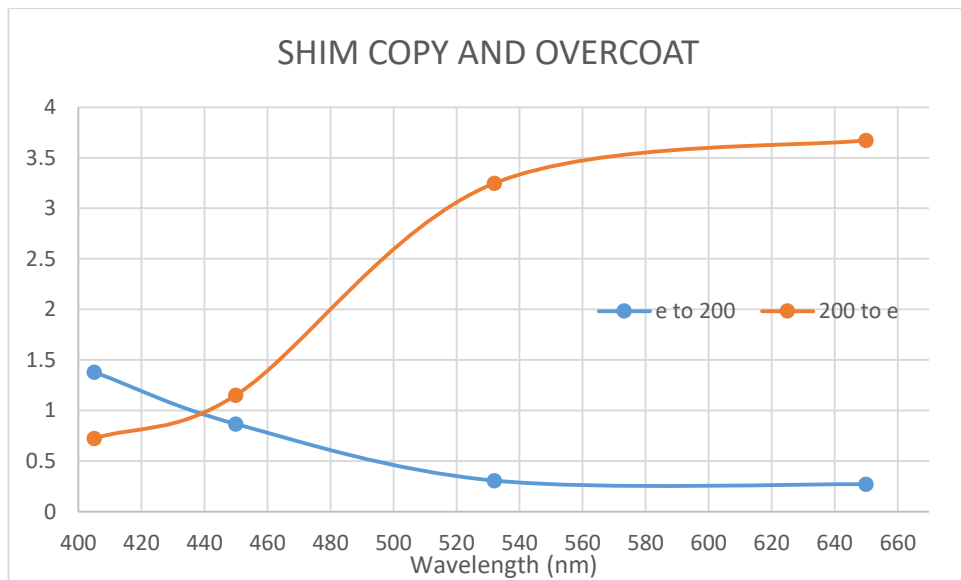
Figure 7. 45. The ratios of the intensity of the two images as a function of illumination wavelength for the in house filled shim polymer copy of master 1.

From the ***Figure 7. 45*** the position of equilibrium for the two images can be obtained. At this position it is assumed that the two images will have an equal amount of intensity distribution. For the fully coated polymer copy of master 1, this position is estimated to occur at ~ 442nm. Further on, from the measurements made on the coated fused silica master which was fully filled with coatings of known refractive indices, the refractive index difference can be estimated.
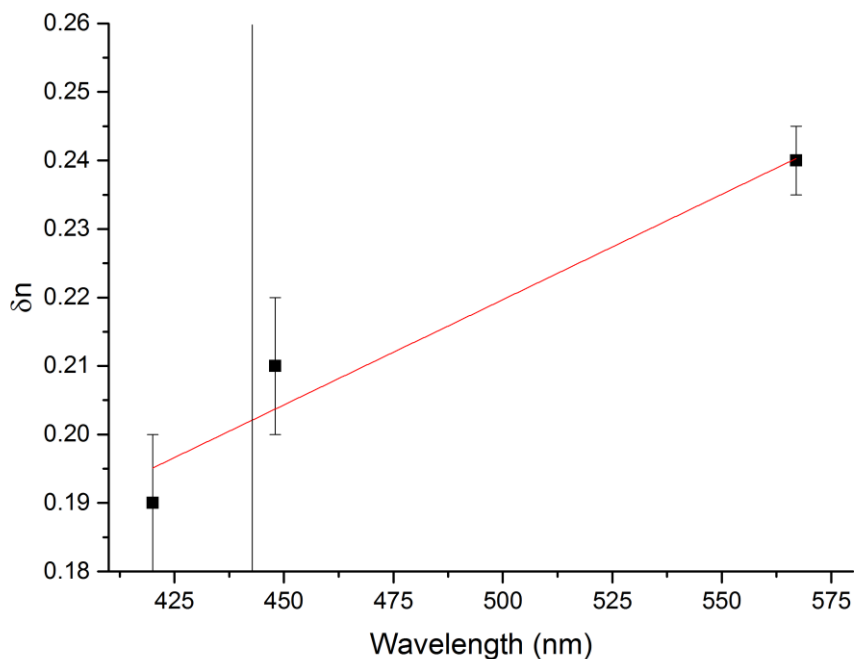
Figure 7. 46. The point of equal intensity distribution for the two images as a function of refractive index difference between the base substrate and the over coat. The line is where the over coated polymer copy of master 1 falls.

In the *Figure 7. 46* above, the line is a fit to the wavelengths of equal cross talk for the fused silica master with known overcoats. On fitting the cross talk wavelength of the polymer copy, a refractive index difference of about 0.21 is observed. It needs to be mentioned that the fused silica masters from which the data points were obtained are considered as perfect without the presence of fabrication errors. If fabrication errors were to be added, the refractive index difference would marginally increase. A simulation was carried out at the illumination wavelength of 442nm and by altering the refractive index difference, the cross talk of equal intensity was found to occur at ~0.22 which is broadly consistent with the estimated value from the measurements. Once again, no errors are considered and the structure is perfect, where in reality it isn't. However, it still proves that as the refractive index difference is lowered, the cross talk wavelength is shifted into the blue, the image from the shorter wavelength is pushed deeper into the UV for an image to occur with no cross talk and the longer wavelength image is not as affected by this. Below in *Figure 7. 47* is an image of the optical output of the element when illuminated by both wavelengths at the same time. The laser beams are combined to focus at a common point by using a 50:50 beam splitter. Dual colour operation is confirmed, despite some cross talk between the images at the lower wavelength, explained by the drop in refractive index difference and the associated fabrication and replication errors in the surface relief profile which are nearly impossible to adequately quantify.
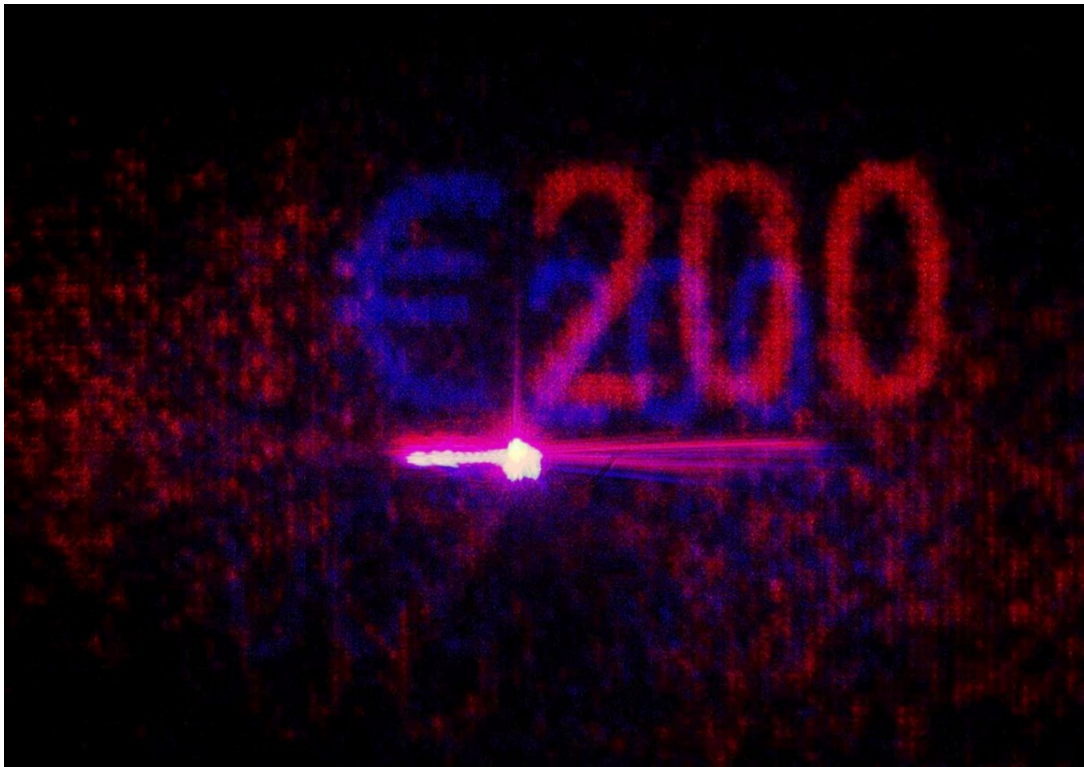

Figure 7. 47. The optical output from the in house filled shim polymer copy of master 1 upon illumination with both lasers simultaneously.

7.13. Conclusions

In this chapter the design, fabrication, experimental testing and effects that physical parameters of the overcoats have on polymer pseudo colour DPE. A technique for the fabrication of hard fused silica masters with a sufficiently accurate compensation scheme to account for volumetric material shrinkages has been developed and tested. The effects that linearization of the diffraction levels have on the optical output have been explored. Improvements in the fill factor of the over coat as well as the reduction of scatter through the reduction of surface scattering have been demonstrated. The effects that coatings have on the diffraction efficiencies of the device have been shown and a fully functional two colour operation polymer DPE has been produced and tested. Suggestions for further improvements have been made in the commercial over coating process to improve the device outputs.

7.14. References

[1] H. Hua, Y. Ha, and J. P. Rolland, "Design of an ultralight and compact projection lens.," *Appl. Opt.*, vol. 42, no. 1, pp. 97–107, 2003.

[2] M. L. Cowan, J. P. Ogilvie, and R. J. D. Miller, "Two-dimensional spectroscopy using diffractive optics based phased-locked photon echoes," *Chem. Phys. Lett.*, vol. 386, no. 1–3, pp. 184–189, 2004.

[3] A. J. Caley, A. J. Waddie, and M. R. Taghizadeh, "A novel algorithm for designing diffractive optical elements for two colour far-field pattern formation," *J. Opt. A Pure Appl. Opt.*, vol. 7, no. 6, p. S276, 2005.

[4] S. Noach, A. Lewis, Y. Arieli, and N. Eisenberg, "Refractive Elements for Spectrum Shaping," vol. 35, no. 19, 1996.

[5] A. Brown, S. Collard, and M. Spearritt, "Recent Trends in Banknote Counterfeiting," pp. 67–74, 2017.

[6] E. Kim and T. Turton, "The next generation banknote project," *Bulletin*, no. March Quarter, pp. 1–12, 2014.

[7] M. D. Austin *et al.*, "Fabrication of 5 nm linewidth and 14 nm pitch features by nanoimprint lithography," *Appl. Phys. Lett.*, vol. 84, no. 26, pp. 5299–5301, 2004.

[8] S. Y. Chou, P. R. Krauss, and P. J. Renstrom, "Imprint of sub-25 nm vias and trenches in polymers," *Appl. Phys. Lett.*, vol. 67, no. 1995, p. 3114, 1995.

[9] M. Colburn *et al.*, "Step and Flash Imprint Lithography: A New Approach to High-Resolution Patterning," *Spie Conf. Emerg. Lithogr. Technol. III*, vol. 3676, no. March, pp. 379–389, 1999.

[10] D. J. Resnick, S. V. Sreenivasan, and C. G. Willson, "Step & flash imprint

lithography," *Mater. Today*, vol. 8, no. 2, pp. 34–42, 2005.

[11] F. Hua *et al.*, "Polymer imprint lithography with molecular-scale resolution," *Nano Lett.*, vol. 4, no. 12, pp. 2467–2471, 2004.

[12] De Vries, A. J.. Structure-properties relationships in biaxially oriented polypropylene films. Polymer Engineering & Science, 23(5), 241-246. 1983. .

[13] H. Schift, "Nanoimprint lithography: An old story in modern times? A review," *J. Vac. Sci. Technol. B Microelectron. Nanom. Struct.*, vol. 26, no. 2, p. 458, 2008.

[14] L. . Heyderman, H. Schift, C. David, J. Gobrecht, and T. Schweizer, "Flow behaviour of thin polymer films used for hot embossing lithography," *Microelectron. Eng.*, vol. 54, no. 3–4, pp. 229–245, 2000.

[15] Y. Hirai, T. Konishi, T. Yoshikawa, and S. Yoshida, "Simulation and experimental study of polymer deformation in nanoimprint lithography," *J. Vac. Sci. Technol. B Microelectron. Nanom. Struct.*, vol. 22, no. 6, p. 3288, 2004.

[16] K. S. Kim, J. H. Kim, H. J. Lee, and S. R. Lee, "Tribology issues in nanoimprint lithography," *J. Mech. Sci. Technol.*, vol. 24, no. 1, pp. 5–12, 2010.

[17] A. I. Isayev and T. Hariharan, "Volumetric effects in the injection molding of polymers," *Polym. Eng. Sci.*, vol. 25, no. 5, pp. 271–278, 1985.

[18] R. W. Gerchberg and W. O. Saxton, "A practical algorithm for the determination of phase from image and diffraction plane pictures," *Optik (Stuttg).*, vol. 35, no. 2, pp. 237–246, 1972.

[19] M. R. Taghizadeh, P. Blair, B. Layet, I. M. Barton, A. J. Waddie, and N. Ross, "Design and fabrication of diffractive optical elements," *Microelectron. Eng.*, vol. 34, no. 3–4, pp. 219–242, 1997.

[20] C. Jalbert, J. T. Koberstein, A. Hariharan, and S. K. Kumar, "End Group Effects on Surface Properties of Polymers: Semiempirical Calculations and Comparison to Experimental Surface Tensions for α,ω-Functional Poly(dimethylsiloxanes)," *Macromolecules*, vol. 30, no. 15, pp. 4481–4490, 1997.

[21] http://www.australianbanknotes.net/ten_dollar_banknotes/r310a.htm.

[22] http://www.banknotenews.com/files/tag-mexico.php.

[23]

http://home.ufam.edu.br/berti/nanomateriais/Nanoimprint20Lithography20 E2809320Patterning20of20Resists20Using20Molding.pdf.

Chapter 8. Conclusions

As mentioned in the introduction chapter, the main theme of the thesis is the numerical and experimental verification of structured micro and nano scaled optical devices. The work described in this thesis is built on from the work previously carried out by Dr Andrew Waddie and Prof. Mohammad Taghizadeh. The collaborators from AWE, Ian Thurston and Micheal Moutrie provided valuable insight into EM shielding of detectors. The design, fabrication and characterisation of the optical sensors was where the added value of the candidate came from. The initial concept of the pulse position gratings is attributed to Dr Paul Blair and the further work carried out with the aim of improvement in the image quality with the aim of mass replication was where the added value came from. The idea for the dual colour diffracted optical elements came from Dr Adam Caley, which was further developed with the aim of using the devices for security applications. This thesis being split into two parts, one looking at optical devices used for sensing applications and the second looking at devices used for mass replication and security applications.

In Chapter 4, the design and experimental verification of an optical waveguide extrinsic fibre optic sensor was demonstrated. The fabricated waveguides had a width of 1μm spaced by 900nm etched into a suitable electro-optic based substrate (Lithium Niobate) and were used for the determination of both the peak EMP field strength as well as the temporal pulse shape of the incident EMP. This sensor design is capable of measuring peak field strengths ranging from 50kV/m to 500kV/m with a pulse duration of the order of a few hundred nanoseconds. The issues which were identified after the fabrication and testing of this device geometry were carefully considered and addressed through a reduction in the device size of the next device geometry.

In Chapter 5, the design and experimental verification of a nanostructured surface plasmon enhanced extrinsic fibre optic sensor was demonstrated. The fabricated nanostructures are made up of periodic arrays of 280nm diameter nanoholes on a periodicity of 620nm. The aforementioned periodic arrays of nanoholes were inscribed on the same electro-optic substrate as used in the previous chapter. The sensor was shown to be capable of determining the peak field strength and temporal pulse shapes of incident EMP with a tested range of 50kV/m to 400kV/m with a pulse duration of the order of a few microseconds. An issue identified during the fabrication of the waveguide based optical sensors were the losses due to the butt coupling of the optical fibres to the

waveguides, which was addressed through increasing the dimensions of the array to match the fibre core size. The alignment procedure of multiple fibres from the waveguide sensor outputs was eliminated by using just one output in this design. The complexity and potential source of errors due to multiple steps during the fabrication procedure of the waveguide was reduced in this design making the processing easier with less steps. During the data analysis from the waveguides, the presence of a high finesse micro cavity was identified, causing the devices to follow a roughly sinusoidal response as a function of increasing incident EMP strength. This problem was addressed by propagating the incident light beam through a much shorter length of material and linearising the response from the nanostructured sensors.

From the table summarising the characteristics of the devices developed in chapters 4 and 5 of this thesis to both commercially available and other optical devices, it can be stated that biggest advantage of these devices comes from their physical footprint. The response of the devices is lower than the other two devices but that comes from the nature of the pulses detected. The noise equivalent voltage of the waveguide sensor is similar to the other two devices while the nanohole sensor is about two orders of magnitude higher. This can be reduced by increasing the sampling frequency of the system. The greatest advantage of the devices developed comes from the volume of metal in the device. Both of the devices have about 9 orders of magnitude less metal in comparison to the commercially available d-dot sensor.

Table 8.1 Comparison of characteristics of EMP sensing devices.

	Waveguide Sensor	Nanohole Sensor	Prodyn AD-20 (Commercial Sensor)	Optical Sensors from literature
Response (GHz)	>0.63	>0.03	>10	>1
Rise Time (ns)	<1.57	<33	<0.029	<1
Output (V)	1-5	1-5	150	n/a
Mass (g)	6.6	6	40	n/a
Dimensions (L x B xW) (mm)	25 x 15 x 8	40 x 20 x 8	390 x 25 x 10	85 x 15 x 10
Noise Equivalent Voltage (nV/Hz$^{1/2}$)	6.8	140	5.2	4 – 20
SNR (50kV/m)	1.6	1.5	n/a	1.5

In terms of EMP sensing on comparing both devices, a reduction in the device size is beneficial to the capabilities of the devices and leads to improvements in both performance of the devices and ease of integration to fibre systems.

In Chapter 6, high frequency pulse modulated gratings were designed and experimentally tested for mass replication and security applications. The gratings had dimensions measuring 250nm on a period of 520nm. These gratings were modulated to generate high fidelity images only upon illumination at the Bragg angle with diffraction efficiencies of ~70% adding an extra security feature. These gratings are designed in the resonance domain due to their feature sizes and the limitations of the scalar domain. The signal window appear in the -1st diffraction order eliminating the scatter due the 0th order. The phase depths are much shallower (of the order of the incident light wavelength) and the structures are binary when compared to multilevel diffractive elements making them suitable to act as masters in the shim formation process during mass replication with less expected material shrinkage to occur.

In Chapter 7, dual colour multilevel diffractive phase elements were designed and fabricated to be used for security applications. The elements were designed in the scalar domain using the IFTA approach and had minimum feature sizes of 6μm and 8μm respectively. The image appears in the 0th order and diffraction efficiencies for blue and red were measured to be ~37% and ~55%. The phase depths are ~8 times deeper compared to elements designed in the resonance domain which introduces a much greater volumetric shrinkage during the replication process. A technique was developed for the fabrication of the hard masters with a sufficiently accurate compensation scheme to account for aforementioned shrinkage, showing a greater precision at shallow depths. The optical outputs from the replicated flexible polymer copies made were greatly improved with improvements made to the infill factor to reduce the 0th order scatter and the cross talk between the two images.

In terms of mass replication and security applications of optical devices, a reduction in the device size does have benefits such as increased diffraction efficiencies, elimination of 0th order scattering causing image degradation, non-normal incidence image formation, less volumetric shrinkage during the replication process and the lack of twin imaging which is usually experienced by scalar domain binary devices. There do exist downfalls as well such as; the resonance domain can only be used for single colour elements which

would appear in the same order, the shallower binary structures are more challenging and time consuming to fabricated accurately and potentially easier to replicate due to the shallow phase depths. Having a reduction in the feature size does lead to an improvement in the device characteristics, but the application governs the final design.

Future Work

With regards to the waveguide based optical sensors, the design could be changed to only have 2 outputs rather than the current 3 which would greatly aid the fabrication process. An alternative approach could be implemented for coupling of light into the waveguides such as surface coupling using a grating and minimise the coupling losses. The waveguide sensors could also be cleaved at an angle prior to coupling with the optical fibres to minimise the effect that the high finesse micro resonator has as well as launching light with a tuneable and scanning across the wavelength range of the light source in order to verify the existence of the cavity.

Further work that can be performed to improve the performance of the nanostructured optical sensors could come from the form of a Bragg mirror which would surround the array and has been shown to increase the plasmonic response. Materials other than noble metals such as doped Zinc Oxide could be investigated as alternative plasmonic layers which will shift the plasmonic resonances into the infra-red enabling the use of single mode fibres with lower transmission losses. Improvements could be made to both the detection electronics as well as the in-house pulse generation system to generate more consistent pulses. Three of these devices can be used in conjunction to try and estimate the direction of the pulse.

The high frequency modulated gratings can be used to generate a metallic shim made for replication in order to verify the predictions made in regards to the volumetric shrinkages of shallower structures.

The scalar domain diffractive elements have been redesigned since the writing of this thesis, and the optical pattern has been changed in order to account for the observed cross talk between the two images. The commercial over coating process can be improved by increasing the deposition rate of material to ensure adequate in filling of the polymer copies or running it a few times in order to achieve greater fill factor.

Chapter 9. Appendices

9.1. Chapter 4

The holders for the waveguide photonic device are fabricated out of fused silica carriers. Fused silica was chosen because for its excellent transmission in the UV range permitting for the use of UV curing optical adhesives for securing the individual components in place. SMF-28e single mode optical fibres with a $10.4 \pm 0.5\mu m$ MFD @ 1550nm were used because of their low transmission losses of 0.2dB/Km at that wavelength. The fibres are terminated by FC/APC butt couplers with the ends cleaved at 8 degrees to the vertical minimising back reflections.

9.1.1. Part 1 (External Holder)

The base carrier is milled from two pieces of solid fused silica which were glued on top of each other with the central groove used for holding and aligning the fibres and photonic device milled out secondarily. The two cuts on the groove where the fibre holders rest are spaced out by 4.02mm and are milled using a 200μm thick blade with a grit size of 1200. The large grit size ensures that no glass chipping occurs during the cutting. Then second groove was then milled inside the first groove, with a width measuring at 3 mm. The purpose of the second groove is for the fibres to rest inside and for the optical cement to flow freely without disrupting the fine alignment between the fibres and the photonic waveguide device. The second groove was milled using a blade with a 800μm thickness and a grit size of 400, to minimise milling time and the lack of need for fine alignment in this part. The third grooves was milled, in order to facilitate the free sliding of the fibre holder holding the three output fibres. This was done because the three adjacently placed fibres are glued in with their polymer outer jackets , which have a combined width of 2.5mm. The side walls in between the central fibre and the two adjacent side fibres were 300μm which brought up the total width up to about 3.2mm, hence preventing the carrier from fitting inside the second groove. Hence two grooves on either side of the second groove are milled with dimensions of 400μm width and 300μm depth. The third grooves were made with the 800μm thick blade with grit size of 400. This is done in order to make sure that the three holders all have a flat surface to rest on and allowing for a precise alignment to be carried out. The CAD drawings produced by using Solid Edge below show the part in all three orientations and all dimensions are in mm.
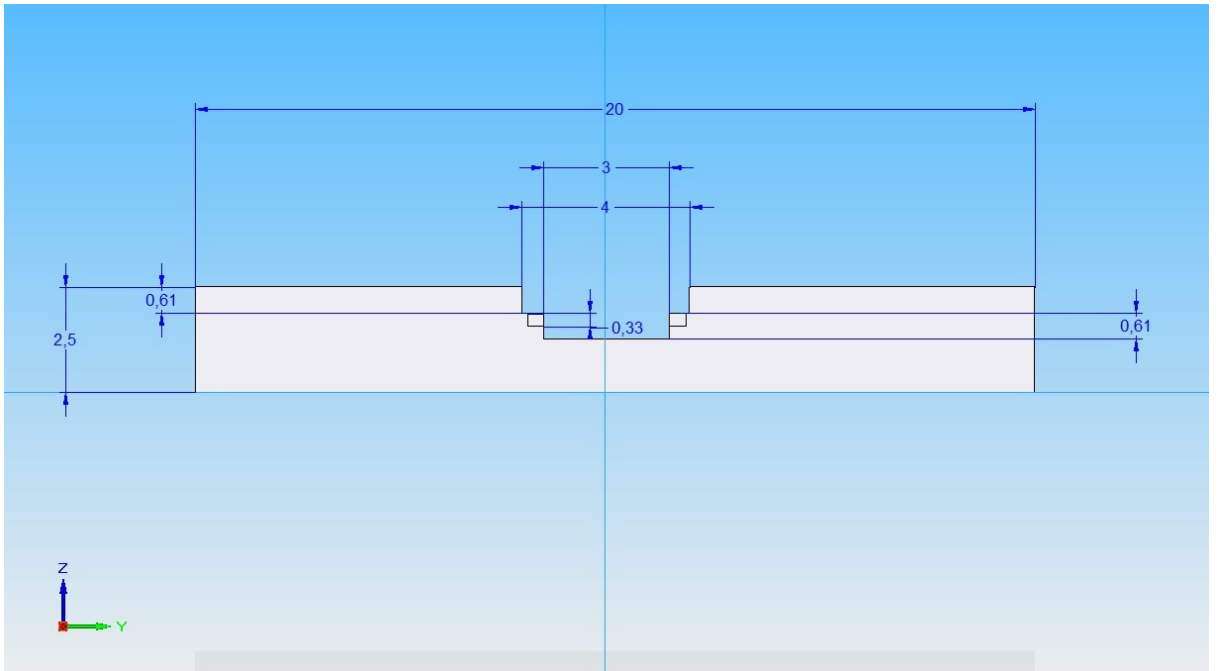
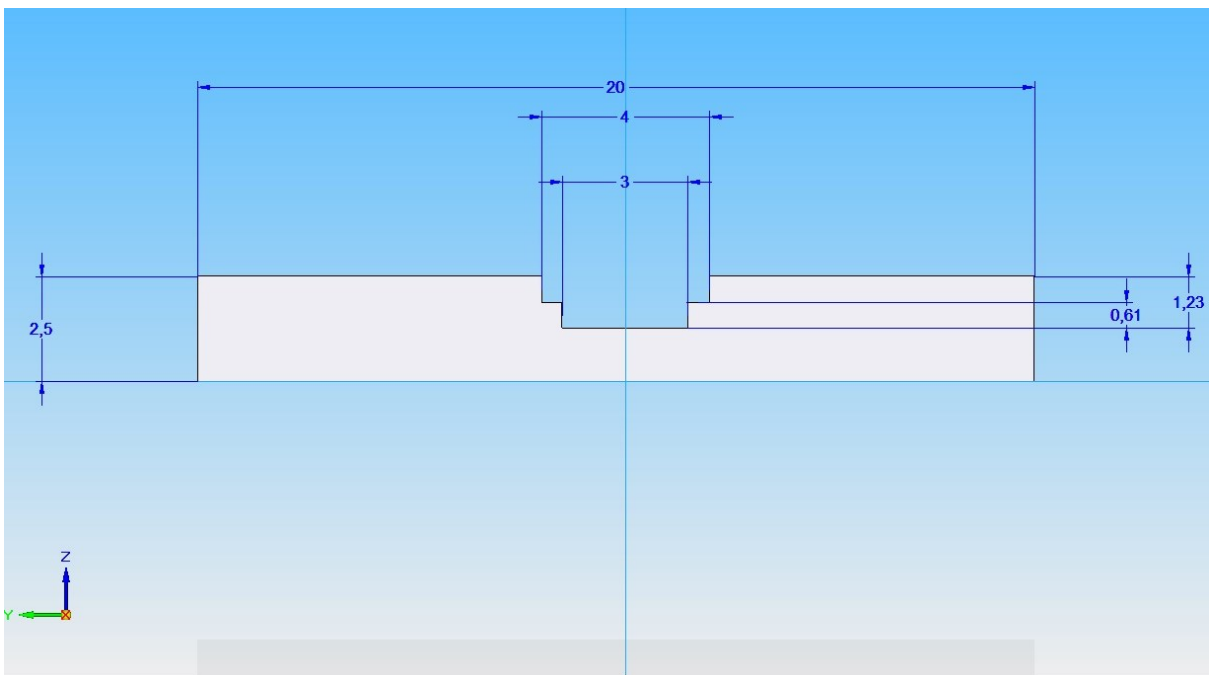*Figure A1. 1 Front view of waveguide sensor carrier (Part 1)*

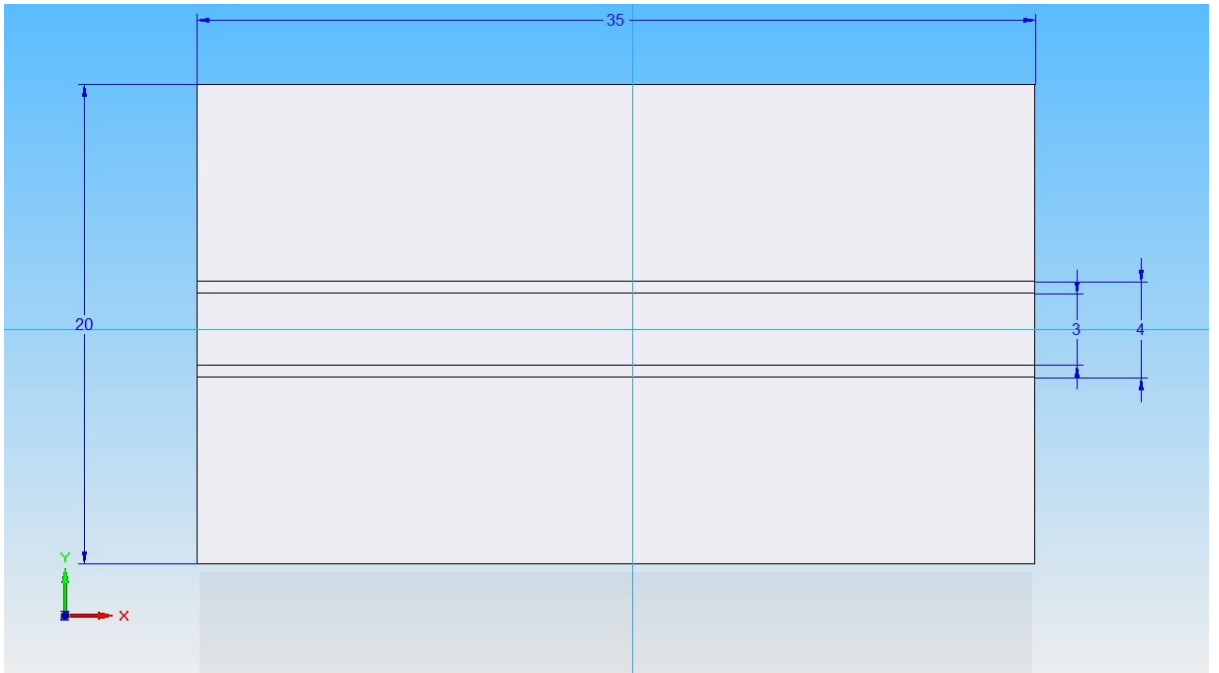*Figure A1. 2 Back view of waveguide sensor carrier (Part 1)*

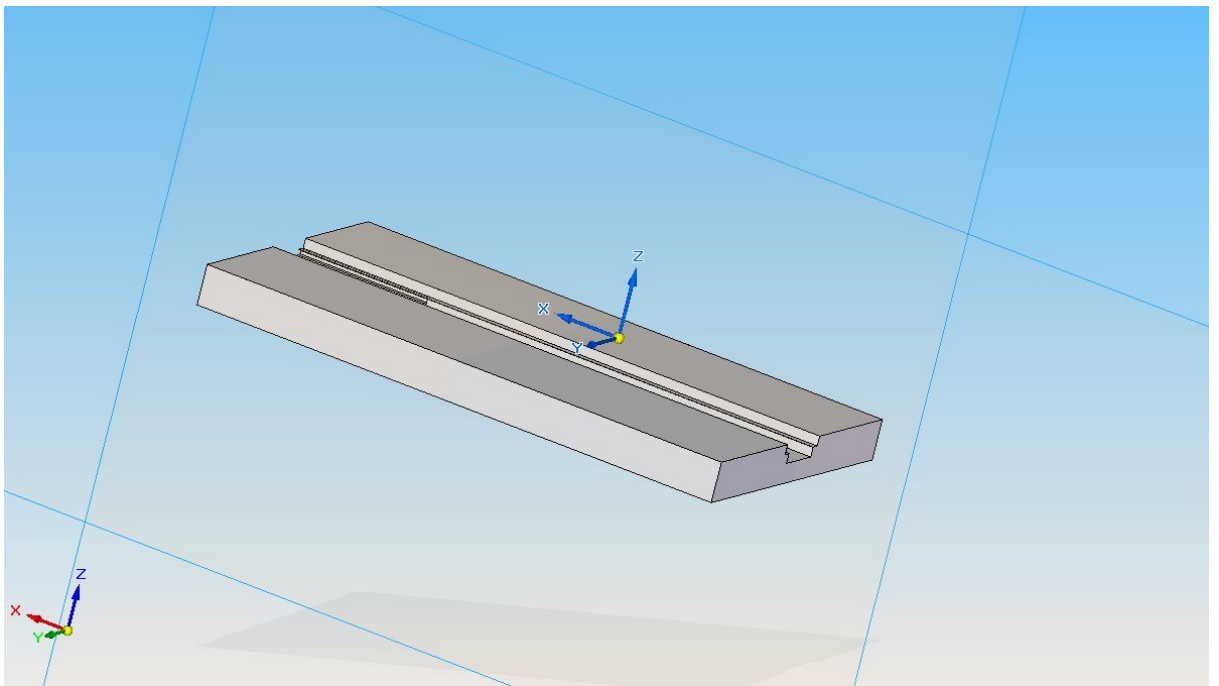*Figure A1. 3 Top view of waveguide sensor carrier (Part 1)*
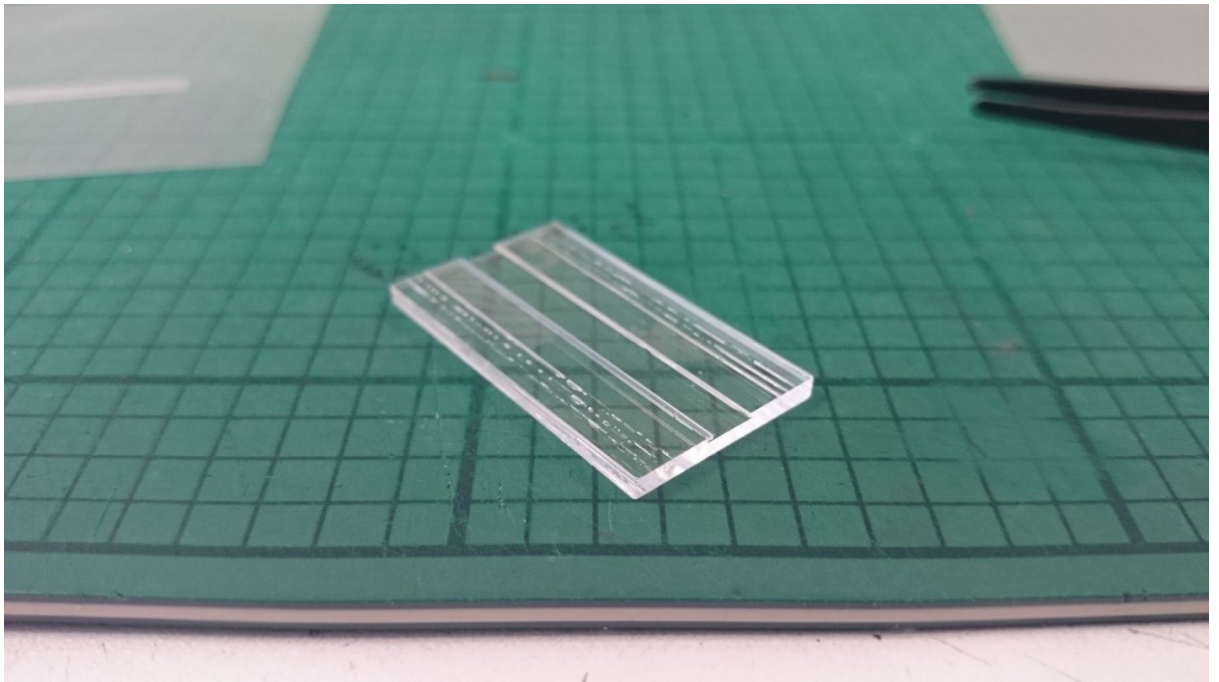

Figure A1. 4 CAD drawing of part 1

Figure A1. 5 Part 1 fabricated from fused silica

9.1.2. Part 2 (Input Fibre Holder)

The input fibre holder is milled from a solid piece of fused silica. The first groove milled in the centre of the carrier was milled using a 100μm thick blade. The groove measures 136μm in width and 300μm in depth. This groove provides the alignment for the input fibre and space for the optical cement to penetrate into without disrupting the positioning of the fibre. A second groove is milled on top of the first. This is carried out using a 200μm thick blade and the groove measures 250μm wide and 54μm deep. Using this setup, the cores of the fibres are flush with the surface of the fused silica top surface. When using the 100μm thick blade for the first set of grooves, issues regarding the blade deflection were noticed. To solve this the blade was sandwiched between two other blades . The cuts were stepped by 40μm for each step. The fibres are secured in place using a thin optical cement (NOA 84), which has a very low viscosity and is ideal for bonding glass. During curing the fibres are pressed down to ensure that the optical cement only flows inside the first groove and does not form a thin layer underneath the fibre due to capillary action, thereby lifting it and producing a source of misalignment. The figures below are CAD drawings showing the part in all three orientations. All dimensions are in mm.
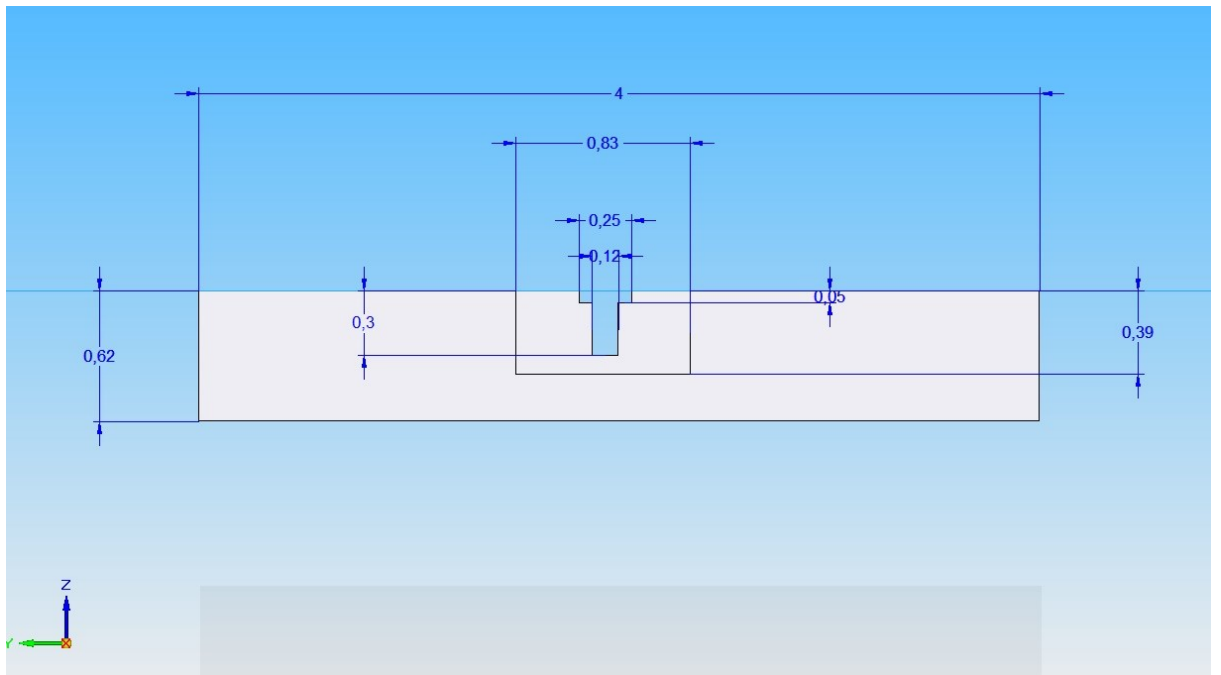
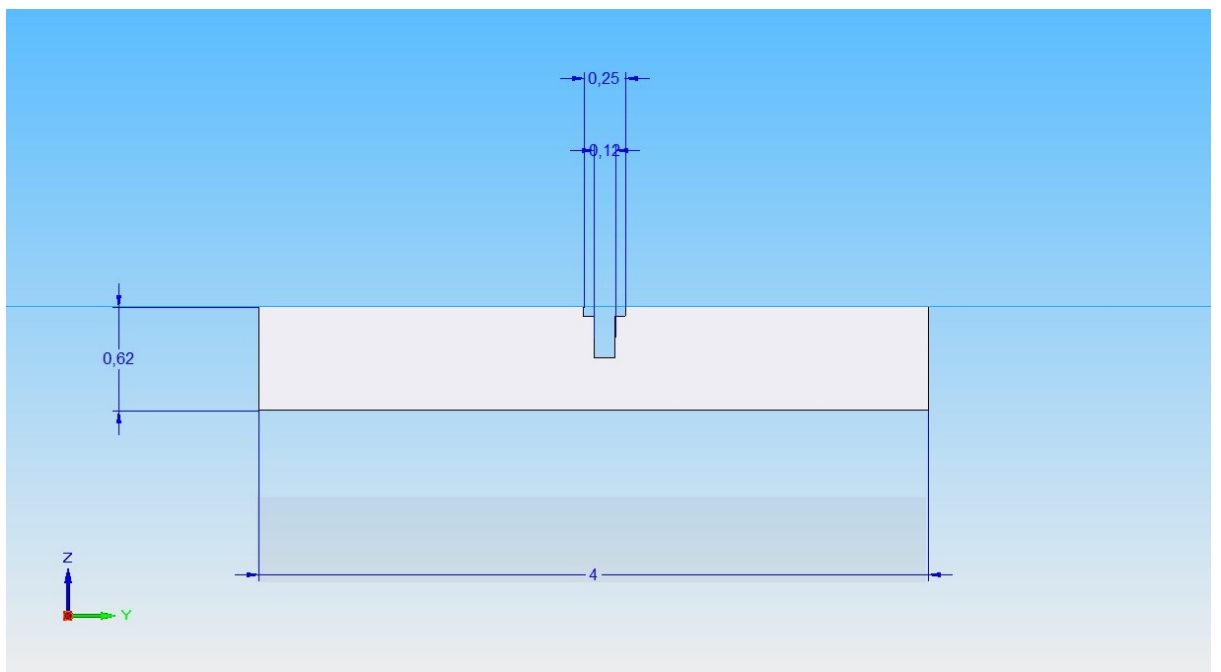*Figure A1. 6 Front view of waveguide sensor carrier (Part 2)*

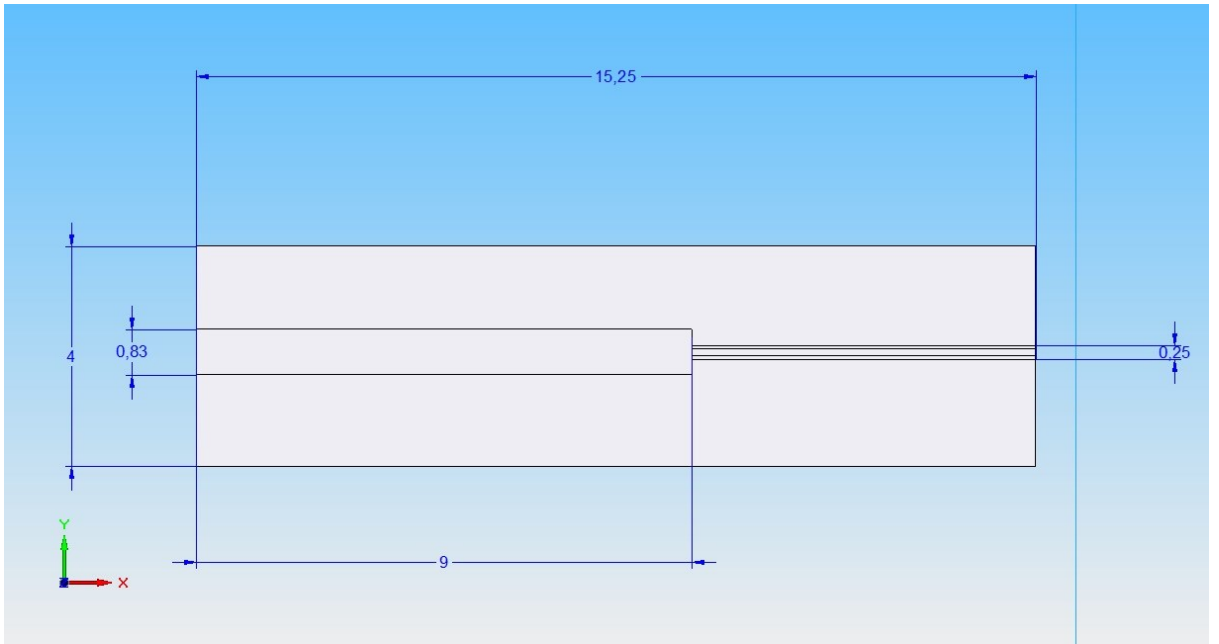*Figure A1. 7 Back view of waveguide sensor carrier (Part 2)*

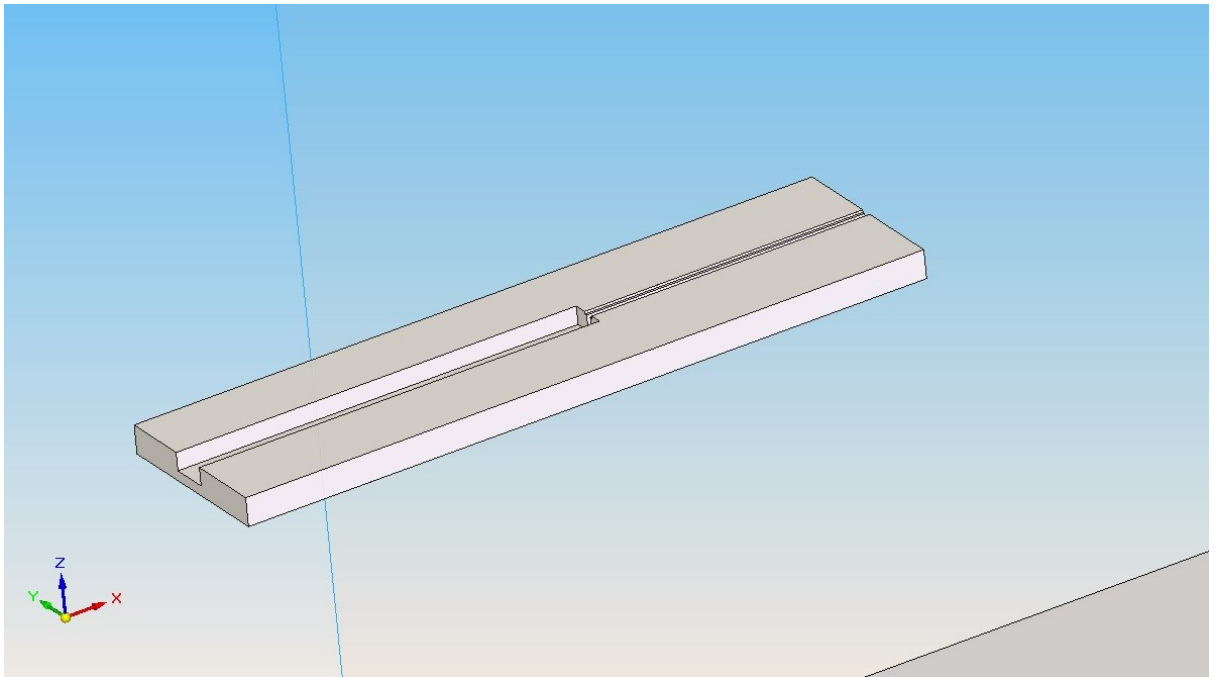*Figure A1. 8 Top view of waveguide sensor carrier (Part 2)*

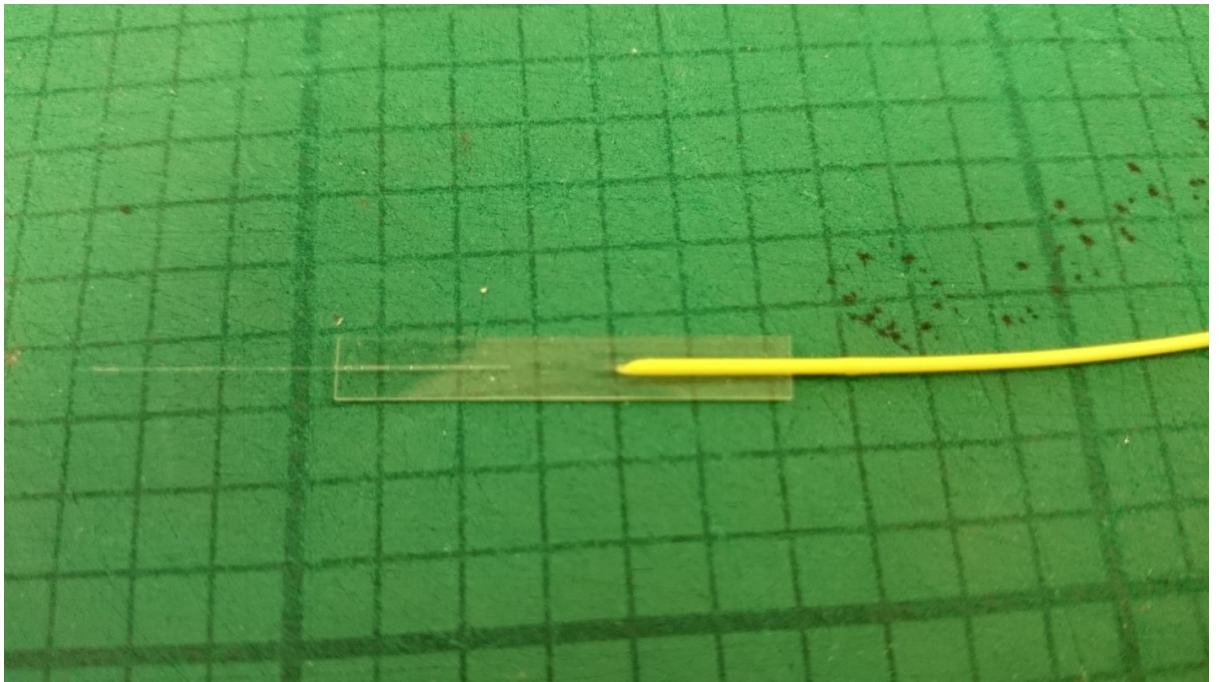
Figure A1. 9 CAD drawing of part 2

Figure A1. 10 Part 2 fabricated from fused silica.

9.1.3. Part 3 (Output Fibre Holder)

The holder for the output fibres is also milled from a fused silica piece. It is fabricated in exactly the same way as the input fibre holder. The spacing between adjacent milled grooves is 1mm. The first set of grooves milled were made using a 100μm thick blade and they measure 136μm wide and 300μm deep. The middle groove is milled first taking a corner of the holder as a reference point and then the two adjacent side grooves are milled by offsetting the 1mm in either direction respectively. The second set of grooves positioned right on top of the first are milled using the 200μm thick blade and measure 250μm wide and 54μm deep from the top surface of the glass carrier plate. The third set of grooves which hold the polymer jackets of the fibres are milled using the 800μm thick blade, they measure 830μm wide and 300μm deep and are spaced by 300μm apart. The third set of grooves are designed for the polymer jackets to rest in and provide the necessary structural rigidity both in terms of securing the fibres as well as handling. The optical cement used for gluing the polymer jackets is (NOA 85), which has high viscosity and is used for bonding glass.
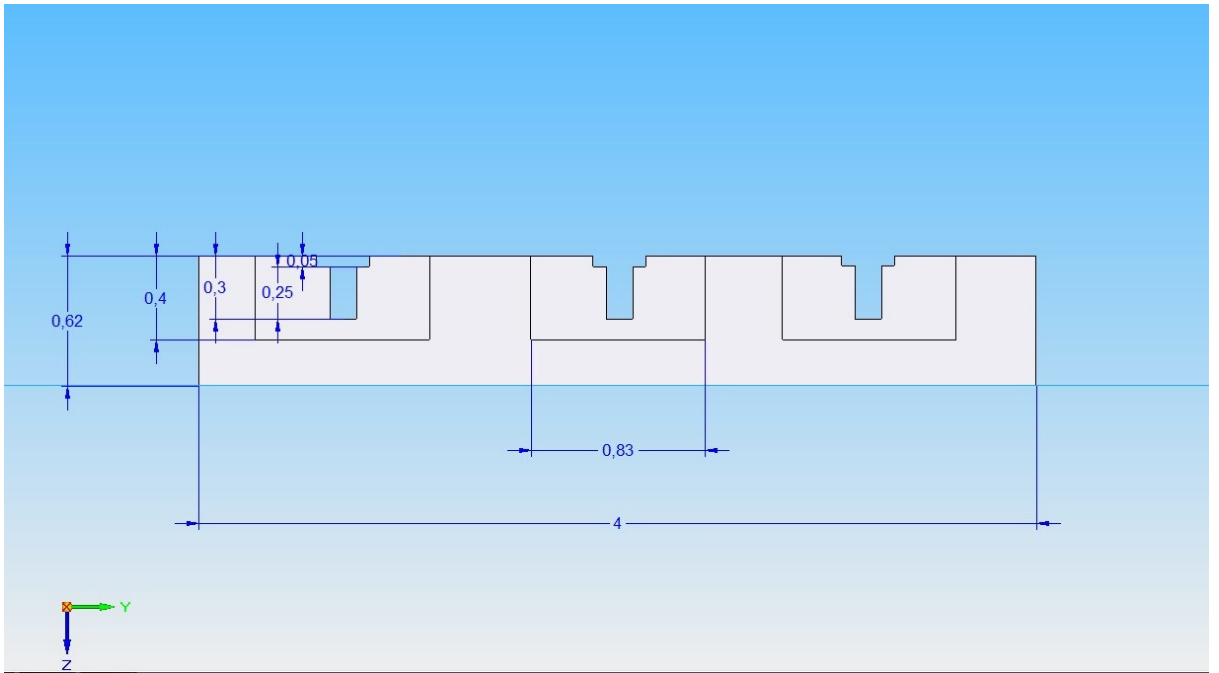
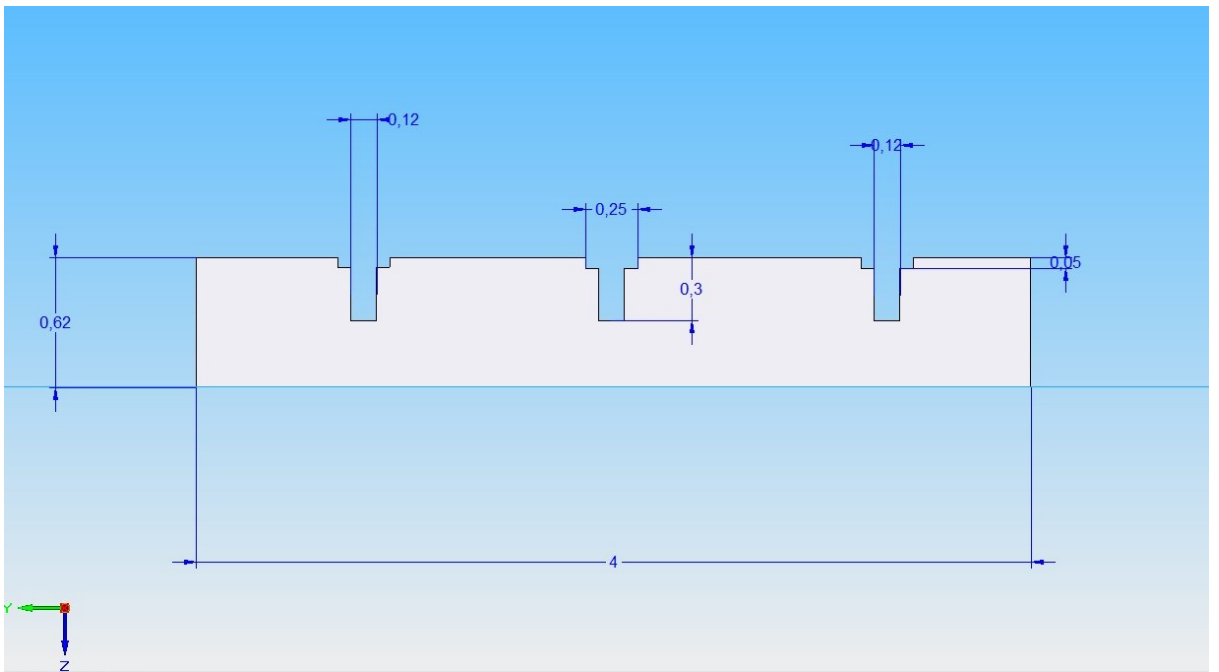*Figure A1. 11 Front view of waveguide sensor carrier (Part 3)*

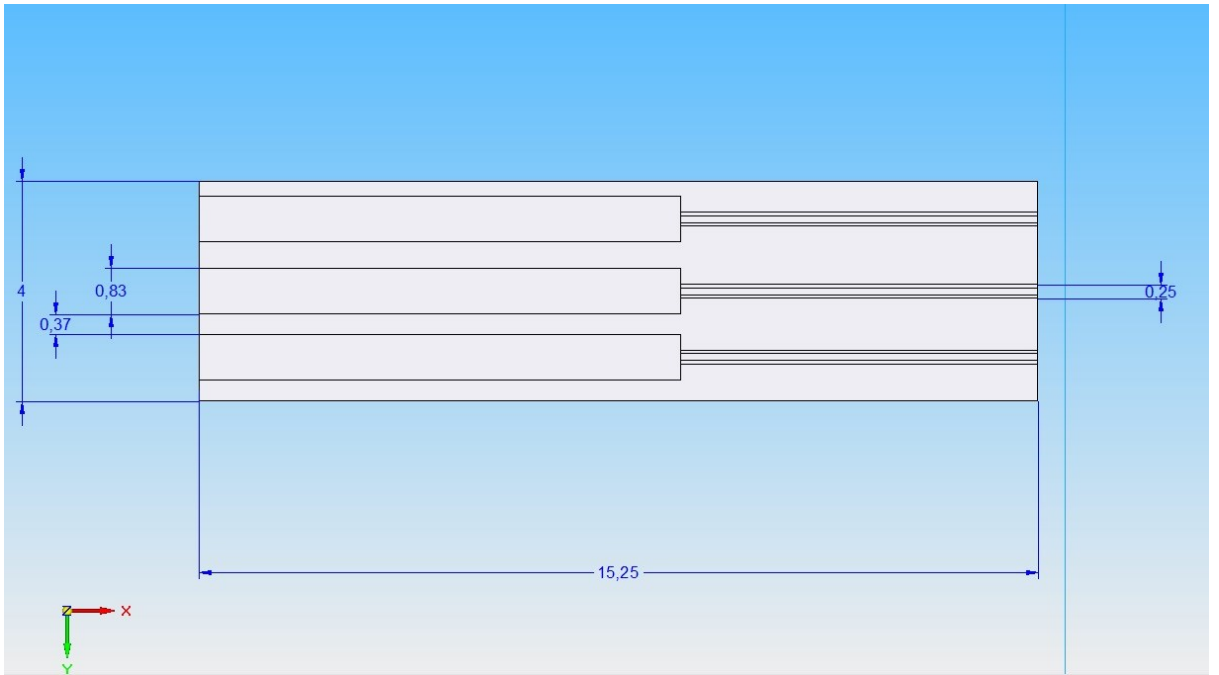*Figure A1. 12 Back view of waveguide sensor carrier (Part 3)*

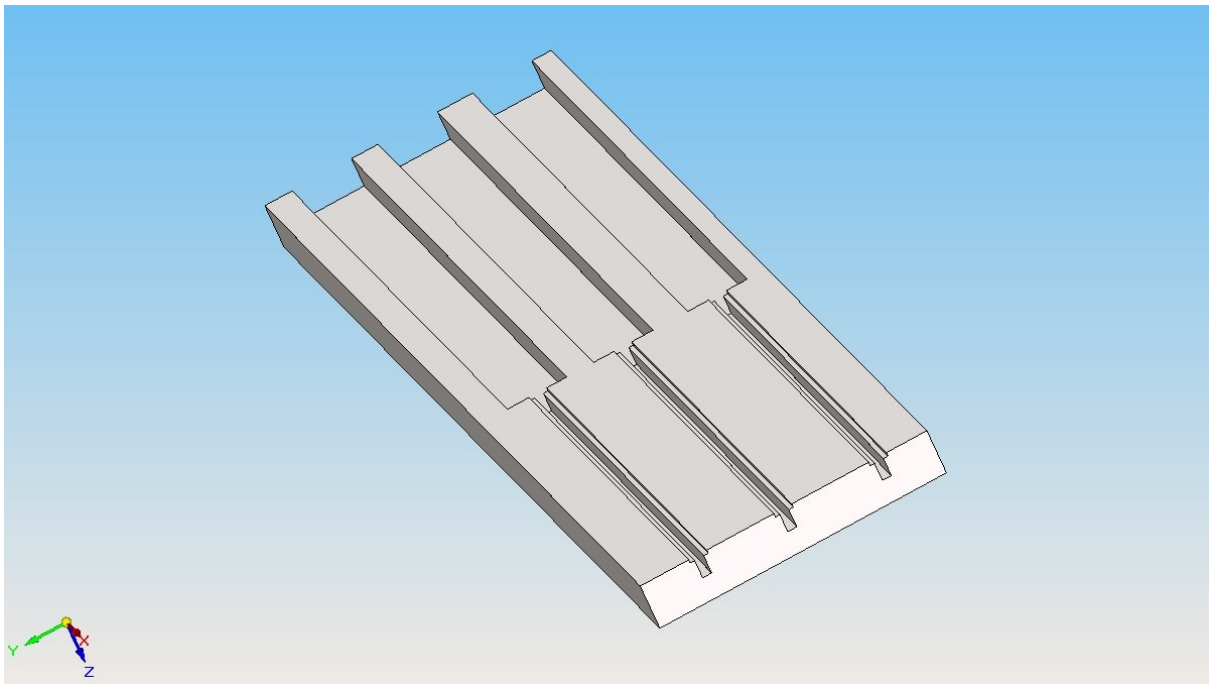*Figure A1. 13 Top view of waveguide sensor carrier (Part 3)*

Figure A1. 14 CAD drawing of part 3
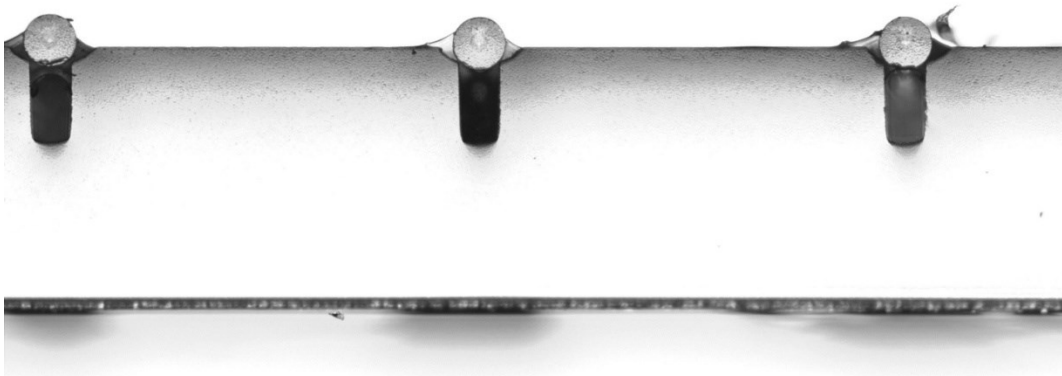
Figure A1. 15 Part 3 fabricated from fused silica

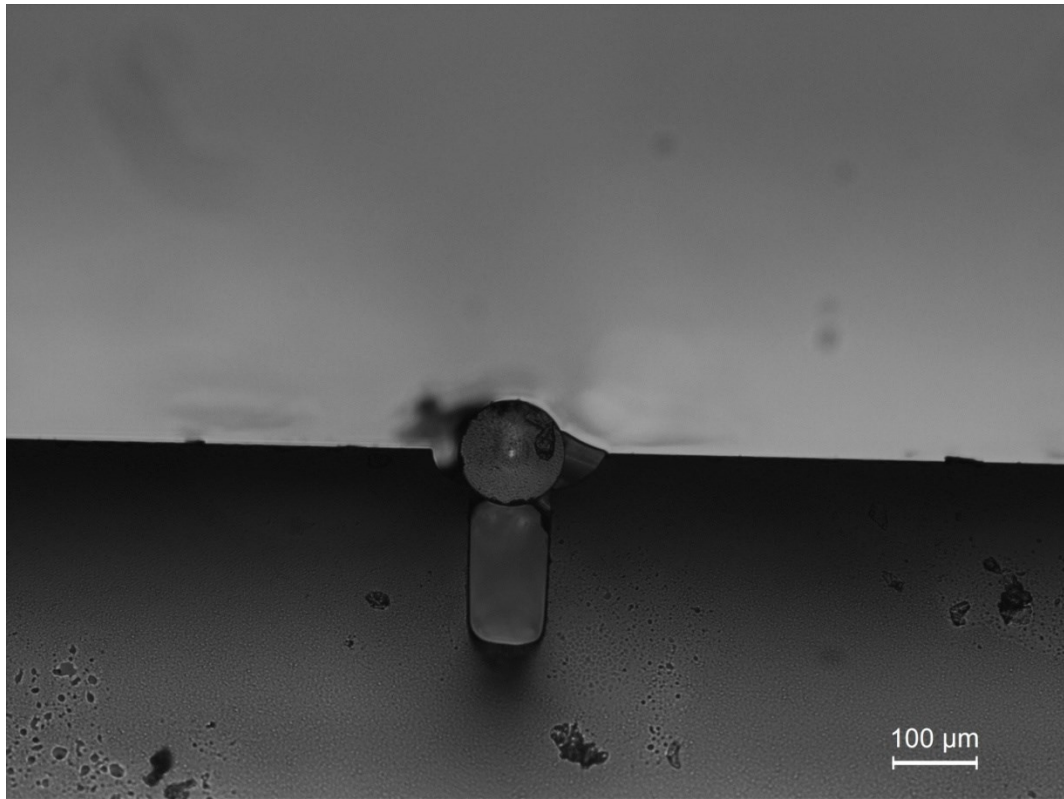*Figure A1. 16 Side view of part 3 with fibers glued in place*

9.1.4. Part 4 (Waveguide Holder)

From rigorous trials it was observed that Lithium Niobate chips easily during milling and dicing. After processing infilling and back polishing the excess material from the waveguides, those are placed with the top surface against a fused silica carrier and diced down into the necessary dimensions. The dicing is carried out at a slow feed speed of 0.5mm/s with a 200μm thick blade with a grit size of 1200. The blade is always preconditioned prior to cutting to ensure that the cuts are clean with minimal chipping and of adequate size (the 200μm blade produces 212μm cuts). The overall dimensions of the waveguide holder are 4mm wide, 4.850mm long and 0.463mm thick.

The sensor is assembled by placing all the parts with their top surfaces against the bottom of the groove surfaces of part 1. The alignment is carried out in real time by launching a red light fibre coupled laser into the input fibre and monitoring the output optical fibre prior to the final curing with all the parts in place.

9.2. Chapter 5

The holder for the nano hole device is made out of fused silica base plates. Fused silica was chosen for its excellent transmission properties in the UV properties in the UV range hence permitting for the use of UV curing optical adhesives as well as the cut quality and the low chip rate experienced during milling. GIF-625 multimode fibres with a 50μm core diameter. The fibres are terminated with FC/PC butt couplers aiding the connection of the device to commercially available laser sources and optoelectronic detection hardware.

The base carrier is milled from one piece of fused silica with dimension as follows; length – 40mm, width – 20mm and thickness – 2.35mm. A groove which holds the fibres is milled across the length of the carrier. The fibres have a polymer buffer jacket which measures 1.95mm in diameter. In order to improve the rigidity of the of the holder, the fibre patch cords are not stripped to their claddings but left with the polymer jackets. The groove which holds this fibre polymer jacket has a width of 2mm and a depth of 1mm. The groove is milled with a 400μm thickness blade with a grit size of 800 to ensure minimal level of material chipping during milling. To achieve the final width of 2mm, the blade was stepped 9 times with a spacing of 200μm between steps. The fibres are secured to the carrier using an epoxy resin which is left to cure and harden for 24 hours before the next cut. After the fibre has been cured in place, a cut which is perpendicular to the fibre is made. This cut is made using the same aforementioned blade and the cut measures 623μm in width with a depth of 1mm. This is the slot where the substrate patterned with the nano holes fits in. The substrate is milled in order for the nano hole arrays to fall right in the centre of the core of the fibre. The bottom edge of the substrate to the bottom of the array measures 0.75mm.